VIBRATIONALLY-MEDIATED CHEMICAL DYNAMICS

EDITED BY: Jacob Dean, Doran Bennett, Margherita Maiuri and Michael Staniforth
PUBLISHED IN: Frontiers in Chemistry

frontiers Research Topics

About Frontiers

Frontiers is more than just an open-access publisher of scholarly articles: it is a pioneering approach to the world of academia, radically improving the way scholarly research is managed. The grand vision of Frontiers is a world where all people have an equal opportunity to seek, share and generate knowledge. Frontiers provides immediate and permanent online open access to all its publications, but this alone is not enough to realize our grand goals.

Frontiers Journal Series

The Frontiers Journal Series is a multi-tier and interdisciplinary set of open-access, online journals, promising a paradigm shift from the current review, selection and dissemination processes in academic publishing. All Frontiers journals are driven by researchers for researchers; therefore, they constitute a service to the scholarly community. At the same time, the Frontiers Journal Series operates on a revolutionary invention, the tiered publishing system, initially addressing specific communities of scholars, and gradually climbing up to broader public understanding, thus serving the interests of the lay society, too.

Dedication to Quality

Each Frontiers article is a landmark of the highest quality, thanks to genuinely collaborative interactions between authors and review editors, who include some of the world's best academicians. Research must be certified by peers before entering a stream of knowledge that may eventually reach the public - and shape society; therefore, Frontiers only applies the most rigorous and unbiased reviews.
Frontiers revolutionizes research publishing by freely delivering the most outstanding research, evaluated with no bias from both the academic and social point of view. By applying the most advanced information technologies, Frontiers is catapulting scholarly publishing into a new generation.

What are Frontiers Research Topics?

Frontiers Research Topics are very popular trademarks of the Frontiers Journals Series: they are collections of at least ten articles, all centered on a particular subject. With their unique mix of varied contributions from Original Research to Review Articles, Frontiers Research Topics unify the most influential researchers, the latest key findings and historical advances in a hot research area! Find out more on how to host your own Frontiers Research Topic or contribute to one as an author by contacting the Frontiers Editorial Office: frontiersin.org/about/contact

VIBRATIONALLY-MEDIATED CHEMICAL DYNAMICS

Topic Editors:
Jacob Dean, Southern Utah University, United States
Doran Bennett, Southern Methodist University, United States
Margherita Maiuri, Politecnico di Milano, Italy
Michael Staniforth, University of Warwick, United Kingdom

Table of Contents

frontiers
in Chemistry

Editorial: Vibrationally-Mediated Chemical Dynamics

Jacob C. Dean[1]*, Doran I. G. Bennett[2], Michael Staniforth[3] and Margherita Maiuri[4]

[1] Department of Physical Science, Southern Utah University, Cedar City, UT, United States, [2] Department of Chemistry, Southern Methodist University, Dallas, TX, United States, [3] Department of Chemistry, University of Warwick, Coventry, United Kingdom, [4] Dipartimento di Fisica, Politecnico di Milano, Milano, Italy

Editorial on the Research Topic

Vibrationally-Mediated Chemical Dynamics

Nuclear motion, or molecular vibrations, mediate essentially all chemical dynamics and reactions. A rich interplay between electronic and nuclear degrees-of-freedom manifests in contexts such as light-induced chemical reactions (photochemistry), electron/charge transfer, and ultrafast energy dissipation. In these contexts, the close connection between chemical structure and molecular vibrations has inspired studies which navigate the *structure-vibration-function* relationship imprinted into the corresponding dynamics. Viewed in this way, molecular vibrations can act as a template for prescribing a particular function to a chemical structure, with the common goal being to design structural motifs which can predictably give rise to a target function in applications of energy capture and conversion, drug discovery, and quantum computing just to name a few. It is our privilege to introduce this Research Topic issue of *Frontiers in Chemistry* which includes a set of 8 articles which collectively journey into this frontier.

The presence of UV photons in the solar spectrum, with energy sufficient to break chemical bonds, obliges all terrestrial organisms to develop UV sunscreens. Importantly, an efficient UV-absorber does not by itself necessarily constitute an effective sunscreen. An ideal candidate must have strong absorptions in the UVA/UVB spectrum while being photostable and biologically inert. Horbury et al. present an investigation on the excited state behavior and screening efficacy of a sinapate-based UV sunscreen inspired by plants. The authors cleverly design a dimerized form of ethyl sinapate to successfully extend the absorption range of the sunscreen while hoping to retain the photostability of its precursor. Indeed, the candidate successfully relaxes back to its ground state with high yield, however under prolonged UV exposure additional photochemistry takes place. The work simultaneously reveals the importance of ultrafast and "ultraslow" timescales in the design of new sunscreens. In the paper presented by Whittock et al. the mycosporine family of UV sunscreens inspired from cyanobacteria, fungi, and algae were evaluated with ultrafast UV pump-IR probe spectroscopy in tandem with an impressive computational analysis. The authors quantified the ground state recovery following two relaxation events through conical intersections (CIs), indicating favorable dynamics for photostability. To accomplish this through probed IR signatures, the authors used density functional theory calculations of the S_0 and S_1 structures where explicit solvation was required due to a sensitivity of the vibrations to the solvent environment.

Biliproteins, found in a vast array of organisms, are unique in their use of linear tetrapyrrole pigments (bilins) for both light-harvesting/energy transfer and photoswitching. The two biological contexts call for different criteria for success: the former requires the pigment to remain rigid to avoid quenching, and the latter demands torsional isomerization for signaling. Staheli et al. characterized this behavior through a bottom-up approach by analyzing the spectroscopic/photophysical properties of the two dipyrrole halves of the bilin framework.

They found that already at the subunit level, the structures garner large absorptivities rivaling chlorophyll, with absorption regions highly sensitive to structure. Without a protein scaffolding however, the dipyrroles are susceptible to inter-ring torsion leading to facile internal conversion on ultrafast timescales. It was found that the local protein environment *in vivo* serves to then restrict or confer this behavior in a controllable way highlighting the interplay of "built-in" intramolecular dynamics and intermolecular interactions.

As displayed in these experimental works, the pervasiveness of conical intersections along "special" nuclear coordinates in steering ultrafast dynamics is an important facet to functional design. Therefore, screening the potential energy topology of photo-active target molecules is a crucial step to drug design in new light-induced therapies. Léger et al. report results from high-level multireference electronic structure calculations applied to a candidate for light-activated cancer treatment. The authors map out the potential energy structure leading to the active biradical form of a cyclopropenone precursor, successfully describing all steps and proving a Norrish type-I reaction mechanism through singlet states. Furthermore, calculations of spectral properties of derivatives of the cyclopropenone containing enediyne revealed potentially more effective compounds. This work demonstrates the power of quantum chemistry in informing targeted drug synthesis. Similarly, Cui et al. have used density functional theory to compare photostability and light-activated dynamics in an unnatural DNA base pair (ZP) along the proton transfer coordinates binding the pair, against their natural DNA counterparts. The authors find a notable difference in the potential energy landscapes along the primary proton transfer coordinates of the ZP pair relative to its GC natural equivalent. Importantly, a CI exists in the GC pair which allows ultrafast recovery of the ground state, while no such CI exists in the ZP pair, suggesting a reduced photostability in ZP following UV absorption.

Following a milestone work on the comprehensive description of the Q_x/Q_y absorption region of chlorophyll-a (Chl-a), Reimers et al. present a holistic paper describing the asymmetry observed between high-resolution Chl-a absorption and fluorescence spectra. The authors combine low temperature (4.5 K) fluorescence line narrowing experiments in multiple solvents with spectral fitting to recover the vibronic properties of various active vibrations of Chl-a. In doing so, the authors present a detailed description of the vibrational content of Chl-a fluorescence spectra. They determine that solvent-induced differences in intensity are a result of Duschinsky mixing of certain modes between the ground and Q_y states. With the aid of DFT, the extent of mode-mixing was fully characterized and

shown to cause absorption/fluorescence asymmetry. The authors highlight the importance of this result in modeling quantum dynamics of Chl-containing light-harvesting complexes.

Finally, vibronic coupling in the excited state manifold of multichromophoric systems has been implicated in facilitating and, at times, steering excited-state dynamics. Sláma et al. demonstrate the utility of modeling donor-acceptor systems with a true vibronic model which treats the electronic and vibrational components equally—an approach that is theoretically practical in all electronic coupling regimes including the so-called intermediate regime where the timescales of both are similar. The authors apply the model to novel *peri*-arylene dyads in two limiting cases—one incorporating parallel transition dipole moments and another orthogonal—successfully reproducing steady-state spectra and population dynamics for both. The authors explain the discrepancy between the zero coupling of the orthogonal dyad and the fast energy transfer measured experimentally by demonstrating that anharmonicity in a multitude of low-frequency modes leads to a cooperative enhancement of electronic coupling through deviations of the nuclear displacements. The results of this work neatly express the utility of the vibronic treatment of molecular states, as well as statistical sampling at finite temperatures using molecular dynamics. Dunnett and Chin on the other hand, report a novel alternative where dissipative quantum dynamics are simulated at a finite temperature using 0 K wave functions. Armed with this novel method, the authors test and successfully simulate several model Hamiltonians, including a vibronic-tunneling system representative of electron transfer. In the process, the authors highlight numerical challenges but ultimately offer a promising vision for a new approach that uses wave function based calculations to simulate finite temperature systems.

AUTHOR CONTRIBUTIONS

JD, DB, and MS drafted, reviewed, and completed the manuscript for submission. All authors provided intellectual contributions to the work.

Check for updates

Exploring the Photochemistry of an Ethyl Sinapate Dimer: An Attempt Toward a Better Ultraviolet Filter

Michael D. Horbury [1]*, Matthew A. P. Turner [2], Jack S. Peters [3], Matthieu Mention [4], Amandine L. Flourat [4], Nicholas D. M. Hine [2], Florent Allais [4] and Vasilios G. Stavros [2]*

[1] School of Electronic and Electrical Engineering, University of Leeds, Leeds, United Kingdom, [2] Department of Chemistry, University of Warwick, Coventry, United Kingdom, [3] Physical and Theoretical Chemistry Laboratory, Department of Chemistry, University of Oxford, Oxford, United Kingdom, [4] URD ABI, CEBB, AgroParisTech, Pomacle, France

The photochemistry and photostability of a potential ultraviolet (UV) radiation filter, dehydrodiethylsinapate, with a broad absorption in the UVA region, is explored utilizing a combination of femtosecond time-resolved spectroscopy and steady-state irradiation studies. The time-resolved measurements show that this UV filter candidate undergoes excited state relaxation after UV absorption on a timescale of ∼10 picoseconds, suggesting efficient relaxation. However, steady-state irradiation measurements show degradation under prolonged UV exposure. From a photochemical standpoint, this highlights the importance of considering both the ultrafast and "ultraslow" timescales when designing new potential UV filters.

Keywords: photoprotection, femtosecond, sinapates, photochemistry, spectroscopy

INTRODUCTION

In recent years, several artificial ultraviolet (UV) filters, serving the purpose of providing a front-line defense to UV radiation exposure, used in commercial sunscreen formulations, have come under scrutiny due to concerns about their safety (Saija et al., 2000; Matsui et al., 2009; Burnett and Wang, 2011; Loden et al., 2011; Afonso et al., 2014; Skotarczak et al., 2015; Sharma et al., 2017). Alongside this "sunscreen controversy," incidences of skin cancer are on the rise (Stavros, 2014), even with increasing use of sunscreen formulations. This highlights the need for, not only improved education on general sun exposure and how to apply sunscreen formulas, but also a requisite for improved formulations containing safer UV filters. These new UV filters need to provide enhanced photoprotection along with being non-toxic, particularly when exposed to UV radiation.

One of the approaches to tackling these issues has been to study the intrinsic properties of photoprotective molecules found throughout nature (Saewan and Jimtaisong, 2015), which has had a few billion years head start in UV photoprotection. To this end, nature-based UV filters found in plants have garnered considerable interest as a starting point. One such molecule is the sinapate ester, sinapoyl malate. Indeed, a structurally related cinnamate, ethylhexyl methoxycinnamate, has already been employed as an artificial UV filter. However this has been recently shown to be genotoxic (Sharma et al., 2017), highlighting the urgent need for new non-toxic UV filters. The photochemistry responsible for sinapoyl malate's photoprotective capabilities has been proposed, along with that for related sinapate esters (Dean et al., 2014; Baker et al., 2016; Horbury et al., 2017a, 2018; Luo et al., 2017; Zhao et al., 2020). These studies have shown that, upon absorption of UV, these sinapate esters undergo an effective and ultrafast (femto- to picosecond, 10^{-15} and 10^{-12} s, respectively) *trans*-to-*cis* and *cis*-to-*trans* photoisomerization, which is responsible

for their apparent long-term photostability and photoprotective nature. Therefore, gaining an understanding of the initial light/matter interaction which drives the overall photochemistry of the molecule can provide powerful insight in the development of new UV filters and there long-term photostability. Additionally, these sinapate esters possess strong absorptions in the UVA (400–315 nm) and in the UVB region (315–280 nm) of the solar spectrum.

While these sinapate esters strongly absorb in the UVA, they do not cover the entirety of the UVA spectrum, i.e., sinapoyl malate's UVA absorption cuts off around 360 nm (Baker et al., 2016), which is particularly pertinent as this spectral region is linked to premature skin aging (Berneburg et al., 2000). Therefore, and ideally, if their absorption can be broadened across the entire UVA spectrum, it provides the means to a superior UV filter, spanning both the UVB and UVA. However, it is worth noting that increasing the UVA absorption does not imply a better UV filter; the molecule still needs to display a high level of photostability. One simple method of broadening, as well as spectrally red-shifting the absorption of these sinapate esters, is to increase the extent of conjugation in the π-system of the chromophore unit. An intuitive starting point is to add functionalization to the acrylic double bond. This was recently shown to be a promising approach by the addition of an identical ester group being added to the double bond of ethyl sinapate (shown in blue in **Figure 1**), which resulted in a redshift of the ground state absorption spectrum along with an increase in photostability (Horbury et al., 2019). We therefore utilize this approach, again, this time by dimerizing ethyl sinapate (Neudörffer et al., 2004). Ethyl sinapate has been shown to display very similar intrinsic properties to the plant UV filter, sinapoyl malate (Horbury et al., 2018). The resultant dimer is dehydrodiethylsinapate (**DHDES**, see **Figure 1**). As anticipated, **DHDES** possess a strong absorption across the (almost) entirety of the UVA region (**Figure 1**).

Whether the *structural* variant of sinapoyl malate, **DHDES**, with its enhanced UVA absorption, possesses the photostability (*dynamics*) displayed by sinapoyl malate and ethyl sinapate is the central question we seek to address in this work. Allied to this is the emerging trends that we may obtain through this work. Therefore, we investigate the photochemistry (*dynamics*) of **DHDES**, as a potential starting point for future nature-inspired UV filters with enhanced *function*; broader UVA coverage and efficient excitation-recovery cycles. To implement our *structure-dynamics-function* approach, we utilize femtosecond (fs) transient electronic (UV/visible, abbreviated to UV/Vis henceforth) absorption spectroscopy (TEAS) which has already provided valuable insight into the photochemistry of sinapate esters and related cinnamates (Vengris et al., 2005; Baker et al., 2016; Horbury et al., 2016, 2017a,b, 2018; Zhao et al., 2020). Additionally, the long-term photostability of this molecule was assessed *via* steady-state UV irradiation, monitored by UV/Vis absorption and ^{1}H NMR spectroscopy. The experiments are complemented by computational results based on (time-dependant) density functional theory.

MATERIALS AND METHODS

Transient Electronic Absorption Spectroscopy

The fs TEAS setup used to explore the photochemistry and photophysics of **DHDES** has been described in detail previously (Greenough et al., 2014a,b), however, information specific to the present experiments is provided herein. Samples of **DHDES** were made to a concentration of 1 mM in ethanol (absolute, VWR), ethylene glycol (technical, Arcos Organics), and glycerol (99.93%, Fisher. The fs pump pulses were generated by an optical parametric amplifier (TOPAS-C, Spectra-Physics) with a fluence of 200–800 µJ·cm^{-2}. The pump excitation wavelength used was
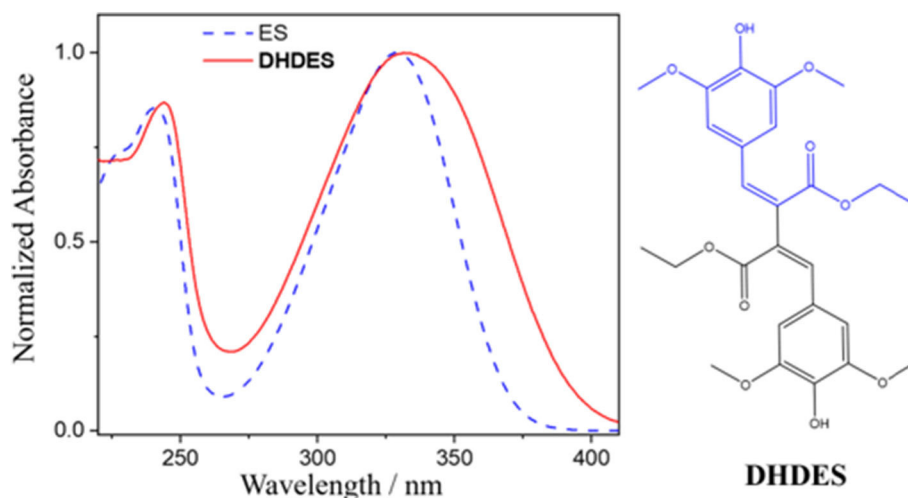

FIGURE 1 | Normalized UV/Vis spectrum of **DHDES** (red) in ethanol. Additionally, the UV/Vis spectrum of ethyl-sinapate (ES) is overlaid (blue dashed line). The chemical structures of **DHDES** is shown right; chemical structure of ES is shown as blue in the structure of **DHDES**.

332 nm for **DHDES** in ethanol, ethylene glycol, and glycerol; this wavelength correspond to the associated UV absorption maxima. The probe pulse was a broadband white light supercontinuum generated in a CaF_2 window with a thickness of 2 mm, providing a probe spectral window of 330–675 nm. The pump-probe time delay (Δt) was varied by adjusting the optical delay of the probe pulse, the maximum obtainable Δt was 2 nanoseconds (ns). Changes in the optical density (ΔOD) of the samples were calculated from transmitted probe intensities, collected using a spectrometer (Avantes, AvaSpec-ULS1650F). The sample delivery system was a flow-through cell (Demountable Liquid Cell by Harrick Scientific Products Inc.) consisting of two CaF_2 windows with a thickness of 1 mm for the front window and 2 mm for the back window, except in the case of **DHDES** in glycerol, where both windows were 2 mm thick due to the build-up pressure in the flow system (owing to glycerol's viscosity). The windows were spaced 100 μm apart to limit temporal dispersion of the pump and probe pulses. The sample was circulated using a diaphragm pump (SIMDOS, KNF) recirculating sample from a 25 mL reservoir to provide each pulse-pair with fresh sample.

Steady-State Difference Spectra

Steady-state UV/Vis absorption spectra of **DHDES** in ethanol, were collected to determine long-term photostability. The sample was irradiated with an arc lamp (Fluorolog 3, Horiba) for up to 2 h, with the UV/Vis spectra taken at various time points, at the corresponding TEAS excitation wavelength, using an 8 nm bandwidth of the irradiation source. The fluence used during irradiation of **DHDES** was set to 100–200 μJ·cm^{-2} to mimic solar incidence conditions. The UV/Vis spectra were measured using a UV/Vis spectrometer (Cary 60, Agilent Technologies).

Computational Calculations

The structure of **DHDES** was generated in its *cis,cis*-isomer and *trans,trans*-isomer (see **Figures 1**, **4**), as well as a contorted *cis,trans*-isomer, using VMD (Humphrey et al., 1996) with the molefacture plugin. Each of these structures underwent a density functional theory (DFT) geometry optimization with a cc-pVTZ basis set (Dunning, 1989) and the PBE0 functional (Adamo and Barone, 1999), using the NWChem software (Valiev et al., 2010). The *cis,trans*-isomer of **DHDES** was significantly energetically disfavored with respect to the other two isomers, and the geometry optimization did not converge with a reasonable level of convergence criteria; therefore this isomer was discounted from further study. Following relaxation, linear-response time-dependant DFT calculations were conducted at the optimized ground state geometries of the *cis,cis*-isomer and *trans,trans*-isomer to obtain their optical absorption spectra. Again, the level of theory was cc-pVTZ/PBE0 and the NWChem software was employed. In all calculations, the conductor-like screening model (COSMO) was used to approximate the effect of the solvent (Klamt and Schüürmann, 1993; York and Karplus, 1999). The default COSMO solvent model for ethanol within NWChem was used, the descriptors of which are based on the Minnesota Solvent Descriptor Database (Winget et al., 1999).

Synthetic Procedures and ^{1}H NMR

DHDES and **Me-DHDES** were synthesized using the procedure published by Mention et al. (2020) ^{1}H NMR spectra of **DHDES** and **Me-DHDES** (we discuss the reason for studying this system below) in $CDCl_3$ were recorded at 300 MHz on a Bruker Fourier 300, pre- and post-irradiation using a Rayonet RPR-200 after irradiation of 60 min at 302 nm; this wavelength was used due to the limited spectral choices of the Rayonet RPR-200.

Fitting

To retrieve the dynamical information contained within the transient absorption spectra, a sequential $\left(A \xrightarrow{\tau_1} B \xrightarrow{\tau_2} C \xrightarrow{\tau_3} D \right)$ global (across all wavelengths 330–675 nm) fitting technique was performed, using the software package Glotaran (Mullen and Van Stokkum, 2007; Snellenburg et al., 2012). The transient absorption spectra of **DHDES** were fit using four time-constants (τ_n, where $n = 1$–4). Each time-constant is linked to an evolution associated difference spectrum (EADS) that represents the evolving spectral features related to that time-constant. All fits were convoluted with a Gaussian function to model our instrument response function (~80 fs, for glycerol ~100 fs). The final time-constant used in our model (τ_4 for **DHDES**) accounts for the long-lived photoproduct; this time-constant is reported to be $>> 2$ ns.

RESULTS

Transient Electronic Absorption Spectroscopy

First, we consider the resulting transient absorption spectra of **DHDES** in ethanol shown in **Figure 2A** (see ESI **Figure S1** for transient absorption spectra of **DHDES** in ethylene glycol and glycerol). Note that the related **Me-DHDES**, a methylated version of **DHDES**, is also shown in **Figure 2B**, but will be discussed later. After initial photoexcitation at 332 nm, the transient absorption spectrum consist of three distinct spectral features, the first being a ground state bleach centered at ~340 nm, the second is a large excited state absorption at ~400 nm and the third is a smaller excited state absorption at ~675 nm. As Δt increases, the excited state absorption at 675 nm begins to decay, leaving a broad flat absorption alongside the large excited state absorption feature at 400 nm. At longer Δt, the ground state bleach and both excited state absorption features tend toward the baseline. Once the excited state absorption features have completely decayed away, a new absorption feature (not immediately evident) spanning 390–600 nm is revealed. Some residual ground state bleach at 340 nm remains. Both features persist beyond the maximum Δt (see ESI **Figure S2** for transient absorption spectrum at $\Delta t = 2$ ns).

The time-constants produced from fitting the transient absorption spectra are provided in **Table 1**, and the corresponding EADS are shown in **Figures 2C,D** (see ESI **Figure S3** for additional EADS for **DHDES** in ethylene glycol and glycerol, along with residuals **Figures S4–S8** for **DHDES** in ethanol, ethylene glycol, glycerol, and **Me-DHDES** in ethanol, respectively).
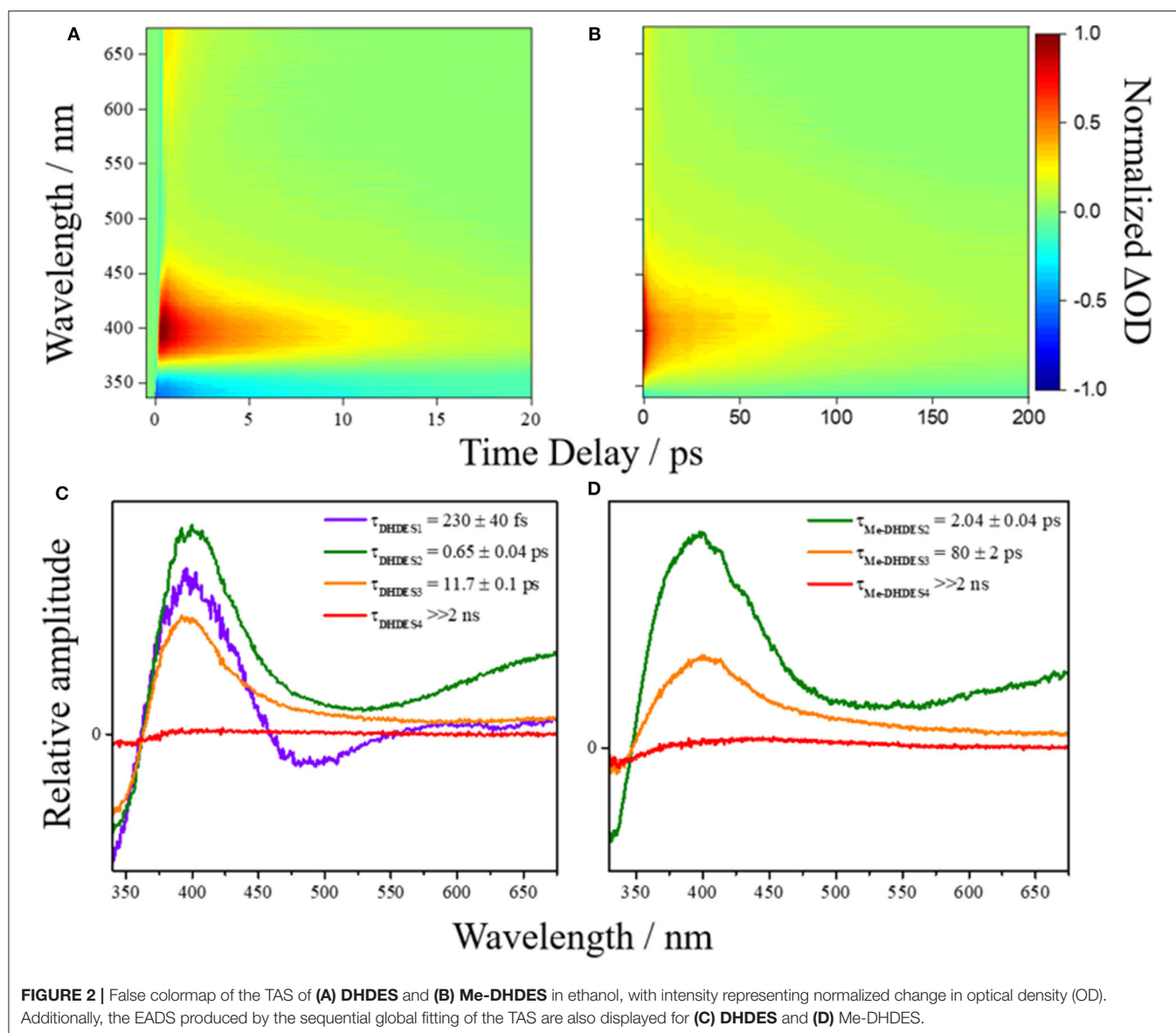
FIGURE 2 | False colormap of the TAS of **(A) DHDES** and **(B) Me-DHDES** in ethanol, with intensity representing normalized change in optical density (OD). Additionally, the EADS produced by the sequential global fitting of the TAS are also displayed for **(C) DHDES** and **(D)** Me-DHDES.

TABLE 1 | The values of the time-constants (τ_{xN}, where x represents either **DHDES** or **Me-DHDES**) provided from globally fitting the transient absorption spectra of **DHDES** in ethanol, ethylene glycol, and glycerol, **Me-DHDES** in ethanol.

	τ_{x1}	τ_{x2}	τ_{x3}
DHDES			
Ethanol	230 ± 40 fs	0.65 ± 0.04 ps	11.7 ± 0.1 ps
Ethylene Glycol	270 ± 40 fs	1.3 ± 0.1 ps	12.5 ± 0.2 ps
Glycerol	100 ± 50 fs	1.36 ± 0.05 ps	39.3 ± 0.4 ps
Me-DHDES	n/a	2.04 ± 0.04 ps	80 ± 2 ps

Errors are quoted to 2σ except when an error returned was less than half the instrument response. In such cases, the error is reported as half the instrument response. For fit residuals, see ESI Figures S4–S7.

Steady-State Irradiation

Steady-state irradiation of **DHDES** in ethanol was carried out to determine its long-term photostability under constant UV exposure. To monitor any changes to the sample, both UV/Vis (**Figure 3A** as well as extracted evolution associated spectra, EAS, **Figure 3B**) and ^{1}H NMR (**Figure 3C** and **Figure S9**) spectra were recorded at various time points of irradiation. Similar experiments were carried out for **Me-DHDES** (see ESI **Figures S10, S11** for further details).

The evolution of the UV/Vis spectra during irradiation for **DHDES** in ethanol, is shown in **Figure 3A** and clearly indicates that the main absorption feature spanning the UVA and UVB regions of the absorption spectrum undergoes a significant decay (~60% reduction in 2 h). However, this decay appears to consist of two distinct spectral evolutions, as represented by the arrows
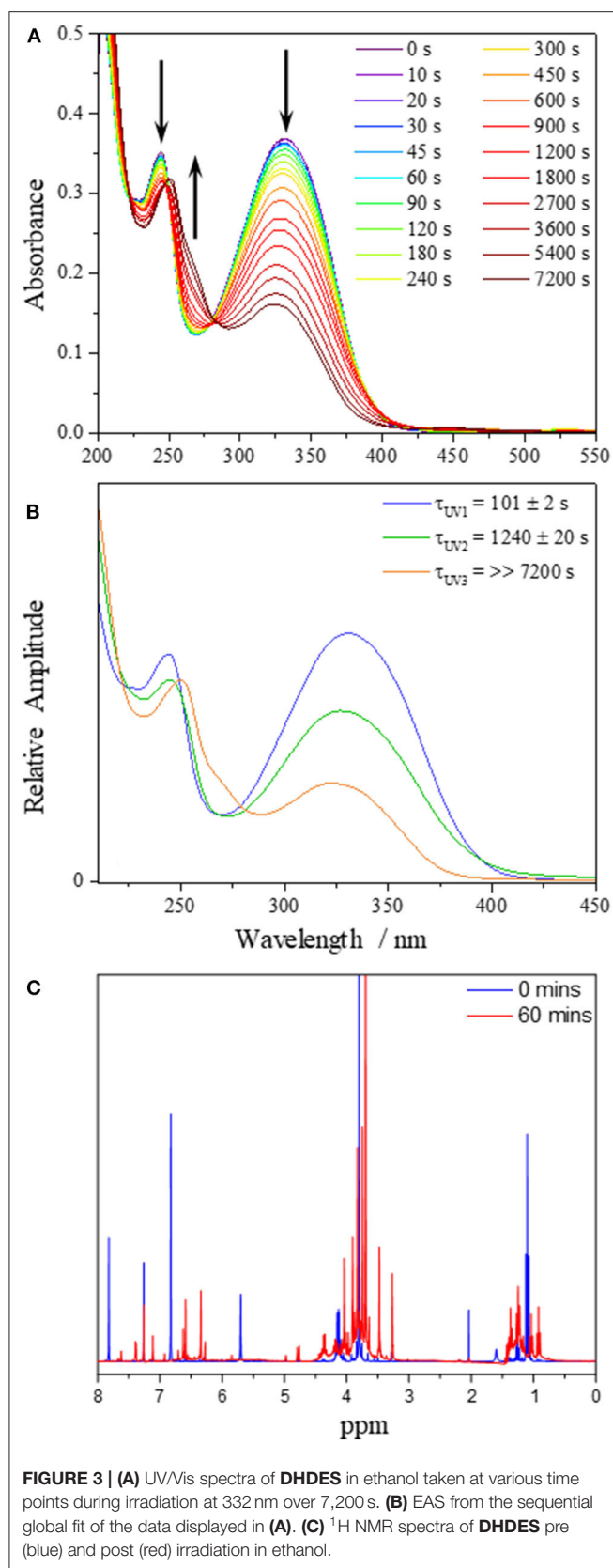
FIGURE 3 | (A) UV/Vis spectra of **DHDES** in ethanol taken at various time points during irradiation at 332 nm over 7,200 s. (B) EAS from the sequential global fit of the data displayed in (A). (C) ^{1}H NMR spectra of **DHDES** pre (blue) and post (red) irradiation in ethanol.

in **Figure 3A**; a decay to yield (existing) features at ~330 and ~240 nm, and a growth of new absorption features at ~250 and ~270 nm.

To better distinguish the processes that are occurring, we performed a sequential global (210–450 nm) fit of the UV/Vis spectra. The resulting EAS and time-constants are shown in **Figure 3B**. Cursory comparison of EAS(τ_{UV1}) (101 ± 2 s) with EAS(τ_{UV2}) (1240 ± 20 s) suggest that upon irradiation of **DHDES**, the absorption intensity drops. Under prolonged irradiation the spectra continue to show a decrease in absorption; however, additional spectral features begin to grow in. These new absorption features consist of a peak at ~270 nm and a marked red-shift of the peak at ~240 nm to ~250 nm as seen in EAS(τ_{UV3}) (>>7,200 s). This is very likely indicative of a new species being generated.

To identify any newly generated species after UV radiation exposure, a ^{1}H NMR spectrum of **DHDES** was taken before and after 60 min irradiation (see **Figure 3C**). One can observe that the peaks corresponding to the benzene ring protons of **DHDES** (6.78 and 7.83 ppm) have disappeared and peaks appear at ~6.4 and ~6.6 ppm, along with many new peaks in the 3.5–5.0 ppm as well as the 0.7–1.5 ppm regions, demonstrating the transformation of the latter into multiple new compounds under radiation (**Figure 3C**). The appearance of broad peaks in the ^{1}H NMR spectrum after irradiation hints at the formation of oligomers. Additionally it is likely that **DHDES** is undergoing an esterification with ethanol when exposed to UV; this has previously been seen with 1,4-diphenyl-1,3-dibutene (Saltiel and Redwood, 2016). We will return to discuss another potential product, a tricyclic compound, in the discussion (*vide infra*).

Computational Results

The calculated ground state isomers of two stable isomers of **DHDES** (*cis,cis*- and *trans,trans*-isomers), are shown in **Figure 4** (*NB* the *trans,trans*-isomer of **DHDES** is also show in in **Figure 1**). The *cis,cis*-isomer has the lower energy of the two conformers with the *trans,trans*-isomer being ~0.3 eV higher in energy. A molecule of this size likely has a complicated ground-state energy surface with multiple local minima corresponding to different stable geometries. As such, it is challenging to determine that the structure chosen for both conformers is the global minimum energy structures and, indeed, it is likely multiple structures exist in solution. Owing to this, the predicted energies for these species, as well as predicted vertical excitation energies, are presented as an approximation of each form rather than as quantitative data. Furthermore, the effect of explicit solvent interactions are not captured by our technique, these likely also have an effect on the relative energies of the species (Zuehlsdorff et al., 2017; Turner et al., 2019). Additionally, the two isomers display several significant differences in geometry, beyond just isomerization around the double bonds. In the case of the *cis, cis*-isomer, the two ethyl sinapate subunits are at ~90° to each other, which hinders conjugation between the two ethyl sinapate subunits. It should be noted that a planar *cis,cis*-**DHDES** is sterically unfavorable, as several atoms would need to occupy

FIGURE 4 | Geometry calculations of the stable ground state isomers **(A)** *cis,cis*-**DHDES** and **(B)** *trans,trans*-**DHDES**. **(C)** Predicted UV/Vis stick spectra (*cis,cis*-**DHDES** blue bars, *trans,trans*-**DHDES** red bars) overlaid with experimental UV/Vis spectrum **of DHDES** in ethanol (black line).
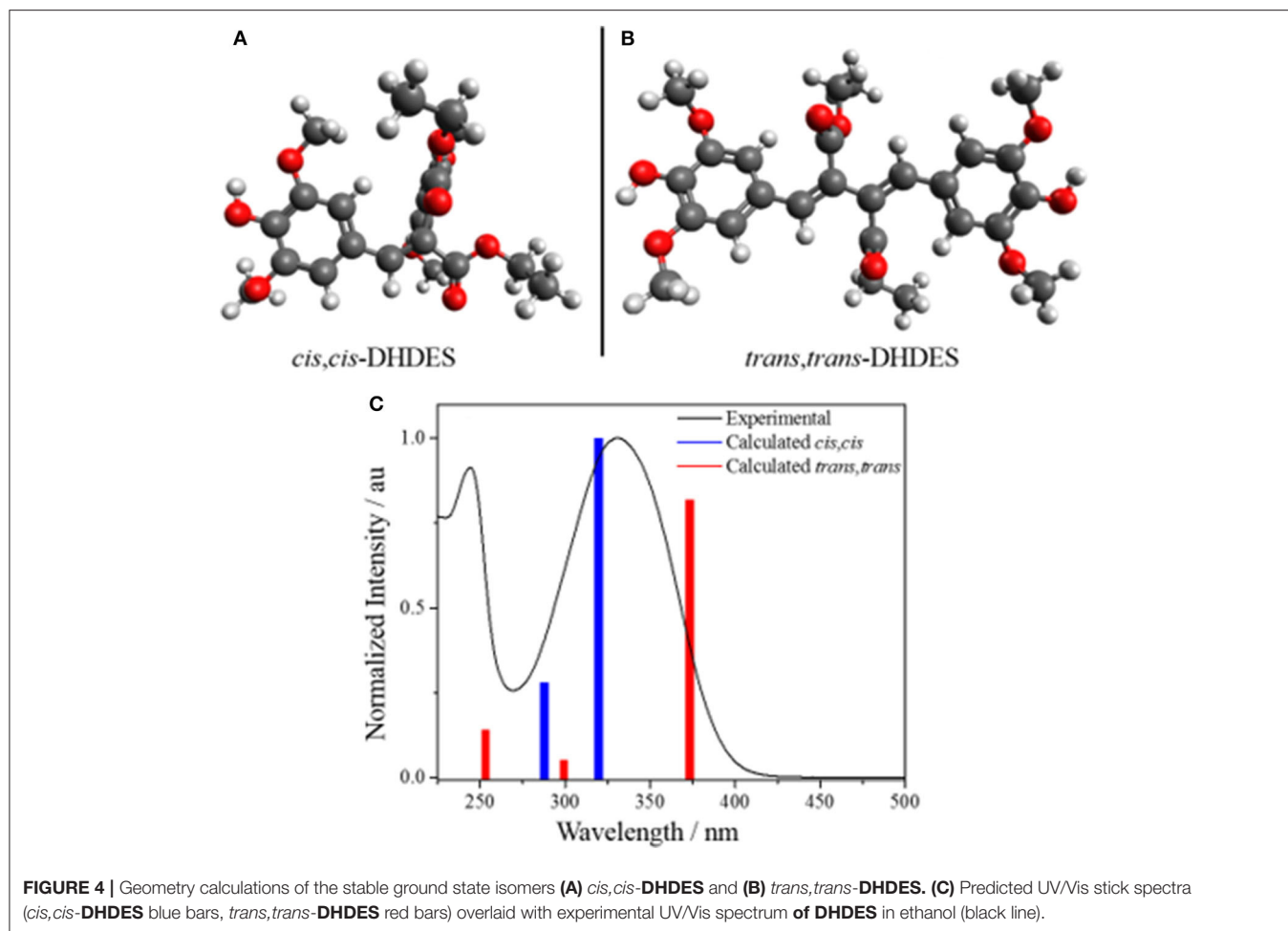
the same space. However, the *trans,trans*-isomer is *almost* planar (∼24° twist between the two benzene rings), but the two ethyl sinapate subunits are sufficiently twisted relative to one another to weaken the extended conjugation across both subunits. This lack of conjugation is further supported by the UV/Vis spectra of **DHDES** (**Figure 1**); if there was extended conjugation across the entire molecule, one would anticipate a starker red-shift in the absorption.

In addition to the calculated geometries, UV/Vis spectra for the *cis,cis*-**DHDES** and *trans,trans*-**DHDES** were calculated, and also shown in **Figure 4**. The spectra show the main absorption peak for *cis,cis*-**DHDES** is at 322 nm, while for *trans,trans*-**DHDES** it is at 371 nm; the *cis,cis*-isomer has a higher oscillator strength. Due to the calculated peaks for both isomers being within the experimental absorption peak, it possible that our sample of **DHDES** contains both *cis,cis*- and *trans,trans*-isomers, which in turn gives rise to the increased broadness in absorption compared to ethyl sinapate (see **Figure 1**). While a calculated energy difference of 0.3 eV would suggest that the *cis,cis*-isomer would be heavily favored, it is possible that the calculated energy difference would be reduced if an explicit solvent model was used. Furthermore, we believe that during the synthesis of **DHDES** both isomers are generated.

DISCUSSION

We now consider the ultrafast photochemistry and photophysics of **DHDES**. As discussed *supra*, due to the lack of conjugation, a consequence of the twisted geometries between the two ethyl sinapate substructures (see **Figures 4A,B**), one would anticipate that initial photoexcitation would yield a transient absorption spectrum analogous to the transient absorption spectrum of ethyl sinapate in ethanol. Whilst this is not immediately apparent in the measured transient absorption spectra of **DHDES**, the EADS(τ_{DHDES1}) (230 ± 40 fs) in ethanol is mildly similar to the first EADS of ethyl sinapate in ethanol (see ESI **Figures S12, S13** for more details). We therefore assign the first time-constant τ_{DHDES1}, and its corresponding EADS(τ_{DHDES1}), to the **DHDES** undergoing a molecular motion that allows for increased coupling between the two ethyl sinapate substructures, thus the decay of the ethyl sinapate-like features; this is substantiated by the significant change between EADS(τ_{DHDES1}) and EADS(τ_{DHDES2}) (0.65 ± 0.04 ps), see **Figure 2C**. With the decay of the ethyl sinapate-like features, the comparison of **DHDES** to ethyl sinapate now ends.

Next, we consider the time-constant τ_{DHDES2} and its corresponding EADS($\tau_{\textbf{DHDES2}}$). The EADS($\tau_{\textbf{DHDES2}}$) is

dominated by two large excited state absorption features at ∼400 and ∼675 nm, which we attribute to a specific **DHDES** isomer (see **Figure 4**). We draw confidence here, by noting that the excited state absorption feature at ∼675 nm is like the excited state absorption seen in TEAS recorded for 1,4-disyringol-1,3-butadiene (DSB, see ESI **Figures S14, S15**). DSB is the backbone structure of **DHDES**, which remains planar, unlike **DHDES**, due to the absence of the ester functionalities (see ESI **Figure S16**). Consequently, it is plausible that the absorption feature at 675 nm in **DHDES** is attributed to a planar form with increased conjugation, akin to DSB. Since *trans,trans*-**DHDES**, is near-planar in the ground state, this isomer serves as the leading candidate; the excess energy imparted by the absorption of a UV photon may allow *trans,trans*-**DHDES** to approach planarity, as excited state population samples the excited state potential energy landscape. While we cannot rule out that this is also happening in *cis,cis*-**DHDES**, one notes that this would require severe nuclear rearrangement, including *cis,cis*-to-*trans,trans* isomerization (*vide supra*), to even approach planarity. With this in mind, we suggest that the excited state absorption seen at 400 nm is likely attributed to the absorption from the *cis,cis*-**DHDES** electronic excited state. When comparing the EADS(τ_{DHDES2}) and EADS(τ_{DHDES3}) (11.7 ± 0.1 ps), the major difference is the absence of the excited state absorption at ∼675 nm. Whether or not this is due to *trans,trans*-**DHDES**, relaxing back to the electronic ground-state on the timescale of τ_{DHDES2}, is unknown. Unfortunately, due to the sample potentially consisting of both isomers of **DHDES**, the transient absorption spectra and EADS are heavily convoluted making it hard to distinguish which process is associated with which **DHDES** isomer.

Thirdly, the EADS(τ_{DHDES3}) resembles the decay of the remaining excited state absorption at 400 nm. As this excited state absorption is attributed to the *cis,cis*-**DHDES** isomer (see above) it represents the decay of the electronically excited state of *cis,cis*-**DHDES**, but with the caveat that the *trans,trans*-**DHDES** could be present and also contributes to the EADS(τ_{DHDES3}) and timescale. Finally, EADS(τ_{DHDES4}) (>>2 ns), models the long-lived photoproduct (see ESI **Figure S2** for transient absorption spectrum at $\Delta t = 2$ ns). Whether this is due to a transient species such as a triplet state or a molecular photoproduct is unknown.

To help determine whether the electronic excited state relaxation, for either isomer, is mediated by a photoisomerization

motion leading to a conical intersection between the electronic excited state and ground state, akin to ethyl sinapate (Horbury et al., 2018), additional TEAS measurements were performed in more viscous solvents: ethylene glycol ($\eta = 21$) (Tsierkezos and Molinou, 1998) and glycerol ($\eta = 1,412$) (Segur and Oberstar, 1951) (see ESI for transient absorption spectra, ethanol $\eta = 1.19$) (Khattab et al., 2012). From these measurements, we determined the viscosity dependence, α, of the time-constant τ_{DHDES2} and τ_{DHDES3}, as these time-constant are linked to the decay of the electronic excited state, which may be mediated by photoisomerization (Espagne et al., 2006; Horbury et al., 2017a). The retrieved α value for τ_{DHDES2} was 0.09 ± 0.06 and for was τ_{DHDES3} 0.18 ± 0.07. The value returned for τ_{DHDES2} suggests that large amplitude nuclear motion linked to this time-constant is minor, meaning that either the *trans,trans*-**DHDES** undergoes very little (large amplitude) nuclear motion to relax or that this process involves a change in electronic states. While τ_{DHDES3} is a smaller value compared to related sinapate esters (∼0.34) (Horbury et al., 2017a), it still suggests that the electronic excited state decay of **DHDES** involves some substantial nuclear motion, of which a photoisomerization could be a candidate.

The incomplete recovery of the ground state bleach suggests that (at least) a small fraction of **DHDES** is not returning to its original form. This incomplete recovery of the ground state bleach is not unexpected as steady-state irradiation has demonstrated **DHDES** degrades over persistent UV exposure. It has previously been reported that a quinone methide species can be formed upon electrochemically-induced oxidation and one could assume that a similar mechanism could also occur upon irradiation, this mechanism is shown in **Scheme 1** (Neudörffer et al., 2006).

Another potential mechanism for the formation of the quinone methide is that it is initiated by O–H bond fission. While one would anticipate that this pathway would be blocked by the presence of an intramolecular hydrogen bond between the hydroxy and methoxy groups, previous studies on syringol, show it can undergo O–H bond fission. Owing to the non-planar geometry of syringol in the excited electronic state, this serves to weaken the intramolecular hydrogen bond sufficiently enough to allow for O–H bond fission to occur (Young et al., 2014). It is therefore not unreasonable to assume that the strained and twisted nature (see above) of **DHDES** induces a similar affect, by weakening the intramolecular hydrogen
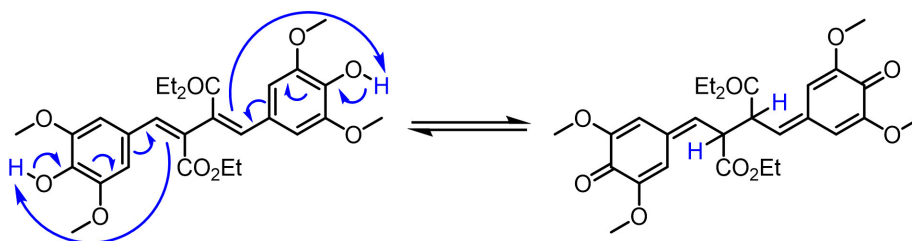
SCHEME 1 | Generation of the quinone methide from **DHDES**.

bonding, thus, opening up the O–H fission pathway along, say, a dissociative $^1\pi\sigma^*$ state, in keeping with previous studies (Roberts and Stavros, 2014).

To test such a hypothesis for O–H bond fission shown in **Scheme 1**, we have replaced O–H with O–CH$_3$; previous studies in similar systems have shown that O–H fission is more facile over O–C fission. (Hadden et al., 2012) Therefore, methylation could lead to stabilization of **DHDES** under prolonged UV exposure. The methylated form of **DHDES**, termed **Me-DHDES**, in ethanol (1 mM), was then studied using TEAS (photoexcited at 310 nm) and steady-state absorption to see if the formation of the proposed quinonic methide species is prevented. The resulting transient absorption spectra and EADS are shown in **Figures 2B,D**. While the spectral features that are present in the transient absorption spectra match the ones seen in **DHDES**, the time-constants (see **Table 1**) clearly differ in two ways: (1) τ_{DHDES1} is absent; and (2) $\tau_{Me-DHDES3}$ is substantially longer than τ_{DHDES3} (80 ± 2 ps versus 12.5 ± 0.2 ps for **DHDES**). However, the EADS($\tau_{Me-DHDES2}$) (2.04 ± 0.04 ps) and EADS($\tau_{Me-DHDES3}$) are remarkably similar spectrally to those of **DHDES**. Therefore, we are confident that **Me-DHDES** undergoes the same relaxation mechanism as

DHDES. Additionally, the steady-state UV/Vis spectra (see ESI **Figure S10**) taken during prolonged UV irradiation and the appearance of new proton peaks in the ^{1}H NMR spectra taken pre- and post-irradiation (see ESI **Figure S11**), demonstrate **Me-DHDES** is also undergoing degradation. Since, the addition of the methoxy group is likely to supress bond-rearrangement proposed in **Scheme 1**, the revised degradation pathway is the formation of the tricyclic compound **X**, formed through a photo cyclo-addition followed by a re-aromatization via an 1,5-H shift (**Scheme 2**); this photoproduct would be expected to exhibit ^{1}H NMR peaks at ∼6.3 and ∼6.6 ppm in **Figure 3C**. Consideration of the above and given the same proton peaks are present in the post-irradiation ^{1}H-NMR spectra of **DHDES** and **Me-DHDES** (see ESI **Figures S9**, **S11**), the degradation pathway between the two is likely the same, this pathway is likely occurring alongside the photoinduced esterification with ethanol (*vide supra*).

CONCLUSION

We have explored the photochemistry and photostability of a potential UV filter, dehydrodiethylsinapate (**DHDES**), which
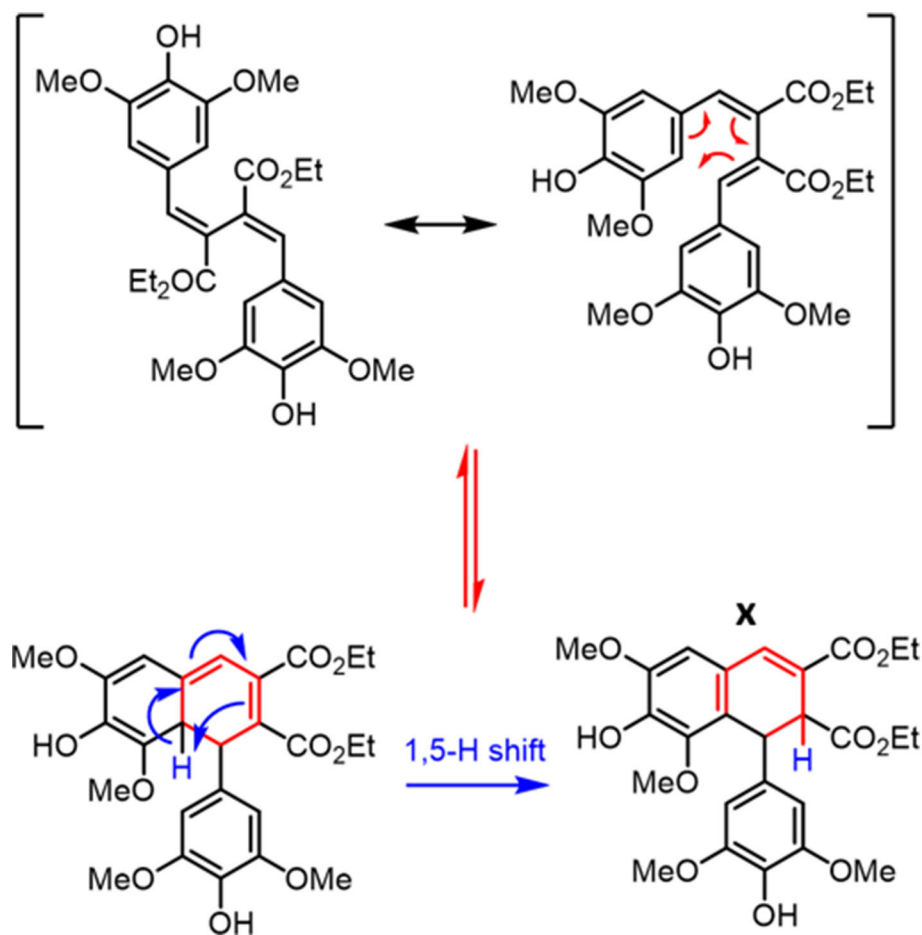
SCHEME 2 | Generation of the tricyclic species **X** from **DHDES**.

provides almost full absorption coverage of the UVA region of the electromagnetic spectrum. This was achieved using a combination of femtosecond transient electronic (UV/Vis) absorption spectroscopy (TEAS) and steady-state UV irradiation, monitored by both UV/Vis and ^{1}H NMR spectroscopy.

The photodynamics observed in the TEAS measurements suggest **DHDES** undergoes an ultrafast electronic excited state relaxation, potentially mediated *via* a photoisomerization pathway. However, the steady-state irradiation studies demonstrate that **DHDES** is not photostable under prolonged UV exposure. We attempted to thwart degradation by protecting the O–H with O–Me without success. Through the result of this methylation in combination with ^{1}H NMR, we have identified a potential cause of degradation, due to the formation of a tricyclic species. It is likely that the tricyclic species further degrades under UV exposure, leading to the formation of the myriad of unidentified molecular species seen in the post irradiation 1H NMR spectrum. Therefore, if one can by-pass the formation of this tricyclic species, this could expand the molecular diversity based around a core DHDES structure, potentially leading to promising next generation, broad-spectrum and nature-inspired, UV filter molecules.

Importantly, this work demonstrates that manipulating a molecules' structure, whilst trying to preserve the ultrafast dynamics, can have both positive and negative implications on its function. Indeed, we have shown that **DHDES** has enhanced UVA absorption, whilst still possessing a short-lived excited state. However, this is at the cost of long term photostability. Undeniably, what pervades the present study is that chemical intuition, increased conjugation and thus broader UVA absorption, does not necessarily result in a better (nature-inspired) UV filter. It is clear that in order to progress this structure-dynamics-function approach, we will need to seek increasing levels of guidance from theory, a current strategy underway in our laboratory, in our search for next generation, nature inspired UV filters which could be included in commercial sunscreen formulations.

DATA AVAILABILITY STATEMENT

The datasets presented in this study can be found in online repositories. The names of the repository/repositories and accession number(s) can be found below: https://zenodo.org/record/3741408, doi: 10.5281/zenodo.3741408.

AUTHOR CONTRIBUTIONS

MH acquired and analyzed the time-resolved and steady-state spectroscopic data and prepared the manuscript. JP provided assistant in the acquisition of the time-resolved and steady-state spectroscopic data. AF, MM, and FA conceived and performed the syntheses, as well as contributing to the preparation of the manuscript. MT and NH performed and analyzed the computational calculations. VS conceived the experiments and provided guidance in data analysis and interpretation and the writing of the manuscript. All authors contributed to the article and approved the submitted version.

ACKNOWLEDGMENTS

SUPPLEMENTARY MATERIAL

The Supplementary Material for this article can be found online at: https://www.frontiersin.org/articles/10.3389/fchem.2020.00633/full#supplementary-material

REFERENCES

Adamo, C., and Barone, V. (1999). Toward reliable density functional methods without adjustable parameters: the PBE0 model. *J. Chem. Phys.* 110, 6158–6170. doi: 10.1063/1.478522

Afonso, S., Horita, K., Silva, J. P. S., Almeida, I. F., Amaral, M. H., Costa, P. C., et al. (2014). Photodegradation of avobenzone: stabilization effect of antioxidants. *J. Photochem. Photobiol. B Biol.* 140, 36–40. doi: 10.1016/j.jphotobiol.2014.07.004

Baker, L. A., Horbury, M. D., Greenough, S. E., Allais, F., Walsh, P. S., Habershon, S., et al. (2016). Ultrafast photoprotecting sunscreens in natural plants. *J. Phys. Chem. Lett.* 7, 56–61. doi: 10.1021/acs.jpclett.5b02474

Berneburg, M., Plettenberg, H., and Krutmann, J. (2000). Photoaging of human skin. *Photodermatol. Photoimmunol. Photomed.* 16, 239–244. doi: 10.1034/j.1600-0781.2000.160601.x

Burnett, M. E., and Wang, S. Q. (2011). Current sunscreen controversies: a critical review. *Photodermatol. Photoimmunol. Photomed.* 27, 58–67. doi: 10.1111/j.1600-0781.2011.00557.x

Dean, J. C., Kusaka, R., Walsh, P. S., Allais, F., and Zwier, T. S. (2014). Plant sunscreens in the UV-B: ultraviolet spectroscopy of jet-cooled sinapoyl malate, sinapic acid, and sinapate ester derivatives. *J. Am. Chem. Soc.* 136, 14780–14795. doi: 10.1021/ja5059026

Dunning, T. H. Jr. (1989). Gaussian basis sets for use in correlated molecular calculations. I. The atoms boron through neon and hydrogen. *J. Chem. Phys.* 90, 1007–1023. doi: 10.1063/1.456153

Espagne, A., Paik, D. H., Changenet-Barret, P., Martin, M. M., and Zewail, A. H. (2006). Ultrafast photoisomerization of photoactive yellow protein chromophore analogues in solution: influence of the protonation state. *ChemPhysChem* 7, 1717–1726. doi: 10.1002/cphc.200600137

Greenough, S. E., Horbury, M. D., Thompson, J. O. F., Roberts, G. M., Karsili, T. N. V., Marchetti, B., et al. (2014a). Solvent induced conformer specific photochemistry of guaiacol. *Phys. Chem. Chem. Phys.* 16, 16187–16195. doi: 10.1039/C4CP02424A

Greenough, S. E., Roberts, G. M., Smith, N. A., Horbury, M. D., Mckinlay, R. G., Zurek, J. M., et al. (2014b). Ultrafast photo-induced ligand solvolysis of cis-[Ru (bipyridine)$_2$(nicotinamide)$_2$]$^{2+}$: experimental and theoretical insight into its photoactivation mechanism. *Phys. Chem. Chem. Phys.* 16, 19141–19155. doi: 10.1039/C4CP02359E

Hadden, D. J., Roberts, G. M., Karsili, T. N., Ashfold, M. N., and Stavros, V. G. (2012). Competing 1 ψ^* mediated dynamics in mequinol: O–H versus O–CH 3 photodissociation pathways. *Phys. Chem. Chem. Phys.* 14, 13415–13428. doi: 10.1039/c2cp42289a

Horbury, M., Flourat, A. L., Greenough, S. E., Allais, F., and Stavros, V. (2018). Investigating isomer specific photoprotection in a model plant sunscreen. *Chem. Commun.* 54, 936–939. doi: 10.1039/C7CC09061G

Horbury, M. D., Baker, L., Quan, W., Greenough, S. E., and Stavros, V. (2016). Photodynamics of potent antioxidants: ferulic and caffeic acids. *Phys. Chem. Chem. Phys.* 18, 17691–7. doi: 10.1039/C6CP01595F

Horbury, M. D., Baker, L. A., Rodrigues, N. D., Quan, W.-D., and Stavros, V. G. (2017b). Photoisomerization of ethyl ferulate: a solution phase transient absorption study. *Chem. Phys. Lett.* 673, 62–67. doi: 10.1016/j.cplett.2017.02.004

Horbury, M. D., Holt, E. L., Mouterde, L. M., Balaguer, P., Cebrián, J., Blasco, L., et al. (2019). Towards symmetry driven and nature inspired UV filter design. *Nat. Commun.* 10:4748. doi: 10.1038/s41467-019-12719-z

Horbury, M. D., Quan, W.-D., Flourat, A., Allais, F., and Stavros, V. (2017a). Elucidating nuclear motions in a plant sunscreen during photoisomerization through solvent viscosity effects. *Phys. Chem. Chem. Phys.* 19, 21127–21131. doi: 10.1039/C7CP04070A

Humphrey, W., Dalke, A., and Schulten, K. (1996). VMD: visual molecular dynamics. *J. Mol. Graph.* 14, 33–38. doi: 10.1016/0263-7855(96)00018-5

Khattab, I. S., Bandarkar, F., Fakhree, M. A. A., and Jouyban, A. (2012). Density, viscosity, and surface tension of water+ ethanol mixtures from 293 to 323K. *Korean J. Chem. Eng.* 29, 812–817. doi: 10.1007/s11814-011-0239-6

Klamt, A., and Schüürmann, G. (1993). COSMO: a new approach to dielectric screening in solvents with explicit expressions for the screening energy and its gradient. *J. Chem. Soc. Perkin Trans.* 2, 799–805. doi: 10.1039/P29930000799

Loden, M., Beitner, H., Gonzalez, H., Edström, D. W., Åkerström, U., Austad, J., et al. (2011). Sunscreen use: controversies, challenges and regulatory aspects. *Br. J. Dermatol.* 165, 255–262. doi: 10.1111/j.1365-2133.2011.10298.x

Luo, J., Liu, Y., Yang, S., Flourat, A. L., Allais, F., and Han, K. (2017). Ultrafast barrierless photoisomerization and strong ultraviolet absorption of photoproducts in plant sunscreens. *J. Phys. Chem. Lett.* 8, 1025–1030. doi: 10.1021/acs.jpclett.7b00083

Matsui, M. S., Hsia, A., Miller, J. D., Hanneman, K., Scull, H., Cooper, K. D., et al. (2009). Non-sunscreen photoprotection: antioxidants add value to a sunscreen. *J. Invest. Dermatol. Symp. Proc.* 14, 56–59. doi: 10.1038/jidsymp.2009.14

Mention, M., Flourat, A. L., Peyrot, C., and Allais, F. (2020). Biomimetic regioselective and high-yielding Cu (I)-catalyzed dimerization of sinapate esters in green solvent CyreneTM: towards sustainable antioxidant and anti-UV ingredients. *Green Chem* 22, 2077–2085. doi: 10.1039/D0GC00122H

Mullen, K. M., and Van Stokkum, I. H. (2007). TIMP: an R package for modeling multi-way spectroscopic measurements. *J. Stat. Softw* 18. doi: 10.18637/jss.v018.i03

Neudörffer, A., Bonnefont-Rousselot, D., Legrand, A., Fleury, M.-B., and Largeron, M. (2004). 4-Hydroxycinnamic ethyl ester derivatives and related dehydrodimers: relationship between oxidation potential and protective effects against oxidation of low-density lipoproteins. *J. Agric. Food Chem.* 52, 2084–2091. doi: 10.1021/jf035068n

Neudörffer, A., Fleury, M.-B., Desvergne, J.-P., and Largeron, M. (2006). Effects of lithium ion-pairing on the electrochemical oxidation of 4-hydroxycinnamate derivatives. *Electrochim. Acta* 52, 715–722. doi: 10.1016/j.electacta.2006.06.001

Roberts, G. M., and Stavros, V. G. (2014). The role of ψ^* states in the photochemistry of heteroaromatic biomolecules and their subunits: insights from gas-phase femtosecond spectroscopy. *Chem. Sci.* 5, 1698–1722. doi: 10.1039/c3sc53175a

Saewan, N., and Jimtaisong, A. (2015). Natural products as photoprotection. *J. Cosmet. Dermatol.* 14, 47–63. doi: 10.1111/jocd.12123

Saija, A., Tomaino, A., Trombetta, D., De Pasquale, A., Uccella, N., Barbuzzi, T., et al. (2000). *In vitro* and *in vivo* evaluation of caffeic and ferulic acids as topical photoprotective agents. *Int. J. Pharm.* 199, 39–47. doi: 10.1016/S0378-5173(00)00358-6

Saltiel, J., and Redwood, C. E. (2016). Photochemistry of the 1, 4-Diphenyl-1, 3-butadienes in Ethanol. Trapping conical intersections. *J. Phys. Chem. A* 120, 2832–2840. doi: 10.1021/acs.jpca.6b02330

Segur, J. B., and Oberstar, H. E. (1951). Viscosity of glycerol and its aqueous solutions. *Ind. Eng. Chem.* 43, 2117–2120. doi: 10.1021/ie50501a040

Sharma, A., Bányiová, K., Babica, P., El Yamani, N., Collins, A. R., and Cupr, P. (2017). Different DNA damage response of cis and trans isomers of commonly used UV filter after the exposure on adult human liver stem cells and human lymphoblastoid cells. *Sci. Tot. Environ.* 593, 18–26. doi: 10.1016/j.scitotenv.2017.03.043

Skotarczak, K., Osmola-Mankowska, A., Lodyga, M., Polanska, A., Mazur, M., and Adamski, Z. (2015). Photoprotection: facts and controversies. *Eur. Rev. Med. Pharmacol. Sci.* 19, 98–112.

Snellenburg, J. J., Laptenok, S., Seger, R., Mullen, K. M., and Van Stokkum, I. H. M. (2012). Glotaran: a java-based graphical user interface for the R package TIMP. *J. Stat. Softw.* 49, 1–22. doi: 10.18637/jss.v049.i03

Stavros, V. G. (2014). A bright future for sunscreens. *Nat. Chem.* 6, 955–956. doi: 10.1038/nchem.2084

Tsierkezos, N. G., and Molinou, I. E. (1998). Thermodynamic properties of water+ ethylene glycol at 283.15, 293.15, 303.15, and 313.15 K. *J. Chem. Eng. Data* 43, 989–993. doi: 10.1021/je9800914

Turner, M., Horbury, M., Stavros, V., and Hine, N. (2019). Determination of secondary species in solution through pump-selective transient absorption spectroscopy and explicit-solvent TDDFT. *J. Phys. Chem. A* 123, 873–880. doi: 10.1021/acs.jpca.8b11013

Valiev, M., Bylaska, E. J., Govind, N., Kowalski, K., Straatsma, T. P., Van Dam, H. J., et al. (2010). NWChem: a comprehensive and scalable open-source solution for large scale molecular simulations. *Comput. Phys. Commun.* 181, 1477–1489. doi: 10.1016/j.cpc.2010.04.018

Vengris, M., Larsen, D. S., Van Der Horst, M. A., Larsen, O. F. A., Hellingwerf, K. J., and Van Grondelle, R. (2005). Ultrafast dynamics of isolated model photoactive yellow protein chromophores: "chemical perturbation theory" in the laboratory. *J. Phys. Chem. B* 109, 4197–4208. doi: 10.1021/jp045763d

Winget, P., Dolney, D. M., Giesen, D. J., Cramer, C. J., and Truhlar, D. G. (1999). *Minnesota Solvent Descriptor Database*. Minneapolis, MN: Department of Chemistry and Supercomputer Institute; University of Minnesota.

York, D. M., and Karplus, M. (1999). A smooth solvation potential based on the conductor-like screening model. *J. Phys. Chem. A* 103, 11060–11079. doi: 10.1021/jp992097l

Young, J. D., Staniforth, M., Dean, J. C., Roberts, G. M., Mazzoni, F., Karsili, T. N., et al. (2014). Towards understanding photodegradation pathways in lignins: the role of intramolecular hydrogen bonding in excited states. *J. Phys. Chem. Lett.* 5, 2138–2143. doi: 10.1021/jz500895w

Zhao, X., Ji, F., Liang, Y., Li, P., Jia, Y., Feng, X., et al. (2020). Theoretical and spectroscopic investigation on ultrafast nonadiabatic photoprotective mechanism of novel ultraviolet protective compounds inspired by natural sunscreens. *J. Lumin.* 223:117228. doi: 10.1016/j.jlumin.2020.117228

Zuehlsdorff, T., Haynes, P., Payne, M., and Hine, N. (2017). Predicting solvatochromic shifts and colours of a solvated organic dye: the example of nile red. *J. Chem. Phys.* 146:124504. doi: 10.1063/1.4979196

Reinvestigating the Photoprotection Properties of a Mycosporine Amino Acid Motif

Abigail L. Whittock [1,2], Matthew A. P. Turner [2,3,4], Daniel J. L. Coxon [2,4,5], Jack M. Woolley [2], Michael D. Horbury [6] and Vasilios G. Stavros [2]*

[1] Analytical Science Centre for Doctoral Training, Senate House, University of Warwick, Coventry, United Kingdom, [2] Department of Chemistry, University of Warwick, Coventry, United Kingdom, [3] Molecular Analytical Science Centre for Doctoral Training, Senate House, University of Warwick, Coventry, United Kingdom, [4] Department of Physics, University of Warwick, Coventry, United Kingdom, [5] Diamond Science and Technology Centre for Doctoral Training, University of Warwick, Coventry, United Kingdom, [6] School of Electronic and Electrical Engineering, University of Leeds, Leeds, United Kingdom

With the growing concern regarding commercially available ultraviolet (UV) filters damaging the environment, there is an urgent need to discover new UV filters. A family of molecules called mycosporines and mycosporine-like amino acids (referred to as MAAs collectively) are synthesized by cyanobacteria, fungi and algae and act as the natural UV filters for these organisms. Mycosporines are formed of a cyclohexenone core structure while mycosporine-like amino acids are formed of a cyclohexenimine core structure. To better understand the photoprotection properties of MAAs, we implement a bottom-up approach by first studying a simple analog of an MAA, 3-aminocyclohex-2-en-1-one (**ACyO**). Previous experimental studies on **ACyO** using transient electronic absorption spectroscopy (TEAS) suggest that upon photoexcitation, **ACyO** becomes trapped in the minimum of an S_1 state, which persists for extended time delays (>2.5 ns). However, these studies were unable to establish the extent of electronic ground state recovery of **ACyO** within 2.5 ns due to experimental constraints. In the present studies, we have implemented transient vibrational absorption spectroscopy (as well as complementary TEAS) with Fourier transform infrared spectroscopy and density functional theory to establish the extent of electronic ground state recovery of **ACyO** within this time window. We show that by 1.8 ns, there is >75% electronic ground state recovery of **ACyO**, with the remaining percentage likely persisting in the electronic excited state. Long-term irradiation studies on **ACyO** have shown that a small percentage degrades after 2 h of irradiation, plausibly due to some of the aforementioned trapped **ACyO** going on to form a photoproduct. Collectively, these studies imply that a base building block of MAAs already displays characteristics of an effective UV filter.

Keywords: photoprotection, photostability, ultrafast, spectroscopy, mycosporine

INTRODUCTION

Ultraviolet (UV) radiation, in particular UVA (315–400 nm) and UVB (280–315 nm), that reaches the Earth's surface has both positive and negative effects on living organisms (Holick, 2004; Lucas et al., 2006; Humble, 2010). Consequently, nature has developed its own photoprotection to safeguard from harmful DNA damage. In humans, this natural photoprotection is achieved by producing melanin pigments that can absorb UVA and UVB radiation before it reaches DNA (Kollias et al., 1991). However, as melanin production is a delayed process and does not absorb all UVA and UVB radiation that reaches the skin, a more immediate form of protection is required, i.e., sunscreens (Eller and Gilchrest, 2000; Brenner and Hearing, 2008; Wang and Lim, 2016). Some UV filters found in sunscreens have been linked to the cause of damaging environmental effects as well as adverse dermatological effects (Bryden et al., 2006; Danovaro et al., 2008; Downs et al., 2013, 2016; Warshaw et al., 2013; Schaap and Slijkerman, 2018). As a result, there is an increased need for the identification of new UV filters that are less harmful to both the environment and humans. Drawing inspiration from nature offers a promising solution to these negative impacts. One approach is to base candidate UV filters off structures observed in plants and microorganisms (Bandaranayake, 1998; Dean et al., 2014; Baker et al., 2016, 2018; Horbury et al., 2017, 2018, 2019; Luo et al., 2017; Zhao et al., 2019a,b).

Cyanobacteria, fungi, macro- and microalgae all synthesize a family of molecules termed mycosporines and mycosporine-like amino acids (Sinha et al., 2007; Balskus and Walsh, 2010). In the literature, mycosporines and mycosporine-like amino acids are used synonymously. However, mycosporines are a family of molecules comprised of a cyclohexenone core and mycosporine-like amino acids are comprised of a cyclohexenimine core (herein both mycosporines and mycosporine-like amino acids will be termed MAAs) (Gao and Garcia-Pichel, 2011). MAAs present a strong absorbance band in the UVA and UVB, and their high photostability makes them highly desirable as potential UV filters (Bandaranayake, 1998; Conde et al., 2000, 2007; Sinha et al., 2000; Moliné et al., 2011; Rastogi and Incharoensakdi, 2014). As the extraction from natural sources and the synthetic preparation of natural MAAs produces small quantities, some work has been carried out on synthetic MAA motifs as an alternative; these molecules have also demonstrated promising levels of photostability thus far (White et al., 1989, 1995; Bandaranayake, 1998; Losantos et al., 2017, 2019; Woolley et al., 2018). Complementary studies, implementing computational and ultrafast spectroscopic techniques have been conducted on various MAA motifs in an effort to guide future UV filter design through knowledge of the photoprotection mechanisms

(Losantos et al., 2017, 2019; Woolley et al., 2018). Their finding will be briefly outlined here.

Losantos et al. (2017) implemented a CASPT2/CASSCF methodology to evaluate the minimum energy paths of a selection of MAA motifs composed of either a cyclohexenone or a cyclohexenimine core. Their results showed that a cyclohexenone core is potentially a poor scaffold for sunscreen applications, as following photoexcitation to the lowest optically bright S_2 excited state, a geometric distortion to a non-planar geometry leads to relaxation to the S_1 state via a S_2/S_1 conical intersection (CI). The electronic excited state population then traverses along the potential energy surface of the S_1, before becoming trapped in a minimum on the S_1 potential energy surface. For the cyclohexenimine core, Losantos et al. (2017) proposed that after initial photoexcitation to the lowest optically bright S_1 excited state, fast relaxation along an out-of-plane geometry distortion leads to an accessible S_1/S_0 CI, resulting in efficient repopulation of the electronic ground state. These results by Losantos et al. (2017) are corroborated by computational studies on the natural MAAs palythine and porphyra-334 (Sampedro, 2011; Koizumi et al., 2017; Hatakeyama et al., 2019). Interestingly, a computational study on gadusol (a molecule closely related to MAAs with a cyclohexenone core) found an accessible barrierless S_1/S_0 CI (Losantos et al., 2015). This, in addition to experimental studies on gadusol which reported high levels of photostability and rapid non-radiative decay as the dominant relaxation pathway (Arbeloa et al., 2011), indicates that molecules with a cyclohexenone core do display a number of ideal properties of a UV filter. Therefore, there is still much to learn about these cyclohexenone systems.

Woolley et al. (2018) and Losantos et al. (2019) have conducted transient electronic absorption spectroscopy (TEAS) experiments on MAA motifs to unravel their photoprotection mechanisms. Woolley et al. (2018) investigated two MAA motifs, the one of interest for this paper being 3-aminocyclohex-2-en-1-one (ACyO), see inset of **Figure 1** for the structure of **ACyO**. Their TEAS experimental results for **ACyO** in methanol (polar protic) and acetonitrile (polar aprotic) demonstrated a persistent excited state absorption (ESA), >2.5 ns, corroborating calculations from Losantos et al. (2017) that (at least a fraction of) **ACyO** becomes trapped in a minimum of the S_1. We note here that the calculated barrier to the S_1/S_0 CI is 0.04 eV for **ACyO** in the gas-phase (Woolley et al., 2018). Whilst population persisted in the excited state for nanoseconds, no real indication as to the percentage of **ACyO** that remained in the electronic excited state can be inferred from the TEAS experiment. This is due to TEAS experimental limitations as Woolley et al. (2018) were unable to observe a ground state bleach (GSB) of **ACyO**. Consequently, they could not establish the extent of electronic ground state recovery which would give a direct measure of the photostability of **ACyO**. Herein, we propose that UV pump infrared probe transient vibrational absorption spectroscopy (TVAS) can be used to measure the extent of vibrational ground state recovery in the electronic ground state on ultrafast timescales after photoexcitation, thus providing insight into the overall electronic ground state recovery of **ACyO**.

Abbreviations: UV, ultraviolet; MAA, mycosporine-like amino acid; ACyO, 3-aminocyclohex-2-en-1-one; TEAS, transient electronic absorption spectroscopy; CI, conical intersection; ESA, excited state absorption; GSB, ground state bleach; TVAS, transient vibrational absorption spectroscopy; DFT, density functional theory; EtOH, ethanol; DMSO, dimethyl sulfoxide; TDDFT, time-dependent density functional theory; FTIR, Fourier transform infrared; TEA, transient electronic absorption; MCT, mercury cadmium telluride; TVA, transient vibrational absorption.

FIGURE 1 | Steady-state UV/visible extinction spectra of **ACyO** in EtOH (black line) and DMSO (red line). Vertical line corresponds to the absorption maxima of each solution; 285 nm for EtOH and 280 nm for DMSO. Inset is the structure of **ACyO** along with its atom numbers.
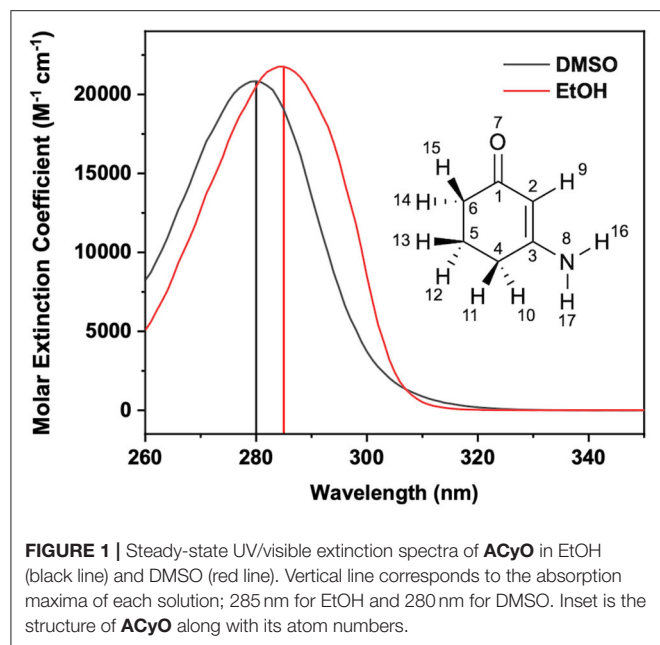
To better understand the behavior of MAA motifs with a cyclohexenone core, we have performed TVAS, along with complementary TEAS and long-term irradiation studies on **ACyO**, to study the GSB recovery of its vibrational modes. We build on a study by Sui et al. (2012) who used density functional theory (DFT) to assign the vibrational modes of **ACyO** in acetonitrile and water; for reasons that will become apparent later, our experiments utilized ethanol (EtOH) and dimethyl sulfoxide (DMSO) as solvents. In order to assign the vibrational modes both in the electronic ground and excited state in EtOH and DMSO, we have implemented implicit- and explicit-solvent DFT and time-dependent DFT (TDDFT) (Casida, 1995) calculations using a similar level of theory to Sui et al. (2012). These high-level calculations were necessary for the identification of any overlapping electronic ground and excited state frequencies that would influence the interpretation of our TVAS data. We report in the present work that TVAS is a powerful technique that can extract GSB recovery quantum yields for the vibrational modes of a molecule on ultrafast timescales by comparing the extent of the bleach recovery with respect to the initial GSB. Previous publications have reported GSB recovery quantum yields, and how such qualitative information provides valuable insight into the efficiency of relaxation pathways (Holm et al., 2003; Rini et al., 2003; Murdock et al., 2014, 2015). For **ACyO**, the resultant quantum yields in addition to its overall photostability demonstrates promising properties that are required of a UV filter, providing some evidence for the photoprotective capabilities of MAAs with a cyclohexenone core.

MATERIALS AND METHODS

ACyO was purchased from Alfa Aesar (95% purity) and solutions of ~40 μM, 4 mM, and 50 mM concentrations were made up

in the two solvents used in this study. EtOH ($\geq$99.8%) and DMSO ($\geq$99.9%) were purchased from VWR Chemicals and Fisher Scientific, respectively.

Steady-State Spectroscopy

ACyO samples in EtOH and DMSO of concentrations ~40 μM contained in a 1 cm path length quartz cuvette were irradiated within a solar simulator (91,191–1,000, Oriel Instruments) which has an output power equivalent to the sun at the Earth's surface (~1,000 W/m^2) for 7,200 s (120 min, 2 h). At various time intervals, UV/visible spectra were recorded using a UV/visible spectrometer (Cary 60, Agilent Technologies). To confirm that the degradation occurring was due to photodegradation, UV/visible spectra of **ACyO** solutions that had not been irradiated were taken before and after 7,200 s.

Fourier transform infrared (FTIR) spectra were obtained using a FTIR spectrometer (VERTEX 70v, Bruker) under a nitrogen environment to remove vibrational modes associated with atmospheric gases. 50 mM **ACyO** solutions in EtOH and DMSO were contained within a demountable liquid cell (Harrick Scientific Products Inc.) with a path length of 100 μm achieved by inserting 100 μm PTFE spacers between two CaF$_2$ windows (front window 1 mm and back window 2 mm thickness). The FTIR spectra were recorded over an energy range of 500–4,000 cm^{-1} with a resolution of 1 cm^{-1}.

Ultrafast Spectroscopy

TEAS and TVAS measurements were taken at the Warwick Center for Ultrafast Spectroscopy (WCUS: www.go.warwick.ac.uk/fac/sci/wcus). The setup of the TEAS experiment has been previously reported (Woolley et al., 2018), but it will be briefly described here. 4 mM solutions of **ACyO** in EtOH and DMSO were circulated through a demountable liquid cell with a path length of 100 μm set up in the same way as for FTIR spectroscopy described above. The samples were continuously circulated through the cell using a diaphragm pump (SIMDOS 02) to ensure a fresh sample was interacting with each laser shot. 800 nm pulses (12 W, 1 kHz, 40 fs) were generated by a Ti:Sapphire regenerative amplified laser system (Dual Ascend Pumped Spitfire Ace, Spectra-Physics) seeded by a Mai Tai (Spectra-Physics). The beam was split into four fractions, each fraction having its own recompression grating. One of the four fractions (3.5 W) was split into two further fractions in order to generate the pump and probe beams required for the TEAS experiments.

The first of the fractions (2.5 W) seeds an optical parametric amplifier (Topas-Prime with UV-extension, Light Conversion) which allows for a tuneable pump beam wavelength that includes 285 and 280 nm for photoexciting **ACyO** in EtOH and DMSO, respectively. These wavelengths were chosen as they correspond to the absorption maximum of each **ACyO** solution as displayed in **Figure 1**. The pump beam was set to a power of ~500 μW and was focused beyond the sample holder to give a beam diameter of 500 μm at the sample holder. The probe beam was generated by focussing 5% of the remaining 1 W fundamental 800 nm beam which had been further attenuated and irised on to a vertically translated CaF$_2$ window (2 mm thickness) to

generate a white light continuum (320–720 nm). The probe pulse polarization was held at the magic angle (54.7°) with regards to the pump pulse polarization; this is done to avoid dynamical contributions from molecular reorientations. The path length of the 800 nm beam used to generate the probe beam can be varied to give pump-probe time delays (Δt) of −1 ps to 2.5 ns using a gold retroreflector mounted on a motorized optical delay line. Before reaching the sample, the pump beam passes through an optical chopper operating at a repetition rate of 500 Hz, blocking every other pulse of the 1 kHz pulse train. This allows for direct comparison of the signal detected by a fiber-coupled spectrometer (AvaSpec-ULS1650F, Avantes) for the pumped and unpumped samples which is displayed as changes in optical density (ΔOD) in the resultant transient electronic absorption (TEA) spectra.

Pump power dependency studies were carried out to ensure that ΔOD was linearly dependent on photon flux (see **Supplementary Figure 1**). Chirp correction of the TEA spectra was achieved using the KOALA package (Grubb et al., 2014). Global fitting of the TEA spectra was employed using the software package Glotaran (Mullen and Van Stokkum, 2007; Snellenburg et al., 2012), and a sequential kinetic model ($A \xrightarrow{\tau_{e1}} B \xrightarrow{\tau_{e2}} C \ldots$) was used over the entire spectral region of our probe (320–720 nm). The evolution associated difference spectra for the time constants of each fit can be found in **Supplementary Figure 2**. The quality of the fits was assessed through the associated residuals, see **Supplementary Figure 2**. The instrument response function, accounting for the temporal resolution of our TEAS measurements, was determined by fitting a Gaussian over the time zero artifacts of solvent-only scans and taking the full width half-maximum, see **Supplementary Figure 3** for the instrument response functions of EtOH and DMSO.

For the TVAS set up, 50 mM **ACyO** solutions in EtOH and DMSO were circulated through a demountable liquid cell the same way as reported above for the TEAS set-up. The pump beam was set to a higher power of 700 μW for the TVAS experiments. The probe beam (240 μW, 360 μm beam diameter) for the TVAS experiment was generated by seeding a second optical parametric amplifier (Topas-C, Spectra-Physics) with a second 3.5 W fraction of the fundamental 800 nm beam. The generated probe beam allows for a tuneable IR wavelength that includes 6,420 and 6,289 nm which were the wavelengths used in this experiment for **ACyO** in EtOH and DMSO, respectively. The path length of the probe beam was varied in a similar way to the TEAS set-up to give Δt of −1 ps to 1.8 ns. Atmospheric absorption lines were excluded by purging the probe line with nitrogen gas. Before the probe beam arrived at the sample compartment, it was incident on a CaF_2 beamsplitter where it was split equally in to reference and probe pulses. The reference pulse did not traverse the sample and was detected for the subtraction of shot-to-shot laser noise. The probe pulse passed through the sample where it was partially absorbed before entering an imaging spectrometer (iHR320, HORIBA Scientific). Once in the spectrometer, the probe was dispersed by a diffraction grating (6 μm blaze, 100 lines mm^{-1} resolution) onto a mercury cadmium telluride (MCT) detector array (FPAS-0144, Infrared

Systems Development) which was made up of two 64-pixel linear arrays—one each for the probe and reference pulses. The MCT detector was cooled using liquid nitrogen to eliminate thermal contributions to the signal. Like in the TEAS experiment, the pump beam passes through an optical chopper operating at a repetition rate of 500 Hz, blocking every other pulse of the 1 kHz pulse train. This allows for direct comparison of the signal for the pumped and unpumped samples which is displayed as ΔOD in the resultant transient vibrational absorption (TVA) spectra.

We converted between pixel number and wavelength using a mid-IR polystyrene calibration card (Perkin Elmer) as our reference. Similarly to the TEAS, pump power dependency studies were carried out, see **Supplementary Figure 4**. Only ~100 cm^{-1} windows were investigated for each solvent environment; this was dictated by the spectral congestion emanating from the solvent and the transition intensity of **ACyO** vibrational modes. Exponential fits of the GSB features were employed to extract time constants associated with the dynamical processes **ACyO** undergoes upon photoexcitation.

Computational Methods

Vibrational frequencies in the electronic ground (S_0) and excited (S_1) state were predicted for **ACyO** in both implicit- and explicit-solvent environments for EtOH and DMSO. The NWChem package (Valiev et al., 2010) was used to perform DFT and TDDFT calculations. These were done at the PBE0/cc-pVTZ level of theory (Davidson, 1996; Perdew et al., 1996; Adamo and Barone, 1999). Implicit-solvent calculations were employed using the COSMO solvent model for both EtOH and DMSO which models each solvent's dielectric parameters (Klamt and Schüürmann, 1993; Winget et al., 1999; York and Karplus, 1999). We add that the level of theory described has previously been used for a similar system studied by Turner et al. (2019) which also performed vibrational frequency calculations. Due to discrepancies in the calculated S_0 vibrational frequencies and their corresponding vibrational modes, in addition to the fact EtOH and DMSO interact strongly with **ACyO**, it was determined that explicit-solvent contributions should be considered. See **Supplementary Table 1** and **Supplementary Figure 5** for implicit-solvent vibrational frequency results. This high-level of theory has been used so that accurate electronic excited state frequencies are predicted, which in turn provides valuable insight into any overlapping electronic ground and excited state frequencies in the TVAS probe region. As a result, reliable GSB recovery quantum yields can be extracted from the TVA spectra. Although neither implicit- or explicit-solvent results are perfect, the scaling factors required for explicit-solvent (0.997 and 0.982 for EtOH and DMSO, respectively) were significantly closer to 1 than implicit-solvent (0.976 for both solvents) indicating improved accuracy for the explicit-solvent calculations. Therefore, the decision was made to report explicit-solvent herein. Further to this, the asymmetry of the 1.8 ns lineout from our TVA spectra can be explained by the computed S_1 frequencies determined by EtOH explicit-solvent (see later discussion). On the other hand, the computed S_1 frequencies for EtOH implicit-solvent do not provide such clarity. Furthermore, regardless of whether an

implicit- or explicit-solvent model is used for **ACyO** in DMSO, there are no overlapping S_1 frequencies with the probed peaks in the TVAS experiment.

Solvent shells were generated through a similar method used by Zuehlsdorff et al. (2017) and Turner et al. (2019). In this, a classical molecular dynamics simulation was performed using the AMBER package (Case et al., 2015). **ACyO**, optimized in DFT at the level of theory discussed previously, was immersed in a 20 Å cube of explicit-solvent (both EtOH and DMSO). The system was heated over 20 ps in the NVT ensemble wherein the temperature is raised from 0 to 300 K. This, along with all further calculations, was achieved using a Langevin thermostat with a collision frequency of 1 ps^{-1}. Following this, a 400 ps pressure equilibration is utilized in the NPT isothermic-isobaric ensemble with the pressure fixed at 1 atm. Next, the system was equilibrated at a constant temperature of 300 K for 100 ps. Finally, snapshots were generated via a further NVT ensemble run, this time with a fixed temperature of 300 K for 8 ns. 2000 snapshots were extracted by recording a frame every 4 ps. By saving every tenth snapshot, 200 of these snapshots were exported. Within each snapshot, the solute and hydrogen bonding solvent molecules were extracted by removing any solvent molecules that were further than 1.5 Å from the solute.

As has been previously conducted by Turner et al. (2019), four snapshots were chosen for each solvent. Each snapshot has a different solvent environment and initial structures are shown in **Supplementary Table 2**. In the case of DMSO, only two solvent molecules were within 1.5 Å of **ACyO** and hence the four chosen snapshots were selected to ensure that the DMSO molecules were in different orientations in each snapshot (see **Supplementary Table 2**). For EtOH, a variety of solvent environments over the 200 snapshots were found, the most common being; one EtOH on the carbonyl oxygen and one EtOH on the amine hydrogen, two EtOH on the carbonyl oxygen and one EtOH on the amine hydrogen, one EtOH on the carbonyl oxygen and two EtOH on the amine hydrogens and finally two EtOH on the carbonyl oxygen and two EtOH on the amine hydrogens. One of each environment was selected for the calculations in order to evaluate the different solvent environments determined by molecular dynamics (see **Supplementary Table 2**). Calculations of full solvent shells were not conducted for the present work. This is due to previous findings by Turner et al. (2019) who found that full solvent shell calculations and smaller clusters with only two solvent molecules did not generate notable differences in the calculated vibrational frequencies. Furthermore, such calculations take significant computational expenditure due to the larger number of atoms.

The DFT calculations that were conducted were as follows: initially a geometry optimisation was employed on all the implicit- and explicit-solvent structures stated above followed by an electronic ground state frequency calculation. Vertical excitations were conducted and the results corroborated previous work stating that the first optically bright state is the S_2 (Sui et al., 2012; Losantos et al., 2017). Following this calculation, electronic excited state geometry relaxation calculations were carried out to determine the relaxed geometry on the S_1 excited state. The S_1 was chosen based on previous work that computed the minimum energy path and found that **ACyO** becomes trapped in the minimum of its S_1 excited state (Losantos et al., 2017; Woolley et al., 2018). Finally, electronic excited state vibrational frequency calculations were conducted on the S_1 relaxed geometry. Only averaged explicit-solvent vibrational frequencies for **ACyO** in EtOH and DMSO are presented herein, but all individual results for the implicit- and explicit-solvent environments can be found in the Supplementary Material including the optimised geometries and vertical excitation results (see **Supplementary Tables 1–5**). We also note that all reported frequencies are between 1,500 and 1,750 cm^{-1} as it is the region of interest for the present work and extensive evaluation of the computed frequencies is outside the scope of this work.

Scaling factors were applied to the calculated S_0 and S_1 frequencies and were calculated by using one experimental peak as a reference so that the calculated frequency exactly matches the reference experimental peak. This method is common practice and has been employed in a similar study by Turner et al. (2019) and Grieco et al. (2018). The chosen S_0 reference peaks were 1,559 and 1,577 cm^{-1} for **ACyO** in EtOH and DMSO, respectively, and were chosen because they were the strongest experimental peaks observed between 1,500 and 1,750 cm^{-1}. As there were no clear experimental S_1 frequencies obtained in this study, we tentatively applied the same scaling factor to the S_1 frequency calculation as was applied to the S_0 frequency calculation for both solvent environments; a similar approach was implemented by Baker et al. (2015). The resultant scaling factors for the averaged explicit-solvents snapshots of **ACyO** in EtOH and DMSO were 0.997 and 0.982, respectively.

RESULTS AND DISCUSSION

We first take a look at the TEA spectra acquired for **ACyO** in EtOH and DMSO which are displayed as false color maps in **Figure 2**; for lineouts of the TEA spectra see **Supplementary Figure 6**. The choice to use EtOH and DMSO as solvents was firstly to demonstrate dynamics in different solvent types (protic and aprotic), and secondly because these solvents displayed clear spectral windows in the region of interest for our FTIR and TVAS experiments. We note here that our TEA spectra strongly correlate with the findings of Woolley et al. (2018); the **ACyO** excited-state dynamics in EtOH are very similar to those observed in methanol (as might be expected; both polar and protic), and the **ACyO** excited state dynamics in DMSO are also very similar to those observed in acetonitrile (both polar and aprotic). Hence only a brief discussion is required here. Starting with **ACyO** in EtOH shown in **Figure 2A**, we observe a negative feature at early pump-probe time delays ($\Delta t < 0.2$ ps) identified as multiphoton initiated dynamics (see **Supplementary Figure 1**), followed by an intense ESA centered at ∼330 nm which blue-shifts out of the probe window and mostly decays by ∼5 ps. A second ESA of less intensity grows in within 5 ps centered at ∼400 nm and persists to the final time delay of our experiment ($\Delta t = 2.5$ ns), see **Supplementary Figure 6A** for lineouts. We now take a look at

FIGURE 2 | TEA spectra represented as false color maps of 4 mM **ACyO** in **(A)** EtOH photoexcited at 285 nm and **(B)** DMSO photoexcited at 280 nm. For **(A,B)** the time delays are plotted linearly until 1 ps and then as a log scale from 1 to 2,500 ps.
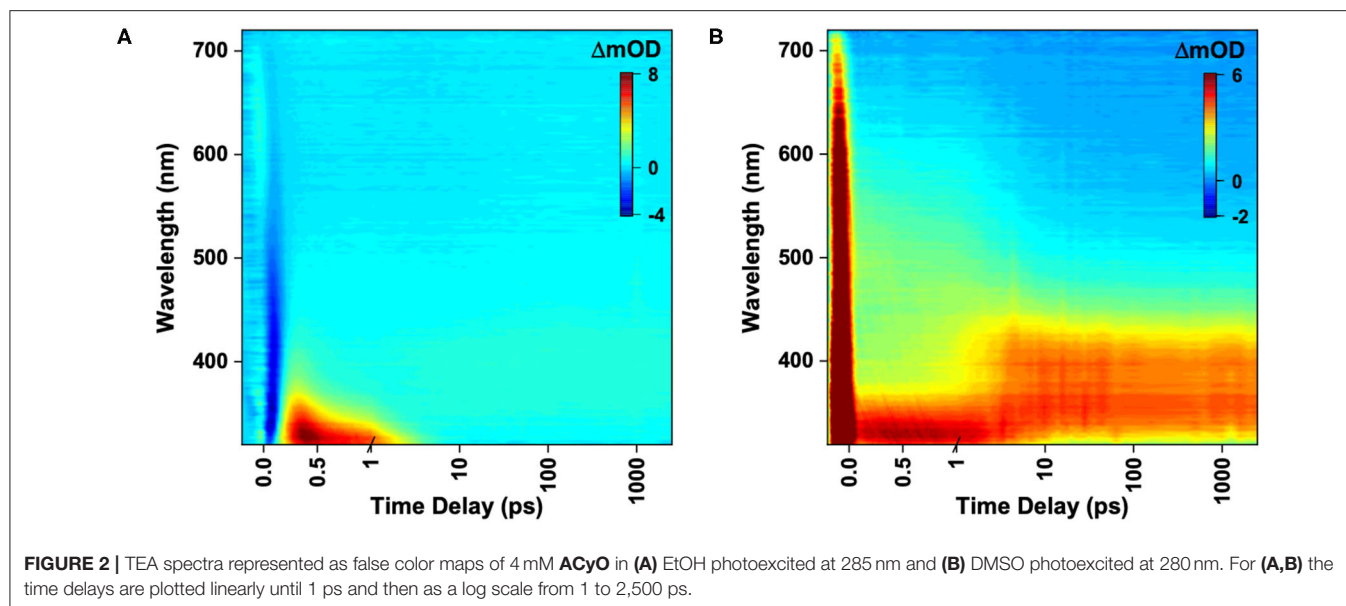
the TEA spectra for **ACyO** in DMSO shown in **Figure 2B**. At early time delays, there is a broad ESA spanning from 320 to 720 nm peaking at ∼330 nm. The broad ESA narrows and the greatest intensity red-shifts to center at ∼370 nm in around 5 ps. This feature then persists to the maximum Δt of the experiment ($\Delta t = 2.5$ ns), see **Supplementary Figure 6B** for lineouts.

Although mentioned previously, it is worth revisiting the proposed cyclohexenone core deactivation pathway upon photoexcitation reported by Losantos et al. (2017) as it is the basis for the time constant assignment presented herein. The vertical excitation calculations that were carried out for the present study corroborate previous work which states that **ACyO** is initially photoexcited to the S_2 through a $\pi_L^* \leftarrow \pi_H$ transition (see **Supplementary Table 4** and **Supplementary Figure 7**) (Sui et al., 2012; Losantos et al., 2017). The computed minimum energy path demonstrates that a similar molecule to **ACyO** ($NHCH_3$ substituent on C_3, herein termed the $NHCH_3$ molecule, see inset of **Figure 1**) studied by Losantos et al. (2017) redistributes its energy after photoexcitation causing a geometric distortion. This leads to an accessible S_2/S_1 CI where it then vibrationally cools to a minimum on the S_1. Woolley et al. (2018) conducted complementary calculations on **ACyO** finding that the calculated energy barrier to the S_1/S_0 CI for **ACyO** in the gas phase is 0.04 eV (Woolley et al., 2018), *cf*. 0.2 eV for the $NHCH_3$ molecule studied by Losantos et al. (2017). We now assign the dynamical processes to the extracted time constants from the global sequential fit, re-evaluating our previous work in light of the present and previous data.

Global fitting of **ACyO** in EtOH extracted three time constants and can be found in **Table 1**; we add that as the negative feature is the result of multiphoton initiated dynamics, it has been omitted from the global fit. We propose that the first time constant, $\tau_{e1} = 0.24$ ps, corresponds to the initial geometry relaxation and solvent rearrangement **ACyO** undergoes in order to traverse the S_2/S_1 CI and populate the S_1 potential energy

TABLE 1 | Time constants and associated errors extracted from the sequential global fit of the TEA spectra for **ACyO** in EtOH and DMSO.

Time constant	EtOH	DMSO
τ_{e1}	0.24 ± 0.035 ps	2.7 ± 0.038 ps
τ_{e2}	1.2 ± 0.035 ps	>2.5 ns
τ_{e3}	>2.5 ns	

surface. We attribute the second time constant, $\tau_{e2} = 1.2$ ps, with the vibrational cooling of **ACyO**, via vibrational energy transfer (both intramolecular and intermolecular), as it samples the S_1 potential energy surface before overcoming the barrier to, and traversing through the S_1/S_0 CI. From the evolution associated difference spectra and lineouts of **ACyO** in EtOH (see **Supplementary Figures 2A, 6A**), narrowing of the ESA is observed which is a good indication that vibrational cooling on the S_1 potential energy surface is occurring (also the case for **ACyO** in DMSO, see **Supplementary Figures 2B, 6B**). We note here that as the ESA (∼330 nm) decays out of the probe window in our TEA spectra, it is possible that τ_{e2} is an underestimation of the time constant associated with repopulation of the electronic ground state. The final time constant, $\tau_{e3} > 2.5$ ns, corresponds to any **ACyO** that has remained trapped in the minimum of the S_1 excited state.

The global fitting of **ACyO** in DMSO extracted two time constants, see **Table 1**. We have assigned the first time constant, $\tau_{e1} = 2.7$ ps, to a collection of processes; geometry relaxation and solvent rearrangement **ACyO** undergoes to reach the S_2/S_1 CI (similar to τ_{e1} for **ACyO** in EtOH), followed by vibrational energy transfer along the S_1 potential energy surface before repopulating the electronic ground state, mediated via the S_1/S_0 CI (similar to τ_{e2} for **ACyO** in EtOH). As with **ACyO** in EtOH, the second time constant, $\tau_{e2} > 2.5$ ns, corresponds to any **ACyO** that is still

populated in the S_1 excited state beyond the final time delay of our experiment. Based on the above assignments, we attribute the ESA at ∼400 nm which grows in within ∼5 ps and persists beyond the final time delay in the TEA spectra of both solvents (**Figures 2A,B**) to ESA from the S_1 minimum. For **ACyO** in DMSO, the ESA at extended time delays (2.5 ns) is still relatively large in intensity; however, from our TVA spectra we know that a large percentage of **ACyO** molecules have already returned to their electronic ground state within ∼5 ps, see later discussion. Plausible explanations are that the strength of the ESA from the S_1 minimum is greater than at other locations along the potential energy surface, or the ESA at early time delays is dampened by a competing stimulated emission. Thus, a reduced population on the S_1 minimum could (and evidently does) result in a more intense ESA. Further to this, we have determined through our TVA spectra that the relaxation mechanism in both solvents is the same, however, there is evidently a solvent dependence on the strength of the ESAs from different positions on the relaxation pathway. For example, the strength of the ESA from the S_1 minimum in EtOH is evidently weaker than the strength of the ESA from the S_1 minimum in DMSO. This highlights the influence of solvent on the oscillator strength, which was previously discussed by Woolley et al. (2018). Furthermore, our assignment here (and below) of population trapped on S_1 concurs with previous work in that there is a barrier to the S_1/S_0 CI (Losantos et al., 2017; Woolley et al., 2018).

However, we highlight again that no indication on the percentage of **ACyO** trapped in the S_1 excited state can be inferred from the TEA spectra. To glean further insight into this, we conducted both TVAS and steady-state irradiation studies. To begin the TVAS discussion, we must first look at the FTIR spectra of **ACyO** in EtOH and DMSO and assign the vibrational modes to the peaks of interest. **Table 2** gives the averaged explicit-solvent calculated S_0 frequencies (with associated scaling factors of 0.997 and 0.982 for EtOH and DMSO, respectively) and associated vibrational modes. **Figure 3** is a visual representation of the calculated frequencies overlaying the FTIR spectra for each **ACyO** solution between 1,500 and 1,750 cm^{-1}. Only this region of the FTIR spectra is displayed as it is the region that is not

masked by solvent absorption and includes the strongest peaks. The relative strengths of the vibrations have also been scaled to match the reference peaks at 1,559 and 1,577 cm^{-1} for **ACyO** in EtOH and DMSO, respectively.

The FTIR spectra for **ACyO** in EtOH and DMSO have many differences such as: peak positions; peak widths; peak intensities; and, to a lesser extent, assigned vibrational modes. This highlights how solvent environment effects the observed FTIR spectra and provides a further justification for our choice to implement explicit-solvent calculations. Similarities between the two spectra are that the strongest peak in each spectrum corresponds to the $C_2=C_3$ stretch (given in **Table 2** are the additional vibrational modes for this peak in each solvent but for simplicity it is referred to as the $C_2=C_3$ stretch herein) and the weaker peaks at highest wavenumbers in the presented spectra in **Figure 3** correspond to the H_{16}-N_8-H_{17} scissor mode, see inset of **Figure 1** for atom numbers. A similar pattern was observed in a previous study which computed the vibrational frequencies for **ACyO** in water and acetonitrile adding further credence to our assignment (Sui et al., 2012).

Generally, the calculated peak positions are in good agreement with the experimental data with the largest error being <20 cm^{-1} for the majority of the calculated frequencies. The only exception to this is the calculated frequency of 1,647 cm^{-1} for **ACyO** in DMSO which is shifted ∼45 cm^{-1} to a higher wavenumber compared to the experimental peak. This could be explained by the fact we only consider two DMSO molecules interacting with **ACyO** in our calculations compared to a full solvation shell interaction between solute and solvent. However, due to the reasonable accuracy for all other frequencies and because this vibrational mode does not have a corresponding S_1 frequency (see later discussion), the computational expenditure required for a full solvent shell calculation is deemed unnecessary.

The TVA spectra for **ACyO** in EtOH and DMSO and their associated tri-exponential fits for the GSB are shown in **Figure 4**. Global fitting was not implemented here as we were only interested in the GSB recovery of the probed vibrational modes. Furthermore, we note that our tri-exponential fits begin at the GSB signal maximum; for **ACyO** in EtOH this was 0.4 ps, and

TABLE 2 | Computed S_0 and S_1 vibrational frequencies and their associated vibrational modes at the PBE0/cc-pVTZ level of theory for **ACyO** in EtOH and DMSO between 1,500 and 1,750 cm^{-1}.

Solvent	S_0 frequencies, cm^{-1} (Rel. strength)	Vibrational mode S_0	S_1 frequencies, cm^{-1} (Rel. strength)	Vibrational mode S_1
EtOH	1,559 (298)	$C_2=C_3$ stretch + $C_1=O_7$ stretch + C_2-H_9 bend	1,517 (12)	H_{10}-C_4-H_{11} scissor
	1,605 (4)	$C_2=C_3$ stretch + $C_1=O_7$ stretch + H_{16}-N_8-H_{17} scissor	1,565 (46)	$C_2=C_3$ stretch + H_{10}-C_4-H_{11} scissor + N_8-H_{17} bend + C_2-H_9 bend
	1,685 (27)	H_{16}-N_8-H_{17} scissor	1,714 (34)	H_{16}-N_8-H_{17} scissor
DMSO	1,577 (185)	$C_2=C_3$ stretch + C_4-H_{10} bend + N_8-H_{17} bend + C_2-H_9 bend	1,523 (91)	$C_2=C_3$ stretch + C_4-H_{10} bend + N_8-H_{17} bend + C_2-H_9 bend
	1,647 (111)	$C_1=O_7$ stretch + H_{16}-N_8-H_{17} scissor	No corresponding frequency	
	1,675 (9)	H_{16}-N_8-H_{17} scissor	1,645 (44)	H_{16}-N_8-H_{17} scissor

The presented frequencies are an average of four explicit-solvent snapshots except for the S_1 EtOH frequencies which are an average of two explicit-solvent snapshots. Scaling factors of 0.997 and 0.982 were applied to the calculated frequencies for **ACyO** *in EtOH and DMSO, respectively. See text for details.*
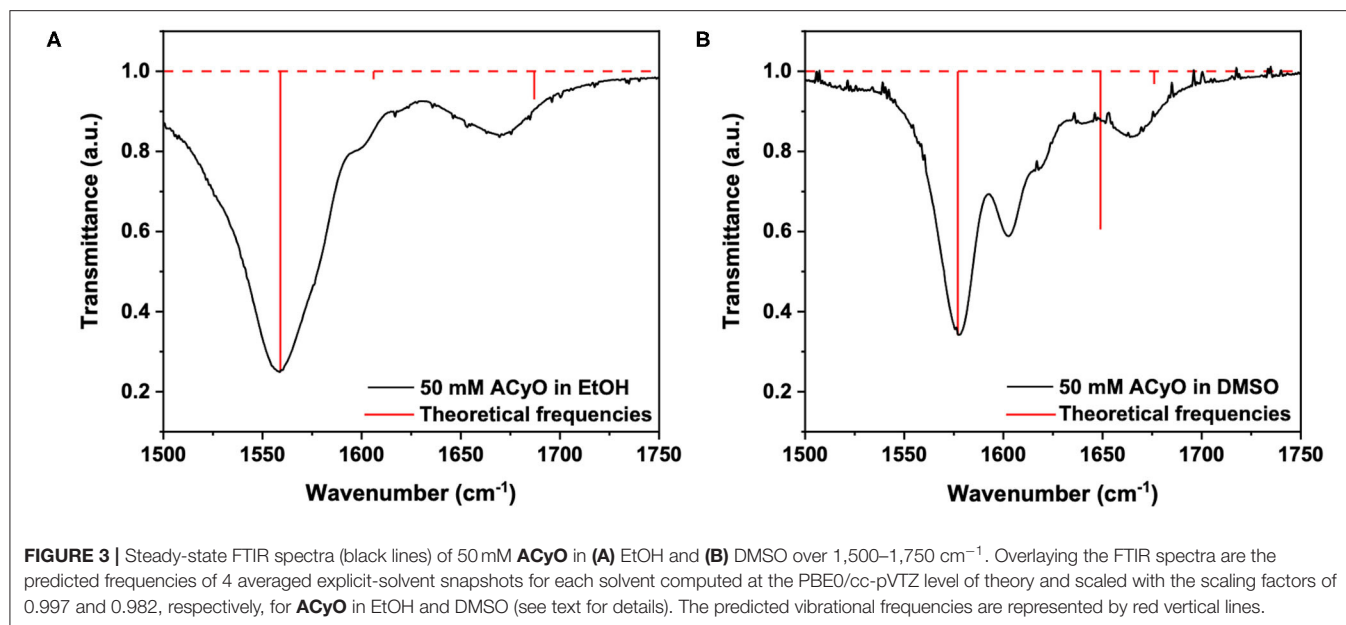
FIGURE 3 | Steady-state FTIR spectra (black lines) of 50 mM **ACyO** in **(A)** EtOH and **(B)** DMSO over 1,500–1,750 cm^{-1}. Overlaying the FTIR spectra are the predicted frequencies of 4 averaged explicit-solvent snapshots for each solvent computed at the PBE0/cc-pVTZ level of theory and scaled with the scaling factors of 0.997 and 0.982, respectively, for **ACyO** in EtOH and DMSO (see text for details). The predicted vibrational frequencies are represented by red vertical lines.

for **ACyO** in DMSO this was 0.7 ps. In fitting this way, we avoid any coherent artifacts that occur at early time delays such as perturbed free induction decay (Hamm, 1995). We start the TVAS discussion by first highlighting that in both solvents, full GSB recovery is not achieved at $\Delta t = 1.8$ ns. This is in accordance with the TEA spectra *supra* which show excited state dynamics persisting beyond $\Delta t = 2.5$ ns. The extracted GSB recovery quantum yields from the integrated signal of each GSB feature were calculated to be 86 and 76% for **ACyO** in EtOH (over 1,540–1,550 cm^{-1}, see later discussion for our choice to use this integration region) and DMSO (over 1,560–1,585 cm^{-1}) respectively. Greater GSB recovery is observed for **ACyO** in EtOH compared to **ACyO** in DMSO by 10%. A similar trend was observed for the long-term irradiation studies of **ACyO** presented below. The two are intuitively related and imply that more **ACyO** molecules in EtOH are able to overcome the barrier to access the S$_1$/S$_0$ CI within $\Delta t = 1.8$ ns. Therefore, there is less population trapped in the electronic excited state that can undergo pathways leading to photodegradation compared to **ACyO** in DMSO. We note here that the GSB recovery quantum yields we quote only consider GSB recovery that occurs within 1.8 ns, and it is possible that further electronic ground state repopulation may occur after that time.

The time constants extracted from the fit for **ACyO** in EtOH (1,559 cm^{-1} peak) and DMSO (1,577 cm^{-1} peak) are reported in **Table 3**. We begin by assigning the dynamical processes of the extracted time constants for **ACyO** in EtOH. The first time constant, $\tau_{v1} = 0.53$ ps, is on a similar timescale to τ_{e2} from the TEA spectra fit which would suggest that similar dynamics are occurring as we have reported; geometry relaxation and solvent rearrangement of **ACyO**, followed by vibrational energy transfer on S$_1$ and then repopulation of S$_0$. However, as TVAS only measures the GSB recovery of the fundamental vibration (being probed) in the electronic ground state, it provides little

information about the dynamics in the electronic excited state, making comparison between τ_{e2} and τ_{v1} tentative. As a result, we note that τ_{v1} may only be incorporating some of the electronic excited state dynamics and repopulation of the electronic ground state is most likely occurring on a longer time scale. The second time constant for the TVA spectra, $\tau_{v2} = 49$ ps, is associated with the vibrational cooling of the electronic ground state through vibrational energy transfer, both intramolecular and intermolecular (to solvent). This longer timescale can only be observed in the TVA spectra as the GSB of **ACyO** falls outside of the probe window for our TEAS experiment. As a result, no spectral signatures of vibrational cooling on the S$_0$ are present in the TEA spectra, and thus no time constant can be assigned to this photophysical process. Furthermore, we do not observe a blue-shifting of the transient vibrational bands with time that is often associated with the anharmonicity of vibrations (Nibbering et al., 2005), and instead observe a slight red-shift for **ACyO** in EtOH (**Figure 4A**). We reconcile this through the following: firstly, it is possible that the probed vibration is relatively harmonic; and secondly, the ESA from the S$_1$ minimum between ∼1,560 and 1,570 cm^{-1}, which contributes toward the GSB recovery and causes an asymmetric line shape at extended time delays (see later discussion), is likely the main cause of the apparent red-shift. For **ACyO** in DMSO (**Figure 4B**), neither a red-shift or a blue-shift is observed, providing confidence that the probed vibrations are relatively harmonic. The final time constant for **ACyO** in EtOH, $\tau_{v3} > 1.8$ ns, is due to the incomplete GSB recovery. Drawing reference to our TEAS data, this is very likely attributed to the long-lived **ACyO** trapped in the minimum of the S$_1$.

The calculated S$_1$ frequencies and associated vibrational modes for **ACyO** in EtOH can be found in **Table 2** and were scaled using the same scaling factor that was applied to the S$_0$ frequencies, 0.997. The reported frequencies are an average

FIGURE 4 | TVA spectra at selected time delays and steady-state FTIR of 50 mM **ACyO** in **(A)** EtOH photoexcited at 285 nm and **(B)** DMSO photoexcited at 280 nm. Scale on left of plots correspond to the change in optical density for the TVA spectra (colored lines) and scale of the right corresponds to the transmittance for the FTIR spectra (black lines). **(C)** Tri-exponential fit of the percentage recovery of the integrated GSB signal from the TVA spectra for **ACyO** in EtOH (1,540–1,550 cm^{-1}). **(D)** Tri-exponential fit of the percentage recovery of the integrated GSB signal from the TVA spectra for **ACyO** in DMSO (1,560–1,585 cm^{-1}). In both **(C,D)**, the open circles are the integrated GSB signal converted to percentage recovery and the red line is the fit. The time delays are plotted linearly until 110 ps then there is a break until 1,300 ps. Between 1,300 and 1,900 ps the scale is plotted logarithmically to show that the fit does not tend to zero.

TABLE 3 | Time constants and associated errors extracted from the tri-exponential fit of the integrated GSB signal from the TVA spectra for **ACyO** in EtOH (1,540–1,550 cm^{-1}) and DMSO (1,560–1,585 cm^{-1}).

Time constant	EtOH (1,559 cm^{-1})	DMSO (1,577 cm^{-1})
τ_{v1}	0.53 ± 0.028 ps	4.7 ± 0.35 ps
τ_{v2}	49 ± 2.9 ps	55 ± 9.0 ps
τ_{v3}	>1.8 ns	>1.8 ns

of two snapshots due to difficulties experienced when running our EtOH explicit-solvent excited state calculations, see the **Supplementary Material** for more details. We draw confidence on the validity of these results from the similarity between the two snapshots, alongside the consistency of the results observed in DMSO. Future studies may invest further into converging more snapshots, but this has a high computational cost and is beyond the scope of the work. The only S_1 frequency which had a clear corresponding S_0 frequency between 1,500 and 1,750 cm^{-1} for **ACyO** in EtOH was for the H_{16}-N_8-H_{17} scissor vibrational mode. This mode is shifted ~30 cm^{-1} in the S_1 to a higher wavenumber of 1,714 cm^{-1}. Additionally, two other excited state

frequencies were found during the calculation in the region of interest. These were computed as 1,517 and 1,565 cm^{-1} and they correspond to the H_{10}-C_4-H_{11} scissor and the $C_2{=}C_3$ stretch (plus several other vibrational modes), respectively, see **Table 2** for full vibrational mode assignment. These vibrational modes are convoluted on top of the GSB of the $C_2{=}C_3$ stretch at 1559 cm^{-1} that we probed in the TVAS experiment. The relative strengths of the two S_1 frequencies are significantly smaller than the S_0 frequency therefore, we would expect any ESAs to be much weaker in intensity compared to the GSB. That being said, from the TVA spectra in **Figure 4**, a small ESA feature is observable at a wavenumber of ~1,570 cm^{-1} and above; present between 10–20 ps and decaying by 50 ps. We are unable to definitely pinpoint the origin of this feature. Possible suggestions include probing: (1) the $C_2{=}C_3$ stretch in S_1; and (2) a higher lying vibration in **ACyO** in the ground electronic state which subsequently cools. Indeed, the decay of this feature matches τ_{v2} adding credence to the latter assignment. Importantly, at 1.8 ns, the asymmetry of the GSB feature insinuates that an ESA is contributing toward the GSB recovery between ~1,560 and 1,570 cm^{-1}. This matches the computed S_1 frequency at 1,565 cm^{-1}, therefore, we assign it to the population of **ACyO** trapped in the S_1 minimum. The ESA does not emerge above baseline due to the fact the transition is six

times weaker than the probed electronic ground state transition, see **Table 2**. Due to the convolution of peaks, we highlight that for the GSB recovery quantum yield and fitting of the GSB, a smaller region (1,540–1,550 cm^{-1}) was integrated between to negate as many contributions from the overlapping ESAs as possible. We appreciate that there is still a possibility that the ESA is contributing to the GSB recovery, hence we report the GSB recovery quantum yield of 86% as being the upper limit in this case.

The TVA spectra of **ACyO** in DMSO is more straightforward to interpret due to no convoluted S$_1$ frequencies computed by TDDFT calculations. A tri-exponential fit of the integrated signal of the 1,577 cm^{-1} vibration (1,560–1,585 cm^{-1}) can be found in **Figure 4** and its corresponding time constants can be found in **Table 3**. The same assignment of the time constants is made for **ACyO** in DMSO as that reported above for **ACyO** in EtOH. τ_{v1} (4.7 ps) is assigned to the geometry relaxation and solvent rearrangement **ACyO** undergoes to access the S$_2$/S$_1$ CI, followed by vibrational cooling on the S$_1$ and traversing through the S$_1$/S$_0$ CI to repopulate the electronic ground state. Like in **ACyO** in EtOH, the timescales of τ_{e1} and τ_{v1} are similar. τ_{v2} (55 ps) is assigned to the vibrational cooling of **ACyO** on the S$_0$ through vibrational energy transfer. Again, comparison to the TEA spectra cannot be made for τ_{v2} due to TEAS experimental limitations as discussed above. The final time constant, $\tau_{v3} > 1.8$ ns, is assigned to any **ACyO** molecules trapped in the minimum of the S$_1$ potential energy surface.

We conclude the TVAS discussion by evaluating the S$_1$ vibrational frequency calculations for **ACyO** in DMSO which can be found in **Table 2**. These computed frequencies are an average of four explicit-solvent snapshots and were simpler to assign to their corresponding electronic ground state frequencies, unlike **ACyO** in EtOH. For the C$_2$=C$_3$ stretch vibration, calculated frequency values of 1,577 cm^{-1} in the S$_0$ state and 1,523 cm^{-1} in the S$_1$ state are reported in **Table 2**. For the H$_{16}$-N$_8$-H$_{17}$ scissor vibration, the calculated frequency values are 1,675 cm^{-1} in the S$_0$ state and 1,645 cm^{-1} in the S$_1$ state. Therefore, upon S$_1$←S$_0$ excitation, the harmonic frequencies of both vibrations are shifted to a lower wavenumber; the frequency of the C$_2$=C$_3$ stretch vibration by ∼50 cm^{-1} and the frequency of the H$_{16}$-N$_8$-H$_{17}$ scissor vibration by ∼30 cm^{-1}. There was no corresponding S$_1$ frequency for the C$_1$=O$_7$ stretch plus H$_{16}$-N$_8$-H$_{17}$ scissor that was computed as 1,647 cm^{-1} in the electronic ground state. Additionally, there were no other new S$_1$ frequencies appearing between 1,500 and 1,750 cm^{-1} and this insinuates that no ESA features should be present in the TVA spectra, which is the case as seen in **Figure 4B**. As a result, we are confident that the GSB recovery quantum yield for **ACyO** in DMSO (76%) is a more accurate value than the GSB recovery quantum yield for **ACyO** in EtOH (86%). We add that a degenerate pump-probe experiment would complement the observed GSB recovery quantum yields obtained from our TVAS experiments; however, for the present study, the TVAS data provides a good starting point with which to progress with future studies.

In our efforts to link our ultrafast dynamics studies of **ACyO** (and the GSB recovery quantum yields thereof) to the long-term photostability of **ACyO**, we performed long-term irradiation studies and the results are presented in **Figure 5**. The data shows that after 7,200 s, only 2.0 and 6.5% degradation of signal at the absorption maxima occurred for **ACyO** in EtOH and DMSO, respectively. Control measurements confirmed that all degradation observed was due to photodegradation, see **Supplementary Figure 8**. The impressive levels of photostability of **ACyO** in both solvents must stem from highly efficient repopulation of the electronic ground state as we observed in our TVAS studies *supra*. In the long-term irradiation study, we see no emergence of an absorbance at ∼400 nm in either solvent, eliminating the possibility that the long-lived feature in the TEA spectra is a photoproduct. This provides further support that the long-lived feature observed in our TEA and TVA spectra is **ACyO** population trapped in S$_1$ state. Losantos et al. (2017) predicted that the cyclohexenone unit they studied would radiatively decay after becoming trapped on the S$_1$ in order to repopulate the molecules' electronic ground state. However, in accordance with Woolley et al. (2018) we observed no radiative decay implying that **ACyO** must recover to the electronic ground state non-radiatively. We draw this conclusion from the fact that no stimulated emission features (induced by one-photon absorption of the pump) are present in the TEA spectra for **ACyO** in both EtOH and DMSO, and that no emission was observed in the steady-state emission spectra of **ACyO** in both solvents when compared to blank scans of solvent-only solutions (spectra not shown). The lack of observed fluorescence would suggest that there is very poor Franck-Condon overlap between the S$_1$ minimum and the electronic ground state. These steady-state results further support our conclusion that the S$_1$/S$_0$ CI is accessed by >75% of **ACyO** molecules on ultrafast timescales as they are able to overcome the mild barrier from the S$_1$ minimum (0.04 eV) (Woolley et al., 2018).

For the **ACyO** population remaining in the excited state at extended time delays, >1.8 ns, it is likely that further repopulation of the electronic ground state and some photoproduct formation occurs. It is important to highlight that the systems we have studied are simple, isolated systems, therefore, we have observed repopulation of the electronic ground state at time beyond 1.8 ns. However, in a more complex environment like a sunscreen formulation, the population of **ACyO** in the S$_1$ excited state persisting beyond 1.8 ns has a greater chance of either forming a photoproduct or transferring that energy through collisions. This reinforces the importance of why an ideal UV filter would return to its electronic ground state on ultrafast timescales and why we conclude that **ACyO** is not a perfect UV filter candidate. We close the discussion by reiterating that more photoproduct formation appears to be occurring for **ACyO** in DMSO which is intuitively related to the lower GSB recovery quantum yield extracted from the TVA spectra presented above. The greater population persisting in the S$_1$ excited state at extended time delays, >1.8 ns, increases the probability for photoproduct formation.

CONCLUSION

Throughout the present work we have demonstrated that although **ACyO** has a long-lived excited state that persists

FIGURE 5 | UV/visible spectra of ~40 μM **ACyO** in **(A)** EtOH and **(B)** DMSO taken over varying durations of irradiation in a solar simulator. Black arrow on each plot denotes a decrease in absorbance at the absorption maxima after 7,200 s and corresponds to 2.0% for **ACyO** in EtOH and 6.5% for **ACyO** in DMSO.
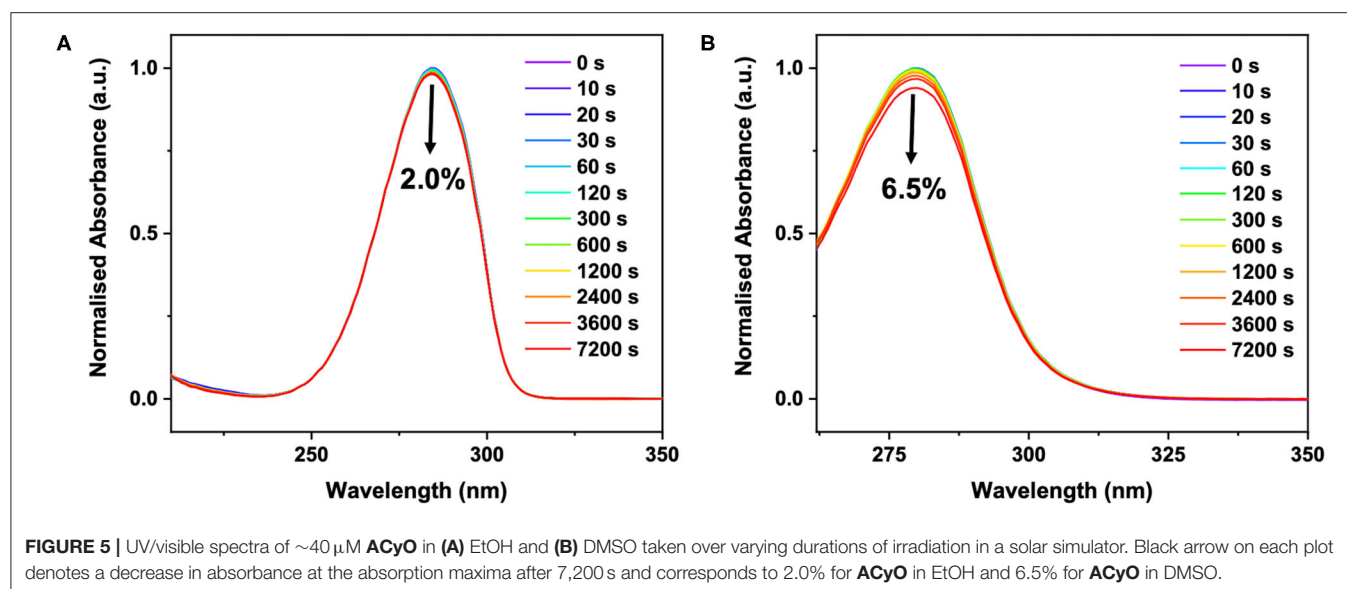
beyond 2.5 ns, the extent of ground state recovery on ultrafast timescales is relatively high. We have determined that >75% of photoexcited **ACyO** in EtOH and DMSO is returning to its electronic ground state within 1.8 ns. These numbers appear to corroborate why **ACyO** displays good photostability in the isolated systems studied. Upon photoexcitation, we demonstrate that the majority of **ACyO** molecules have sufficient energy to overcome the S_1/S_0 CI barrier and relax non-radiatively on ultrafast timescales. Although **ACyO** displays long-lived features in accordance with previous studies (Losantos et al., 2017; Woolley et al., 2018), we propose that the cyclohexenone core is not as poor a UV filter as initially predicted, supporting nature's choice of the cyclohexenone core in MAAs. However, for an ideal UV filter we would ideally like as-close-to complete GSB recovery within ultrafast timescales; further studies on molecules with a cyclohexenone unit are therefore most-certainly warranted so as to provide clearer insight in to their photoprotective mechanisms, and how these mechanisms are influenced with substituent. In particular, how the GSB recovery quantum yield is influenced as we move progressively toward gadusol is one avenue to be explored, which could eventually guide the future design of UV filters based on MAAs.

In this present work, we have demonstrated that TVAS is a very powerful method when allied with appropriate high-level theory (in this case using explicit-solvent methodology which is important to consider when solute and solvent interact strongly with each other) for extracting accurate GSB recovery information. The combination of this high-level theory and TVAS enables vibrational ESA bands to be identified when selecting an integration region, allowing for the origins of a molecule's photostability to be traced. TVAS provides invaluable dynamical information that cannot be extracted from TEAS. Therefore, we suspect that this technique will see increasing use in the field of sunscreen science.

DATA AVAILABILITY STATEMENT

The datasets presented in this study can be found in online repositories. The names of the repository/repositories and accession number(s) can be found below: Zenodo repository doi: 10.5281/zenodo.3885450.

AUTHOR CONTRIBUTIONS

ALW conducted the majority of the experimental and computational work and took lead in writing the manuscript. MAPT ran the molecular dynamics simulations and provided support for the computational analysis. MAPT and JMW supervised the writing of the manuscript. DJLC and MDH helped conduct the transient vibrational absorption spectroscopy experiments presented in this paper. VGS conceived the experiment, supervised the writing of the manuscript, and supported the data analysis. All authors contributed to the article and approved the submitted version.

ACKNOWLEDGMENTS

SUPPLEMENTARY MATERIAL

The Supplementary Material for this article can be found online at: https://www.frontiersin.org/articles/10.3389/fchem. 2020.574038/full#supplementary-material

REFERENCES

Adamo, C., and Barone, V. (1999). Toward reliable density functional methods without adjustable parameters: the PBE0 model. *J. Chem. Phys.* 110:6158. doi: 10.1063/1.478522

Arbeloa, E. M., Bertolotti, S. G., and Churio, M. S. (2011). Photophysics and reductive quenching reactivity of gadusol in solution. *Photochem. Photobiol. Sci.* 10, 133–142. doi: 10.1039/C0PP00250J

Baker, L. A., Horbury, M. D., Greenough, S. E., Allais, F., Walsh, P. S., Habershon, S., et al. (2016). Ultrafast photoprotecting sunscreens in natural plants. *J. Phys. Chem. Lett.* 7, 56–61. doi: 10.1021/acs.jpclett.5b02474

Baker, L. A., Horbury, M. D., Greenough, S. E., Coulter, P. M., Karsili, T. N. V., Roberts, G. M., et al. (2015). Probing the ultrafast energy dissipation mechanism of the sunscreen oxybenzone after UVA irradiation. *J. Phys. Chem. Lett.* 6, 1363–1368. doi: 10.1021/acs.jpclett.5b00417

Baker, L. A., Staniforth, M., Flourat, A. L., Allais, F., and Stavros, V. G. (2018). Gas-solution phase transient absorption study of the plant sunscreen derivative methyl sinapate. *ChemPhotoChem* 2, 743–748. doi: 10.1002/cptc.201800060

Balskus, E. P., and Walsh, C. T. (2010). The genetic and molecular basis for sunscreen biosynthesis in cyanobacteria. *Science* 329, 1653–1656. doi: 10.1126/science.1193637

Bandaranayake, W. M. (1998). Mycosporines: are they nature's sunscreens? *Nat. Prod. Rep.* 15, 159–172. doi: 10.1039/a815159y

Brenner, M., and Hearing, V. J. (2008). The protective role of melanin against UV damage in human skin. *Photochem. Photobiol.* 84, 539–549. doi: 10.1111/j.1751-1097.2007.00226.x

Bryden, A. M., Moseley, H., Ibbotson, S. H., Chowdhury, M. M., Beck, M. H., Bourke, J., et al. (2006). Photopatch testing of 1155 patients: results of the U.K. multicentre photopatch study group. *Br. J. Dermatol.* 155, 737–747. doi: 10.1111/j.1365-2133.2006.07458.x

Case, D. A., Berryman, J. T., Betz, R. M., Cerutti, D. S., Cheatham, T. E. III, Darden, T.A., et al. (2015). *AMBER 2015.* University of California: San Francisco, CA.

Casida, M. E. (1995). "Time-dependent density functional response theory for molecules," in *Recent Advances in Density Functional Methods,* ed D. P. Chong (Singapore: World Scientific), 155–192.

Conde, F. R., Churio, M. S., and Previtali, C. M. (2000). The photoprotector mechanism of mycosporine-like amino acids. Excited-state properties and photostability of porphyra-334 in aqueous solution. *J. Photochem. Photobiol. B Biol.* 56, 139–144. doi: 10.1016/S1011-1344(00)00066-X

Conde, F. R., Churio, M. S., and Previtali, C. M. (2007). Experimental study of the excited-state properties and photostability of the mycosporine-like amino acid palythine in aqueous solution. *Photochem. Photobiol. Sci.* 6, 669–674. doi: 10.1039/b618314j

Danovaro, R., Bongiorni, L., Corinaldesi, C., Giovannelli, D., Damiani, E., Astolfi, P., et al. (2008). Sunscreens cause coral bleaching by promoting viral infections. *Environ. Health Perspect.* 116, 441–447. doi: 10.1289/ehp.10966

Davidson, E. R. (1996). Comment on "comment on Dunning's correlation-consistent basis sets". *Chem. Phys. Lett.* 260, 514–518. doi: 10.1016/0009-2614(96)00917-7

Dean, J. C., Kusaka, R., Walsh, P. S., Allais, F., and Zwier, T. S. (2014). Plant sunscreens in the UV-B: ultraviolet spectroscopy of jet-cooled sinapoyl malate, sinapic acid, and sinapate ester derivatives. *J. Am. Chem. Soc.* 136, 14780–14795. doi: 10.1021/ja5059026

Downs, C. A., Kramarsky-Winter, E., Fauth, J. E., Segal, R., Bronstein, O., Jeger, R., et al. (2013). Toxicological effects of the sunscreen UV filter, benzophenone-2, on planulae and *in vitro* cells of the coral, stylophora pistillata. *Ecotoxicology* 23, 175–191. doi: 10.1007/s10646-013-1161-y

Downs, C. A., Kramarsky-Winter, E., Segal, R., Fauth, J., Knutson, S., Bronstein, O., et al. (2016). Toxicopathological effects of the sunscreen UV filter, oxybenzone (benzophenone-3), on coral planulae and cultured primary cells and its environmental contamination in Hawaii and the U.S. virgin Islands. *Arch. Environ. Contam. Toxicol.* 70, 265–288. doi: 10.1007/s00244-015-0227-7

Eller, M. S., and Gilchrest, B. A. (2000). Tanning as part of the eukaryotic SOS response. *Pigment Cell Res.* 13, 94–97. doi: 10.1034/j.1600-0749.13.s8.17.x

Gao, Q., and Garcia-Pichel, F. (2011). Microbial ultraviolet sunscreens. *Nat. Rev. Microbiol.* 9, 791–802. doi: 10.1038/nrmicro2649

Grieco, C., Kohl, F. R., Zhang, Y., Natarajan, S., Blancafort, L., and Kohler, B. (2018). Intermolecular hydrogen bonding modulates o-h photodissociation in molecular aggregates of a catechol derivative. *Photochem. Photobiol.* 95, 163–175. doi: 10.1111/php.13035

Grubb, M. P., Orr-Ewing, A. J., and Ashfold, M. N. R. (2014). KOALA: a program for the processing and decomposition of transient spectra. *Rev. Sci. Instrum.* 85:064104. doi: 10.1063/1.4884516

Hamm, P. (1995). Coherent effects in femtosecond infrared spectroscopy. *Chem. Phys.* 200, 415–429. doi: 10.1016/0301-0104(95)00262-6

Hatakeyama, M., Koizumi, K., Boero, M., Nobusada, K., Hori, H., Misonou, T., et al. (2019). Unique structural relaxations and molecular conformations of porphyra-334 at the excited state. *J. Phys. Chem. B* 123, 7649–7656. doi: 10.1021/acs.jpcb.9b03744

Holick, M. F. (2004). Sunlight and vitamin D for bone health and prevention of autoimmune diseases, cancers, and cardiovascular disease. *Am. J. Clin. Nutr.* 80, 1678s—1688s. doi: 10.1093/ajcn/80.6.1678S

Holm, A.-K., Rini, M., Nibbering, E. T. J., and Fidder, H. (2003). Femtosecond UV/mid-IR study of photochromism of the spiropyran 1′,3′-dihydro-1′,3′,3′-trimethyl-6-nitrospiro[2H-1-benzopyran-2,2′-(2H)-indole] in solution. *Chem. Phys. Lett.* 376, 214–219. doi: 10.1016/S0009-2614(03)00949-7

Horbury, M. D., Flourat, A. L., Greenough, S. E., Allais, F., and Stavros, V. G. (2018). Investigating isomer specific photoprotection in a model plant sunscreen. *ChemComm* 54, 936–939. doi: 10.1039/C7CC09061G

Horbury, M. D., Holt, E. L., Mouterde, L. M. M., Balaguer, P., Cebrián, J., Blasco, L., et al. (2019). Towards symmetry driven and nature inspired UV filter design. *Nat. Commun.* 10:4748. doi: 10.1038/s41467-019-12719-z

Horbury, M. D., Quan, W.-D., Flourat, A. L., Allais, F., and Stavros, V. G. (2017). Elucidating nuclear motions in a plant sunscreen during photoisomerization through solvent viscosity effects. *Phys. Chem. Chem. Phys.* 19, 21127–21131. doi: 10.1039/C7CP04070A

Humble, M. B. (2010). Vitamin D, light and mental health. *J. Photochem. Photobiol. B Biol.* 101, 142–149. doi: 10.1016/j.jphotobiol.2010.08.003

Klamt, A., and Schüürmann, G. (1993). COSMO: a new approach to dielectric screening in solvents with explicit expressions for the screening energy and its gradient. *J. Chem. Soc. Perkin. Trans.* 2, 799–805. doi: 10.1039/P29930000799

Koizumi, K., Hatakeyama, M., Boero, M., Nobusada, K., Hori, H., Misonou, T., et al. (2017). How seaweeds release the excess energy from sunlight to surrounding sea water. *Phys. Chem. Chem. Phys.* 19, 15745–15753. doi: 10.1039/C7CP02699D

Kollias, N., Sayre, R. M., Zeise, L., and Chedekel, M. R. (1991). New trends in photobiology; photoprotection by melanin. *J. Photochem. Photobiol. B* 9, 135–160. doi: 10.1016/1011-1344(91)80147-A

Losantos, R., Churio, M. S., and Sampedro, D. (2015). Computational exploration of the photoprotective potential of gadusol. *ChemistryOpen* 4, 155–160. doi: 10.1002/open.201402125

Losantos, R., Funes-Ardoiz, I., Aguilera, J., Herrera-Ceballos, E., Garcia-Iriepa, C., Campos, P. J., et al. (2017). Rational design and synthesis of efficient sunscreens to boost the solar protection factor. *Angew. Chem. Int. Ed.* 56, 2632–2635. doi: 10.1002/anie.201611627

Losantos, R., Lamas, I., Montero, R., Longarte, A., and Sampedro, D. (2019). Photophysical characterization of new and efficient synthetic sunscreens. *Phys. Chem. Chem. Phys.* 21, 11376–11384. doi: 10.1039/C9CP01267B

Lucas, R., McMichael, T., Smith, W., and Armstrong, B. (2006). "Solar ultraviolet radiation. global burden of disease from solar ultraviolet radiation," in *Environmental Burden of Disease Series, No. 13* eds. A. Prüss-Üstün, H. Zeeb, C. Mathers, and M. Repacholi (Geneva: World Health Organization), 1–87.

Luo, J., Liu, Y., Yang, S., Flourat, A. L., Allais, F., and Han, K. (2017). Ultrafast barrierless photoisomerization and strong ultraviolet absorption of photoproducts in plant sunscreens. *J. Phys. Chem. Lett.* 8, 1025–1030. doi: 10.1021/acs.jpclett.7b00083

Moliné, M., Arbeloa, E. M., Flores, M. R., Libkind, D., Farías, M. E., Bertolotti, S. G., et al. (2011). UVB photoprotective role of mycosporines in yeast: photostability and antioxidant activity of mycosporine-glutaminol-glucoside. *Radiat. Res.* 175, 44–50. doi: 10.1667/RR2245.1

Mullen, K. M., and Van Stokkum, I. H. M. (2007). TIMP: an R package for modeling multi-way spectroscopic measurements. *J. Stat. Softw.* 18, 1–46. doi: 10.18637/jss.v018.i03

Murdock, D., Harris, S. J., Clark, I. P., Greetham, G. M., Towrie, M., Orr-Ewing, A. J., et al. (2015). UV-induced isomerization dynamics of N-Methyl-2-pyridone in solution. *J. Phys. Chem. A* 119, 88–94. doi: 10.1021/jp511818k

Murdock, D., Harris, S. J., Luke, J., Grubb, M. P., Orr-Ewing, A. J., and Ashfold, M. N. R. (2014). Transient UV pump–IR probe investigation of heterocyclic ring-opening dynamics in the solution phase: the role played by no* states in the photoinduced reactions of thiophenone and furanone. *Phys. Chem. Chem. Phys.* 16, 21271–21279. doi: 10.1039/C4CP03653K

Nibbering, E. T. J., Fidder, H., and Pines, E. (2005). ULTRAFAST CHEMISTRY: using time-resolved vibrational spectroscopy for interrogation of structural dynamics. *Annu. Rev. Phys. Chem.* 56, 337–367. doi: 10.1146/annurev.physchem.56.092503.141314

Perdew, J. P., Ernzerhof, M., and Burke, K. (1996). Rationale for mixing exact exchange with density functional approximations. *J. Chem. Phys.* 105, 9982–9985. doi: 10.1063/1.472933

Rastogi, R. P., and Incharoensakdi, A. (2014). UV radiation-induced biosynthesis, stability and antioxidant activity of mycosporine-like amino acids (MAAs) in a unicellular cyanobacterium gloeocapsa sp. CU2556. *J. Photochem. Photobiol. B Biol.* 130, 287–292. doi: 10.1016/j.jphotobiol.2013.12.001

Rini, M., Holm, A.-K., Nibbering, E. T. J., and Fidder, H. (2003). Ultrafast UV-mid-IR investigation of the ring opening reaction of a photochromic spiropyran. *J. Am. Chem. Soc.* 125, 3028–3034. doi: 10.1021/ja028262j

Sampedro, D. (2011). Computational exploration of natural sunscreens. *Phys. Chem. Chem. Phys.* 13, 5584–5586. doi: 10.1039/c0cp02901g

Schaap, I., and Slijkerman, D. M. E. (2018). An environmental risk assessment of three organic UV-filters at lac bay, bonaire, southern caribbean. *Mar. Pollut. Bull.* 135, 490–495. doi: 10.1016/j.marpolbul.2018.07.054

Sinha, R. P., Klisch, M., Gröniger, A., and Häder, D.-P. (2000). Mycosporine-like amino acids in the marine red alga gracilaria cornea - effects of UV and heat. *Environ. Exp. Bot.* 43, 33–43. doi: 10.1016/S0098-8472(99)00043-X

Sinha, R. P., Singh, S. P., and Hader, D. P. (2007). Database on mycosporines and mycosporine-like amino acids (MAAs) in fungi, cyanobacteria, macroalgae, phytoplankton and animals. *J. Photochem. Photobiol. B Biol.* 89, 29–35. doi: 10.1016/j.jphotobiol.2007.07.006

Snellenburg, J. J., Laptenok, S., Seger, R., Mullen, K. M., and Van Stokkum, I. H. M. (2012). Glotaran: a java-based graphical user interface for the R package TIMP. *J. Stat. Softw.* 49, 1–22. doi: 10.18637/jss.v049.i03

Sui, X.-X., Li, L., Zhao, Y., Wang, H.-G., Pei, K.-M., and Zheng, X. (2012). Resonance raman and density functional study of the excited state structural dynamics of 3-amino-2-cyclohexen-1-one in water and acetonitrile solvents. *Spectrochim. Acta A* 85, 165–172. doi: 10.1016/j.saa.2011.09.055

Turner, M. A. P., Turner, R. J., Horbury, M. D., Hine, N. D. M., and Stavros, V. G. (2019). Examining solvent effects on the ultrafast dynamics of catechol. *J. Chem. Phys.* 151:084305. doi: 10.1063/1.5116312

Valiev, M., Bylaska, E. J., Govind, N., Kowalski, K., Straatsma, T. P., Van Dam, H. J. J., et al. (2010). NWChem: a comprehensive and scalable open-source solution for large scale molecular simulations. *Comput. Phys. Commun.* 181, 1477–1489. doi: 10.1016/j.cpc.2010.04.018

Wang, S. Q., and Lim, H. W. (2016). *Principles and Practice of Photoprotection.* Switzerland: ADIS.

Warshaw, E. M., Wang, M. Z., Maibach, H. I., Belsito, D. V., Zug, K. A., Taylor, J. S., et al. (2013). Patch test reactions associated with sunscreen products and the importance of testing to an expanded series: retrospective analysis of North American contact dermatitis group data, 2001 to 2010. *Dermatitis* 24, 176–182. doi: 10.1097/DER.0b013e3182983845

White, J. D., Cammack, J. H., and Sakuma, K. (1989). The synthesis and absolute configuration of mycosporins. A novel application of the Staudinger reaction. *J. Am. Chem. Soc.* 111, 8970–8972. doi: 10.1021/ja00206a059

White, J. D., Cammack, J. H., Sakuma, K., Rewcastle, G. W., and Widener, R. K. (1995). Transformations of quinic acid. Asymmetric synthesis and absolute configuration of mycosporin i and mycosporin-gly. *J. Org. Chem.* 60, 3600–3611. doi: 10.1021/jo00117a008

Winget, P., Dolney, D. M., Giesen, D. J., Cramer, C. J., and Truhlar, D. G. (1999). *Minnesota Solvent Descriptor Database.* Minneapolis, MN: Department of Chemistry and Supercomputer Institute; University of Minnesota.

Woolley, J. M., Staniforth, M., Horbury, M. D., Richings, G. W., Wills, M., and Stavros, V. G. (2018). Unravelling the photoprotection properties of mycosporine amino acid motifs. *J. Phys. Chem. Lett.* 9, 3043–3048. doi: 10.1021/acs.jpclett.8b00921

York, D. M., and Karplus, M. (1999). A smooth solvation potential based on the conductor-like screening model. *J. Phys. Chem. A* 103, 11060–11079. doi: 10.1021/jp992097l

Zhao, X., Luo, J., Liu, Y., Pandey, P., Yang, S., Wei, D., et al. (2019a). Substitution dependent ultrafast ultraviolet energy dissipation mechanisms of plant sunscreens. *J. Phys. Chem. Lett.* 10, 5244–5249. doi: 10.1021/acs.jpclett.9b02175

Zhao, X., Luo, J., Yang, S., and Han, K. (2019b). New insight into the photoprotection mechanism of plant sunscreens: adiabatic relaxation competing with nonadiabatic relaxation in the cis → trans photoisomerization of methyl sinapate. *J. Phys. Chem. Lett.* 10, 4197–4202. doi: 10.1021/acs.jpclett.9b01651

Zuehlsdorff, T. J., Haynes, P. D., Payne, M. C., and Hine, N. D. M. (2017). Predicting solvatochromic shifts and colours of a solvated organic dye: The example of nile red. *J. Chem. Phys.* 146:124504. doi: 10.1063/1.4979196

Anharmonic Molecular Motion Drives Resonance Energy Transfer in *peri*-Arylene Dyads

Vladislav Sláma[1], Václav Perlík[1], Heinz Langhals[2], Andreas Walter[2], Tomáš Mančal[1], Jürgen Hauer[3] and František Šanda[1]*

[1] Institute of Physics, Faculty of Mathematics and Physics, Charles University, Prague, Czechia, [2] Department of Chemistry, Ludwig-Maximilians-Universität München, Munich, Germany, [3] Professur für Dynamische Spektroskopien, Fakultät für Chemie, Technische Universität München, Munich, Germany

Spectral and dynamical properties of molecular donor-acceptor systems strongly depend on the steric arrangement of the constituents with exciton coupling J as a key control parameter. In the present work we study two *peri*-arylene based dyads with orthogonal and parallel transition dipoles for donor and acceptor moieties, respectively. We show that the anharmonic multi-well character of the orthogonal dyad's intramolecular potential explains findings from both stationary and time-resolved absorption experiments. While for a parallel dyad, standard quantum chemical estimates of J at 0 K are in good agreement with experimental observations, J becomes vanishingly small for the orthogonal dyad, in contrast to its ultrafast experimental transfer times. This discrepancy is not resolved even by accounting for harmonic fluctuations along normal coordinates. We resolve this problem by supplementing quantum chemical approaches with dynamical sampling of fluctuating geometries. In contrast to the moderate Gaussian fluctuations of J for the parallel dyad, fluctuations for the orthogonal dyad are found to follow non-Gaussian statistics leading to significantly higher effective J in good agreement with experimental observations. In effort to apply a unified framework for treating the dynamics of optical coherence and excitonic populations of both dyads, we employ a vibronic approach treating electronic and selected vibrational degrees on an equal footing. This vibronic model is used to model absorption and fluorescence spectra as well as donor-acceptor transport dynamics and covers the more traditional categories of Förster and Redfield transport as limiting cases.

Keywords: perylene dyads, vibronic transport, MD/QC, Förster transport, ultrafast energy transfer

1. INTRODUCTION

Peri-arylenes and their heterodimers are suitable model systems to study excitation energy transfer due to their chemical versatility and convenient spectroscopic properties, such as high fluorescence quantum yield and photostability (Langhals, 2005, 2013). They were applied as laser dyes (Löhmannsröben and Langhals, 1989; Qian et al., 2003), fluorescent light collectors (Garvin, 1960; Seybold and Wagenblast, 1989; Langhals et al., 1998; Kalinin et al., 2001; Langhals, 2019), fluorescent probes (Bo et al., 2013), or fluorophores for single-molecule spectroscopy (Mais et al., 1997; Lang et al., 2005). Their significant charge transport abilities (Huang et al., 2011) can be extended over larger aggregates, which makes them suitable building blocks for organic

photovoltaics (Hofmann et al., 2010; Holcombe et al., 2011). The family of *peri*-arylenes (also called rylenes), e.g., perylene, terrylene, and their chemical derivatives, exhibits similar spectroscopic properties (Herrmann and Müllen, 2006) such as fluorescence lifetimes around 5 ns with quantum yield near unity. Their absorption and fluorescence spectra are dominated by a transition between the highest occupied and the lowest unoccupied molecular orbital in the visible spectral region with characteristically strong vibronic progression peaks arising from a ring stretching mode around $1,400$ cm^{-1} (Ambrosino and Califano, 1965).

Peri-arylenes can be chemically linked to form dyads, the spectral features and excitation energy transfer dynamics of which are fine-tuned by their relative geometric arrangement and side group substitutions (Langhals and Gold, 1996, 1997; Langhals and Saulich, 2002; Osswald and Würthner, 2007; Fron et al., 2008). These structural parameters are readily modified by well-established synthetic routes (Langhals, 2013), leading to a large variation of intermolecular coupling in different *peri*-arylene dyads. Accordingly, optical response and excitation transfer between donor and acceptor moieties may occur under weak intermolecular coupling (Würthner et al., 2001) described by Förster theory (Förster, 1948) or in a scenario where the intermolecular coupling dominates over electron-vibrational modulations described by Redfield theory (Redfield, 1957). Various approaches have been developed to interpolate between these limits (Šanda and Mukamel, 2006, 2008; Tanimura, 2006; Zimanyi and Silbey, 2012; Fujihashi and Kimura, 2013). Regardless wide range of realizable coupling strengths in dyadic systems, a common feature in all *peri*-arylenes is the aforementioned pronounced vibronic progression in their spectra, representing strong modulation of electronic transition by an underdamped ring stretching mode. Such a scenario implies to treat this vibration on an equal footing with electronic degrees of freedom (Polyutov et al., 2012; Butkus et al., 2014; Perlík et al., 2014; Hestand and Spano, 2018). The effects of the remaining vibrations are already moderate and their perturbative treatment can be justified for a broad family of *peri*-arylene dyadic systems.

In the present work, we use this vibronic approach (Perlík and Šanda, 2017) to unify the treatment of two *peri*-arylene dyads with parallel and orthogonal transition dipole moments of donor and acceptor, as depicted in **Figure 1**. The parallel arrangement leads to coupling strengths beyond the Förster limit, while the geometry of the orthogonal dyad suggests very weak interchromophoric coupling. Within the vibronic framework, we reproduce the absorption and fluorescence spectra and demonstrate that the employed vibronic approach tracks excitation energy transfer through the entire energy ladder of vibronic states for both marginal and strong couplings.

The speed of donor-to-acceptor transport is primarily determined by donor-acceptor coupling constant J. The ultrafast transfer times reported in literature are thus one primary source of J estimates. Alternatively, the value of J can be derived from a microscopic model using quantum chemical methods. The orthogonal dyad was reported (Langhals et al., 2010; Langhals and Walter, 2020) to represent a challenging

case in this context: Despite the apparent lack of coupling in the optimal ground state geometry, transient absorption experiments show transfer time in the sub-10 ps range. This apparent discrepancy was attributed to thermally induced deviations from a strictly orthogonal molecular geometry. While this hypothesis was supported by temperature- and solvent-dependent experiments (Langhals et al., 2010; Nalbach et al., 2012), a microscopic understanding of the observed transfer times and coupling strengths is still missing; normal mode fluctuation analysis of the intra-dyad coupling underestimated the coupling strength by an order of magnitude. We resolve this problem by supplementing a microscopic density functional theory (DFT) parametrization with molecular dynamics (MD) sampling of molecular geometries. We demonstrate that the intramolecular potential has a multi-well character, and that the typical geometry at room temperature deviates significantly from the minimal energy geometry. This anharmonic character is not captured by a standard linearization of forces around the global potential minimum, which explains why harmonic approaches consistently underestimate J in the orthogonal dyad.

Hence, we present how a vibronic approach describes absorption and fluorescence spectra of the two *peri*-arylene dyads in vastly different coupling regimes and how the model can be parameterized by a microscopic MD/DFT approach, which in the case of the orthogonal dyad uncovers the anharmonic character of the potential landscape determining J.

The paper is organized as follows: In section 2, we describe the methods used to obtain the quantum chemical estimates of couplings at finite temperatures and beyond the dipole-dipole approximation (section 2.1) and introduce the vibronic model of optical dynamics (section 2.2). We also give brief accounts of sample preparation and spectral measurements. In section 3, we fit the absorption and fluorescence spectra of both dyads using a vibronic model and determine J of the parallel dyad (section 3.1). The population dynamics for both dyads are discussed and an effective coupling for the orthogonal dyad is determined in section 3.2. We then proceed (section 3.3) to test quantum chemical calculations of J and demonstrate that the entire configuration space of the orthogonal dyad must be sampled to obtain estimates for J in agreement with experimental observations. In section 4, we conclude.

2. METHODS

2.1. Estimates of Intermolecular Coupling

Dynamics of the optical coherence of the investigated dyads are induced by interaction ($\hat{V}_{AD}$) between the electronic structures of donor ($\hat{H}_{el}^D$) and acceptor ($\hat{H}_{el}^A$) and are further modulated by dynamics of nuclei ($\hat{H}_{nc}$)

$$\hat{H} = \hat{H}_{el}^A + \hat{H}_{el}^D + \hat{H}_{nc} + \hat{V}_{AD}. \tag{1}$$

In the Born-Oppenheimer approximation electronic and nuclear motions are separated (Atkins and Friedman, 2011). In the following we refer to the local instantaneous electronic eigenstates ($k = 0, 1, \dots$) satisfying

$$\hat{H}_{el,\boldsymbol{R}}^A \Psi_{k,\boldsymbol{R}}^A(\boldsymbol{r}_A) = E_{k,\boldsymbol{R}}^A \Psi_{k,\boldsymbol{R}}^A(\boldsymbol{r}_A) \tag{2}$$

FIGURE 1 | Simulated donor-acceptor systems. **(A)** Perylene-benzoperylene bisimide dyad in orthogonal arrangement. The distance between centers of the transition charge centroids is 16 Angstrom. **(B)** S-13-obisim-terylene dyad in parallel arrangement.
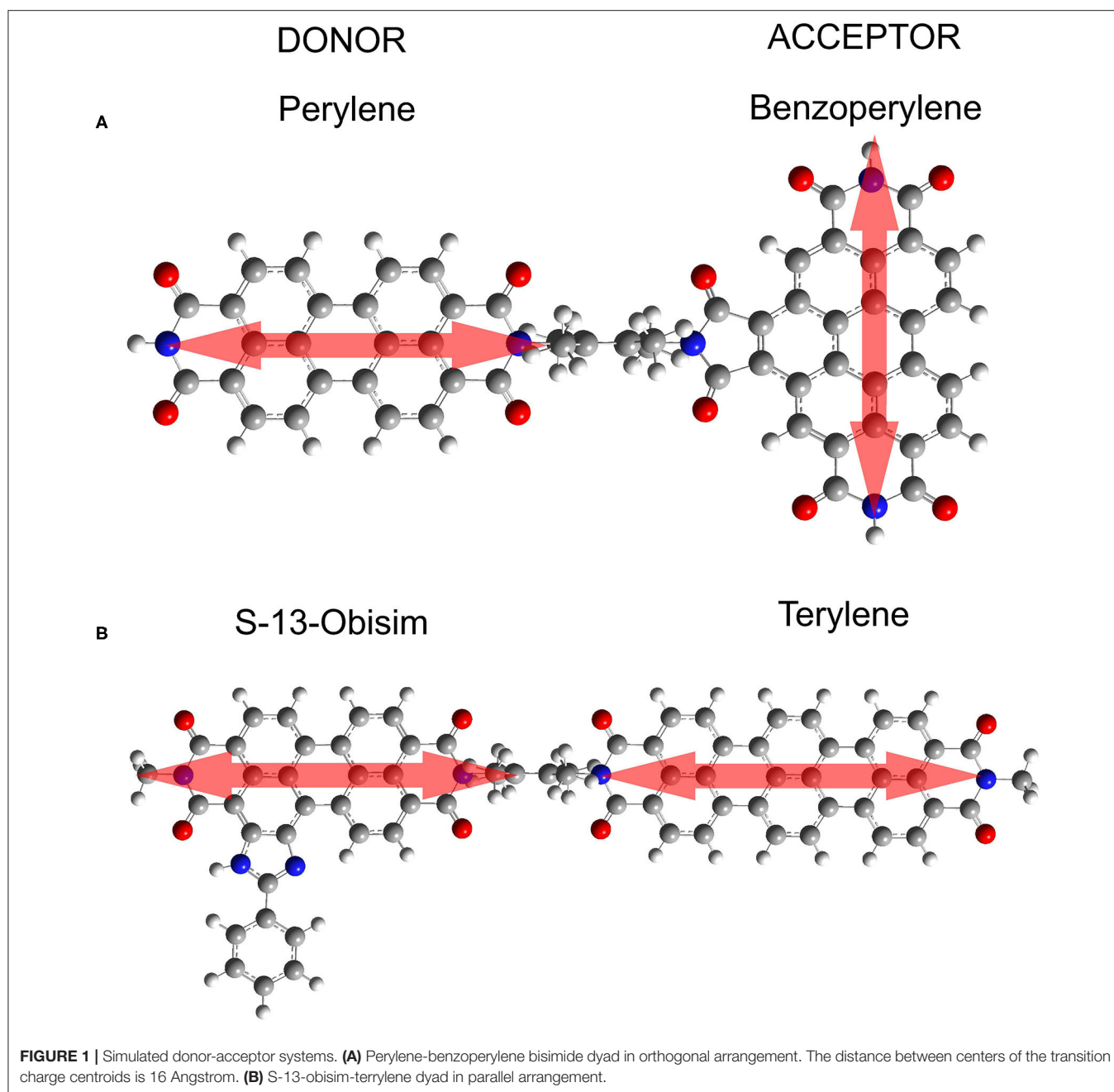
where $\boldsymbol{r}_A = (r_1, r_2, \dots)$ is a collection of electronic coordinates on the acceptor, and the parameter $\boldsymbol{R}$ stands for molecular geometry specified by a collection of nuclear coordinates. The complete information of the many-body wavefunction is excessively abundant, and for most purposes is reduced to the one-particle transition densities (McWeeny, 1960) between the electronic states k and k' defined as

$$
\begin{aligned}
\rho^A_{kk',\boldsymbol{R}}(r) = \int & \Psi^A_{k,\boldsymbol{R}}(r_1, r_2, \dots) \Psi^{*A}_{k',\boldsymbol{R}}(r_1, r_2, \dots) \\
& \times \sum_{j \in \{A\}} \delta(r - r_j) \prod_{i \in \{A\}} dr_i.
\end{aligned} \tag{3}
$$

The donor variables E^D, $\boldsymbol{r}_D$, Ψ^D, ρ^D are defined analogously.

Interchromophore coupling accounts for electrostatic interaction of electronic coordinates r_i of, e.g., the acceptor ($i \in \{A\}$) with those of donor ($j \in \{D\}$) and for their interaction with nuclear coordinates R_J (of proton number Z_J) outside the acceptor (including a linker)

$$
\hat{V}_{AD} = \sum_{\substack{i \in \{A\} \\ j \in \{D\}}} \frac{1}{|r_i - r_j|} - \sum_{\substack{i \in \{A\} \\ J \notin \{A\}}} \frac{Z_J}{|r_i - R_J|} - \sum_{\substack{I \notin \{D\} \\ j \in \{D\}}} \frac{Z_I}{|R_I - r_j|}. \tag{4}
$$

Intermolecular exciton transfer occurs predominantly between the two lowest excited states $|\Psi_{1,\mathbf{R}}^{A}\rangle|\Psi_{0,\mathbf{R}}^{D}\rangle$ and $|\Psi_{0,\mathbf{R}}^{A}\rangle|\Psi_{1,\mathbf{R}}^{D}\rangle$. Resonance coupling between them

$$J_{\mathbf{R}} \equiv \langle\Psi_{1,\mathbf{R}}^{A}|\langle\Psi_{0,\mathbf{R}}^{D}|\hat{V}_{AD}|\Psi_{0,\mathbf{R}}^{A}\rangle|\Psi_{1,\mathbf{R}}^{D}\rangle \quad (5)$$

can be recast in terms of transition densities as

$$J_{\mathbf{R}} = \int \frac{\rho_{01,\mathbf{R}}^{A}(r_a)\rho_{01,\mathbf{R}}^{D}(r_d)}{|r_a - r_d|}dr_a dr_d. \quad (6)$$

The direct discretization of Equation (6) known as the transition density cube (TDC) method (Krueger et al., 1998) shall be used at short intermolecular distances. When the molecules are far apart (with respect to molecular size), Equation (6) is well-approximated by classical interaction between point dipoles $\vec{\mu}_{\mathbf{R}}^{A(D)} \equiv \int \vec{r}\rho_{01,\mathbf{R}}^{A(D)}(r)dr$.

At finite temperatures $1/k_B\beta$, electronic structures and couplings depend on the molecular geometry sampled along the Boltzmann distribution with expectation values $\langle\dots\rangle$ obeying

$$\langle f \rangle \equiv \frac{\int f(\mathbf{R})e^{-\beta E(\mathbf{R})}d\mathbf{R}}{\int e^{-\beta E(\mathbf{R})}d\mathbf{R}}. \quad (7)$$

Here, we evaluate the ground state energies

$$E(\mathbf{R}) \equiv \langle\Psi_{0,\mathbf{R}}^{A}|\langle\Psi_{0,\mathbf{R}}^{D}|\hat{H}|\Psi_{0,\mathbf{R}}^{A}\rangle|\Psi_{0,\mathbf{R}}^{D}\rangle \quad (8)$$

using density functional theory (DFT) which draws upon recasting Equation (8) in the form of Kohn-Sham functional (Parr and Yang, 1989). In particular, we evaluated $E(\mathbf{R})$ using GAUSSIAN 09 quantum chemistry package (Frisch et al., 2009) at DFT level with B3LYP functional and 6-311(d,p) basis set.

For calculation of the transition densities $\rho_{01}^{D(A)}$ of donor (acceptor) the linker molecule was replaced by a methyl group, and TD-DFT was employed using long range corrected CAM-B3LYP functional, which is known to provide correct (experimental) excitation energies for aromatic hydrocarbon derivatives (de França et al., 2018).

The coupling estimates are usually feasible for a zero temperature geometry $\mathbf{R}_0$, characterized by the minimal ground state energy $E(\mathbf{R}_0) \leq E(\mathbf{R})$. For the orthogonal dyad, however, $J_{\mathbf{R}_0} \approx 0$, and the thermal fluctuations might dominate the effective value of transport. We thus explore distributions of coupling $\langle\delta(J - J_{\mathbf{R}})\rangle$. To avoid costly complete exploration of high dimensional $\mathbf{R}$ configuration space, we compare sampling by normal mode analysis (NMA) and by molecular dynamics (MD).

In the NMA, energy is expanded to second order $E(\mathbf{R}) = E(\mathbf{R}_0) + \sum_{I,J}\mathcal{E}_{IJ}(R_I - R_{0,I})(R_J - R_{0,J})$ around the minimum. The Hessian $\mathcal{E}_{IJ} \equiv \frac{\partial E}{\partial R_I \partial R_J}$ is diagonalized to obtain the normal mode coordinates. Geometry sampling is restricted along a single normal coordinate, otherwise weighted according to Equation (7), and the couplings on the samples are evaluated using TDC (Equation 6).

However, the NMA ignores the complexity of potential surfaces. An alternative approach is thus to employ MD to sample molecular geometries, avoiding also the harmonic approximation

to $E(\mathbf{R})$ inherent to NMA. Using the AMBER package (Case et al., 2014) with GAFF force field (Wang et al., 2004) and RESP charges (Bayly et al., 1993) calculated by Gaussian09 software (Frisch et al., 2009) the conformation space sampling was performed for an NpT ensemble of a single *peri*-arylene dyad with 2,697 toluene solvent molecules at atmospheric pressure and room temperature of 300 K and a 0.2 fs time-step was used for numerical integration of equations of motion. After an initial 10 ns for equilibration, the dyad geometries were sampled at 40 fs frequency and used for a QC calculation of resonance coupling.

In transport simulations, such as below, costly sampling of coupling distributions is usually avoided by representing coupling as a single effective value. In most situations, thermal fluctuations are minor $|\langle J^2\rangle - \langle J\rangle^2| \ll \langle J\rangle^2$ and the effective coupling should be compared with the mean value, which often corresponds to that of $\mathbf{R}_0$ geometry $J \equiv \langle J\rangle \approx J_{\mathbf{R}_0}$. At the other extreme, major fluctuations $\langle J\rangle < \sqrt{\langle J^2\rangle}$, which are applicable to the orthogonal dyad, where the geometric symmetries require $\langle J\rangle = 0$ (and symmetric coupling distributions), the coupling distribution should be effectively represented by $J \equiv \sqrt{\langle J^2\rangle}$, which scales with $\propto J^2$, as expected for Förster transfer.

2.2. Vibronic Model for *peri*-arylene Dyads

What remains is to connect the microscopic parameterizations of the previous section to the vibronic dynamics of Perlík and Šanda (2017). To this end, we formally define excitonic states and energies by fixing $H_{el}^{A(D)}$ at typical geometry $\mathbf{R}_0$. To model absorption and fluorescence spectra as well as population dynamics, the relevant states are: the ground state $|g\rangle \equiv |\Psi_{0,\mathbf{R}_0}^{A}\rangle|\Psi_{0,\mathbf{R}_0}^{D}\rangle$ and two singly excited states $|e_A\rangle \equiv |\Psi_{1,\mathbf{R}_0}^{A}\rangle|\Psi_{0,\mathbf{R}_0}^{D}\rangle$ and $|e_D\rangle \equiv |\Psi_{0,\mathbf{R}_0}^{A}\rangle|\Psi_{1,\mathbf{R}_0}^{D}\rangle$. To complete the Frenkel exciton Hamiltonian the effective intermolecular coupling J between $|e_A\rangle$ and $|e_D\rangle$ is added (other elements of $\hat{V}_{AD}$ are neglected)

$$\hat{H}_F = \epsilon^A|e_A\rangle\langle e_A| + \epsilon^D|e_D\rangle\langle e_D| + J(|e_A\rangle\langle e_D| + |e_D\rangle\langle e_A|) \quad (9)$$

where $\epsilon^A \equiv E_{1,\mathbf{R}_0}^{A} - E_{0,\mathbf{R}_0}^{A}$ and $\epsilon^D \equiv E_{1,\mathbf{R}_0}^{D} - E_{0,\mathbf{R}_0}^{D}$. We next introduce vibronic dynamics by separating from $\hat{H}_{nc}$ the underdamped ring stretching vibrations q_A of *peri*-arylenes around 1,400 cm^{-1}

$$\hat{H}_{vib}^{A} = \frac{\hat{p}_A^2}{2m} + \sum_{j=0}^{1}V(q_A - d_j^A)|\Psi_{j,\mathbf{R}_0}^{A}\rangle\langle\Psi_{j,\mathbf{R}_0}^{A}|, \quad (10)$$

where d_j^A are displacements of electronic surface $V(q)$ (vibrational states shall be labeled $\nu_A = 0, 1, \dots$.) and introduce them into the system Hamiltonian $\hat{H}_s$

$$\hat{H}_s = \hat{H}_F + \hat{H}_{vib}^{A} \otimes \mathbb{1}^D + \mathbb{1}^A \otimes \hat{H}_{vib}^{D}. \quad (11)$$

Diagonalization of vibronic Hamiltonian Equation (11) explains the peak position and magnitudes in the absorption and fluorescence spectra.

Other low-frequency vibrations and solvent degrees of freedom affect line-widths and shapes. They are treated as bath fluctuations and their effect is represented by the magnitude

λ_V (λ_W) and inverse timescale Λ_V (Λ_W) of linear (quadratic) stretch vibration-to-bath coupling (Caldeira and Leggett, 1983). Similar parameters λ_U and Λ_U are introduced for the magnitude and rate of electronic dephasing. Their microscopic definitions are summarized in **Supplementary Material**, section 1. These parameters are estimated by fitting the absorption spectrum, their microscopic calculations are principally possible but a challenging task (Olbrich and Kleinekathöfer, 2010; Olbrich et al., 2011; Renger et al., 2018).

The optical probes are described by the interaction Hamiltonian

$$\hat{H}_i = \mu_A(t)|e_A\rangle\langle g| + \mu_D(t)|e_D\rangle\langle g| + h.c., \tag{12}$$

where $\mu_{A(D)}(t) \equiv \vec{\mu}_{A(D)} \cdot \vec{E}(t)$ is the projection of the laser field $\vec{E}(t)$ on the transition dipole $\vec{\mu}_A$ ($\vec{\mu}_D$) between the g and e states of the acceptor (donor) at $\mathbf{R}_0$ geometry, respectively. The transition dipole dependencies on vibrational coordinates q_A, q_D are usually neglected in the Condon approximation.

Details of the simulations, i.e., the quantum master equation to describe vibronic population transfer and second cumulants for line-shapes, were published previously (Perlík and Šanda, 2017). We also adopted correction factors Ω, and Ω^3 to connect absorption and fluorescence spectra, respectively, with the response functions along (Angulo et al., 2006).

2.3. Sample Preparation

The preparation of the orthogonal dyad has been published previously (Langhals et al., 2008).

The parallel dyad was synthesized in two steps. The linker was first substituted at the terrylene molecule: Terrylene anhydride carboximide was solubilized by means of the long-chain secondary alkyl substituent 1-nonyldecyl at the nitrogen atom and condensed with an excess of 2,3,5,6-tetramethylbenzene-1,4-diamine (see **Supplementary Material**, section 3.1 for detail of synthesis). The free primary amino group of the thus obtained terrylenebiscarboximide was in the second step further condensed with an imidazoloperyleneanhydridecarboximde to obtain the dyad with a rigid, orthogonal spacer between the two chromophores for electronic decoupling, where the two peripheric *sec*-alkyl substituents render both a sufficiently high solubility and a low tendency for aggregation. Hence, any potential red-shift upon covalent linking of donor and acceptor moieties is due to electronic coupling and not due to aggregation effects (see **Supplementary Material**, section 3.2 for detail of synthesis).

2.4. Spectroscopic Methods

All absorption and fluorescence emission measurements on both investigated substances were performed in chloroform at an optical density (OD) of 0.35 at the respective absorption maxima at an optical path length of 1 cm. Absorption and fluorescence spectra were recorded at a resolution of 1 nm. Reabsorption of fluorescence light caused by the significant overlap of absorption and fluorescence spectra was corrected according to procedures described previously (Didraga et al., 2004; Lincoln et al., 2016).

3. RESULTS

3.1. Absorption and Fluorescence Spectra

The absorption $S(\Omega)$ and fluorescence $F(\Omega)$ spectra of constituent *peri*-arylene subunits in the visible reveal a single electronic transition modulated by a strong vibronic progression peaks. They stem from electron couplings to a ring stretching mode around $\omega \approx 1,400$ cm^{-1}. The magnitudes of the progression peaks are significantly asymmetric between absorption and fluorescence $S(\epsilon + \omega) \neq F(\epsilon - \omega)$, which clearly rule out the standard harmonic model of vibration (Angulo et al., 2006). Thus, for the sake of simplicity we adopted the anharmonic oscillator model (Anda et al., 2016; Galestian Pour et al., 2017) $V(q) = \frac{1}{2}m\omega^2\hat{q}^2 + \alpha\hat{q}^3$, while retaining the Born-Oppenheimer and the Condon approximations. The frequencies, displacement, and anharmonicities for this vibrational stretch mode are obtained by comparing positions and magnitudes of progression peaks of absorption and fluorescence following a previously established protocol (Galestian Pour et al., 2017). We also fit the spectral profiles and Stokes shift to obtain the bath parameters λ and Λ, which are summarized in **Table 1**. These constituent parameter fits are then fixed, and intermolecular coupling is varied to match the dyad absorption.

Comparison between the monomeric and dyadic absorption spectra indicates the parametric regime for each orientation. The absorption spectrum of the orthogonal dyad can be almost perfectly reconstructed by a simple addition of the donor and acceptor absorption lineshapes (see **Figure 2**, bottom left). The dyadic absorption spectrum thus does not provide means to quantify the magnitude of coupling J, but limits the parameters to the weak coupling regime consistent with Förster theory. In contrast, the difference between the absorption of the strongly coupled parallel dyad and its constituents (**Figure 2**, bottom right) sets J within the range of -150 to -250 cm^{-1} (**Figure 2** shows best fit at $J = -200 cm^{-1}$), which suggests a departure from Förster theory.

TABLE 1 | Parametrization (in cm^{-1}) of the vibronic model for the absorption and fluorescence spectra of the dyads constituents.

Molecule dyad role	Perylene orthogonal donor	Benzoperylene orthogonal acceptor	S-13-obisim parallel donor	Terrylene parallel acceptor
ω	1,470	1,420	1,370	1,380
$d^2 m\omega/(2h)$	0.8	0.7	0.6	0.5
α	−35	−10	−13	6
$E_1 - E_0$	21,650	19,100	17,000	15,450
Λ_U	200	360	180	330
Λ_V	200	270	40	30
Λ_W	–	–	20	15
λ_U	350	260	260	300
λ_V	200	270	300	250
λ_W	0	0	20	15
μ	0.8	1	0.8	0.9

FIGURE 2 | Experimental and simulated absorption (blue lines) and fluorescence (red lines) spectra for acceptor **(top)**, donor **(middle)**, and dyad **(bottom)**. The dashed black line combines absorption of donor and acceptor $S_A + S_D$. Left: Orthogonal dyad. Right: Parallel dyad.

3.2. Population Dynamics

In section 3.1, we have successfully simulated the linear optical responses of both dyads, however, the spectrum of the orthogonal dyad does not allow for a reliable determination of the value of J, other than that it must be in the weak coupling regime. Donor to acceptor transfer rates can be used instead to bring the comparison with experiment. Transient absorption measurement by Langhals et al. (Figure 2 in Langhals et al., 2010) have reported single lifetime of $\tau = 9.4$ ps associated with transfer from donor to vibrationless acceptor. At early times around hundred femtosecond traces of vibrational relaxation are visible.

We have simulated the population evolution for the orthogonal dyad after the experimentally employed (Langhals et al., 2010) excitation at $23,000$ cm^{-1}, which corresponds to the first donor excited vibrational state. We have used the full vibronic model parameterized from absorption/fluorescence of constituents as given in **Table 1**. The intermolecular coupling

was varied to reproduce the experimentally determined transport dynamics best fitted at $J = 16$ cm^{-1}.

Simulations (**Figure 3**, top) show early vibrational relaxation localized at the donor molecule around 100 fs, followed by slower exciton transport in picoseconds. The two timescales are thus well separated providing the standard picture of Förster type of transport in the usual experimental observation window > 100 fs limited by narrowband excitation. To demonstrate the compatibility with the celebrated Förster formula

$$\frac{1}{\tau} = \frac{1}{\hbar^2 c}|J|^2 \int_0^\infty \frac{F_D(\Omega)S_A(\Omega)}{\Omega^4}d\Omega, \qquad (13)$$

we applied it using the aforementioned coupling constant $J = 16$ cm^{-1} to yield $\tau = 11$ps, which compares well to the observed $\tau = 9.4$ps. Alternatively, taken from the coupling point of view, Förster theory would require $J = 17$ cm^{-1} to correctly estimate the experimental lifetimes (Megerle et al., 2009;

Langhals et al., 2010). This good agreement makes our vibronic treatment truly unified approach to *peri*-arylene aggregates as this essentially weak system-bath coupling perturbative scheme works well even for the weak intermolecular coupling (orthogonal) case.

The more complicated transport dynamics of the strongly coupled parallel dyad is depicted in lower panel of **Figure 3**. Transport has been simulated using the parameters for donor and acceptor moieties given in **Table 1** and at a resonance coupling of $J = -200 \text{ cm}^{-1}$. The donor and acceptor principal transitions are shifted by approximately one vibrational quantum. The vibronic states are thus highly delocalized appearing at resonances $\epsilon^D + n\omega \approx \epsilon^A + (n+1)\omega$. To understand the underlying transport dynamics through the vibronic energy ladder in detail, we simulated populations of the donor P^D, the acceptor P^A (dotted lines), and the total populations of the resonance manifolds (solid lines in **Figure 3**).

The parallel dyad is assumed to be excited by a narrowband pulse at 18,250 cm^{-1} around the $\epsilon^D + \omega \approx \epsilon^A + 2\omega$ resonance, i.e. tuned to the first vibrational excited state of donor, ensuring the dynamics is comparable to that of the orthogonal dyad studied above. The initial population of acceptor $P^A(\Delta t = 0) = 0.4$ is only slightly lower than that of the donor $P^D(\Delta t = 0) = 0.6$ as a result of high delocalization. One vibrational quantum is lost within approximately 200 fs (yellow line in **Figure 3B**) to appear at lower $\epsilon^D \approx \epsilon^A + \omega = 16,500 \text{ cm}^{-1}$.

resonance (orange line). This transition corresponds to the early $\Delta t < 200$ fs component of biexponential relaxation. The asymptotic component after 200 fs is seemingly connected with further relaxation from the resonance and final localization in the acceptor vibrational ground state $|e_A; \nu_A, \nu_D = 0\rangle$ at 15, 100cm^{-1} (red line). The relaxation is nevertheless completed within 1 ps as the exciton dynamics between these strongly coupled chromophores is significantly faster dynamics as compared to the orthogonal case. The two processes thus appear at quite similar timescales, providing the example of truly vibronic relaxation dynamics. The experimental confirmation of this behavior, and thus confirmation of J estimate, is a matter of ongoing research.

3.3. Distributions of the Intermolecular Coupling

Having established estimates for the intermolecular coupling J for both dyads based on fits to experimental data, we can now proceed to develop sound procedures for its quantum chemical calculations.

The DFT-optimized geometry $\boldsymbol{R}_0$ of the dyad displayed at **Figure 1A** has orthogonal dipoles and vanishing coupling $J_{\boldsymbol{R}_0} = 0$ (within numerical error) as expected from symmetry. We identified five lowest (i.e., thermally populated) normal modes which correspond to bending and torsion of the dyad (Langhals et al., 2010). Coupling distributions calculated at room temperature along each of these coordinates are approximately Gaussian with zero mean $\bar{J} \equiv \langle J \rangle \approx 0$. Typical values of coupling estimated as standard deviations $\sqrt{\langle J^2 \rangle}$ are summarized in the **Table 2**. These values are an order of magnitude too small to explain the experimentally observed transfer times. In other words, no normal mode can be associated with the required coupling fluctuations.

We now turn to an exploration of the complete $E(\boldsymbol{R})$ landscapes. Regular samplings of the (high dimensional) configuration space are inefficient. We have thus used MD software package AMBER and sampled geometries with 40 fs time step after an initial 10 ns equilibration (when the geometry fluctuations become stable) at room temperature (300 K) in two runs (production times 80 ps, 40 ps) to check that trajectory is not biased. For each geometry, the coupling was estimated using the methods of section 2.1. The distributions for the orthogonal dyad, shown on the left panel of **Figure 4**, are—within statistical error—symmetric around $J = 0$. Nevertheless, the absolute

FIGURE 3 | Population evolutions for the orthogonal **(A)** and parallel **(B)** dyad. Parameters are the same as for **Figure 2**. Population evolution of donor (light blue), acceptor (dark blue) states as well as populations of resonant levels around the color-coded energies. The inset shows these energies with respect to the absorption (full blue area) and emission spectrum (gray dashed lines).

TABLE 2 | Five lowest normal modes and standard deviation of coupling distributions $\langle J^2 \rangle$ for orthogonal dyad.

Normal mode	Frequency [cm^{-1}]	$\sqrt{\langle J^2 \rangle}$
1	7.93	1.55
2	8.4	0.22
3	12.39	0.09
4	20.81	1.34
5	21.98	0.02

In all cases $\langle J \rangle \approx 0$.

FIGURE 4 | Histogram of coupling strengths for the orthogonal dyad **(left)**. Mean and standard deviations are $\langle J \rangle = 0\,\mathrm{cm}^{-1}$, $\sqrt{\langle J^2 \rangle - \langle J \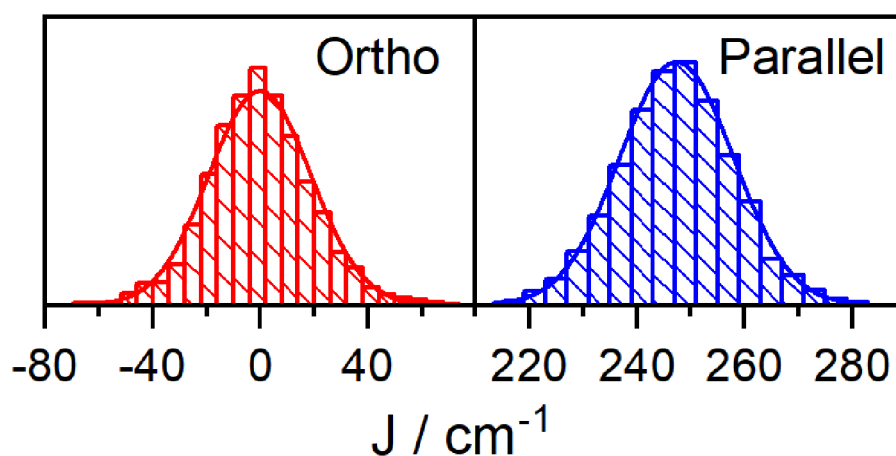rangle^2} = 19\,\mathrm{cm}^{-1}$. **(Right)** Parallel dyad and $\langle J \rangle = -247\,\mathrm{cm}^{-1}$, $\sqrt{\langle J^2 \rangle - \langle J \rangle^2} = 11\,\mathrm{cm}^{-1}$.

values of the coupling are rather large, with median of $|J|$ to be 12 cm^{-1} and a mean value $\langle |J| \rangle = 15$ cm^{-1}. In the context of Förster transport and its $\propto J^2$ scaling, the standard deviation $\sqrt{\langle J^2 \rangle} = 19$ cm^{-1} is the most meaningful measure for an effective coupling constant. Therefore, we observe an enhancement of the intermolecular coupling after MD analysis over the values obtained after NMA. This is surprising and calls for a detailed investigation. We noticed, that the distribution has thicker tails than Gaussian fit, this deviation has been quantified by estimating Pearson's kurtosis $\kappa_J = \frac{\langle (J - \bar{J})^4 \rangle}{\langle (J - \bar{J})^2 \rangle^2} = 3.66$, large excess over $\kappa = 3$ of normal distribution. With this estimate, the distribution can be rejected to follow Gaussian statistics at standard 95% confidence level (test accounted for correlations appearing along MD trajectory, see **Supplementary Material**, section 2 for details).

Non-Gaussian statistics can represent anharmonic vibrational motions in complex multi-well potential landscapes. To underline the evidence of anharmonic effects, we studied longer MD trajectories until 800 ps (20,000 configurations with 40 fs time-step) at various temperatures, while avoiding costly QC calculations.

In detail, we recorded the displacements from R_0 geometries at 10, 50, 100, and 300 K and transformed out the translational and rotational motion of the dyad (Amadei et al., 2000). Next, we identified the normal modes of GAFF (MD) potentials, noting that these normal modes correspond well to those obtained from CAM-B3LYP. The statistics of the projection on normal modes were calculated and compared to the Gaussian statistics of approximate (NMA) harmonic dynamics. While statistics of most coordinates including NM1, NM2 (shown in **Supplementary Material**, section 2) follows a standard harmonic pattern, we found handful coordinates (namely modes 3, 15, 39, 45, 64, 67, and 78) with significant deviations. As an example we demonstrate such a behavior by showing the statistics of the third normal mode at

various temperatures in **Figure 5**. At 300 K, the temperature at which the experiments were conducted, the unimodal statistics deviates only moderately from a Gaussian distribution $\kappa_{NM3} = 2.67$, but are clearly displaced from the global potential minima R_0. Thus the molecular motions are not driven by the harmonic potential explored by NMA, the unimodal character is rather related to the central limit theorem. The distinctly multi-well character appears when MD's are run at lower temperatures: Statistics show two peaks consistent with a double well potential at intermediate temperatures 50–100 K (kurtosis $\kappa = 1.43$) -2.05 then becoming centered around the global minima at 10 K, where we finally approach the Gaussian statistics $\kappa = 3.00$ of (NMA) harmonic approximation. Nongaussian statistics are demonstrated in **Supplementary Material**, section 2 also for other modes 15, 39, 45, 64, 67, and 78.

Caution is needed, however, for appropriate interpretation of these non-Gaussian displacement projections, one should not link them straightforwardly to a simple anharmonic potential energy profiles along a single normal mode coordinate (normal modes are approximately harmonic). The double-well type potential type becomes apparent in higher dimensions when more than two normal modes are combined. Accordingly, none of the normal mode show a clear correlation with donor-acceptor coupling J. The enhancement of J is better linked with combinations of several low-energy normal modes (correlation statistics in **Supplementary Material**, section 2). In other words, the complex multidimensional potential landscape is the physical source of the observed enhancement of J, which is not apparent in a pure NMA.

For the parallel oriented dyad, calculated with the same technical settings, the dipoles of donor and acceptor are parallel in the optimal geometry R_0. We obtain $J = -230$ cm^{-1}, using the TDC method (Equation 6) for the optimal ground state geometry, which is a higher value than predicted in the dipole
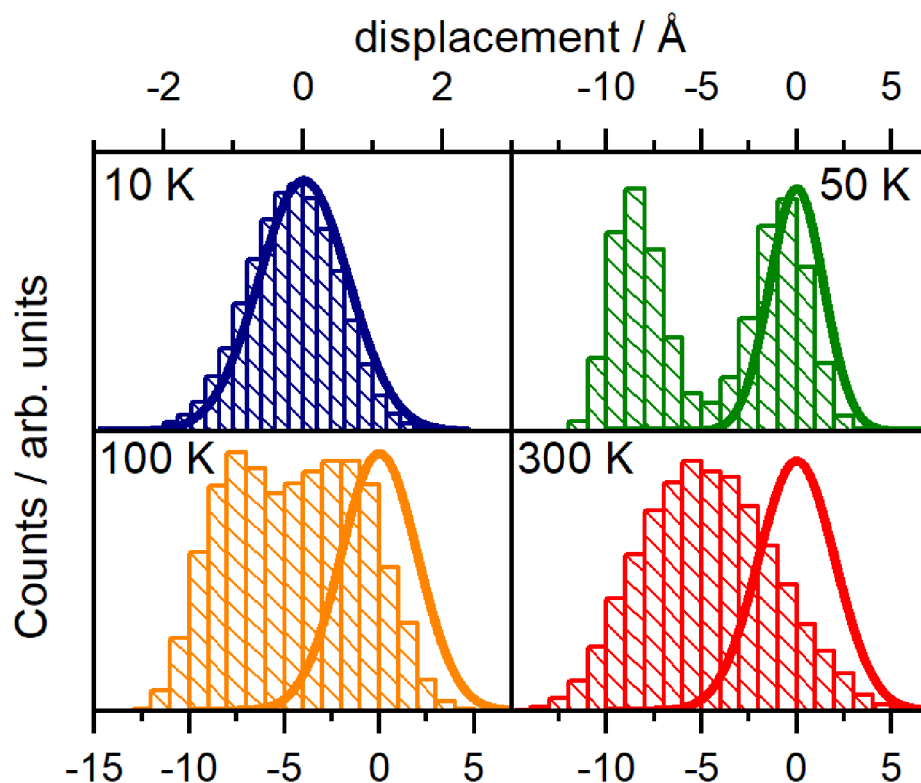
FIGURE 5 | Normal mode displacement probability distribution for selected an harmonic normal mode 3 of the orthogonal dyad. Statistics are derived from 20,000 configurations over 800 ps MD trajectories. Thick lines correspond to a displacement according to a harmonic approximation, adopted in normal mode analysis.

approximation ($J = -150 \text{cm}^{-1}$; both at $\boldsymbol{R}_0$). The distributions of coupling (MD sample of N = 1,000 geometries) in the right panel of **Figure 4** is energetically narrow and peaked at $J = -247 \text{cm}^{-1}$, (standard deviation $\sqrt{\langle J^2 \rangle - \langle J \rangle^2} = 11 \text{cm}^{-1}$). In contrast to the ortho-case, the Pearson kurtosis $\kappa = 3.12$ does not significantly exceed the typical Gaussian result considering the sample range and correlation time (see **Supplementary Material**, section 2). To transcend the sole focus on the fourth moment we have further used the Smirnov-Kolmogorov test (Lilliefors, 1967; Weiss, 1987) but even here no statistically significant difference from the normal distribution was found at the standard confidence level 0.95. The contribution of fluctuations is thus insignificant for the parallel dyad, i.e., the distribution has a rather small standard deviation with respect to the mean, and the coupling obtained by TCD for optimal geometry $\boldsymbol{R}_0$ is $J = -230 \text{ cm}^{-1}$. The quantum chemical estimate of the intermolecular coupling in the parallel dyad was not substantially altered by MD sampling of geometries in comparison with the TDC evaluation at optimal geometry (-247 vs. -230cm^{-1}). As mentioned in previous section, the value for J obtained from fitting the absorption spectrum of the parallel dyad is markedly lower at -200 cm^{-1}. We attribute this difference to the fact that DFT-based calculations neglect shielding effects from solvent molecules, and thus tend to overestimate interchromophoric couplings (Hsu et al., 2001; Renger and Müh, 2012).

4. DISCUSSION

We have developed a vibronic model of excitonic transport in *peri*-arylene dyads that is applicable to a variety of geometric arrangements and transport regimes. In particular, we studied donor-acceptor dyads in the orthogonal and parallel spatial arrangements.

The Förster regime of transport dynamics was reproduced theoretically within a vibronic model for the orthogonal dyad. This assignment is supported by a flawless reconstruction of the orthogonal dyad's absorption spectrum by its constituents, and furthermore by the reported single-exponential transport within the usual observation window. Previously reported inconsistencies between experimental transport times and microscopic QC parameterizations of a Förster model should thus be untangled from the latter end. The deficiencies of the normal mode approach to thermal fluctuations were overcome by MD sampling of the molecular geometries. The analysis found somewhat complex, but quantitatively adequate fluctuation statistics of intermolecular coupling. Anharmonic potentials of low-frequency modes serve as a physical explanation. One may speculate about alternative models to rationalize the fast transport in the orthogonal dyad. For instance, we tried to estimate the possible mediation through excited states of the linker molecule, or the electron transfer through linker. Due

to the unfavorable geometric orientation of the donor, linker and acceptor molecules, we found no electronic state on the linker molecule that would strongly interact with both donor and acceptor. The electron transfer mechanism can also be ruled out because the charge transfer states donor-linker and acceptor-linker are at least 8,000 cm^{-1} higher than the local excited states and their coupling was found in the range of 100 cm^{-1} using a multistate FCD approach (Nottoli et al., 2018) with wB97XD functional.

We also investigated the excited state as a possible source of the orthogonality breaking. However, the results of QC calculations of the excited state exhibit perfect orthogonal arrangement of the transition dipoles for the optimal structure. Also, accounting for an implicit solvent effect using polarizable continuum model of GAUSSIAN (Mohamed et al., 2016) has not altered the optimal geometry nor improves the estimate of J.

We thus remain with the complex anharmonic surfaces treated by the explicit MD as the key factor for explaining the high rates of excitation transport in the orthogonal dyad. Closer examination points toward a multi-well picture of the potential landscape for vibrational motions. This is not unprecedented, as similar picture have been advocated to explain temperature-dependent spectral densities, for example in photosynthetic units (Rancova and Abramavicius, 2014). In the same spirit, the geometry statistics of **Figure 5** tends toward a unimodal, almost Gaussian distribution at higher temperatures. The distribution's width is, however, different from estimates derived from the surfaces around a global potential minimum.

This observation calls for a cautious inspection of the functional central limit theorem in a physical context: While indeed the composition of many stochastic vibrational coordinates bring the statistics of fluctuations toward the Brownian bridge (Donsker, 1951), and could be thus mapped onto the system of harmonic oscillators at a given temperature (Chernyak et al., 2006), these mappings are themselves temperature dependent. The anharmonic nature of low frequency vibrations is manifested as the need for *ad hoc* corrections to parameterizations of standard harmonic bath models when the temperature dependent optical spectra are studied.

The transport dynamics of the parallel dyad reveal the interplay of excitonic transport and vibrational relaxation. This allows us to track the relaxation pathways within the dyad; the presented vibronic framework is essential for these purposes. For the parallel dyad the vibronic methodology is essential to describe the relaxation pathways within the dyad. The two main factors determining relaxation dynamics are the strong interchromophoric coupling, on the one hand, and resonance between the donor-acceptor gap and the high frequency underdamped stretch mode on the other. Both factors are evident in the absorption spectrum as the levels are shifted and dipoles redistributed among the states in resonance, which means that the linear spectra can not be easily reconstructed from a simple sum of the constituents.

The presented work highlights several possible directions of future research. In general, the study of donor-acceptor systems would benefit from a unified theoretical treatment of exciton transport. Fluorescence labels used to track single

protein dynamics by analyzing photon arrival trajectories can be mentioned as an example, where a wide parametric range enters the analysis of excitation quenching (Yang et al., 2003). Largely different couplings also pertains to various stages of light harvesting in photosynthetic complexes.

From a theoretical perspective, a stochastic extension of the presented vibronic model in the spirit of Šanda et al. (2010) and Šanda and Mukamel (2011) promises a profound analysis of dynamical dipoles and their couplings. A more sophisticated inclusion of dynamical dipoles into the vibronic dynamics using a Hamiltonian description applicable at any temperature and its correct MD/DFT microscopic parametrization would be challenging, but would provide a significant test of transport theory.

The couplings from DFT was slightly overestimated compared to the transport data fit due to the neglect of solvent-induced shielding effects in the present DFT. Explicit inclusion of solvent molecules would be a costly, but straightforward way to avoid the extreme of complete neglect or macroscopic scaling for the rather small, compact dyads.

DATA AVAILABILITY STATEMENT

The raw data supporting the conclusions of this article will be made available by the authors, without undue reservation.

AUTHOR CONTRIBUTIONS

FUNDING

ACKNOWLEDGMENTS

SUPPLEMENTARY MATERIAL

The Supplementary Material for this article can be found online at: https://www.frontiersin.org/articles/10.3389/fchem.2020.579166/full#supplementary-material

REFERENCES

Amadei, A., Chillemi, G., Ceruso, M. A., Grottesi, A., and Di Nola, A. (2000). Molecular dynamics simulations with constrained roto-translational motions: theoretical basis and statistical mechanical consistency. *J. Chem. Phys.* 112, 9–23. doi: 10.1063/1.480557

Ambrosino, F., and Califano, S. (1965). The vibrational spectrum of perylene. *Spectrochim. Acta* 21, 1401–1409. doi: 10.1016/0371-1951(65)80050-9

Anda, A., De Vico, L., Hansen, T., and Abramavicius, D. (2016). Absorption and fluorescence lineshape theory for polynomial potentials. *J. Chem. Theory Comput.* 12, 5979–5989. doi: 10.1021/acs.jctc.6b00997

Angulo, G., Grampp, G., and Rosspeintner, A. (2006). Recalling the appropriate representation of electronic spectra. *Spectrochim. Acta Part A* 65, 727–731. doi: 10.1016/j.saa.2006.01.007

Atkins, P., and Friedman, R. (2011). *Molecular Quantum Mechanics*. Oxford: OUP Oxford.

Bayly, C. I., Cieplak, P., Cornell, W., and Kollman, P. A. (1993). A well-behaved electrostatic potential based method using charge restraints for deriving atomic charges: the RESP model. *J. Phys. Chem.* 97, 10269–10280. doi: 10.1021/j100142a004

Bo, F., Gao, B., Duan, W., Li, H., Liu, H., and Bai, Q. (2013). Assembly-disassembly driven "off-on" fluorescent perylene bisimide probes for detecting and tracking of proteins in living cells. *RSC Adv.* 3, 17007–17010. doi: 10.1039/c3ra42284d

Butkus, V., Valkunas, L., and Abramavicius, D. (2014). Vibronic phenomena and exciton-vibrational interference in two-dimensional spectra of molecular aggregates. *J. Chem. Phys.* 140:034306. doi: 10.1063/1.4861466

Caldeira, A. O., and Leggett, A. J. (1983). Path integral approach to quantum Brownian motion. *Phys. A* 121, 587–616. doi: 10.1016/0378-4371(83)90013-4

Case D. A., Babin V., Berryman J. T., Betz R. M., Cai Q., Cerutti D. S., et al. (2014). *AMBER 14*. San Francisco, CA: University of California.

Chernyak, V., Šanda, F., and Mukamel, S. (2006). Coherence and correlations in multitime quantum measurements of stochastic quantum trajectories. *Phys. Rev. E* 73:036119. doi: 10.1103/PhysRevE.73.036119

de França, B. M., Bello Forero, J. S., Garden, S. J., Ribeiro, E. S., da S.Souza, R., Teixeira, R. S., et al. (2018). Green fluorescence pyrene-based dye as a new π-extended system: synthesis, photophysical and theoretical studies. *Dyes Pigments* 148, 444–451. doi: 10.1016/j.dyepig.2017.09.003

Didraga, C., Pugžys, A., Hania, P. R., von Berlepsch, H., Duppen, K., and Knoester, J. (2004). Structure, spectroscopy, and microscopic model of tubular carbocyanine dye aggregates. *J. Phys. Chem. B* 108, 14976–14985. doi: 10.1021/jp048288s

Donsker, M. D. (1951). An invariance principle for certain probability limit theorems. *Mem. Am. Math. Soc.* 6, 1-12.

Förster, T. (1948). Zwischenmolekulare Energiewanderung und Fluoreszenz. *Ann. Phys.* 437, 55–75. doi: 10.1002/andp.19484370105

Frisch et al., M. J. (2009). *Gaussian 09, Revision E.01*. Wallingford, CT: Gaussian, Inc.

Fron, E., Schweitzer, G., Osswald, P., Würthner, F., Marsal, P., Beljonne, D., et al. (2008). Photophysical study of bay substituted perylenediimides. *Photochem. Photobiol. Sci.* 7, 1509–1521. doi: 10.1039/b813737d

Fujihashi, Y., and Kimura, A. (2013). Improved variational master equation theory for the excitation energy transfer. *J. Phys. Soc. Jpn.* 83:014801. doi: 10.7566/JPSJ.83.014801

Galestian Pour, A., Lincoln, C. N., Perlík, V., Šanda, F., and Hauer, J. (2017). Anharmonic vibrational effects in linear and two-dimensional electronic spectra. *Phys. Chem. Chem. Phys.* 19, 24752–24760. doi: 10.1039/C7CP05189A

Garvin, R. L. (1960). The collection of light from scintillation counters. *Rev. Sci. Instr.* 31, 1010–1011. doi: 10.1063/1.1717105

Herrmann, A., and Müllen, K. (2006). From industrial colorants to single photon sources and biolabels: the fascination and function of rylene dyes. *Chem. Lett.* 35, 978–985. doi: 10.1246/cl.2006.978

Hestand, N. J., and Spano, F. C. (2018). Expanded theory of H- and J- molecular aggregates: the effects of vibronic coupling and intermolecular charge transfer. *Chem. Rev.* 118, 7069–7163. doi: 10.1021/acs.chemrev.7b00581

Hofmann, C. C., Lindner, S. M., Ruppert, M., Hirsch, A., Haque, S. A., Thelakkat, M., et al. (2010). Mutual interplay of light harvesting and triplet sensitizing in a perylene bisimide antenna- fullerene dyad. *J. Phys. Chem. B* 114, 9148–9156. doi: 10.1021/jp1035585

Holcombe, T. W., Norton, J. E., Rivnay, J., Woo, C. H., Goris, L., Piliego, C., et al. (2011). Steric control of the donor/acceptor interface: implications in organic photovoltaic charge generation. *J. Am. Chem. Soc.* 133, 12106–12114. doi: 10.1021/ja203235z

Hsu, C.-P., Fleming, G. R., Head-Gordon, M., and Head-Gordon, T. (2001). Excitation energy transfer in condensed media. *J. Chem. Phys.* 114, 3065–3072. doi: 10.1063/1.1338531

Huang, C., Barlow, S., and Marder, S. R. (2011). Perylene-3,4,9,10-tetracarboxylic acid diimides: synthesis, physical properties, and use in organic electronics. *J. Organ. Chem.* 76, 2386–2407. doi: 10.1021/jo2001963

Kalinin, S., Speckbacher, M., Langhals, H., and Johansson, L. B.-Å. (2001). A new and versatile fluorescence standard for quantum yield determination. *Phys. Chem. Chem. Phys.* 3, 172–174. doi: 10.1039/b007671f

Krueger, B. P., Scholes, G. D., and Fleming, G. R. (1998). Calculation of couplings and energy-transfer pathways between the pigments of LH2 by the *ab initio* transition density cube method. *J. Phys. Chem. B* 102, 5378–5386. doi: 10.1021/jp9811171

Lang, E., Würthner, F., and Köhler, J. (2005). Photophysical properties of a tetraphenoxy-substituted perylene bisimide derivative characterized by single-molecule spectroscopy. *ChemPhysChem* 6, 935–941. doi: 10.1002/cphc.200400555

Langhals, H. (2005). Control of the interactions in multichromophores: novel concepts. Perylene bisimides as components for larger functional units. *Helv. Chim. Acta* 88, 1309–1343. doi: 10.1002/hlca.200590107

Langhals, H. (2013). "Chromophores for picoscale optical computers," in *Fundamentals of Picoscience*, ed K. Sattler (CRC Press: Taylor & Francis), 705–727. doi: 10.1201/b15523-47

Langhals, H. (2019). *Primary Methods of Generating Solar Power by Using the Targeted Modification of Fluorescent Systems*. Habilitation. Freiburg: Albert-Ludwigs-Universitat Freiburg.

Langhals, H., Esterbauer, A. J., Walter, A., Riedle, E., and Pugliesi, I. (2010). Förster resonant energy transfer in orthogonally arranged chromophores. *J. Am. Chem. Soc.* 132, 16777–16782. doi: 10.1021/ja101544x

Langhals, H., and Gold, J. (1996). Tangentially coupled π systems and their through-space interaction - trichromophoric perylene dyes. *J. Prakt. Chem.* 338, 654–659. doi: 10.1002/prac.199633801124

Langhals, H., and Gold, J. (1997). Chiral bifluorophoric perylene dyes with unusually high CD effects - a simple model for the photosynthesis reaction center. *Liebigs Ann.* 1151–1153. doi: 10.1002/jlac.199719970615

Langhals, H., Karolin, J., and Johansson, L. B.-Å. (1998). Spectroscopic properties of new and convenient standards for measuring fluorescence quantum yields. *J. Chem. Soc.*, *Faraday Trans.* 94, 2919–2922. doi: 10.1039/a804973d

Langhals, H., Poxleitner, S., Krotz, O., Pust, T., and Walter, A. (2008). FRET in orthogonally arranged chromophores. *Eur. J. Org. Chem.* 4559–4562. doi: 10.1002/ejoc.200800451

Langhals, H., and Saulich, S. (2002). Bichromophoric perylene derivatives: energy transfer from non fluorescent chromophores. *Chem. Eur. J.* 8, 5630–5643. doi: 10.1002/1521-3765(20021216)8:24<5630::AID-CHEM5630>3.0.CO;2-Z

Langhals, H., and Walter, A. (2020). FRET in dyads with orthogonal chromophores and minimal spectral overlap. *J. Phys. Chem. A* 124, 1554–1560. doi: 10.1021/acs.jpca.9b11225

Lilliefors, H. W. (1967). On the Kolmogorov-Smirnov test for normality with mean and variance unknown. *J. Am. Stat. Assoc.* 62, 399–402. doi: 10.1080/01621459.1967.10482916

Lincoln, C. N., Hayden, J., Galestian Pour, A., Perlík, V., Šanda, F., and Hauer, J. (2016). A quantitative study of coherent vibrational dynamics probed by heterodyned transient grating spectroscopy. *Vib. Spectrosc.* 85, 167–174. doi: 10.1016/j.vibspec.2016.04.018

Löhmannsröben, H., and Langhals, H. (1989). Laser performance of perylenebis (dicarboximide) dyes with long secondary alkyl chains. *Appl. Phys. B* 48, 449–452. doi: 10.1007/BF00694678

Mais, S., Tittel, J., Basché, T., Bräuchle, C., Göhde, W., Fuchs, H., et al. (1997). Terrylenediimide: a novel fluorophore for single-molecule spectroscopy and microscopy from 1.4 K to room temperature. *J. Phys. Chem. A* 101, 8435–8440. doi: 10.1021/jp9719063

McWeeny, R. (1960). Some recent advances in density matrix theory. *Rev. Mod. Phys.* 32, 335–369. doi: 10.1103/RevModPhys.32.335

Megerle, U., Pugliesi, I., Schriever, C., Sailer, C., and Riedle, E. (2009). Sub-50 fs broadband absorption spectroscopy with tunable excitation: putting the analysis of ultrafast molecular dynamics on solid ground. *Appl. Phys. B* 96, 215–231. doi: 10.1007/s00340-009-3610-0

Mohamed, N. A., Bradshaw, R. T., and Essex, J. W. (2016). Evaluation of solvation free energies for small molecules with the AMOEBA polarizable force field. *J. Comput. Chem.* 37, 2749–2758. doi: 10.1002/jcc.24500

Nalbach, P., Pugliesi, I., Langhals, H., and Thorwart, M. (2012). Noise-induced Förster resonant energy transfer between orthogonal dipoles in photoexcited molecules. *Phys. Rev. Lett.* 108:218302. doi: 10.1103/PhysRevLett.108.218302

Nottoli, M., Jurinovich, S., Cupellini, L., Gardiner, A. T., Cogdell, R., and Mennucci, B. (2018). The role of charge-transfer states in the spectral tuning of antenna complexes of purple bacteria. *Photosynth. Res.* 137, 215–226. doi: 10.1007/s11120-018-0492-1

Olbrich, C., and Kleinekathöfer, U. (2010). Time-dependent atomistic view on the electronic relaxation in light-harvesting system II. *J. Phys. Chem. B* 114, 12427–12437. doi: 10.1021/jp106542v

Olbrich, C., Strümpfer, J., Schulten, K., and Kleinekathöfer, U. (2011). Theory and simulation of the environmental effects on FMO electronic transitions. *J. Phys. Chem. Lett.* 2, 1771–1776. doi: 10.1021/jz2007676

Osswald, P., and Würthner, F. (2007). Effects of bay substituents on the racemization barriers of perylene bisimides: resolution of atropo-enantiomers. *J. Am. Chem. Soc.* 129, 14319–14326. doi: 10.1021/ja074508e

Parr, R. G., and Yang, W. (1989). *Density Functional Theory of Atoms and Molecules*. New York, NY: Oxford University Press.

Perlík, V., Lincoln, C. N., Šanda, F., and Hauer, J. (2014). Distinguishing electronic and vibronic coherence in 2D spectra by their temperature dependence. *J. Phys. Chem. Lett.* 5, 404–407. doi: 10.1021/jz402468c

Perlík, V., and Šanda, F. (2017). Vibrational relaxation beyond the linear damping limit in two-dimensional optical spectra of molecular aggregates. *J. Chem. Phys.* 147:084104. doi: 10.1063/1.4999680

Polyutov, S., Kühn, O., and Pullerits, T. (2012). Exciton-vibrational coupling in molecular aggregates: electronic versus vibronic dimer. *Chem. Phys.* 394, 21–28. doi: 10.1016/j.chemphys.2011.12.006

Qian, G., Yang, Y., Wang, Z., Yang, C., Yang, Z., and Wang, M. (2003). Photostability of perylene orange, perylene red and pyrromethene 567 laser dyes in various precursors derived gel glasses. *Chem. Phys. Lett.* 368, 555–560. doi: 10.1016/S0009-2614(02)01906-1

Rancova, O., and Abramavicius, D. (2014). Static and dynamic disorder in bacterial light-harvesting complex LH2: a 2DES simulation study. *J. Phys. Chem. B* 118, 7533–7540. doi: 10.1021/jp5043156

Redfield, A. G. (1957). On the theory of relaxation processes. *IBM J. Res. Dev.* 1, 19–31. doi: 10.1147/rd.11.0019

Renger, T., Dankl, M., Klinger, A., Schlücker, T., Langhals, H., and Müh, F. (2018). Structure-based theory of fluctuation-induced energy transfer in a molecular dyad. *J. Phys. Chem. Lett.* 9, 5940–5947. doi: 10.1021/acs.jpclett.8b02403

Renger, T., and Müh, F. (2012). Theory of excitonic couplings in dielectric media. Foundation of Poisson-TrEsp method and application to photosystem I trimers. *Photosynth. Res.* 111, 47–52. doi: 10.1007/s11120-011-9685-6

Šanda, F., and Mukamel, S. (2006). Cooperative effects in photon statistics of molecular dimers with spectral diffusion. *J. Chem. Phys.* 124:124103. doi: 10.1063/1.2174001

Šanda, F., and Mukamel, S. (2008). Stochastic Liouville equations for coherent multidimensional spectroscopy of excitons. *J. Phys. Chem. B* 112, 14212–14220. doi: 10.1021/jp801457c

Šanda, F., and Mukamel, S. (2011). Novel coherent two dimensional optical spectroscopy probes of chirality exchange and fluctuations in molecules. *J. Chem. Phys.* 135:194201. doi: 10.1063/1.3658277

Šanda, F., Perlík, V., and Mukamel, S. (2010). Exciton coherence length fluctuations in chromophore aggregates probed by multidimensional optical spectroscopy. *J. Chem. Phys.* 133:014102. doi: 10.1063/1.3442415

Seybold, G., and Wagenblast, G. (1989). New perylene and violanthrone dyestuffs for fluorescent collectors. *Dyes Pigm.* 11, 303–317. doi: 10.1016/0143-7208(89)85048-X

Tanimura, Y. (2006). Stochastic Liouville, Langevin, Fokker-Planck, and master equation approaches to quantum dissipative systems. *J. Phys. Soc. Jpn.* 75:082001. doi: 10.1143/JPSJ.75.082001

Wang, J., Wolf, R. M., Caldwell, J. W., Kollman, P. A., and Case, D. A. (2004). Development and testing of a general AMBER force field. *J. Comput. Chem.* 25, 1157–1174. doi: 10.1002/jcc.20035

Weiss, M. S. (1987). Modification of the Kolmogorov-Smirnov statistics for use with correlated data. *J. Am Stat. Assoc.* 73, 872–875. doi: 10.1080/01621459.1978.10480116

Würthner, F., Thalacker, C., Diele, S., and Tschierske, C. (2001). Fluorescent J-type aggregates and thermotropic columnar mesophases of perylene bisimide dyes. *Chem. Eur. J.* 7, 2245–2253. doi: 10.1002/1521-3765(20010518)7:10<2245::AID-CHEM2245>3.0.CO;2-W

Yang, H., Luo, G., Karnchanaphanurach, P., Louie, T.-M., Rech, I., Cova, S., et al. (2003). Protein conformational dynamics probed by single-molecule electron transfer. *Science* 302, 262–266. doi: 10.1126/science.1086911

Zimanyi, E. N. and Silbey, R. J. (2012). Theoretical description of quantum effects in multi-chromophoric aggregates. *Philos. Trans. R. Soc. A* 370, 3620–3637. doi: 10.1098/rsta.2011.0204

Proton Transfer and Nitro Rotation Tuned Photoisomerization of Artificial Base Pair-ZP

Xixi Cui, Yu Zhao, Zhibing Li, Qingtian Meng* and Changzhe Zhang*

Shandong Province Key Laboratory of Medical Physics and Image Processing Technology, School of Physics and Electronics, Shandong Normal University, Jinan, China

Recently, the successful incorporation of artificial base pairs in genetics has made a significant progress in synthetic biology. The present work reports the proton transfer and photoisomerization of unnatural base pair ZP, which is synthesized from the pyrimidine analog 6-amino-5-nitro-3-(1-β-D-2′-deoxyribo-furanosyl)-2 (1H)-pyridone (Z) and paired with its Watson-Crick complement, the purine analog 2-amino-8-(1′-β-D-2′- deoxyribofuranosyl)-imidazo[1,2-a]-1,3,5-triazin-4(8H)-one (P). To explain the mechanism of proton transfer process, we constructed the relaxed potential energy surfaces (PESs) linking the different tautomers in both gas phase and solution. Our results show that the double proton transfer in the gas phase occurs in a concerted way both in S_0 and S_1 states, while the stepwise mechanism becomes more favorable in solution. The solvent effect can promote the single proton transfer, which undergoes a lower energy barrier in S_1 state due to the strengthened hydrogen bond. In contrast to the excited state ultrafast deactivation process of the natural bases, there is no conical intersection between S_0 and S_1 states along the proton transfer coordinate to activate the decay mechanism in ZP. Of particular relevance to the photophysical properties, charge-transfer character is obviously related to the nitro rotation in S_1 state. We characterized the molecular vibration effect on the electronic properties, which reveals the electronic excitation can be tuned by the rotation-induced structural distortion accompanied with the electron localization on nitro group.

Keywords: proton transfer, potential energy surface, photoisomerization, artificial bases, *ab initio*

INTRODUCTION

In the field of biochemistry, the four natural nucleotide letters [guanine (G), cytosine (C), adenine (A), and thymine (T)] can encode virtually all genetic information. Their selective pairings to form two base pairs (i.e., AT and CG) through complementary hydrogen-bond formation underlie the storage and retrieval of all biological information. Expanding the two-base-pair genetic alphabet has been a quest in the design of artificial life since the DNA structures were discovered, followed by the mechanism of genetic material transfer being understood during cell replication (Watson and Crick, 1953a,b). In the past few years, Romesberg et al. reported a class of unnatural base pairs formed between nucleotides containing hydrophobic nucleobases, successfully replicating artificial base pairs *in vivo* (McMinn et al., 1999; Tae et al., 2001; Malyshev et al., 2014). Moreover, they have optimized different components of semisynthetic organisms by using genetic and chemical approaches, eventually making them grow robustly and be capable of storing the increased

information unrestrictedly in practice (Zhang et al., 2017). In 2019, Benner and collaborators doubled the number of life's building blocks, creating a synthetic, eight-letter language (G, C, A, T, and Z, P, B, S) (Hoshika et al., 2019), which forms the base pairs through hydrogen bonding interactions and seems to store and transcribe information (Geyer et al., 2003; Yang et al., 2006; Kim et al., 2014; Zhang et al., 2015; Biondi and Benner, 2018). Previous studies demonstrated that the artificial base pairs can not only mimic the natural base pairs in terms of both structure and stability (Chawla et al., 2016), but also present novel characters in contrast to the natural bases. For example, it has been revealed that DNA strands containing artificial ZP base pairs could better combine with breast cancer cells by exponential enrichment experiment and thus can be transformed into "cancer cell hunters" (Sefah et al., 2014).

Current advances in the synthesis of artificial bases require further insight into the stability and photochemistry properties of the additional genetic code. As is known, the proton and electron transfer play an important role in regulating the properties of the system, and therefore attract widespread attention both in experimental and theoretical studies (Florián and Leszczyński, 1996; Guallar et al., 1999; Sauri et al., 2013; Bull and Thompson, 2018; Zhao et al., 2018a,b; Gonzalez-Garcia et al., 2019; Liu et al., 2019; Cheng et al., 2020; Liu S. S. et al., 2020). Especially, the proton transfer between two pairing bases acts as a key part in many biological and chemical phenomena and processes, like genetic mutation, radiation-induced DNA damage and dynamics of charge transfer in DNA. For example, Jośe Ortega et al. studied the double proton transfer of GC base pair in B-DNA and illustrated the influence of DNA biological environment on the stability of the genetic code (Soler-Polo et al., 2019). In addition, another work reports the DNA damage due to hydrogen-bonded proton transfer in the protonated GC base pairs (Lin et al., 2011). Recently, one steered molecular dynamic simulation presents that the tautomerization of the T*-A* mispair via double proton transfer is an effective pathway of the T-A to C-G transition (Tolosa et al., 2020).

Although great efforts have been made to study the proton transfer reaction of natural base pairs, to the best of our knowledge, the tautomerism of artificial bases are still poorly understood. On the basis of the mentioned above, we presented a detailed theoretical study on the proton transfer process and photoisomerization of the artificial bases ZP, paired by the pyrimidine analog 6-amino-5-nitro-3-(1-β-D-2'-deoxyribofuranosyl)-2(1H)-pyridone (Z) and its Watson-Crick complement, the purine analog 2-amino-8-(1'-β-D-2'-deoxyribofuranosyl)-imidazo[1,2-a]-1,3,5-triazin-4(8H)-one (P) (Yang et al., 2007, 2011; Chen et al., 2011), as shown in **Scheme 1**. It is found that the double proton transfer in the gas phase is a concerted mechanism both in ground (S_0) and the first excited (S_1) states, while the process in solution turns to be stepwise along the S_0-PES and only single proton transfer is available in the S_1 state. The solvent effect is not only conducive to the single proton transfer but also beneficial to the stabilization of related ZP products in both S_0 and S_1 states. Compared with the case in S_0 state, the proton transfer undergoes a low energy barrier reaction pathway in S_1 state due to the hydrogen bond enhancement.

SCHEME 1 | View of ZP with corresponding atom labels involved in three possible hydrogen-bonds.
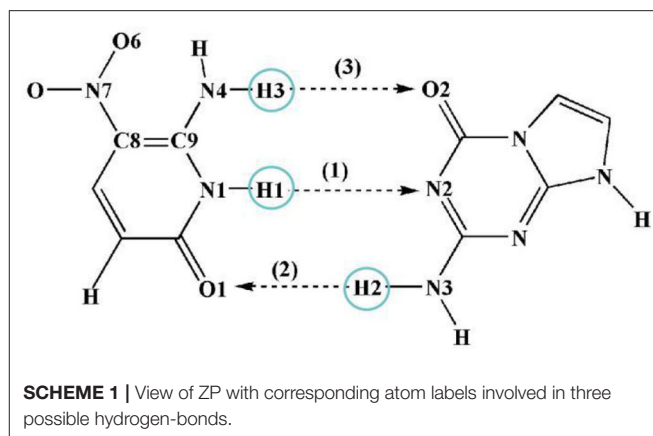
Previous studies revealed that the existence of conical intersection of natural bases leads to highly efficient radiationless deactivation pathways, which returns the molecules to their ground states before chemical reactions in the excited states can lead to profound damage, and thus endow additional photostability of the natural base pairs (Sobolewski and Domcke, 2004; Sobolewski et al., 2005; Groenhof et al., 2007; Schwalb et al., 2009). However, there is no conical intersection between S_0 and S_1 states along the proton transfer coordinate to activate this decay mechanism in ZP. Clearly, the artificial base pair ZP has a longer lifetime in the S_1 state and possesses weaker photostability than that of natural base pair GC.

Furthermore, our results show that the optimized configuration of ZP in S_1 state is a non-planar structure induced by the nitro rotation accompanied with electron localization on nitro group, which indicates the lowest excited singlet state of ZP possesses charge-transfer character. It is well-known that the molecular distortion induced by the vibration is an inherent property of a molecule, which can also be activated by external energy pulse and lead to the changes of the geometric as well as the electronic properties (Huynh and Meyer, 2007; Sánchez-Carrera et al., 2010; Zimmerman et al., 2013; Feng et al., 2016; Zhang et al., 2016). Accordingly, it is worth illustrating the influence of nitro rotation on the absorption spectra and electron distribution of the system. It can be seen that the absorption maximum of ZP presents continuous red-shift associated with the rotation-induced electron localization on nitro group, and thus broadens the absorption spectrum compared with the case of natural base pairs. Our work demonstrates the proton transfer mechanism and the photophysical behaviors of artificial bases to evaluate the stability of artificial bases as the genetic code. The corresponding results can also serve as an impetus for the design of target drug based on unnatural bases.

COMPUTATIONAL DETAILS

Here, the structures of ZP base pair in S_0 and S_1 states were fully optimized by using the DFT and TD-DFT methods at the B3LYP-D3(BJ)/ 6-311++G(d,p) level (Lee et al., 1988; Becke, 1993; Theilacker et al., 2011), which have been successful applied in

other similar systems (Mazurkiewicz et al., 2006; Jiao et al., 2009). Corresponding calculations were also confirmed by utilizing the wB97-XD (Chai and Head-Gordon, 2008) and M06-2X (Zhao and Truhlar, 2008) functionals and the wave function methods (DLPNO-STEOM-CCSD and CASSCF) (Andersson et al., 1990, 1992; Hald et al., 2000; Schreiber et al., 2008; Triandafillou and Matsika, 2013). In this work, the bulk solvent (water) has been modeled with the integral equation formalism polarizable continuum model (IEFPCM) (Mennucci et al., 1997; Tomasi et al., 2005). All molecular configurations were verified to be local minima with no imaginary frequency and no constrain of bond lengths and angles were adopted except for additional remarks. To illustrate the proton transfer mechanism, the relaxed PESs linking the different tautomers in both gas and solution were constructed by scanning the bond length of N1-H1 and H2-N3 with a step of 0.05 Å. Subsequently, to adequately investigate the intermolecular hydrogen bonding interactions of ZP system, the infrared (IR) spectra, reduced density gradient (RDG), topological properties and electrostatic potential (ESP) were calculated based on optimized structures and visualized by Multiwfn program (Lu and Chen, 2012). Moreover, the variation tendencies of the electron distribution, orbital energies and absorption spectrum with the nitro rotation were also presented by utilizing the single-point calculation based on rotation-distorted configurations. The electronic excitation types were confirmed from the hole-electron distributions drawn by the Multiwfn program (Liu Z. Y. et al., 2020). The C_{hole}-C_{ele} diagram is employed to smooth out the complex isosurfaces of hole and electron distribution. All calculations were carried out by the Gaussian 16 suite of programs (Frisch et al., 2016), except that the DLPNO-STEOM-CCSD method was completed by the ORCA package (Neese, 2012, 2017).

RESULTS AND DISCUSSION

Three possible hydrogen-bonded proton-transfer pathways of ZP base pair are considered as shown in **Scheme 1**. H1 proton transfer from the N1 site of Z base to the N2 site of P base is defined as the SPT1. The H2 proton transfer from the N3 site of P base to the O1 site of Z base is viewed as SPT2. Meanwhile, the H3 proton transfer from the N4 site of Z base to the O2 site of P base is regarded as SPT3. Our calculated results reveal that the SPT1 is the most common route followed by SPT2, however, SPT3 is unavailable in both S_0 and S_1 states.

Proton Transfer in the Gas Phase

Since the main purpose of the present work is to investigate the proton transfer reaction and photophysical properties of ZP in solution, it is helpful to first know relevant basic information about ZP in the gas phase. To this end, the gaseous mechanism of proton transfer is firstly demonstrated in detail by constructing the PESs of the S_0 and S_1 states as functions of N1-H1 and H2-N3 bonds shown in **Figure 1**. The structures of normal ZP (A_0, A_1), dual-proton transfer ZP-DPT (C_0, C_1), and single-proton transfer ZP-SPT2 (D_1) are obtained (**Supplementary Figure 1** and **Supplementary Table 1**), with a subsequent vibrational frequency analysis to ensure the validity of these structures. As shown in **Figure 1**, the energies of structure A_0 and A_1 are the minima in the S_0 and S_1 states, respectively, which indicates the canonical Watson-Crick configuration is the most stable whether in S_0 or S_1 state. Subsequently, it is realized that the double-proton-transfer process can take place in both S_0 and S_1 states. As shown in **Table 1**, the concerted mechanism is recognized in S_0 state with a reaction barrier of 16.8 kcal/mol, and the reverse barrier is 4.6 kcal/mol. However, there are two possible paths

FIGURE 1 | PESs on both S_0 and S_1 states of ZP as the functions of N1-H1 and H2-N3 length in the gas phase. **(A)** S_0 state PES; **(B)** S_1 state PES.
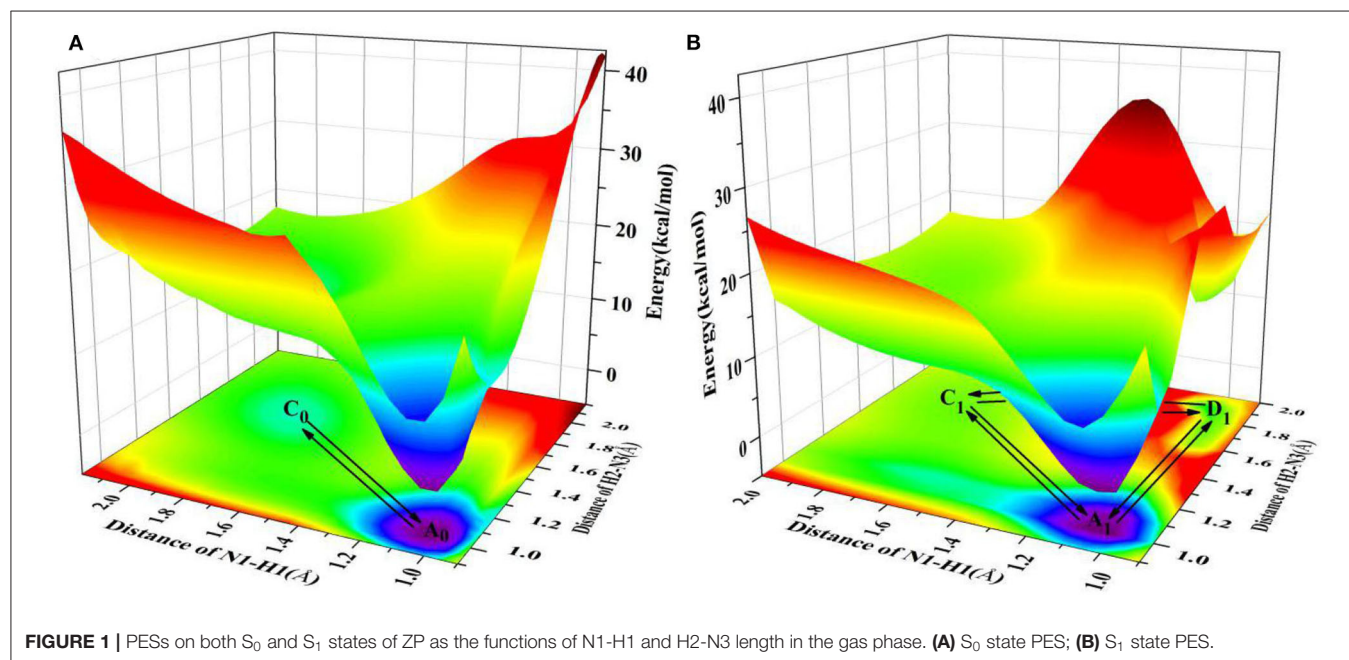
in the S_1 state: the stepwise reaction undergoes ZP $\underset{9.3 \text{ kcal/mol}}{\overset{23.4 \text{ kcal/mol}}{\rightleftarrows}}$

ZP-SPT2 $\underset{14.9 \text{ kcal/mol}}{\overset{13.6 \text{ kcal/mol}}{\rightleftarrows}}$ ZP-DPT and the concerted path involves

the transfer of ZP $\underset{2.8 \text{ kcal/mol}}{\overset{15.6 \text{ kcal/mol}}{\rightleftarrows}}$ ZP-DPT. Above discussion reveals

that the double-proton-transfer in both S_0 and S_1 states is a concerted process, however, the product ZP-DPT is unstable due to the low reverse reaction barrier. On the other hand, the single-proton-transfer can occur in S_1 state and the 9.3 kcal/mol reverse barrier allows the product ZP-SPT2 sufficiently long-lived.

Proton Transfer in Solution

It is well-known that the biological micro-surrounding or aqueous solution plays an important role in the proton transfer

TABLE 1 | The potential barrier of proton transfer process (ΔE) and reverse reaction (ΔE$_{re}$) in the gas phase and solution.

	Structure	Reaction mechanism	ΔE(ΔE$_{re}$) (kcal/mol)		
			SPT1[a]	SPT2[b]	DPT[c]
Gas phase	WC-ZP-S_0	Concerted	/	/	16.8 (4.6)
	WC-ZP-S_1	Concerted	/	/	15.6 (2.8)
		Stepwise	/	23.4 (9.3)	13.6 (14.9)
Aqueous phase	WC-ZP-S_0	Concerted	/	/	18.6 (5.9)
		Stepwise	8.9 (1.7)	/	5.8 (0.2)
	WC-ZP-S_1	Stepwise1	5.9 (3.2)	/	/
		Stepwise2	/	25.2 (0.17)	/

[a]H1 proton transfer from the N1 site of Z base to the N2 site of P base.
[b]H2 proton transfer from the N3 site of P base to the O1 site of Z base.
[c]Double-proton transfer with H1 and H2.

process, which has been investigated both experimentally and theoretically (Adhikary et al., 2009; Kumar and Sevilla, 2009; Ceron-Carrasco et al., 2011). Therefore, it is necessary to consider the solvent effect in the extended calculations to explore the mechanism of proton transfer for the ZP base pairs in biological environment. Here, the SPT3 is unavailable in both S_0 and S_1 states (**Supplementary Figure 3**), and thus we constructed the 2-dimension relaxed PESs with respect to the N-H bond length of ZP in S_0 and S_1 states. As shown in **Figure 2**, there are six local minimum points in the PESs, namely A_0, B_0, C_0 (S_0), and A_1, B_1, D_1 (S_1), and the related geometric configurations are displayed in **Supplementary Figure 2** and **Supplementary Table 2**. Similar to the case in gas phase, the configurations A_0 and A_1 are the most stable in S_0 and S_1 respectively, revealed by the corresponding energies of reactants and products listed in **Supplementary Table 3**. As shown in **Figure 2A**, there are two paths for the double proton transfer in the S_0 state: ZP $\underset{5.9 \text{ kcal/mol}}{\overset{18.6 \text{ kcal/mol}}{\rightleftarrows}}$ ZP-DPT and ZP $\underset{1.7 \text{ kcal/mol}}{\overset{8.9 \text{ kcal/mol}}{\rightleftarrows}}$

ZP-SPT1 $\underset{0.2 \text{ kcal/mol}}{\overset{5.8 \text{ kcal/mol}}{\rightleftarrows}}$ ZP-DPT. Obviously, the stepwise process

is more likely to happen than the concerted mechanism in S_0 state. It can also be seen that the product ZP-DPT is unstable due to the shallow potential energy well. In addition, there are two single proton transfer pathways in S_1 state (**Figure 2B**), which are ZP $\underset{3.2 \text{ kcal/mol}}{\overset{5.9 \text{ kcal/mol}}{\rightleftarrows}}$ ZP-SPT1 and ZP $\underset{0.17 \text{ kcal/mol}}{\overset{25.2 \text{ kcal/mol}}{\rightleftarrows}}$ ZP - SPT2. For

the latter one, it takes place through a high energy barrier of 25.2 kcal/mol, and the whole process is endothermic by 25.0 kcal/mol. It is important to note that the barrier for the reverse process is only 0.17 kcal/mol, which indicates the energy well of the product is quite unlikely to support any bound states, so
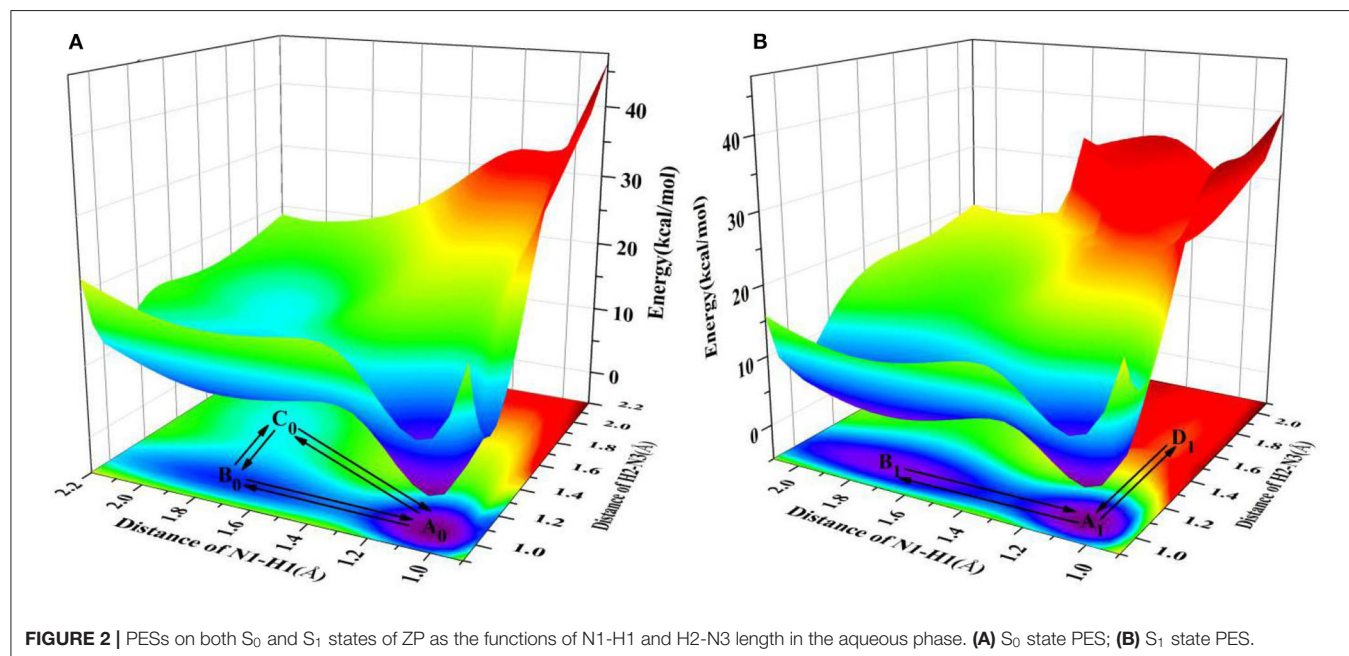

FIGURE 2 | PESs on both S_0 and S_1 states of ZP as the functions of N1-H1 and H2-N3 length in the aqueous phase. **(A)** S_0 state PES; **(B)** S_1 state PES.

we speculate that the ZP→ZP-SPT2 process will not occur in the S$_1$ state. On the other hand, the energy of the product ZP-SPT1 is just 2.7 kcal/mol higher than that of the reactant (**Table 1** and **Supplementary Table 3**), and the obvious potential well in **Figure 2A** shows that the ZP-SPT1 is relatively stable in the S$_1$ state. Parenthetically, the H1 atom of the N-H···N fragment is firstly transferred in both S$_0$ and S$_1$ states. Also, the reverse barrier of the ZP→ZP-SPT1 process is a non-negligible obstacle, so once the ZP-SPT1 configuration is formed, it will probably survive for a relatively long period. It should be noticed that the potential barrier in S$_1$ state is 3.0 kcal/mol lower than that of S$_0$ state, which indicates an easier transfer of proton H1 in S$_1$ state. Above discussions are reproduced with considering the explicit solvent molecules (5 H$_2$O molecules) by using the DFT and TD-DFT methods at the B3LYP-D3(BJ)/ 6-311++G(d,p) level as shown in **Supplementary Figure 4** and **Supplementary Table 4**.

To further explain the mechanism of excited-state proton transfer in the solvent, we calculated the hydrogen bond parameters of the ZP system. The corresponding electronic distribution of ZP and its tautomers are shown in **Figure 3**. In addition, the parameters of bond length and bond angle related to the intermolecular hydrogen bond are listed in **Supplementary Table 2**. Herein, we just investigated the hydrogen bond N1-H1···N2, because it is the primary reaction path in both S$_0$ and S$_1$ states. Upon photo-excitation, the bond length of N1-H1 is changed from 1.04 Å (S$_0$) to 1.05 Å (S$_1$), while the bond length of the hydrogen bond H1···N2 is changed from 1.86 Å (S$_0$) to 1.78 Å (S$_1$). Meanwhile, the bond angle of N1-H1···N2 is changed from 179.0° (S$_0$) to 179.2° (S$_1$). These phenomena indicate that the intermolecular hydrogen bond N1-H1···N2 is enhanced in the S$_1$ state, which provides the driving force for H1 proton transfer in the excited state.

To further reveal the intermolecular hydrogen bonding interactions of ZP in real space, the RDG versus sign(λ_2)ρ

is displayed via the Multiwfn and the VMD programs (see **Supplementary Figure 5**). The relevant formulas can be written as

$$\text{RDG}(r) = \frac{1}{2(3\pi^2)^{1/3}} \frac{|\nabla\rho(r)|}{\rho(r)^{4/3}}, \tag{1}$$

$$\Omega(r) = \text{sign}(\lambda_2(r))\rho(r) \tag{2}$$

in which $\lambda_2(r)$ reflects the type of interaction and the electron density $\rho(r)$ is used to give the strength of interaction. Besides, the sign(λ_2)ρ is a good indicator to characterize the interaction strength (Johnson et al., 2010). Specifically, if the value of sign(λ_2)ρ is negative, the interaction is attractive and is zero meaning that there is a weak interaction, while a positive value of sign(λ_2)ρ is an indication of non-bonding repulsive interaction. The spike peak of ZP is located around −0.03 a.u. to −0.04 a.u. in the S$_0$ state, while the S$_1$ state spike peak is between −0.04 a.u. and −0.05 a.u., and the isosurface of the hydrogen bond H1···N2 in S$_1$ state is deeper blue distinctly than that in S$_0$ state. These calculations indicate that the H1···N2 is strengthened upon photo-excitation. Similar trends are considered in the topology structure (**Supplementary Figure 6** and **Supplementary Table 5**) and the IR spectra (**Supplementary Figure 7**) of ZP. We also calculated the ESP along the N1-H1···N2 proton transfer path (**Supplementary Figure 8**) to recognize the electrostatic interaction between molecules. The related results show the ESP of the H1 proton in S$_1$ is significantly higher than that in S$_0$, which leads to an easier proton transfer from N1 to N2 in S$_1$ state. However, the ESP of ZP-SPT1 in the S$_0$ state is much higher than that in S$_1$ state, indicating the reverse proton transfer is more likely to take place in S$_0$ state. Similar trends can also be observed in the differences of atom charges in the S$_0$ and S$_1$ states. As shown in **Supplementary Table 6**, the charge of N1
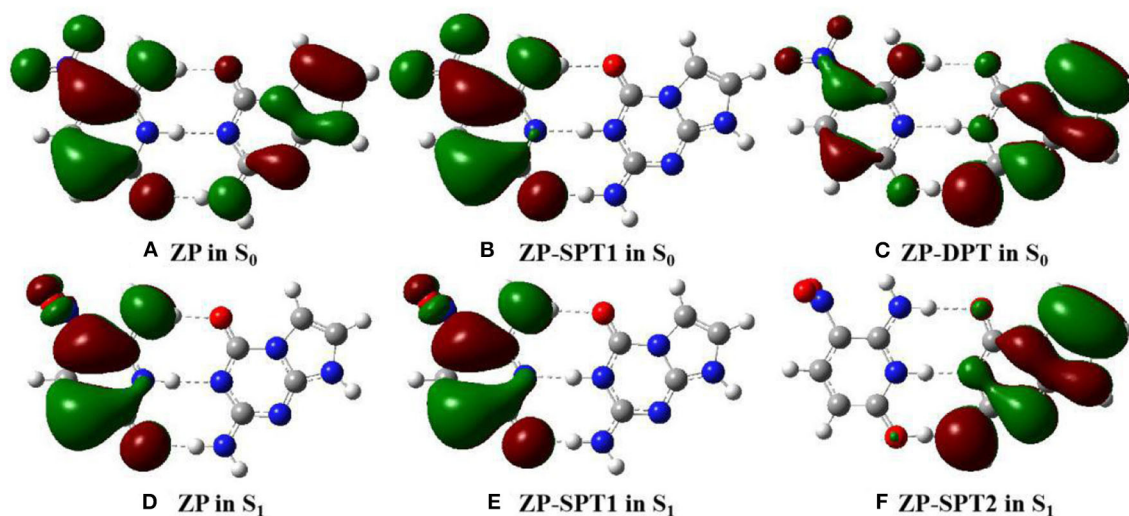

FIGURE 3 | View of HOMO for the normal ZP and tautomers in solution at B3LYP-D3(BJ)/6-311++G(d,p)/IEFPCM level. The green opaque shade and red opaque shade are for positive and negative parts of the wave function (isovalue = 0.02), respectively. **(A)** ZP in S$_0$. **(B)** ZP-SPT1 in S$_0$. **(C)** ZP-DPT in S$_0$. **(D)** ZP in S$_1$. **(E)** ZP-SPT1 in S$_1$. **(F)** ZP-SPT2 in S$_1$.

is changed form −0.268 (S_0) to −0.265(S_1), while the charge of N2 is changed form −0.424 (S_0) to −0.438 (S_1), which has contributions to the H1 proton transfer in the excited state.

In summary, the solvent effect can decrease the potential barriers of single proton transfer, and thus promote the reaction in both S_0 and S_1 states. On the other hand, we presented the different trends of proton transfer between ZP and natural base pair GC, which has similar three intermolecular hydrogen bonds like ZP. Although the most easily transferred site is also the H1 proton, the photophysical properties of ZP are different from the GC. Previous studies have proposed a coupled intermolecular electron-proton transfer mechanism for ultrafast electronic deactivation of the GC base pair (**Supplementary Figure 9A** calculated at CASSCF/CASSPT2 level), which demonstrates the barrierless minimum energy pathway in S_1 state finally leads to a conical intersection with the S_0 state at the N1-H1 bond length of about 2.35 Å, and the S_1 state population returns to S_0 and the initial Watson-Crick structure is restored. However, the PESs of the S_0 and S_1 states of ZP are almost parallel (**Supplementary Figures 9B–11**), which supports ZP having a longer lifetime in the S_1 state and possessing weaker photostability than that of natural base pair GC.

Rotation Modulation of the Electronic Transition

The optimized geometries and related electron distributions for the normal ZP and tautomers are depicted in **Figure 3**. It can be seen that the canonical ZP Watson-Crick configuration in

the S_0 state is a co-planar structure, in which electrons are delocalized on two bases. However, the rotation of the NO_2 group on the C5 position of the Z base makes the system non-planar in the S_1 state, and the electrons concentrated on the Z-base. Obviously, the nitro rotation dominates the transient changes of the electron distributions. It is well-known that as one of the molecular inherent properties, the structural vibrations are persistent, which has been proved to be an important role in the geometries as well as the electronic properties. Accordingly, it is essential to monitor the change of electronic properties along with the geometrical distortions. Here, we considered the configuration of nitro rotation mode, which is quantified by dihedral angle δ(O6-N7-C8-C9).

As a spectral indicator of electronic properties of ZP, the variation tendency of the absorption maximum with the nitro rotation is recorded (**Supplementary Figure 12**). The calculated results shows a continuous red-shift with the enlargement of the dihedral angles δ(O6-N7-C8-C9) and thus indicates a broad absorption spectrum (**Supplementary Figure 13**). To examine the electron excitation characteristics, we plot the HOMO and LUMO of the ZP base pair. As seen from **Figure 4**, the electron in both the HOMO and LUMO transfers from the aromatic ring to the nitro group with the enlargement of the dihedral angles. Besides, the hole-electron analysis is also utilized to reveal the nature of electron excitation (i.e., the departure and arrival of the excited electrons). As shown in **Figure 5**, the ZP undergoes the charge transfer excitation at the most stable geometry in S_0 with δ = 0°, where the electrons are transferred from P base
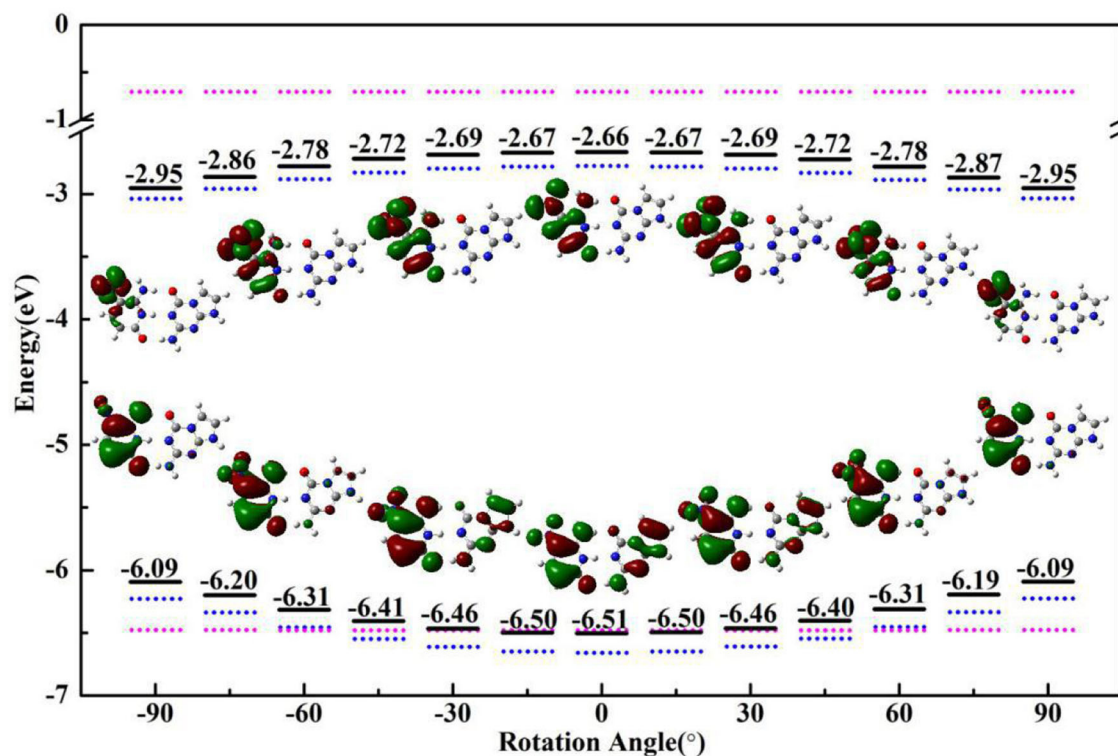

FIGURE 4 | The HOMO/LUMO energy and electron distribution of ZP (black solid line), single Z (blue dotted line) and P (pink dotted line) with the rotational displacements of −90°, −60°, −30°, 0°, 30°, 60°, 90°.
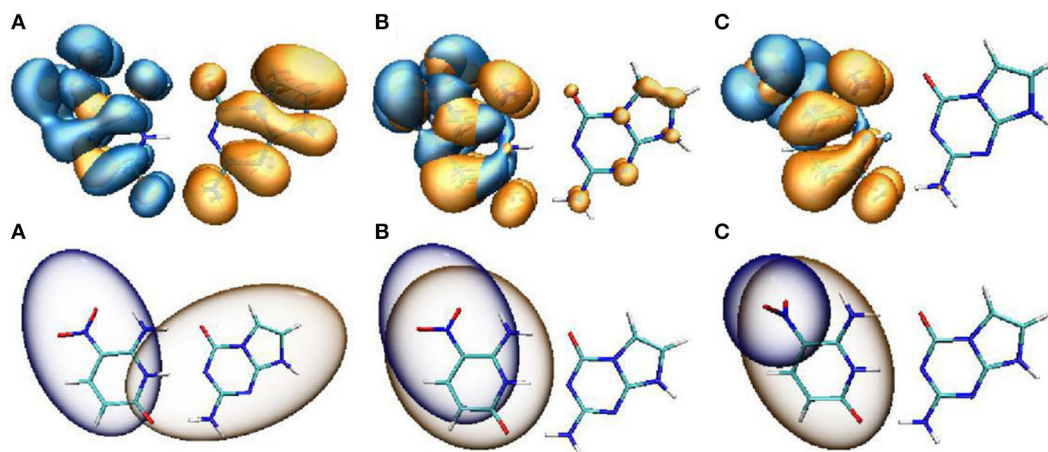
FIGURE 5 | Hole-electron distribution (upper panel) and the C_{hole}-C_{ele} diagrams (lower panel) of ZP with the rotational displacements of 0° **(A)**, 45° **(B)**, 90° **(C)**. Orange and blue regions (isovalue = 0.0002) denote the electron distributions and the holes, respectively.

to Z base. However, the vertical electronic excitation induced charge transfer characteristics become increasingly weak with the enlargement of the dihedral angles. It can be seen that both electrons and holes convergence to the nitro group accompanied with the increase of the rotational displacements, and thus lead to an easier electronic transition from S_0 to S_1.

An analysis of HOMO-LUMO gap is also particularly associated with the absorption characters. In general, a small energy gap is advantageous to the electronic transition from HOMO to LUMO. As shown in **Figure 4**, the HOMO-LUMO gap calculated at the optimized geometries with different dihedral angles in S_0 state gradually decreases with the increase of the nitro rotation, which is consistent with the red-shift in the absorption spectra. Specifically, the HOMO energies increase with the augment of the dihedral angles, while the LUMO energies decrease with the increase of the dihedral angles, which leads to the narrowing of the HOMO-LUMO energy gap (consistent with the energy difference between the S_0 and vertical S_1 states as shown in **Supplementary Figure 14**) and thus gives rise to the significant red-shift in the absorption spectra. Furthermore, the variation trends of the orbital energies of the separated Z-base and P-base were presented. The structures of single Z-base and P-base are extracted from the optimized geometries of ZP corresponding to different dihedral angles. It can be seen that the HOMO and LUMO energies of Z-base gradually increase and decrease along the positive and negative displacement directions, respectively. However, the orbital energy of P-base is insensitive to the nitro rotation, which remains relatively a constant. These observations indicate the variation of the orbital energies of Z-base induced by the nitro rotation is responsible for the spectral red-shift of ZP base pair. In fact, it is understandable because the orbital energy is an effective parameter to measure the electron-binding ability of a molecule. When the orbital energy is low, the ability of this molecule in binding electron is relatively large, which indicates an electron is prone to be captured. Obviously, the nitro rotation enhances binding ability of LUMO and

recedes electron-binding ability of HOMO, respectively, which is conducive to the vertical electronic excitation. In a word, ZP possesses charge-transfer character due to the rotation-induced electron localization on the nitro group, and the transition of ZP from S_0 to S_1 is also regulated by the molecular structural fluctuations accompanied with the nitro rotation. The above conclusions have been examined at the wB97-XD and M06-2X functionals (**Supplementary Figures 15, 16**).

CONCLUSION

In this paper, we investigated the intermolecular proton-transfer mechanism and photoisomerization of artificial base pair-ZP. Our results demonstrate that the double proton transfer takes place in a concerted way both in the S_0 and S_1 states in the gas phase. Under the water environment, the stepwise mechanism is more favorable along the S_0-PES and only single proton transfer is available in the S_1 state. The solvent effect promotes the single proton transfer in both S_0 and S_1 states by decreasing the activation energy and stabilizing the products. In addition, the proton transfer reaction is more likely to occur in the S_1 state because of the excited-state hydrogen bond enhancement. Unlike the excited-state ultrafast deactivation process of the natural bases, there is no conical intersection along the proton transfer coordinate of ZP, which suggests ZP having a longer lifetime in the S_1 state and possessing weaker photostability than that of natural base pair GC. Corresponding electron distribution reveals that the lowest excited singlet state of ZP possesses charge transfer characters, where the electron transfers from the aromatic ring to the nitro group induced by the photoexcitation. Moreover, we characterized the molecular vibration effect on the electronic excitation. It can be seen that the absorption maximum shows a continuous red-shift with the increase of the dihedral angles δ(O6-N7-C8-C9) due to the narrowing HOMO-LUMO energy gap with the nitro rotation, which indicates a broadened absorption spectrum in contrast to the case of natural base pairs. It can be concluded that the electronic transition of ZP from

S_0 to S_1 state can be tuned by the rotation-induced structural distortion accompanied with the electron localization on nitro group. This work provides an in-depth understanding on the biological process involved with artificial bases, which may also trigger more promising application prospects on the design of biological drug based on unnatural bases base pairs.

DATA AVAILABILITY STATEMENT

The raw data supporting the conclusions of this article will be made available by the authors, without undue reservation.

AUTHOR CONTRIBUTIONS

XC, YZ, and ZL carried out the *ab initio* calculation. XC analyzed the results and wrote the manuscript. QM and CZ supervised this project. All authors contributed to the article and approved the submitted version.

FUNDING

SUPPLEMENTARY MATERIAL

The Supplementary Material for this article can be found online at: https://www.frontiersin.org/articles/10.3389/fchem.2020.605117/full#supplementary-material

REFERENCES

Adhikary, A., Khanduri, D., and Sevilla, M. D. (2009). Direct observation of the hole protonation state and hole localization site in DNA-oligomers. *J. Am. Chem. Soc.* 131, 8614–8619. doi: 10.1021/ja9014869

Andersson, K., Malmqvist, P., and Roos, B. O. (1992). Second-order perturbation theory with a complete active space self-consistent field reference function. *J. Phys. Chem.* 96, 1218–1226. doi: 10.1063/1.462209

Andersson, K., Malmqvist, P. A., Roos, B. O., Sadlej, A. J., and Wolinski, K. (1990). Second-order perturbation theory with a CASSCF reference function. *J. Phys. Chem.* 94, 5483–5488. doi: 10.1021/j100377a012

Becke, A. D. (1993). Density-functional thermochemistry. III. The role of exact exchange. *J. Chem. Phys.* 98, 5648–5652. doi: 10.1063/1.464913

Biondi, E., and Benner, S. A. (2018). Artificially expanded genetic information systems for new aptamer technologies. *Biomedicine* 6:53. doi: 10.3390/biomedicines6020053

Bull, G. D., and Thompson, K. C. (2018). Proton transfer and tautomerism in 2-Aminopurine-Thymine and Pyrrolocytosine-Guanine base pairs. *Biochemistry-us* 57, 4547–4561. doi: 10.1021/acs.biochem.8b00521

Ceron-Carrasco, J. P., Zuniga, J., Requena, A., Perpete, E. A., Michaux, C., and Jacquemin, D. (2011). Combined effect of stacking and solvation on the spontaneous mutation in DNA. *Phys. Chem. Chem. Phys.* 13, 14584–14589. doi: 10.1039/c1cp20946a

Chai, J. D., and Head-Gordon, J. D. (2008). Long-range corrected hybrid density functionals with damped atom-atom dispersion corrections. *Phys. Chem. Chem. Phys.* 10, 6615–6620. doi: 10.1039/b810189b

Chawla, M., Credendino, R., Chermak, E., Oliva, R., and Cavallo, L. (2016). Theoretical characterization of the H-bonding and stacking potential of two nonstandard nucleobases expanding the genetic alphabet. *J. Phys. Chem. B* 120, 2216–2224. doi: 10.1021/acs.jpcb.6b00125

Chen, F., Yang, Z. Y., Yan, M. C., Alvarado, B., Wang, G. G., and Benner, S. A. (2011). Recognition of an expanded genetic alphabet by type-II restriction endonucleases and their application to analyze polymerase fidelity. *Nucl. Acids Res.* 39, 3949–3961. doi: 10.1093/nar/gkq1274

Cheng, R. D., Martens, J., and Fridgen, T. D. (2020). A vibrational spectroscopic and computational study of gaseous protonated and alkali metal cationized G-C base pairs. *Phys. Chem. Chem. Phys.* 22, 11546–11557. doi: 10.1039/D0CP00069H

Feng, Y. W., Zhang, F. Y., Song, X. Y., and Bu, Y. X. (2016). Molecular vibrations induced potential diradical character in hexaazapentacene. *J. Phys. Chem. C* 120, 10215–10226. doi: 10.1021/acs.jpcc.6b03891

Florián, J., and Leszczyński, J. (1996). Spontaneous DNA mutations induced by proton transfer in the Guanine·Cytosine base pairs: an energetic perspective. *J. Am. Chem. Soc.* 118, 3010–3017. doi: 10.1021/ja951983g

Frisch, M. J., Trucks, G. W., Schlegel, H. B., Scuseria, G. E., Robb, M. A., Cheeseman, J. R., et al. (2016). *Gaussian 16. Version A.03. Inc.* Wallingford, CT.

Geyer, C. R., Battersby, T. R., and Benner, S. A. (2003). Nucleobase pairing in expanded Watson-Crick-like genetic information systems. *Structure* 11, 1485–1498. doi: 10.1016/j.str.2003.11.008

Gonzalez-Garcia, M. C., Herrero-Foncubierta, P., Castro, S., Resa, S., Alvarez-Pez, J. M., Miguel, D., et al. (2019). Coupled excited-state dynamics in N-substituted 2-methoxy-9-acridones. *Front. Chem.* 7:129. doi: 10.3389/fchem.2019.00129

Groenhof, G., Schafer, L. V., Boggio-Pasqua, M., Goette, M., Grubmuller, H., and Robb, M. A. (2007). Ultrafast deactivation of an excited cytosine-guanine base pair in DNA. *J. Am. Chem. Soc.* 129, 6812–6819. doi: 10.1021/ja069176c

Guallar, V., Douhal, A., Moreno, M., and Lluch, J. M. (1999). DNA mutations induced by proton and charge transfer in the low-lying excited singlet electronic states of the DNA base pairs: a theoretical insight. *J. Phys. Chem. A* 103, 6251–6256. doi: 10.1021/jp9908496

Hald, K., Hattig, C., and Jorgensen, P. (2000). Triplet excitation energies in the coupled cluster singles and doubles model using an explicit triplet spin coupled excitation space. *J. Chem. Phys.* 113, 7765–7772. doi: 10.1063/1.1316033

Hoshika, S., Leal, N. A., Kim, M. J., Kim, M. S., Karalkar, N. B., Kim, H. J., et al. (2019). Hachimoji DNA and RNA: a genetic system with eight building blocks. *Science* 363, 884–887. doi: 10.1126/science.aat0971

Huynh, M. H. V., and Meyer, T. J. (2007). Proton-coupled electron transfer. *Chem. Rev.* 107, 5004–5064. doi: 10.1021/cr0500030

Jiao, D. S., Wang, H. Y., Zhang, Y. L., and Tang, Y. (2009). A DFT study of thymine and its tautomers. *Can. J. Chemistry* 87, 406–415. doi: 10.1139/v08-168

Johnson, E. R., Keinan, S., Mori-Sanchez, P., Contreras-Garcia, J., Cohen, A. J., and Yang, W. T. (2010). Revealing noncovalent interactions. *J. Am. Chem. Soc.* 132, 6498–6506. doi: 10.1021/ja100936w

Kim, H. J., Leal, N. A., Hoshika, S., and Benner, S. A. (2014). Ribonucleosides for an artificially expanded genetic information system. *J. Org. Chem.* 79, 3194–3199. doi: 10.1021/jo402665d

Kumar, A., and Sevilla, M. D. (2009). Influence of hydration on proton transfer in the guanine-cytosine radical cation (G•+-C) base pair: a density functional theory study. *J. Phys. Chem. B* 113, 11359–11361. doi: 10.1021/jp903403d

Lee, C., Yang, W., and Parr, R. G. (1988). Development of the Colle-Salvetti correlation-energy formula into a functional of the electron density. *Phys. Rev. B* 37, 785–789. doi: 10.1103/PhysRevB.37.785

Lin, Y. X., Wang, H. Y., Gao, S. M., and Schaefer, H. F. (2011). Hydrogen-bonded proton transfer in the protonated guanine-cytosine $(GC+H)^+$ base pair. *J. Phys. Chem. B* 115, 11746–11756. doi: 10.1021/jp205403f

Liu, H., Cao, J. W., and Bian, W. S. (2019). Double proton transfer in the dimer of formic acid: an efficient quantum mechanical scheme. *Front. Chem.* 7:676. doi: 10.3389/fchem.2019.00676

Liu, S. S., Lu, J. J., Lu, Q., Fan, J. Z., Lin, L. L., Wang, C. K., et al. (2020). Theoretical study on the sensing mechanism of novel hydrazine sensot TAPHP and its SEIPT and ICT processes. *Front. Chem.* 7:932. doi: 10.3389/fchem.2019.00932

Liu, Z. Y., Lu, T., and Chen, Q. X. (2020). An sp-hybridized all-carboatomic ring, cyclo[18]carbon: electronic structure, electronic spectrum, and optical nonlinearity. *Carbon* 165, 461–467. doi: 10.1016/j.carbon.2020.05.023

Lu, T., and Chen, F. W. (2012). Multiwfn: a multifunctional wavefunction analyzer. *J. Comput. Chem.* 33, 580–592. doi: 10.1002/jcc.22885

Malyshev, D. A., Dhami, K., Lavergne, T., Chen, T. J., Dai, N., Foster, J. M., et al. (2014). A semi-synthetic organism with an expanded genetic alphabet. *Nature* 509, 385–388. doi: 10.1038/nature13314

Mazurkiewicz, K., Bachorz, R. A., Gutowski, M., and Rak, J. (2006). On the unusual stability of valence anions of thymine based on very rare tautomers: a computational study. *J. Phys. Chem. B* 110, 24696–24707. doi: 10.1021/jp065666f

McMinn, D. L., Ogawa, A. K., Wu, Y. Q., Liu, J. Q., Schultz, P. G., and Romesberg, F. E. (1999). Efforts toward expansion of the genetic alphabet: recognition of a highly stable, self-pairing hydrophobic base. *J. Am. Chem. Soc.* 121, 11585–11586. doi: 10.1021/ja9925150

Mennucci, B., Cancès, E., and Tomasi, J. (1997). Evaluation of solvent effects in isotropic and anisotropic dielectrics and in ionic solutions with a unified integral equation method: theoretical bases, computational implementation, and numerical applications. *J. Phys. Chem. B* 101, 10506–10517. doi: 10.1021/jp971959k

Neese, F. (2012). The ORCA program system, Wiley Interdiscip. *Comput. Mol. Sci.* 2, 73–78. doi: 10.1002/wcms.81

Neese, F. (2017). Software update: the ORCA program system, version 4.0, Wiley Interdiscip. *Comput. Mol. Sci.* 8:e1327. doi: 10.1002/wcms.1327

Sánchez-Carrera, R. S., Paramonov, P., Day, G. M., Coropceanu, V., and Brédas, J. L. (2010). Interaction of charge carriers with lattice vibrations in oligoacene crystals from naphthalene to pentacene. *J. Am. Chem. Soc.* 132, 14437–14446. doi: 10.1021/ja1040732

Sauri, V., Gobbo, J. P., Serrano-Perez, J. J., Lundberg, M., Coto, P. B., Serrano-Andres, L., et al. (2013). Proton/hydrogen transfer mechanisms in the guanine-cytosine base pair: photostability and tautomerism. *J. Chem. Theory. Comput.* 9, 481–496. doi: 10.1021/ct3006166

Schreiber, M., Silva, M. R., Sauer, S. P. A., and Thiel, W. (2008). Benchmarks for electronically excited states: CASSPT2, CC2, CCSD, and CC3. *J. Chem. Phys.* 128:134110. doi: 10.1063/1.2889385

Schwalb, N. K., Michalak, T., and Temps, F. (2009). Ultrashort fluorescence lifetimes of hydrogen-bonded base pairs of guanosine and cytidine in solution. *J. Phys. Chem. B* 113, 16365–16376. doi: 10.1021/jp904883n

Sefah, K., Yang, Z. Y., Bradley, K. M., Hoshika, S., Jimenez, E., Zhang, L. Q., et al. (2014). *In vitro* selection with artificial expanded genetic information systems. *Proc. Natl. Acad. Sci. U. S. A.* 111, 1449–1454. doi: 10.1073/pnas.1311778111

Sobolewski, A. L., and Domcke, W. (2004). *Ab initio* studies on the photophysics of the guanine–cytosine base pair. *Phys. Chem. Chem. Phys.* 6, 2763–2771. doi: 10.1039/B314419D

Sobolewski, A. L., Domcke, W., and Hattig, C. (2005). Tautomeric selectivity of the excited-state lifetime of guanine/cytosine base pairs: the role of electron-driven proton-transfer processes. *Proc. Natl. Acad. Sci. U. S. A.* 102, 17903–17906. doi: 10.1073/pnas.0504087102

Soler-Polo, D., Mendieta-Moreno, J. I., Trabada, D. G., Mendieta, J., and Ortega, J. (2019). Proton transfer in guanine-cytosine base pairs in B-DNA. *J. Chem. Theory. Comput.* 15, 6984–6991. doi: 10.1021/acs.jctc.9b00757

Tae, E. J. L., Wu, Y. Q., Xia, G., Schultz, P. G., and Romesberg, F. E. (2001). Efforts toward expansion of the genetic alphabet: replication of DNA with three base pairs. *J. Am. Chem. Soc.* 123, 7439–7440. doi: 10.1021/ja010731e

Theilacker, K., Arbuznikov, A. V., Bahmann, H., and Kaupp, M. (2011). Evaluation of a combination of local hybrid functionals with DFT-D3 corrections for the calculation of thermochemical and kinetic data. *J. Phys. Chem. A* 115, 8990–8996. doi: 10.1021/jp202770c

Tolosa, S., Sansón, J. A., and Hidalgo, A. (2020). Mechanisms of the T-A to C-G transition studied by SMD simulations: deamination vs. tautomerisation. *J. Mol. Liq.* 308:113036. doi: 10.1016/j.molliq.2020.113036

Tomasi, J., Mennucci, B., and Cammi, R. (2005). Quantum mechanical continuum solvation models. *Chem. Rev.* 105, 2999–3093. doi: 10.1021/cr9904009

Triandafillou, C. G., and Matsika, S. (2013). Excited-state tautomerization of gas-phase cytosine. *J. Phys. Chem. A* 117, 12165–12174. doi: 10.1021/jp407758w

Watson, J. D., and Crick, F. H. (1953a). Molecular structure of nucleic acids: a structure for deoxyribose nucleic acid. *Nature* 171, 737–738. doi: 10.1038/171737a0

Watson, J. D., and Crick, F. H. (1953b). General implications of the structure of deoxyribonucleic acid. *Nature* 171, 964–967. doi: 10.1038/171964b0

Yang, Z. Y., Chen, F., Alvarado, J. B., and Benner, S. A. (2011). Amplification, mutation, and sequencing of a six-letter synthetic genetic system. *J. Am. Chem. Soc.* 133, 15105–15112. doi: 10.1021/ja204910n

Yang, Z. Y., Hutter, D., Sheng, P. P., Sismour, A. M., and Benner, S. A. (2006). Artificially expanded genetic information system: a new base pair with an alternative hydrogen bonding pattern. *Nucl. Acids Res.* 34, 6095–6101. doi: 10.1093/nar/gkl633

Yang, Z. Y., Sismour, A. M., Sheng, P. P., Puskar, N. L., and Benner, S. A. (2007). Enzymatic incorporation of a third nucleobase pair. *Nucl. Acids Res.* 35, 4238–4249. doi: 10.1093/nar/gkm395

Zhang, F. Y., Feng, Y. W., Song, X. Y., and Bu, Y. X. (2016). Computational insights into intriguing vibration-induced pulsing diradical character in perfluoropentacene and the perfluorination effect. *Phys. Chem. Chem. Phys.* 18, 16179–16187. doi: 10.1039/C6CP01706A

Zhang, L. Q., Yang, Z. Y., Sefah, K., Bradley, K. M., Hoshika, S., Kim, M. J., et al. (2015). Evolution of functional six-nucleotide DNA. *J. Am. Chem. Soc.* 137, 6734–6737. doi: 10.1021/jacs.5b02251

Zhang, Y. K., Lamb, B. M., Feldman, A. W., Zhou, A. X., Lavergne, T., Li, L. J., et al. (2017). A semisynthetic organism engineered for the stable expansion of the genetic alphabet. *Proc. Natl. Acad. Sci. U. S. A.* 114, 1317–1322. doi: 10.1073/pnas.1616443114

Zhao, J. F., Dong, H., and Zheng, Y. J. (2018a). Theoretical insights into the excited state double proton transfer mechanism of deep red pigment alkannin. *J. Phys. Chem. A* 122, 1200–1208. doi: 10.1021/acs.jpca.7b10492

Zhao, J. F., Dong, H., and Zheng, Y. J. (2018b). Elaborating the excited state multiple proton transfer mechanism for 9H-pyrido[3,4-b]indole. *J. Lumin.* 195, 228–233. doi: 10.1016/j.jlumin.2017.11.026

Zhao, Y., and Truhlar, D. G. (2008). The M06 suite of density functionals for main group thermochemistry, thermochemical kinetics, noncovalent interactions, excited states, and transition elements: two new functionals and systematic testing of four M06-class functionals and 12 other functionals. *Theor. Chem. Acc.* 120, 215–241. doi: 10.1007/s00214-007-0310-x

Zimmerman, P. M., Musgrave, C. B., and Head-Gordon, M. (2013). A correlated electron view of singlet fission. *Acc. Chem. Res.* 46, 1339–1347. doi: 10.1021/ar3001734

Asymmetry in the Q_y Fluorescence and Absorption Spectra of Chlorophyll *a* Pertaining to Exciton Dynamics

Jeffrey R. Reimers[1], Margus Rätsep[2] and Arvi Freiberg[2,3]*

[1] *School of Chemistry, The University of Sydney, Sydney, NSW, Australia,* [2] *Institute of Physics, University of Tartu, Tartu, Estonia,* [3] *Institute of Molecular and Cell Biology, University of Tartu, Tartu, Estonia*

Significant asymmetry found between the high-resolution Q_y emission and absorption spectra of chlorophyll-a is herein explained, providing basic information needed to understand photosynthetic exciton transport and photochemical reactions. The Q_y spectral asymmetry in chlorophyll has previously been masked by interference in absorption from the nearby Q_x transition, but this effect has recently been removed using extensive quantum spectral simulations or else by analytical inversion of absorption and magnetic circular dichroism data, allowing high-resolution absorption information to be accurately determined from fluorescence-excitation spectra. To compliment this, here, we measure and thoroughly analyze the high-resolution differential fluorescence line narrowing spectra of chlorophyll-a in trimethylamine and in 1-propanol. The results show that vibrational frequencies often change little between absorption and emission, yet large changes in line intensities are found, this effect also being strongly solvent dependent. Among other effects, the analysis in terms of four basic patterns of Duschinsky-rotation matrix elements, obtained using CAM-B3LYP calculations, predicts that a chlorophyll-a molecule excited into a specific vibrational level, may, without phase loss or energy relaxation, reemit the light over a spectral bandwidth exceeding 1,000 cm^{-1} (0.13 eV) to influence exciton-transport dynamics.

Keywords: absorption-emission asymmetry, differential fluorescence line narrowing, coherent energy redistribution, exciton transport, photosynthesis, density functional theory, Duschinsky rotation

INTRODUCTION

Chlorophyll-a (Chl-a) is the most common chlorophyllide utilized in natural photosynthesis (van Grondelle et al., 1994; Blankenship et al., 2004; Grimm et al., 2006; Laisk et al., 2009). For all processes in which this molecule is involved, including light capture, coherent and incoherent exciton transport, and charge transport, the dissipation of energy (the *reorganization energy* λ) through intramolecular nuclear relaxation is a critical process (Hush, 1958; May and Kühn, 2008). Critical for exciton transport are both the ground-state reorganization energy $λ^E$ and excited-state reorganization energy $λ^A$, which can be measured and partitioned into individual vibrational

components using modern high-resolution techniques (Rebane and Avarmaa, 1982; Avarmaa and Rebane, 1985; Jaaniso and Avarmaa, 1986; Renge et al., 1987; Sild and Haller, 1988; Gillie et al., 1989; den Hartog et al., 1998; Rätsep et al., 1998, 2009a, 2011, 2019b; Zazubovich et al., 2001; Rätsep and Freiberg, 2003; Hughes et al., 2004; Purchase and Völker, 2009; Jankowiak et al., 2011; Pieper and Freiberg, 2014; Adolphs et al., 2016; Leiger et al., 2017). For excited-state properties, hole-burning techniques are commonly applied, but there are still ambiguities in the baseline limit quantitative analysis, with fluorescence-excitation being a more robust technique provided that the contribution from the zero-phonon line (ZPL) can be determined by other means (Reimers et al., 2013; Pieper et al., 2018). For ground-state vibrations, only relatively recently has the differential fluorescence line-narrowing techniques (ΔFLN) (Rätsep and Freiberg, 2003, 2007; Rätsep et al., 2009a, 2019a) been developed to deliver similar results. These techniques provide critical vibrational data required for studies of, e.g., coherent energy transport in photosystems (Renger et al., 1996; Huo and Coker, 2010; Rivera et al., 2013; Kreisbeck et al., 2014; Müh et al., 2014; Romero et al., 2014; Malý et al., 2016; Duan et al., 2017; Ren et al., 2018; Cao et al., 2020; Tomasi and Kassal, 2020).

It is very convenient in quantum dynamics calculations of energy and/or electron transport to assume that the reorganization energy has the same value and the same distribution amongst normal modes on both the ground and excited state (Rebane, 1970). In this situation, both low-resolution and high-resolution absorption and emission spectra are symmetric, i.e., after appropriate normalization and reflection of (say) the emission spectrum about its origin, the two spectra are identical. The observed low-resolution spectra for Chl-a (Rätsep et al., 2009a), bacteriochlorophyll-a (BChl-a) (Rätsep et al., 2011), and pheophytin–a (Pheo-a) (Rätsep et al., 2019b) are significantly asymmetric. Various explanations of this could be envisaged suggestive that quantum dynamics calculations preformed assuming symmetry should give realistic results: the vibrational frequency of some key modes could be different in the ground and excited states, or the most intense lines in absorption and emission could be of the same nature, with just their intensities modulated. Nevertheless, the observation of high-resolution data showed that such scenarios do not apply: many of the intense modes in either absorption or emission are just not seen at all in the other spectrum (Rätsep et al., 2011, 2019b), suggesting the possibility of serious failure for symmetry-based quantum dynamics models for exciton transfer. As before, only through the measurement of both high-resolution absorption and emission spectra can the implications of this for quantum dynamics be made apparent. Of important note, the asymmetry is shown to be environment-dependent (Rätsep et al., 2011, 2019b), allowing, in principle, metal chelation and changes to nearby residues and solvent location to modulate transport in a protein environment.

For Chl-a, BChl-a, and Pheo-a, the lowest-energy excited state is Q_y and the next state is Q_x (Gouterman et al., 1963). For Chl-a, a critical qualitative feature contributing to absorption-emission asymmetry is that the Q_x–Q_y energy spacing is small, resulting in overlapping absorptions. Indeed, the nature of Q_x and its spectral impact had been debated for over 50 years,

with all issues being resolved in 2013 using a model involving strong resonant non-adiabatic coupling mixing the natures of the Q_x and Q_y states (Reimers et al., 2013). Non-adiabatic coupling splits the absorption intensity of the Q_x state into two separate spectral regions, the lower-energy component centered around a strongly perturbed Q_y vibrational mode in the region of the Q_y origin plus 300–1,000 cm^{-1}, with the higher-energy component placed 1,000–1,300 cm^{-1} further away. Before this assignment was established, it was hypothesized that just one of the two resolved component bands depicted Q_x, leading to two competitive assignments based upon the chosen component. Neither of the assignments could account for all observed (and calculated) data, leading to the extended debate. That strong non-adiabatic coupling dominates the spectral properties is a rather unusual situation in molecular spectroscopy. As a result, no approach based on the Born-Oppenheimer approximation (Huang Rhys factors, Herzberg-Teller couplings, etc.) can account for the observed spectra properties. In particular, the Q_x origin transition energy, as perceived by quantum-chemical calculations, pertains to a region of *minimal* absorption *between* the two observed *x*-polarized spectral peaks. Nevertheless, the naïve assignment of Q_x to one of the two observed peaks still remains common practice (Sirohiwal et al., 2020), resulting in serious overestimation of the observed Q_x–Q_y spacing.

Despite the complexity of observed absorption spectra owing to the strong Q_x–Q_y non-adiabatic interaction, a simple interpretation of the observed spectral properties is still possible (Reimers et al., 2013). Details pertaining to the location, width, and intensity of each of the two *x*-polarized absorption components can be understood in terms of one parameter: the energy difference ΔE between the Q_x and Q_y states. This is controlled by the magnesium coordination, as well as external environmental influences (Reimers et al., 2013). In gas-phase complexes, and 5-coordinate solvents and most protein environments, the *x*-polarized absorption becomes hidden underneath the strong Chl-a Franck-Condon 0–1 vibrational sideband centered at the origin plus ~1,300 cm^{-1}. However, in 6-coordinate environments, this component moves into a sparser spectral region at about half this spacing and, hence, often becomes clearly resolved.

Understanding the breakdown of the Born-Oppenheimer approximation for Chl-a is critical to any quantitative analysis pertaining to both low-resolution and high-resolution absorption spectra. It allows the observed (Avarmaa and Rebane, 1985) high-resolution fluorescence-excitation spectra to be separated into broad underlying contributions associated with Q_x, as well as high-resolution features depicting the intrinsic nature of Q_y (Reimers et al., 2013). This has led to the first quantitative high-resolution description of Q_y absorption. Details of the non-adiabatic coupling between Q_y and Q_x in chlorophyllides have also been studied recently using two-dimensional spectroscopies (Bukarte et al., 2020), revealing properties critical to function. Ultrafast relaxation of light energy absorbed with *x*-polarization to energy emitted with *y*-polarization is controlled largely by ΔE (Reimers et al., 2013).

To investigate the absorption-emission asymmetry of Chl-a in high resolution, what therefore remains is the measurement and interpretation of its high-resolution emission

spectrum. Herein, we measure and analyze the Q_y emission spectra of Chl-a using the ΔFLN technique in two different solvents: trimethylamine (TEA) and 1-propanol. The identified asymmetry in combination with low-resolution absorption-emission spectra is then interpreted based on the results of density-functional theory (DFT) simulation of the electronic and nuclear structures. A self-consistent set of spectroscopic approximations is used in both the experimental data analysis and in the interpretation of the DFT simulations.

All calculations reported in the main text are performed in the gas phase. Treatments of solvent through implicit and/or explicit methods can be very successful (Hush and Reimers, 2000; Tomasi, 2011; Mennucci, 2012; Skyner et al., 2015; Zuehlsdorff and Isborn, 2018; Caricato, 2019; Cerezo et al., 2020), but no such approach has been demonstrated as yet to be successful for understanding chlorophyll bandshapes. Indeed, results presented in **Supplementary Table 1** using commonly applied solvation treatments fail to provide qualitatively useful information, as has been previously noted for bacteriochlorophyll-a (Higashi et al., 2014). Spectra of Chl-a complexes have been recorded in the gas phase (Shafizadeh et al., 2011; Kjær et al., 2020), but as yet no high-resolution information is available. We demonstrate that use of gas-phase calculations allows for the key qualitative features that control absorption-emission asymmetry in Chl-a to be identified. In this process, a map is created that shows how the most important high-resolution vibrational lines observed in absorption-type experiments relate to those observed in emission-type experiments.

METHODS

Sample Preparation and Spectral Measurements

Chl-a powder purchased from Sigma-Aldrich was stored in the dark at $-18°C$ before dissolving in high-grade solvents of 1-propanol and TEA. Plastic (polymethyl methacrylate) cuvettes of 5 mm path length were used as sample containers. Pigment concentrations below 4×10^{-6} M were used in fluorescence measurements, providing optical densities <0.05 at the Q_y absorption maximum. This low concentration of Chl-a largely eliminated aggregation and self-absorption effects.

Absorption and fluorescence measurements were made using an experimental setup that has been previously described (Rätsep et al., 2009a, 2019a). It consists of a Andor Shamrock 0.3 m spectrograph equipped with a thermo-electrically cooled CCD camera, a highly stabilized tungsten light source, and a He bath cryostat. Selective excitation of fluorescence was performed using a model 375 dye laser of <0.5 cm^{-1} linewidth, pumped by a Spectra Physics Millennia solid state laser. The inhomogeneous spectral resolution of the measurements was 6.6 cm^{-1}.

Dipole Strength Representation of the Observed Spectra

Absorption and emission band strengths were obtained from raw observed spectra through the application of appropriate frequency scaling. Absorption spectra were scaled by ν^{-1} while

emission spectra were scaled by ν^{-3}, as absorption and emission strengths are proportional to νM^2 and $\nu^3 M^2$, respectively, where $M^2 \equiv I$ is the band strength (Einstein, 1916) and ν is the absorption frequency. As all emission spectra were recorded linearly in wavelength, the total scaling of the emission spectra used was ν^{-5}, with the additional factor of ν^{-2} required so as to preserve the integrated emission probability.

Vibrational Structure of the Spectra

In the Huang-Rhys approximation (Huang et al., 1950), the relative band strength of the 0-n_i transition delivering n_i quanta into vibrational mode i is given by the Poisson distribution

$$I_i = e^{-S_i} S_i^{n_i} / n_i! \tag{1}$$

where S_i is the Huang-Rhys factor for mode i. The relative band strength of the transitions from the zero-point level of one state to an arbitrary level $\boldsymbol{n} \equiv \{n_1, n_2, ... n_i ...\}$ of the other state compared to that of the origin line strength, I_{00}, is given by

$$\frac{I_{\boldsymbol{n}}}{I_{00}} = \prod_i \frac{S_i^{n_i}}{n_i} \tag{2}$$

which reduces to

$$\frac{I_i}{I_{00}} = S_i \tag{3}$$

for the 0–1 transition in mode i. The total Huang-Rhys factor for the electronic transition is thus given as

$$S_{vib} = \sum_i S_i = \frac{1}{I_{00}} \sum_i I_i = \frac{I_{vib}}{I_{00}} \tag{4}$$

where I_{vib} is the total band strength attributable to 0–1 transitions, and the total band strength is decomposed as

$$I_{tot} = I_{00} + I_{vib} + I_{mq} \tag{5}$$

where I_{mq} is the component attributable to multi-quanta (i.e., $\sum_i n_i > 1$) transitions. The reorganization energy distributed by each mode is given by

$$\lambda_i = h\nu_i S_i \tag{6}$$

and the total reorganization energy by.

$$\lambda = \sum_i \lambda_i. \tag{7}$$

DFT Calculations

Ground and Q_y excited-state optimized structures for Chl-a, modified with methyl replacing phytyl, are evaluated by the CAM-B3LYP (Yanai et al., 2004), MN15 (Yu et al., 2016), ωB97xD (Chai and Head-Gordon, 2008), and B3LYP (Becke, 1993) methods using Gaussian-16 (Frisch et al., 2016) with the 6-31G* basis set (Hehre et al., 1972). Replacement of phytyl with methyl is not expected to have noticeable influences on the properties of interest herein, although its replacement with H

(making a carboxylic acid) can be influential (Fiedor et al., 2003, 2008; Palm et al., 2019). Also, the choice of basis set has a small influence (Rätsep et al., 2011), but as this is much less than the effect of solvent variation, it is not pursued herein. As was already mentioned in the introduction, only gas-phase calculations are reported in the main text, but in the **Supplementary Material** results are presented using both implicit solvation, applying the polarizable-continuum model (PCM) (Tomasi et al., 2005), and/or explicit solvation. All such calculations include the D3(BJ) dispersion correction (Goerigk and Grimme, 2011).

The normal modes for both states are determined analytically and projected onto curvilinear coordinates using the DUSHIN program (Reimers, 2001). This approach expresses the geometry changes calculated by the various methods between the ground and excited states in terms of bond-length, bond-angle, and bond-torsion changes, these then being projected onto ground- and excited-state normal coordinates evaluated by Gaussian-16. The force-constant matrix after transformation to these redundant internal coordinates (Wilson et al., 1955) may optionally be scaled by factors of 0.95, 0.95, and 0.99 for the stretching, bending, and torsional motions, respectively. These factors were previously obtained by fitting the observed and CAM-B3LYP/6-31G* calculated vibrational frequencies of free-base porphyrin for all modes except the CH and NH stretches (Rätsep et al., 2011).

RESULTS AND DISCUSSION

Interpretation of Low-Resolution and High-Resolution Spectra

The observed low-resolution and high-resolution (ΔFLN) fluorescence spectra of Chl-a in solid matrices of TEA and 1-propanol at 4.5 K are shown in **Figure 1**. The low-resolution fluorescence spectra were obtained following non-resonant excitation at 407 nm and are broad; in contrast, the resonantly excited ΔFLN spectra demonstrate a clear-cut vibrational structure, demonstrating the significant advantages of this technique. According to Equation (5), the ΔFLN spectrum displays an origin band that comprises the ZPL and PSB components, with intertwined $I_{vib} + I_{mq}$ vibrational sidebands extending toward longer wavelengths. The shape of the origin band $I_{00}(\nu)$ is known to depend on the excitation wavelength, with significant variations observed even for small changes within the inhomogeneous spread of ZPL frequencies, showing enhancement of the electron-phonon coupling strength with increasing transition wavelength (Rätsep et al., 2009b; Renge et al., 2011). Comparing the low-resolution spectra obtained in different environments, one may conclude that the vibrational sideband is more intense in 1-propanol than in TEA, details of which are revealed by the ΔFLN spectra. These important variances will be in detail elaborated below.

Figure 2 shows the vibrational parts of the ΔFLN spectra, presented as a function of the frequency difference $\Delta\nu$ from the ZPL maximum. These are displayed with their identified origin band profiles $I_{00}(\nu)$ subtracted to enhance clarity in the
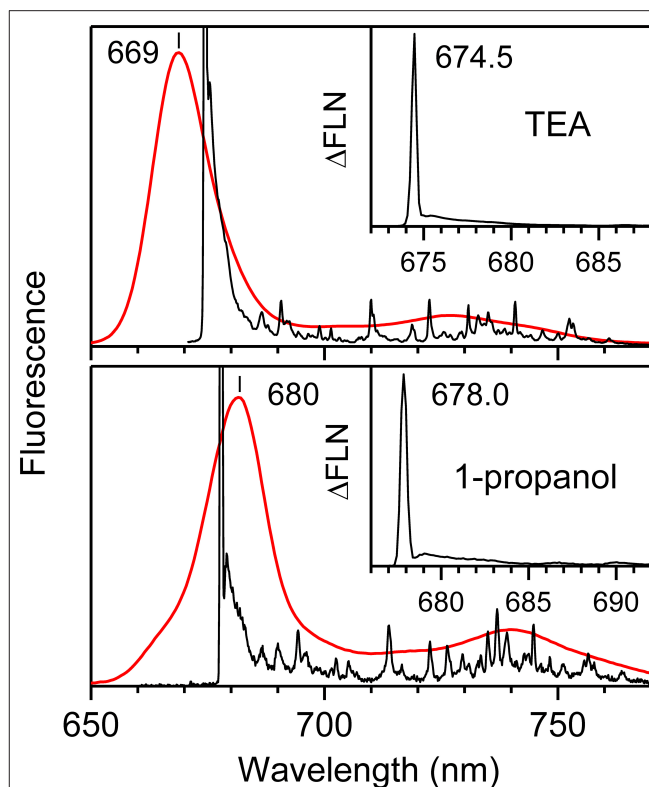
FIGURE 1 | Low-resolution (red, excited at 407 nm) and high-resolution (black) ΔFLN fluorescence spectra of Chl-a in solid solutions of TEA and 1-propanol measured at 4.5 K. The ΔFLN spectra are vertically amplified to highlight the rich vibrational sideband structure. Insets show the in-scale origin parts of the ΔFLN spectra revealing intense ZPLs and weak PSBs in the red side.

low-frequency region up to about 600 cm^{-1}. The $I_{00}(\nu)$ profiles, shown in green in the main figures and their insets, are expressed as a sum of two contributions: a Gaussian ZPL function fitted to an observed resolution of 6.6 cm^{-1} and a phonon side band (PSB) fitted to a standard form (Pajusalu et al., 2014).

In **Figure 3**, the two ΔFLN spectra are overlaid to facilitate detailed comparison: most lines appear to share common frequencies, with in only a few cases frequency shifts being apparent that are most likely associated with specific solvation effects. In contrast, it is clear that the intensity patters change significantly. Hence, vibrational frequencies are mostly insensitive to the environment, whereas the associated intensities, which depend on the details of the vibrational motions, are very sensitive.

For quantitative evaluation, the observed ΔFLN spectra were fitted with Equation (5), using a model containing 215 vibrational modes for Chl-a in 1-propanol and 296 models for Chl-a in TEA. For the spectrum in TEA, this was done using a fully automated procedure in which all frequency intervals were set to be less than the spectral resolution of the measurement, whereas for the 1-propanol spectrum, the frequencies were optimized to create a model containing the fewest-possible number of modes. These two approaches, full automation and human perceptive intuition,
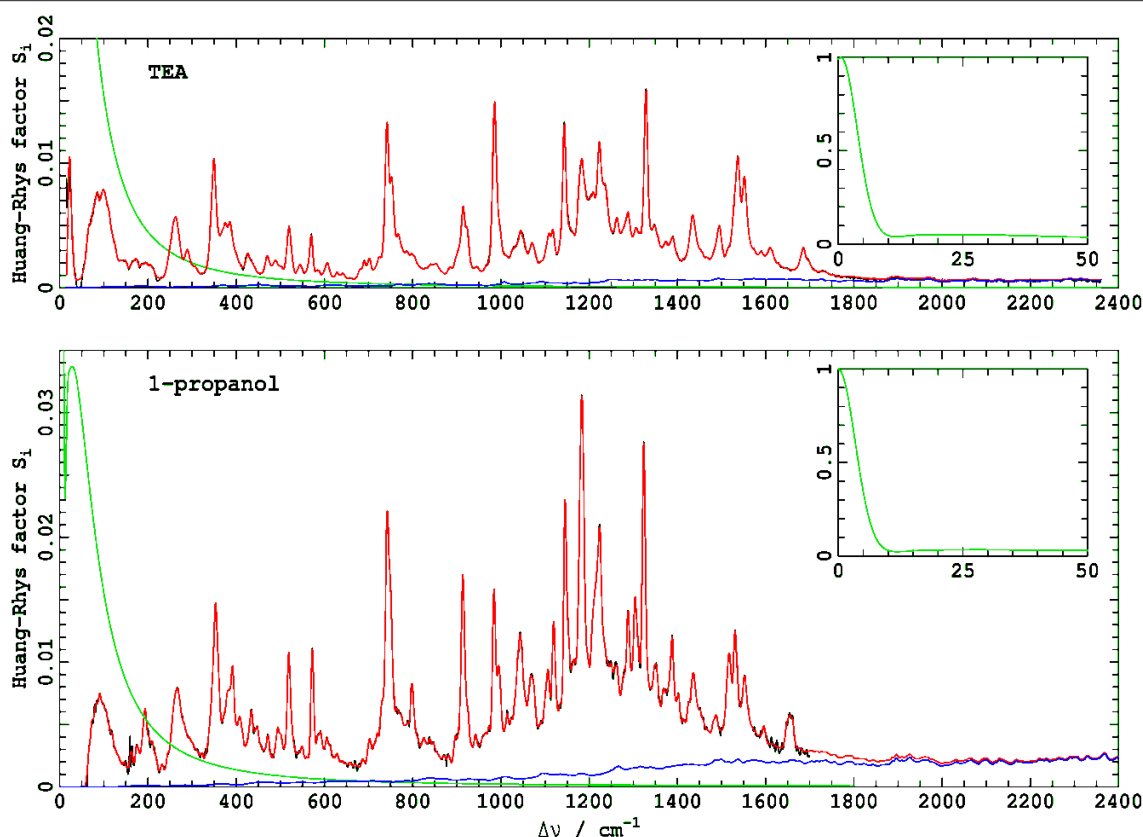
FIGURE 2 | Vibrational parts of the ΔFLN spectra of Chl-a in TEA and 1-propanol recorded at 4.5 K. The green curves, shown on a different scale in the insets, indicate origin band profiles $I_{00}(\nu)$ that are subtracted from experimental ΔFLN spectra to enhance clarity in the low-frequency region. The Huang-Rhys model fits (red) to the experimental vibrational contribution (black) was performed with the lineshape of every vibrational transition set to that observed for the 0–0 line, $I_{00}(\nu)$. Contributions to the fit arising from multi-quanta transitions are shown in blue. The spectra are normalized to give a peak height of the 0–0 line of unity, allowing the Huang-Rhys factor S_i for any non-overlapped 0–1 transition to be read off the y axis from its peak height. The $I_{00}(\nu)$ profiles (green) are expressed as a sum of two contributions: a Gaussian ZPL fitted to an observed resolution of 6.6 cm⁻¹ and a PSB fitted to a standard form (Pajusalu et al., 2014).

yield results of similar quality and usefulness. In both cases, the associated Huang-Rhys factors S_i were optimized to minimize the difference between the observed and fitted spectra. By using $I_{00}(\nu)$ as the profile for each and every vibrational line (Rebane, 1970), the fundamental and multi-quanta contributions $I_{vib}(\nu) + I_{mq}(\nu)$ were determined simultaneously during the fitting.

In **Figure 2**, the fitted spectra in red are overlaid on top of the observed spectra shown in black. That very little black color can be seen in the figures is indicative of the very high quality of the fitted results. Contributions to the spectra from multi-quanta excitations $I_{mq}(\nu)$ indicated in blue are small yet significant to the quantitative analysis. Note that, in these figures, the y-axis is labeled as "Huang-Rhys factor S_i," reflecting traditional analysis methods. If a 0-1 vibrational line is isolated from all others, then the height of the line in this presentation is its Huang-Rhys factor. However, as the shape of each line is taken to be $I_{00}(\nu)$, both presented spectra embody strong line overlap and hence interpretation of line data in this way is qualitatively indicative but not quantitatively accurate.

The obtained $\{\nu_i, S_i\}$ data sets provide a quantitative description of the observed spectra and can qualitatively be

partitioned into regions associated with resolved spectral peaks and diffuse background regions. The present data could be partitioned into 44 regions/blocks for 1-propanol and 72 regions for TEA, with each region identified with some particular resolved emission (see **Tables 1**, **2** as well as the related **Supplementary Tables 4, 5**, respectively). This partitioning was done so as to preserve the originally fitted total reorganization energy within each region, with an effective Huang-Rhys factor determined to suit. This results in reduced region-based data sets $\{\nu_j, S_j\}$ defined with

$$\lambda_j = \sum_i^{\text{region } j} \lambda_i, \quad S_j = \frac{1}{\nu_{max,j}} \lambda_j, \qquad (8)$$

where $\nu_{max,j}$ is the frequency of the identified peak in region j. In this way, the background signal, which provides a substantial fraction to the whole, is accumulated to its embodied ΔFLN peak. The resulting description, therefore, achieves simplicity whilst retaining key features required in, e.g., quantum simulations of exciton transport. Further similar simplifications retaining just
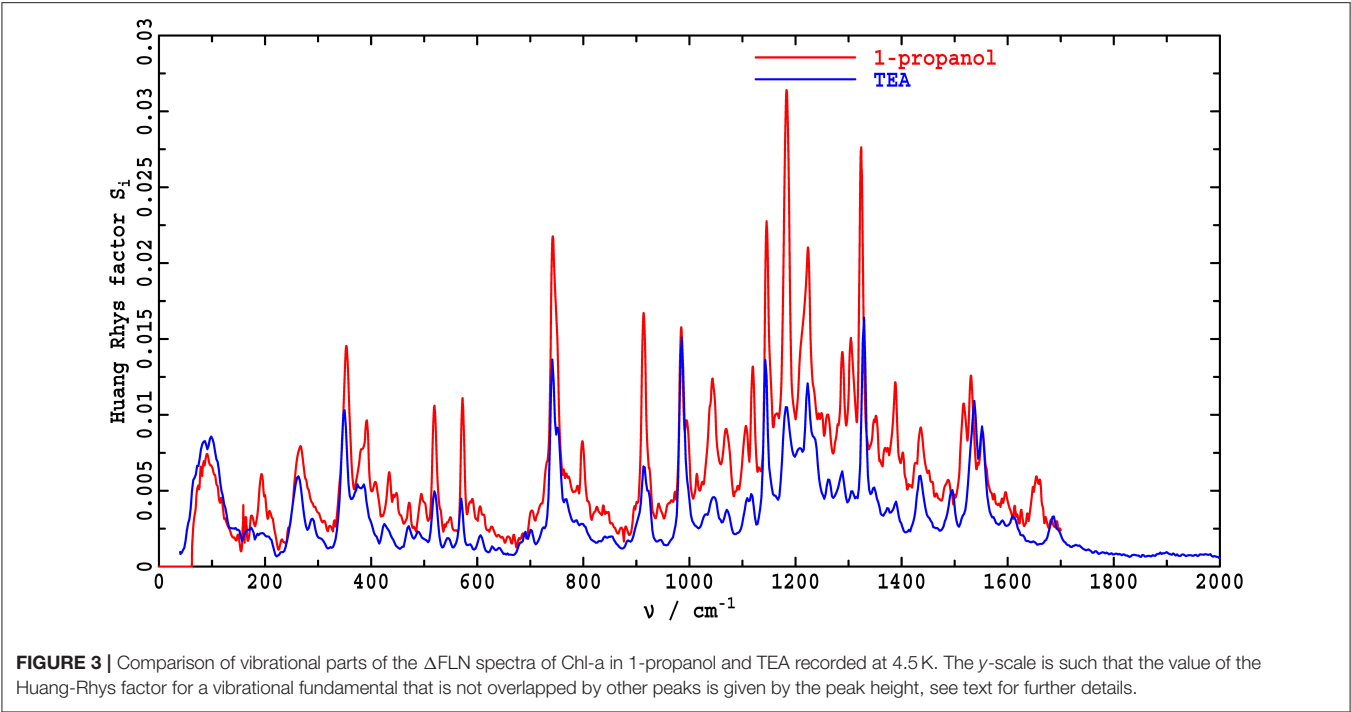
FIGURE 3 | Comparison of vibrational parts of the ΔFLN spectra of Chl-a in 1-propanol and TEA recorded at 4.5 K. The *y*-scale is such that the value of the Huang-Rhys factor for a vibrational fundamental that is not overlapped by other peaks is given by the peak height, see text for further details.

TABLE 1 | Resolved component regions *j* fitted according to Equation (8) in **Supplementary Table 5** to the observed ΔFLN spectrum of Chl-a in 1-propanol at 4.5 K, depicting the component peak frequencies ν_j (cm^{-1}), the range of individual frequencies included in each region (cm^{-1}), the net emission reorganization energy λ_j^E (cm^{-1}) for each region, and the effective emission Huang-Rhys factor S_j^E required to reproduce this.

ν_j	Range	1,000 S_j^E	λ_j^E	ν_j	Range	1,000 S_j^E	λ_j^E
92[a]	66–151	41.2	3.8	985	958–1,008	31.7	31.2
194	157–210	16.5	3.2	1,016	1,015	3.0	3.0
267	218–315	33.1	8.8	1,043	1,023–1,049	23.8	24.8
353	322–366	30.6	10.8	1,064	1,055–1,080	16.5	17.5
380	372–379	7.1	2.7	1,107	1,086–1,107	11.5	12.7
392	385–392	11.1	4.3	1,120	1,113–1,135	16.3	18.3
408	400–414	7.0	2.9	1,146	1,145–1,167	36.3	41.6
434	422–435	5.9	2.6	1,183	1,174–1,192	46.8	55.4
448	442–456	5.2	2.3	1,224	1,198–1,250	55.9	68.5
472	463–479	3.3	1.6	1,261	1,258–1,271	7.8	9.9
495	487–502	6.0	3.0	1,288	1,277–1,289	13.5	17.5
519	510–541	14.3	7.4	1,306	1,296–1,311	18.1	23.6
549	549–560	2.2	1.2	1,324	1,317–1,339	29.5	39.1
573	573–584	11.8	6.8	1,352	1,347–1,359	8.5	11.5
591	592	2.5	1.5	1,374	1,368–1,381	7.4	10.1
606	599–613	4.3	2.6	1,388	1,388–1,395	8.6	12.0
664	620–697	5.7	3.8	1,402	1,403	2.8	4.0
703	703	2.2	1.6	1,436	1,414–1,465	15.7	22.6
743	712–755	47.7	35.5	1,488	1,471–1,495	3.8	5.6
763	763–775	8.0	6.1	1,517	1,502–1,521	12.0	18.3
798	782–805	11.2	8.9	1,531	1,525–1,536	11.4	17.5
838	810–882	8.4	7.1	1,552	1,542–1,585	11.0	17.0
914	903–933	27.5	25.1	1,596	1,596	1.2	1.9
942	942–951	2.7	2.6	1,654	1,648–1,661	6.3	10.4
Total						715	650

[a]*It is unclear as to whether all or part of this emission should be attributed to intramolecular vibrations, as reported in this table and elsewhere, or else to intermolecular phonons.*

TABLE 2 | Resolved component regions *j* fitted according to Equation (8) in **Supplementary Table 6** to the observed ΔFLN spectrum of Chl-a in TEA at 4.5 K, depicting the component peak frequencies ν_j (cm^{-1}), the range of individual frequencies included in each region (cm^{-1}), the net emission reorganization energy λ_j^E (cm^{-1}) for each region, and the effective emission Huang-Rhys factor S_j^E required to reproduce this.

ν_j	Range	1,000 S_j^E	λ_j^E	ν_j	Range	1,000 S_j^E	λ_j^E
22	10–41	13.1	0.3	1,032	1,018–1,036	2.8	2.9
66	41–87	20.1	1.3	1,046	1,036–1,060	6.2	6.5
99	87–115	20.3	2.0	1,071	1,060–1,090	4.5	4.8
123	115–155	4.2	0.5	1,109	1,090–1,113	4.8	5.4
174	155–190	3.3	0.6	1,117	1,113–1,127	4.2	4.7
206	190–220	2.4	0.5	1,144	1,127–1,150	15.9	18.2
263	220–280	14.6	3.8	1,157	1,150–1,170	6.3	7.3
289	280–312	4.5	1.3	1,183	1,170–1,192	15.2	18.0
330	312–335	1.1	0.4	1,209	1,192–1,213	14.0	16.9
349	335–362	17.3	6.0	1,223	1,213–1,229	13.6	16.6
375	362–380	7.0	2.6	1,236	1,229–1,242	7.5	9.3
386	380–412	6.7	2.6	1,263	1,242–1,272	5.9	7.5
425	412–432	1.6	0.7	1,275	1,272–1,283	2.9	3.7
436	432–458	1.0	0.5	1,288	1,283–1,301	5.7	7.4
471	458–477	2.2	1.1	1,306	1,301–1,311	2.7	3.6
489	477–500	3.1	1.5	1,315	1,311–1,320	2.0	2.7
520	500–530	7.0	3.6	1,329	1,320–1,335	17.0	22.5
545	530–558	1.5	0.8	1,342	1,335–1,347	3.1	4.1
570	558–575	4.2	2.4	1,354	1,347–1,367	2.7	3.7
587	575–593	0.8	0.5	1,374	1,367–1,378	1.6	2.3
606	593–612	1.6	0.9	1,390	1,378–1,419	4.0	5.6
628	612–632	0.7	0.4	1,435	1,419–1,460	10.6	15.2
642	632–648	0.6	0.4	1,467	1,460–1,472	0.8	1.1
691	648–695	3.5	2.4	1,478	1,472–1,485	1.1	1.7
702	695–718	3.3	2.3	1,495	1,485–1,502	5.1	7.7
725	718–730	2.2	1.6	1,507	1,502–1,513	1.4	2.2
742	730–745	16.2	12.0	1,519	1,513–1,525	2.9	4.5
752	745–756	8.5	6.4	1,537	1,525–1,542	14.2	21.8
767	756–775	5.0	3.8	1,552	1,542–1,557	9.9	15.4
798	775–803	3.2	2.6	1,562	1,557–1,579	2.7	4.2
811	803–820	0.6	0.5	1,590	1,579–1,597	0.9	1.4
854	820–860	2.4	2.0	1,610	1,597–1,634	2.7	4.4
885	860–890	1.7	1.5	1,649	1,634–1,667	0.1	0.1
915	890–930	14.2	12.9	1,686	1,667–1,693	3.4	5.7
946	930–955	1.2	1.1	1,698	1,693–1,705	1.2	2.0
986	955–1018	25.3	24.9	1,710	1,705–1,723	0.2	0.3
Total						426	370

a few critical modes may be required to enhance computational efficiency in such applications.

From the fits, the total Huang-Rhys factors S_{vib} are determined to be 0.72 in 1-propanol and 0.43 in TEA. Similarly, the total emission reorganization energies λ^E are determined to be 650 cm^{-1} and 370 cm^{-1}, respectively; these and other deduced reorganization energies are collected into **Table 3**.

Fluorescence spectra at low resolution can be predicted based on the ΔFLN data analysis by broadening the spectra from the Huang-Rhys model to match that apparent in experimental low-resolution spectra. Results so obtained are indicated by red dashed lines in **Figure 4**, where they are compared to directly observed low-resolution emission spectra (red solid lines, denoted as EMI). In TEA, the observed and simulated low-resolution spectra are in reasonable agreement, validating the extensive experimental and computational procedures used in obtaining and interpreting the high-resolution ΔFLN data. From low-resolution spectra, the absorption and emission reorganization energies can be

TABLE 3 | Calculated (for methyl Chl-a) and observed (for Chl-a) reorganization energies (in cm^{-1}) for *y*-polarized Franck-Condon allowed Q_y absorption (λ^A) and emission (λ^E), compared to analogous results for Pheo-a (Rätsep et al., 2019b) and BChl-a (Rätsep et al., 2011).

Method	Mg Coord.	Pheo-a		BChl-a		Chl-a	
		λ^A	λ^E	λ^A	λ^E	λ^A	λ^E
Obs.[j1] 4.5 K TEA ΔFLN and SEF	-	317	395				
Obs.[j1] low res. 4.5 K TEA	-	355	402				
Obs.[j2] 1.7 K EtOH/MeOH low res. MCD	-	424					
Obs.[j3] 4 K TEA ΔFLN	6				219		
Obs.[j3,j4] 5 K HB	5			378			
Obs.[j3] 295 K TEA	5			335	185		
Obs.[j3] 4.5 K TEA low res.	6			196	236		
Obs.[j3] 4.5 K TEA low res.	- 5	-	-	335	260		
Obs. 5 K TEA, low res.	5					~300[h]	458
Obs. 5 K TEA, ΔFLN	5						370
Obs. 295 K TEA, low res.	5						413
Obs.[j2] 4 K wet ether FE	5[f]					262[e]	
Obs. 295 K wet ether, low res.	5					264[i]	438
Obs.[j5] 4 K 1-propanol ΔFLN	6						650
Obs.[j2] 4 K 1-propanol low res.	6					~420[b]	~650[a]
Obs.[j5] 295 K 1-propanol low res.	5					~490[c]	492
Obs.[j2,j6] PS-I-200 HB	5					547[g]	
Obs.[j2,j7] WSCP HB	5					645[g]	
CAM-B3LYP/6-31G* from calc. energies	4	1,214[d,j1]	481[j1]	350[j3]	210[j3]	607[j2]	517[j2]
CAM-B3LYP/6-31G* from scaled frequencies	4			300[j3]	200[j3]	567	492
B3LYP/6-31G* from calc. energies	4	184[j1]	165[j1]	130[j3]	150[j3]	243	245
MN15/6-31G* from calc. energies	4	493[j1]	282[j1]	184	167	390	358
ωB97XD/6-31G* from calc. energies	4	1,609[d,j1]	594[j1]	310[j3]	1,140[j3]	713	606

[a] *Observed spectrum (Rätsep et al., 2009a) is deconvoluted (see **Figure 5**) into two bands representing the dominant 6-coordinate species (85%) and a secondary 5-coordinate one using the spectral bandshape from ΔFLN, indicating that the ΔFLN results accurately depict traditional low-resolution data.*

[b] *Observed absorption and MCD spectra are fitted to a model depicting 85% 6-coordinate species, scaling the bandshape observed in wet ether by FE (see **Figure 6**) (Reimers et al., 2013).*

[c] *Very crude estimate for the 5-coordinate species assuming that the x polarized absorption commences is located 1,000 cm^{-1} above Q_x origin and has the same intensity as that observed for the 6-coordinate species.*

[d] *One poorly represented mode depicting aromaticity in Q_y involving interactions with nitrogen lone-pair orbitals; neglecting this results become CAM-B3LYP 465 cm^{-1}, ωB97XD 475 cm^{-1}.*

[e] *After removal of Q_x using full-quantum spectral simulations (Reimers et al., 2013).*

[f] *Ligand is water (Reimers et al., 2014).*

[g] *From hole-burning (HB) data, but qualitatively unreliable owing to baseline uncertainties (Reimers et al., 2013).*

[h] *After approximate removal of Q_x band using the bandshape deduced in wet ether (Reimers et al., 2013).*

[i] *From analytical inversion (Reimers and Krausz, 2014) of absorption and MCD data (Umetsu et al., 1999).*

[j] *References: 1- (Rätsep et al., 2019b), 2- (Reimers et al., 2013), 3- (Rätsep et al., 2011), 4- (Zazubovich et al., 2001), 5- (Rätsep et al., 2009a), 6- (Gillie et al., 1989), 7- (Hughes et al., 2010).*

determined using

$$\lambda^A = h \frac{\int_0^\infty A(\nu)d\nu}{\int_0^\infty A(\nu)/\nu d\nu} - h\nu_{00},$$

$$\lambda^E = h\nu_{00} - h \frac{\int_0^\infty E(\nu)/\nu^2 d\nu}{\int_0^\infty E(\nu)/\nu^3 d\nu}, \quad (9)$$

respectively, where $A(\nu)$ is the observed absorption coefficient and $E(\nu)$ the observed emission intensity. Note that, as emission intensities are sensitive to the spectral scan rate, $E(\nu)$ corresponds to the emission observed when the spectrum is scanned at a constant rate of change of frequency; spectra $E(\lambda)$ scanned at a constant rate of change of wavelength $\lambda = c/\nu$ are related via $E(\nu) = E(\lambda)/\nu^2$. For TEA,

taking ν_{00} to be the frequency of the broad ZPL maximum, this gives $\lambda^E = 458$ cm^{-1}, larger than the ΔFLN value of 370 cm^{-1}.

Much larger differences are seen in **Figure 4** for the analogous comparison of low-resolution spectra obtained by broadening the ΔFLN spectrum and from direct observation of emission in 1-propanol. A plausible explanation of the difference is that some Chl-a molecules have 5-coordinate Mg atoms, even at the low temperatures used; the ΔFLN spectra select only for the major (6-coordinate) component, whereas the EMI spectrum captures all emission. In **Figure 5**, the observed low-resolution emission spectrum is approximately separated into 5-coordinate (15%) and 6-coordinate (85%) components, yielding a 6-coordinate reorganization energy of ~650 cm^{-1}, in good agreement with the value obtained for the pure 6-coordinate species using ΔFLN.
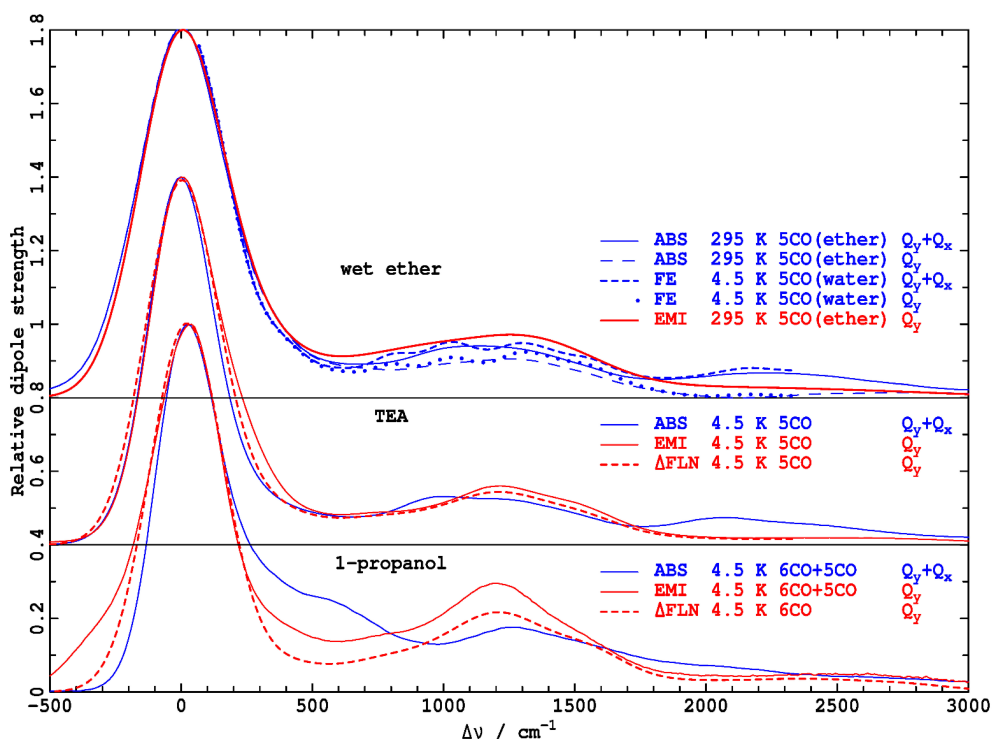
FIGURE 4 | Absorption dipole strengths $A(\nu - \nu_{\max})/\nu$, blue, and reflected emission dipole strengths $E(-\nu + \nu_{\max})/\nu^3$, red, for Chl-a in solvents with varying Mg coordination (CO), as determined by: ABS- absorption spectroscopy (in ether (Umetsu et al., 1999), TEA, and 1-propanol), perhaps in combination with analytical MCD data inversion (Reimers and Krausz, 2014) to extract the Q_y component, FE- broadened high-resolution fluorescence excitation (Avarmaa and Rebane, 1985), perhaps after subtraction of the Q_y component obtained during full-quantum spectral simulation (Reimers et al., 2013), EMI- emission spectroscopy (in ether (Reimers et al., 2014), TEA, and 1-propanol), ΔFLN- broadened delta fluorescence line narrowing data (in TEA and 1-propanol).

Analogous data pertaining to the Q_y absorption spectrum of Chl-a is difficult to obtain owing to interference from the Q_x band. High-resolution fluorescence excitation (FE) spectra of Chl-a have been measured by Avarmaa and Rebane (1985), and subsequently the doubly-peaked *x*-polarized intensity was subtracted using an extensive quantum-mechanical non-adiabatic coupling model, combined with a Huang-Rhys analysis of the observed vibrational structure (Reimers et al., 2013). The resulting Q_y vibrational frequencies and Huang-Rhys factors are reproduced in **Supplementary Table 6**. The solvent used by Avarmaa and Rebane is best characterized as wet ether (Reimers et al., 2014), with, at the low temperatures used, water coordinating the chlorophyll Mg atom. The original observed FE spectrum, as well as that after subtraction of Q_x, both after broadening to match low-resolution (Umetsu et al., 1999) absorption spectra observed in ether at room temperature, are shown in **Figure 4**. In an alternate approach, the Q_x component of the room-temperature absorption (ABS) spectrum has been subtracted using an analytical technique for the inversion of observed absorption and magnetic circular dichroism (MCD) data (Reimers and Krausz, 2014). The total absorption and resulting Q_y-component spectrum are also shown in the figure.

As seen, the full absorption spectrum is in good agreement with that obtained by broadening the observed FE spectrum, and the two Q_y-only components are also in good agreement. Both approaches lead to the conclusion that the absorption

reorganization energy is $\lambda^A = 262$ cm^{-1}, much less than the emission reorganization energy determined from the low-resolution room-temperature spectrum in ether, $\lambda^E = 438$ cm^{-1}. This is visually very apparent from the absorption and fluorescence spectra compared in **Figure 4**.

Similar accurate descriptions of the Q_y absorption in 1-propanol and TEA are not available. Yet rough estimates can be made by partitioning *x* and *y* polarization, assuming that the Q_x band profile is not solvent dependent, and, for 1-propanol, as in **Figure 5**, that the Q_y absorption bandshape of the 5-coordinate species is the same as that for the 6-coordinate one. Results for the separation of the two species in 1-propanol at 4 K are shown in **Figure 6**. They provide rough estimates of absorption reorganization energy of $\lambda^A = 420$ cm^{-1} for the 6-coordinate species and 490 cm^{-1} for the 5-coordinate one. As for ether, absorption reorganization energies appear to be much less than those in emission.

Relating the Observed High-Resolution Absorption and Emission Properties Based Upon DFT Calculations of the Duschinsky Matrix

From **Figure 3**, as well as **Tables 1**, **2**, and **S6**, it is clear that the vibrational frequencies in different solvents and in the S_0 ground state and Q_y excited states are quite similar, yet the vibrational
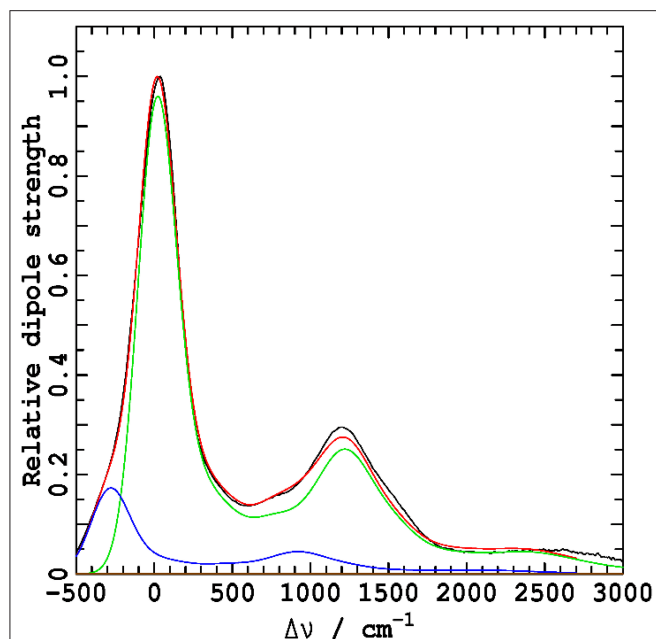
FIGURE 5 | The observed emission spectrum of Chl-a in 1-propanol at 4.5 K (black, the EMI spectrum from **Figure 4**) is interpreted in terms of contributions from molecules with 6-coordinate Mg (green, 85%) and 5-coordinated Mg (blue, 15%). The 6-coordinate component bandshape is taken to be that as observed by ΔFLN, broadened with a Gaussian inhomogeneous distribution function fitted with FWHM = 280 cm^{-1} (taken from **Figure 4**). The 5-coordinate component bandshape is crudely taken to be the same as that for the 6-coordinate species. In this way, the fit is done using only three adjustable parameters: the relative component composition, the component ZPL frequency difference, and the FWHM. The sum of the two contributions is shown in red and closely approximates the observed emission.
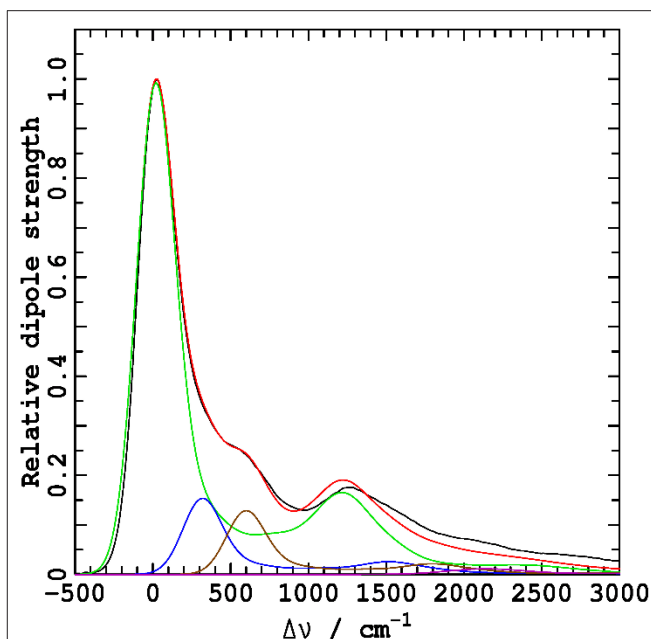

FIGURE 6 | Separation of the observed (Rätsep et al., 2009a) absorption spectrum $A(\nu)$ of Chl-a in 1-propanol at 4.5 K, frequency-weighted as $A(\nu)/\nu$ to reveal the dipole strength (black), into two *y*-polarized components arising from molecules with 6-coordinate magnesium (green, 85%) and 5-coordinate magnesium (blue, 15%, 295 cm^{-1} higher in energy), and the *x*-polarized intensity (blue, the result of strong non-adiabatic coupling between vibrational lines of Q_y and the Q_x origin), using for it the spectral profile extracted from MCD data in wet ether (Reimers et al., 2013). The two absorption bandshape profiles are assumed to be the same and are set to that depicted by the bandshape for Chl-a in wet ether at 4.2 K determined from FE (**Supplementary Table 3**), located and scaled to fit the observed absorption (red).

intensities (Huang-Rhys factors) and associated reorganization energies can show large differences. Vibrational motions in the two states are clearly similar, but small differences can have profound effects. For example, two (or more) modes of very similar frequencies can mix strongly with each other as a function of small environmentally introduced changes in their frequency differences, moving in and out of resonance. Alternatively, one mode can retain its basic form in the other state yet mix very slightly with a large number of modes that span a wide frequency range. While the mixing with any one mode remains small, the effects of mixing with many modes can reinforce each other to manifest profound consequences. To quantify this, the required tool is the Duschinsky rotation matrix

$$\mathbf{D} = \left(\mathbf{C}^{\mathbf{S_0}}\right)^T \mathbf{C}^{\mathbf{Q_y}} \tag{10}$$

where $\mathbf{C}^{\mathbf{S_0}}$ are the normal modes of vibration of the ground state and $\mathbf{C}^{\mathbf{Q_y}}$ are those for the excited state. These normal-mode matrices are expressed in terms of mass-weighted Cartesian coordinates. Duschinsky matrices can also be used to understand how the normal modes of vibration respond to other changes, e.g., solvent changes. Unfortunately, the Duschinsky matrix contains n^2 elements, where n is the number of

vibrational modes, for which little direct evidence is provided by experimental measurements, as most observed properties depend on combinations of multiple Duschinsky-matrix elements.

Following the success with similar studies on BChl-a (Rätsep et al., 2011) and Pheo-a (Rätsep et al., 2019b), we turn to DFT calculations of **D** to relate the vibrational motions of the S_0 and Q_y states of Chl-a. To be useful, such calculations must first describe adequately the Huang-Rhys factors pertinent to absorption and emission. Unfortunately, previous experience with chlorophyllide spectral modeling has indicated that different possible density-functional approaches, as well as alternative *ab initio* or semi-empirical methods, can lead to errors in predicted reorganization energies by an order of magnitude or much more, as well as predicted absorption and/or emission profiles that do not resemble those observed (Rätsep et al., 2011, 2019b). To find a suitable computational method, we sampled four DFT approaches–CAM-B3LYP (Yanai et al., 2004; Kobayashi and Amos, 2006), B3LYP (Becke, 1993), MN15 (Yu et al., 2016), and ωB97XD (Chai and Head-Gordon, 2008)–as these have previously offered results of interest.

The observed and calculated emission and absorption reorganization energies for Chl-a are compared in **Table 3**, along
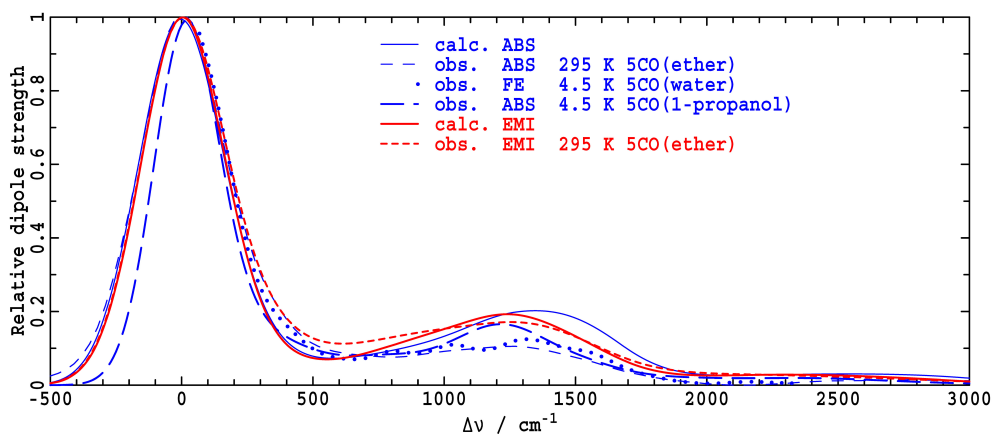
FIGURE 7 | Low-resolution Q_y gas-phase spectra calculated from the CAM-B3LYP vibrational frequencies and displacements for absorption (ABS or FE), $A(\nu - \nu_{max})/\nu$, and reflected emission (EMI), $E(-\nu + \nu_{max})/\nu^3$, are compared to those deduced from experimental data for 5-coordinate species. For the absorption spectra, the coordinating ligand is either ether (see **Figure 4**), water from wet-ether solution (see **Figure 4**), or 1-propanol (**Figure 6**), with ether being the ligand for the emission spectrum (see **Figure 4**).

with those for Pheo-a and BChl-a. CAM-B3LYP was previously identified (Rätsep et al., 2011, 2019b) as the best choice for BChl-a and Pheo-a, and this remains the case for Chl-a too. It is a hybrid functional with asymptotic potential correction, a type of method identified as the entry level for spectroscopic calculations on aromatic molecules (Cai et al., 2006) (as is ωB97xD, but ωB97xD is prone to larger errors). Using B3LYP, low chlorophyllide reorganization energies similar to the experiment have been predicted, but the associated spectral profiles have had no relationship to those observed. MN15 appears to be a method of interest and the only identified alternative to CAM-B3LYP. Yet CAM-B3LYP and MN15 both showed serious failures for a single, though different, mode in absorption for Pheo-a (Rätsep et al., 2019b). Hence, we see that just because a method usefully describes most vibrations of interest, it does not mean that all such vibrations are reliably defined. For CAM-B3LYP, the poorly described mode depicts aromaticity in the Q_y state and is affected by non-adiabatic coupling to nitrogen (n,π^*) states that only exist in pheophytins, so the error is not relevant to Chl-a.

That the CAM-B3LYP results present a useful starting point for understanding the observed high-resolution data that is demonstrated in **Figure 7**, where low-resolution simulated absorption and emission spectra are compared to observed results. The calculated gas-phase emission spectrum closely resembles the shown observed emission in ether at 295 K, with the differences being less than the observed changes presented in **Figure 4** as a function of solvent. The calculated gas-phase absorption spectrum depicts a 0–1 vibrational sideband in the 800–1,600 cm^{-1} region that is significantly enhanced compared to the shown observed spectra taken in ether, and somewhat enhanced compared to the observed spectrum (taken from **Figure 6**) in 1-propanol. Such enhancements are expected based on the overestimation of the absorption reorganization energy reported in **Table 3**. Of note, however, is that this effect is not mode specific and

hence a qualitatively indicative depiction of the high-resolution information is expected.

The computational method chosen must also accurately represent the vibrational frequencies of Chl-a. In applying CAM-B3LYP results to interpret chlorophyllide spectra, it is common to rescale the force constants as a crude correction for anharmonicity (Rätsep et al., 2011, 2019b), which slightly reduces the calculated reorganization energies, to make them closer to those observed (**Table 3**). Analogously scaled CAM-B3LYP/6-31G* values are known to reproduce the observed high-resolution data for 90 vibrations of porphyrin to within a root-mean-square error of 22 cm^{-1} (Rätsep et al., 2019b), and hence are expected to be reliable also for Chl-a.

Table 4 presents the high-resolution results from the CAM-B3LYP calculations in terms of modes of Q_y predicted to dominate absorption, modes of the ground state predicted to dominate emission, and the critical Duschinsky matrix elements that interconnect them. Some key modes in one state may be directly mapped onto key modes in the other state, the simple situation that gives rise to absorption-emission asymmetry, but other key modes are extremely mixed and have no clear assignment, leading to the absence of absorption-emission asymmetry. In the table, 30 of the 37 observed modes listed for absorption and/or emission are assigned to calculated modes based on proximity and reorganization energy. This mapping includes the most important modes either observed or calculated in both absorption and emission. It is thus likely that the analysis captures the essential qualitative elements of the intrinsic relationships, without addressing important quantitative subtleties such as the observed dependence of emission on solvent and coordination. Indeed, most observed modes in emission are related to those in absorption by this procedure.

How the Duschinsky matrix elements control absorption/emission asymmetry is shown in **Figure 8**. In

TABLE 4 | Tentative relationships between observed Chl-a Q_y vibrational modes (Reimers et al., 2013) from fluorescence excitation (Avarmaa and Rebane, 1985) in wet (Reimers et al., 2014) ether at 4.2 K and observed S_0 modes from FLN in 1-propanol or TEA at 4.5 K, see **Tables 1**, **2**.

^1Q_y FE wet ether		^1Q_y calc.		^1Q_y assignment in terms of S_0 modes	S_0 calc.		S_0 ΔFLN TEA		S_0 ΔFLN 1-propanol	
ν_i	λ_i	ν_i	λ_i		ν_i	λ_i	ν_i	λ_i	ν_i	λ_i
–	-						22	0.3	-	-
		64	16	42% 64, 28% 41, 19% 54	41, 64	12				
110	1	96,99	7	100% 93, 89% 99	93,99	7	99	2	92[b]	4[b]
190	1	155	5	98% 154	154	5	170–210	1	194	3
263	2	241,263	3	96% 244, 95% 267	244,267	3	263	4	267	9
344	3	343	4	98% 345	345	2	349	6	353	11
370–390	3	375,385	4	95% 388, 82% 391	388,391	3	370–390	5	370–390	7
435–470	1	464	2	75% 470	470	2	430–450	1	430–450	5
		494	2	81% 501	501	3				
515	0.3	505	3	75% 513	513	1	520	4	519	7
563	3	589	2	99% 593	593	2	570	2	573	7
739	11	731,735	20	60% 737, 51% 749, 35% 739	737,739	16	742	12	745	36
788	3	837	4	87% 839	839	2	798	3	798	9
925	3	917	7	39% 895, 24% 897	895,897	15	915	13	914	25
966	23	977,979	36	87% 977, 45% 986	977	40	986	25	985	31
1,034	6						1,046	7	1,043	25[c]
1,070	8	1,084, 1,092	8	91% 1093	1,093	1	1,071	5	1,064	18[c]
1,107	4	1,110	2	50% 1,110, 17% 1,102, 18% 1,122	1,102, 1,122	3	1,109	5	1,107	13[c]
1,132	5	1,131	15	70% 1,131, 18% 1,149	1,131	10	1,117	5	1,120	18
					1,149[a]	12	1,144	18	1,146	42
1,165	8	1,159	14	37% 1167	1,167	12	1,183	18	1,183	55
1,196	5	1,193	9	38% 1,184, 5% 1,192	1,192	5	1,209	17		
		1,212	5	33% 1,221, 60% 1,211	1,211	26	1,236	9		
1,228	15	1,224	47	23% 1,211, 60% 1,221	1,221	35	1,223	17	1,224	69
1,253	18	1,260	15	89% 1262	1,262	11	1,263	8	1,261	10
1,286	16	1,285, 1,287, 1,288	13	86% 1,283, 82% 1,286, 60% 1,287	1,286, 1,287, 1,288	9	1,288	7	1,288	18
		1,306	6	26% 1,288, 16% 1,312, 17% 1348	1,288[a]	3				
		1,323	10	46% 1324, 20% 1338, 11% 1331	1,324	17	1,306	4	1,306	24
		1,329	12	31% 1,321, 27% 11,348, 15% 1,338	1,321[a]	37	1,329	23	1,324	39
1,332	18	1,332	17	56% 1,331, 16% 1,321, 11% 1,338	1,331	0				
					1,338[a]	4	1,354	4	1,352	12
1,369	10	1,364	4	44% 1,366, 12% 1,380, 13% 1,388	1,366	2	1,374	2	1,374	10
1,393	7	1,392	7	22% 1,396, 17% 1,380, 14% 1,384	1,396	5	1,390	6	1,388	12
1,415	6	1,423	10	31% 1,458, 18% 1,441						
		1,424	5	48% 1,422, 25% 1,441	1,422	5				
					1,441	5	1,435	15	1,436	23
		1,459	0	57% 1,465	1,458	5	1,467	1	1,488	6
1,446	8	1,466	3	45% 1,470, 13% 1,522	1,470	0				
1,510[d]	18	1,501	15	55% 1,481,1,486	1,481, 1,486	24	1,519	5	1,517	18
1,530	9	1,530	66	46% 1,538, 24% 1,590	1,538	26	1,537	22	1,531	18
1,587	11	1,570	42	24% 1,562, 17% 1,568	1,568	11	1,552	15	1,552	17
		1,595	29	54% 1,617, 19% 1,590	1,617	8	1,686	6	1,654	10
1,665	4	1,608	3	45% 1,590, 24% 1,617	1,590	11	1,610	4	1,596	2
	188		415	Total, listed modes		355		301		500
	262		567	Total, all modes		492		370		650

These are obtained by assigning the observed lines to modes calculated for methyl Chl-a using CAM-B3LYP and the calculated Duschinsky matrix elements to map the calculated modes of Q_y onto those of S_0.

[a] No clear assignment, distributed over many Q_y modes.

[b] It is unclear as to whether all or part of this emission should be attributed to intramolecular vibrations, as reported in this table and elsewhere, or else to intermolecular phonons; modes of lower frequency are not easily identifiable in spectra.

[c] No plausible assignment.

[d] Broad band, originally listed at 1,493 cm^{-1} but the peak in this region is at 1,510 cm^{-1}.

FIGURE 8 | The origin of 20 significant Q_y normal modes of Chl-a from CAM-B3LYP/6-31G* calculations in terms of the S_0 normal modes (blue), as well as the fractional contribution of each ground-state mode to the excited-state absorption displacement δ_i^A to control its Huang-Rhys factor (red); see Equation (10).
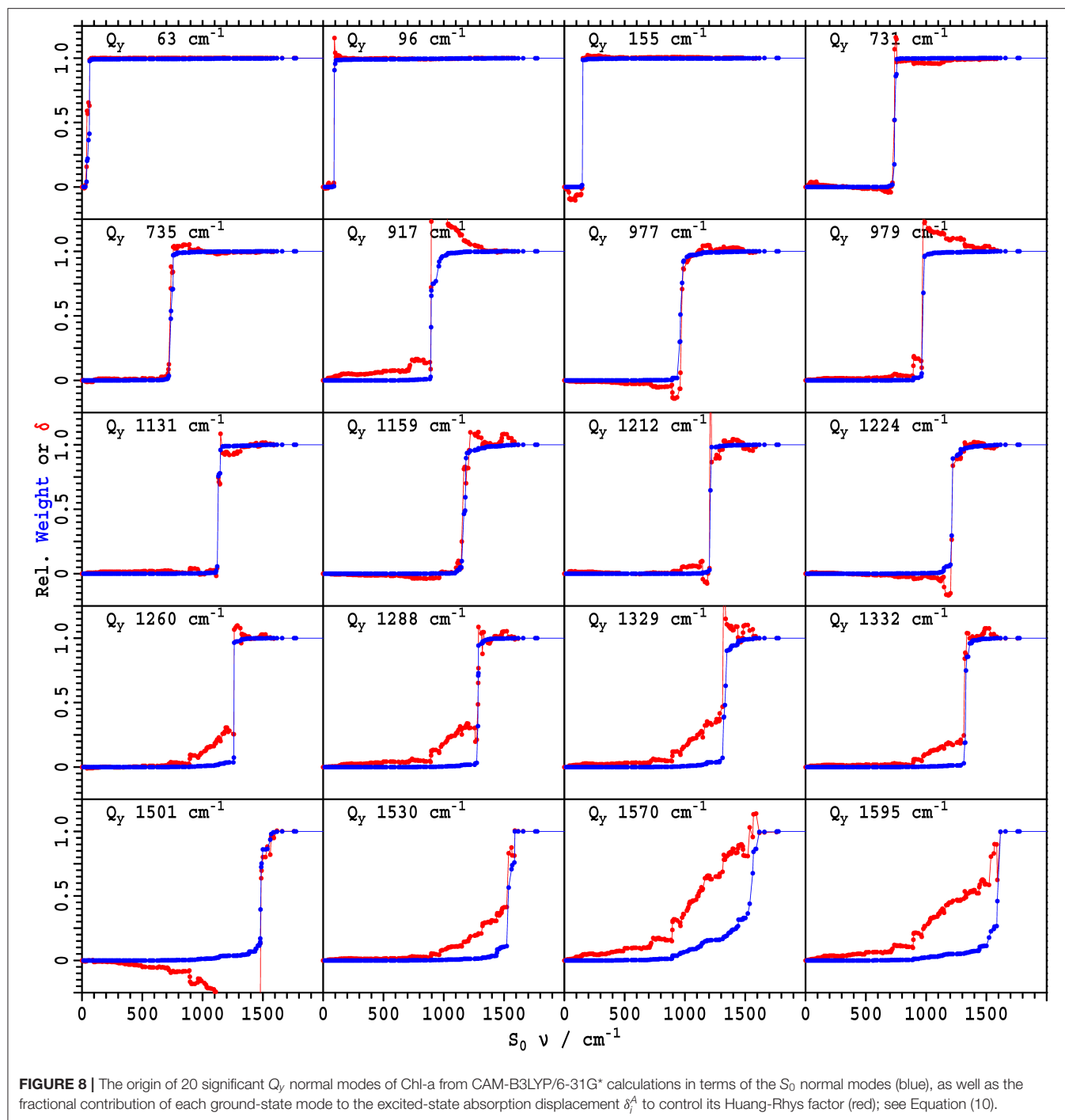
this figure, for 20 vibrational modes of Q_y, the mode origin and the development of its Huang-Rhys factor is indicated in terms of contributions from each ground-state mode. The Huang-Rhys factors in absorption and emission, S_i^A and S_i^E, respectively, can be expressed as

$$S_i^A = \left(\delta_i^A\right)^2/2 \text{ and } S_i^E = \left(\delta_i^E\right)^2/2 \qquad (11)$$

in terms of dimensionless nuclear displacements on the ground state δ_i^E and excited state δ_i^A

$$\delta_i^E = -\left(\frac{2\pi \nu_i^{S_0}}{\hbar}\right)^{1/2} \sum_{j=1}^{N} C_{ji}^{S_0} m_j^{1/2} \Delta x_j,$$

$$\delta_i^A = \left(\frac{2\pi \nu_i^{Q_y}}{\hbar}\right)^{1/2} \sum_{j=1}^{N} C_{ji}^{Q_y} m_j^{1/2} \Delta x_j, \qquad (12)$$

where Δx_j is the change in Q_y from S_0 of a Cartesian coordinate of an atom of mass m_j, or its equivalent after curvilinear transformation (Reimers, 2001). The displacements are related through the Duschinsky matrix (Equation 10) as

$$\delta_i^A = - \sum_{k=1}^{n} \left(\frac{\nu_i^{Q_y}}{\nu_k^{S_0}} \right)^{1/2} D_{ki} \delta_k^E, \quad \text{where } 1 = \sum_{k=1}^{n} D_{ki}^2 \qquad (13)$$

(Note that the Duschinsky matrix is orthogonal in rectilinear coordinates but not necessarily so in curvilinear coordinates, see **Supplementary Material** for the details of treatment in this case). Of interest, the frequency-weighting term in Equation (13) shows how low-frequency modes in emission can preferentially contribute to absorption intensity.

Full depictions of how each ground-state mode contributes to the vibrational density and displacement (Equation 13) are provided in **Supplementary Figures 1, 2**. For some key modes, enhanced descriptions are provided in **Figure 8**. This figure shows the cumulative contribution D_{ik}^2 of each ground-state vibration k to the excited state vibration i, which is shown in blue (also some key contributions are listed in **Table 4**). Typically, just a small number of ground-state modes mix to form each excited state, with the blue curves approximating Heaviside step functions. Hence a close correlation is observed between ground- and excited-state vibrational frequencies, with the resulting frequencies depending only on sums of densities D_{ik}^2. Shown also in red are the (fractional) cumulative contributions $\left(\nu_i^{Q_y} / \nu_k^{S_0} \right)^{1/2} D_{ik} \delta_k^E / \delta_i^A$ of each ground-state mode to the excited-state displacement δ_i^A. As these contributions to the displacement are signed, the Huang-Rhys factors embody both constructive and destructive interferences. When the shown curves resemble Heaviside step functions, there is symmetry between absorption and emission (i.e., the transition moment in absorption matches that in emission), but in many cases interferences dominate and absorption/emission symmetry is lost.

A simple case (**Figure 8**, **Table 4**) is the mode predicted in absorption at 155 cm^{-1} and in emission at 154 cm^{-1}, with a similarity of 98% as revealed by the Duschinsky matrix. These vibrations are attributed to the significant absorption and emission observed in the 190 cm^{-1} region.

Next, we consider some lines with large reorganization energy observed in Q_y at 1,228 cm^{-1} with $\lambda^A = 47$ cm^{-1} that is assigned to ground-state modes observed at 1,223 cm^{-1} with $\lambda^E = 17$ cm^{-1} in TEA and at 1,224 cm^{-1} with $\lambda^E = 69$ cm^{-1} in 1-propanol. The calculations indicate that two modes (23% 1,211 cm^{-1} and 60% 1,221 cm^{-1}) mix to dominate the observed effects, sometimes constructively and sometimes destructively. Such mixing could explain the observed very large solvent dependence of the ΔFLN spectra, as it would be very sensitive to the environment. This mode has the largest observed reorganization energy in the ΔFLN spectra in 1-propanol, but a similar situation is found also for the 2nd-largest mode observed at 1,183 cm^{-1} in both 1-propanol and TEA, this time presenting solvent-dependent reorganization energies of 55 cm^{-1} and 18 cm^{-1}, respectively. For the 2nd-largest mode, the calculations indicate that various ground-state modes contribute to the

excited-state vibration (calculated at 1,159 cm^{-1}), again allowing solvent effects to dramatically change mode intensities. A similar situation exists for the mode with the largest reorganization energy observed by ΔFLN in TEA (at 986 cm^{-1}) that is assigned to interference between the calculated ground-state vibrations at 977 cm^{-1} and 979 cm^{-1}.

Also of interest are the modes with large reorganization energy observed by ΔFLN in TEA at 1,144 cm^{-1} and in 1-propanol at 1,146 cm^{-1}. These are assigned to a calculated ground-state vibration at 1,149 cm^{-1} that is made up of many small contributions from excited-state modes spanning 1,100–1,300 cm^{-1}. Hence the calculations predict that this intense mode in emission has no counterpart in absorption, and indeed no counterpart is obvious from the observed fluorescence-excitation spectra.

Lastly, we consider eight example modes from the important high-frequency region calculated in Q_y between 1,260 and 1,595 cm^{-1} (**Figure 8**, **Table 4**). For these, the absorption Huang-Rhys factor is predicted to arise following extensive constructive interference involving many ground-state modes ranging often over 1,000 cm^{-1} in frequency. Emission/absorption symmetry is intrinsically lost through this process. The larger the number of modes involved and the greater the spread of frequencies, the more similar the reorganization energies observed by ΔFLN in TEA and in 1-propanol become. Hence, for the high-frequency modes, the major effect of solvent variation becomes frequency shifts associated with localized aspects of solvation. Also, energy absorbed by one of these high-frequency modes, in the absence of relaxation processes, will be re-emitted by all coupled ground-state modes and hence can be spread out into a band that is over 1,000 cm^{-1} wide.

In **Supplementary Material**, analogous results to those in **Table 4** are presented in **Supplementary Table 2** for the situation in which one 1-propanol ligand is bound to the Mg of Chl-a. Unfortunately, as detailed in **Supplementary Table 1**, approaches such as this using explicit solvation and/or implicit solvation fail to reproduce the basic observed changes in the absorption and emission reorganization energies from **Table 3**. Hence, details in the differences found between the high-resolution analyses presented in **Table 4**, **Supplementary Table 2** are not expected to be meaningful. There are two qualitative features of interest, however. First, the basic pattern depicted in **Table 4** does not change, indicating that many key calculated features are invariant to the treatment of solvation. Second, the calculations predict that some bands undergo small frequency changes but factors of three change in intensity, in going from the isolated molecule to the 1-propanol cluster, just as observed modes show large changes in intensity on changing the solvent from TEA to 1-propanol (**Supplementary Table 3**). Therefore, in principle, the calculations embody all features needed to interpret the experimental data.

CONCLUSIONS

The experimental data fitting is done adopting a Huang-Rhys model (Huang et al., 1950). This assumes that just two

electronic states are involved, that the Born-Oppenheimer (Born and Oppenheimer, 1927) and Franck-Condon (Condon, 1928) approximations hold, that the potentials-energy surfaces are harmonic, that the ground- and excited-state vibrational frequencies are identical, and that the Duschinsky rotation matrix (Duschinsky, 1937) is the unit matrix, yielding vibrational frequencies ν_i, Huang-Rhys factors S_i, and associated reorganization energies $h\nu_i S_i$ for each state. Unfortunately, this analysis is lacking in that it allows different vibrational frequencies to be determined for each state yet is internally based on the assumption that the same vibrational frequencies occur in each state. To resolve this paradox, the experimental data is augmented with the Duschinsky rotation matrices from the DFT calculations, providing links between the observed modes in absorption and those in emission. The simulated spectra therefore correspond to a modified Huang-Rhys model, in which the initial-state vibrational frequency is taken to be the average initial-state frequency, as weighted by the Duschinsky-matrix elements pertaining to each excited-state frequency (Reimers, 2001). A feature of the calculations, which is sometimes critical and sometimes not, is the use of a harmonic potential approximation in curvilinear coordinates to take into account the often very large anharmonic effects operative in large molecules (Reimers, 2001). The net result is that each intense high-resolution line in absorption is mapped onto an absorption mode predicted by the calculations. This mapping is accomplished by: (1) assigning a key observed line in absorption to lines predicted in the calculations, (2) applying the calculated Duschinsky matrix to the predicted line onto one or more lines calculated in emission, and (3) assigning the predicted emission line(s) onto an observed emission line(s). This allows the observed high-resolution absorption-emission asymmetry to be understood.

Theoretical prediction of absorption and emission spectra, for a molecule the size of chlorophyll, to the accuracy needed to interpret either low-resolution or high-resolution spectra, remains a serious challenge. Required is the determination of the optimized geometry, vibrational frequencies, and associated normal modes of vibration in both the ground and excited electronic states. The only readily applicable approach of reasonable accuracy is DFT, applied using its time-dependent formalism (Casida, 1995) (TD-DFT) to model excited states. One needs to choose between a wide variety of available density functionals, however, with a desired outcome being that any sensible choice leads to the same basic qualitative conclusions. Also, previous similar studies for BChl-a and Pheo-a indicate that different modern approaches can predict results showing great disparity, with most not even qualitatively depicting the basic observed absorption and emission spectral properties (Rätsep et al., 2011, 2019b). A reason for this is that a critical property responsible for the usefulness of the chlorophyllides in light harvesting, transport, and energy conversion is the very low value of their emission and absorption reorganization energies, resulting in difficult quantitative calculations that portray related properties. The only satisfactory density functional so far identified is CAM-B3LYP (Yanai et al., 2004; Kobayashi and

Amos, 2006); the conclusion confirmed also here in case of Chl-a. This is a functional embodying long-range correction of the potential so as to be able to treat charge-transfer states, without which the lowest-energy non-charge transfer states like Q_y and Q_x are poorly represented (Cai et al., 2002, 2006; Magyar and Tretiak, 2007; Peach et al., 2008).

While the highly environment sensitive contribution of the Q_x state to absorption has long been known as a major source of asymmetry between observed low-resolution absorption and emission spectra of Chl-a, the measurement before (Rätsep et al., 2009a) and herein of phonon-sideband-free high resolution emission spectra using ΔFLN, to complement existing high-resolution absorption spectra (Avarmaa and Rebane, 1985), indicates that significant asymmetry remains even after the effects (Reimers et al., 2013) of Q_x absorption are negated. Further, measuring ΔFLN in two different solvents, TEA which results in 5-coordinate magnesium, and 1-propanol, with the coordination increasing to 6, reveals strong solvent-dependence for vibrational line intensities. With the exception of vibrational modes involved in specific solvation effects, only small changes in vibrational frequency are found to accompany these large changes in line intensity. Also, as found for BChl-a (Rätsep et al., 2011) and Pheo-a (Rätsep et al., 2019b), the most intense vibrational lines observed in either one of absorption or emission can be absent in the other spectroscopic results, indicating that absorption-emission asymmetry arises from fundamental changes in the vibrational descriptions of the S_0 and Q_y states.

The large absorption-emission asymmetry, as well as the strong solvent dependence of the emission line strengths, is attributed to properties of the Duschinsky rotation matrix that maps the form of the vibrational motions in Q_y onto those of S_0. Four distinct types of properties are predicted and correlated with experimental observations: (1) some modes retain their form in the two electronic states, leading to high-resolution absorption/emission symmetry; (2) some modes mix strongly with just a few other modes of similar frequency, making line intensities strongly dependent on subtle solvent-induced changes in frequency of the coupled modes, as well as providing significant absorption/emission asymmetry; (3) some modes mix very strongly, so strong that dominant lines in either absorption or emission have no counterpart; and (4) strong mixing, particularly for key high-frequency modes, can result in absorption at one vibrational frequency, without phase loss or energy relaxation, producing emission spanning over a thousand cm^{-1}.

These results are particularly pertinent to computational modes describing exciton transport in photosystems. If vibrational relaxation occurs before reemission, then quantum coherence of the energy-transport process is lost, reducing the process to one of classical kinetics, with re-emission expected over the broad allowed range. If there is no vibrational relaxation and full absorption-emission asymmetry, then energy is simply stored on a chromophore and then passed on coherently. The modeling of exciton transport usually involves understanding the competition between these processes, competition between

coherent and incoherent transport mechanisms. A new dimension to this is demanded by the results obtained: a chromophore that absorbs an exciton at a specific energy can also coherently reemit it, in a very mode-specific way, over a wide energy range. Energy change and decoherence are therefore no longer intrinsically coupled.

Finally, we note that the calculations embody all effects needed for a detailed understanding of the effects of solvent on high-resolution spectroscopic properties, but still fail to qualitatively describe the actual observed effects. It is likely that large-sample modern treatments that fully solvate the chromophore with explicitly represented solvent molecules, combined with inclusion of long-range dielectric properties (Hush and Reimers, 2000; Skyner et al., 2015; Zuehlsdorff and Isborn, 2018; Cerezo et al., 2020), are required for further progress.

DATA AVAILABILITY STATEMENT

The original contributions presented in the study are included in the article/**Supplementary Material**, further inquiries can be directed to the corresponding author.

AUTHOR CONTRIBUTIONS

JR designed and performed the calculations and spectral data fitting. MR performed the sample preparation and experimental measurements. AF designed the research. All authors contributed to the manuscript.

SUPPLEMENTARY MATERIAL

The Supplementary Material for this article can be found online at: https://www.frontiersin.org/articles/10.3389/fchem.2020.588289/full#supplementary-material

Supplementary Material provided for (i) additional results tables, (ii) data files providing the optimized coordinates **x**, vibrational frequencies **ν**, and normal modes **C** of methyl Chl-a porphyrin in its ground state Q_y state, as well as the associated Duschinsky matrix **D** and curvilinear projections δ^A and δ^E of the ground-to-excited state geometry changes onto the two sets of normal modes, and the associated reorganization energies, and (iii) pdf files showing pictorially the form of the ground-state and excited-state normal modes.

REFERENCES

Adolphs, J., Berrer, M., and Renger, T. (2016). Hole-burning spectroscopy on excitonically coupled pigments in proteins: theory meets experiment. *J. Am. Chem. Soc.* 138, 2993–3001. doi: 10.1021/jacs.5b08246

Avarmaa, R. A., and Rebane, K. K. (1985). High-resolution optical spectra of chlorophyll molecules. *Spectrochim. Acta A* 41, 1365–1380. doi: 10.1016/0584-8539(85)80189-6

Becke, A. D. (1993). Density-functional thermochemistry. III. The role of exact exchange. *J. Chem. Phys.* 98, 5648–5652. doi: 10.1063/1.464913

Blankenship, R. E., Madigan, M. T., and Bauer, C. E. (eds.). (2004). *Anoxygenic Photosynthetic Bacteria*. Dordrecht: Kluwer.

Born, M., and Oppenheimer, R. (1927). Zur Quantentheorie der Molekeln (On the quantum theory of molecules). *Ann. Phys.* 389, 457–484. doi: 10.1002/andp.19273892002

Bukarte, E., Haufe, A., Paleček, D., Büchel, C., and Zigmantas, D. (2020). Revealing vibronic coupling in chlorophyll c1 by polarization-controlled 2D electronic spectroscopy. *Chem. Phys.* 530:110643. doi: 10.1016/j.chemphys.2019.110643

Cai, Z.-L., Crossley, M. J., Reimers, J. R., Kobayashi, R., and Amos, R. D. (2006). Density-functional theory for charge-transfer: the nature of the N-bands of porphyrins and chlorophylls revealed through CAM-B3LYP, CASPT2, and SAC-CI calculations. *J. Phys. Chem. B* 110, 15624–15632. doi: 10.1021/jp063376t

Cai, Z.-L., Sendt, K., and Reimers, J. R. (2002). Failure of time-dependent density-functional theory for large extended pi systems. *J. Chem. Phys.* 117, 5543–5549. doi: 10.1063/1.1501131

Cao, J., Cogdell, R. J., Coker, D. F., Duan, H.-G., Hauer, J., Kleinekathöfer, U., et al. (2020). Quantum biology revisited. *Sci. Adv.* 6:eaaz4888. doi: 10.1126/sciadv.aaz4888

Caricato, M. (2019). Coupled cluster theory with the polarizable continuum model of solvation. *Int. J. Quantum Chem.* 119:e25710. doi: 10.1002/qua.25710

Casida, M. E. (1995). "Time-dependent density functional response theory for molecules," in *Recent Advances in Density Functional Methods,*

Part 1, ed D. P. Chong (Singapore: World Scientific), 155–192. doi: 10.1142/9789812830586_0005

Cerezo, J., Aranda, D., Avila Ferrer, F. J., Prampolini, G., and Santoro, F. (2020). Adiabatic-molecular dynamics generalized vertical hessian approach: a mixed quantum classical method to compute electronic spectra of flexible molecules in the condensed phase. *J. Chem. Theory Comput.* 16, 1215–1231. doi: 10.1021/acs.jctc.9b01009

Chai, J.-D., and Head-Gordon, M. (2008). Long-range corrected hybrid density functionals with damped atom-atom dispersion corrections. *Phys. Chem. Chem. Phys.* 10, 6615–6620. doi: 10.1039/b810189b

Condon, E. U. (1928). Nuclear motions associated with electron transitions in diatomic molecules. *Phys. Rev.* 32:858. doi: 10.1103/PhysRev.32.858

den Hartog, F. T. H., Dekker, J. P., van Grondelle, R., and Völker, S. (1998). Spectral distributions of "Trap" pigments in the RC, CP47, and CP47-RC complexes of photosystem II at low temperature: a fluorescence line-narrowing and hole-burning study. *J. Phys. Chem. B* 102, 11007–11016. doi: 10.1021/jp9832793

Duan, H.-G., Prokhorenko, V. I., Cogdell, R. J., Ashraf, K., Stevens, A. L., Thorwart, M., et al. (2017). Nature does not rely on long-lived electronic quantum coherence for photosynthetic energy transfer. *Proc. Natl. Acad. Sci. U.S.A.* 114, 8493–8498. doi: 10.1073/pnas.1702261114

Duschinsky, F. (1937). Acta Physiochim. *URSS* 7:551.

Einstein, A. (1916). Strahlungs-emission und -absorption nach der quantentheorie. *Verhandlungen der Deutschen Physikalischen Gesellschaft* 18, 318–323.

Fiedor, L., Kania, A., Myśliwa-Kurdziel, B., Orzeł Ł., and Stochel, G. (2008). Understanding chlorophylls: central magnesium ion and phytyl as structural determinants. *Biochim. Biophys. Acta – Bioenerg.* 1777, 1491–1500. doi: 10.1016/j.bbabio.2008.09.005

Fiedor, L., Stasiek, M., Myśliwa-Kurdziel, B., and Strzałka, K. (2003). Phytol as one of the determinants of chlorophyll interactions in solution. *Photosyn. Res.* 78, 47–57. doi: 10.1023/A:1026042005536

Frisch, M. J., Trucks, G. W., Schlegel, H. B., Scuseria, G. E., Robb, M. A., Cheeseman, J. R., et al. (2016). *Gaussian 16 Revision C.01*. Wallingford, CT: Gaussian Inc.

Gillie, J. K., Small, G. J., and Golbeck, J. H. (1989). Nonphotochemical hole burning of the native antenna complex of photosystem I (PSI-200). *J. Phys. Chem.* 93, 1620–1627. doi: 10.1021/j100341a085

Goerigk, L., and Grimme, S. (2011). A thorough benchmark of density functional methods for general main group thermochemistry, kinetics, and noncovalent interactions. *Phys. Chem. Chem. Phys.* 13, 6670–6688. doi: 10.1039/c0cp02984j

Gouterman, M., Wagnière, G. H., and Snyder, L. C. (1963). Spectra of porphyrins: part II. Four orbital model. *J. Mol. Spectrosc.* 11, 108–127. doi: 10.1016/0022-2852(63)90011-0

Grimm, B., Porra, R. J., Rüdiger, W., and Scheer, H. (eds.). (2006). *Chlorophylls and Bacteriochlorophylls*. Dordrecht: Springer. doi: 10.1007/1-4020-4516-6

Hehre, W. J., Ditchfield, R., and Pople, J. A. (1972). Self-consistent molecular orbital methods. XII. Further extensions of gaussian-type basis sets for use in molecular orbital studies of organic molecules. *J. Chem. Phys.* 56, 2257–2261. doi: 10.1063/1.1677527

Higashi, M., Kosugi, T., Hayashi, S., and Saito, S. (2014). Theoretical study on excited states of bacteriochlorophyll a in solutions with density functional assessment. *J. Phys. Chem. B* 118, 10906–10918. doi: 10.1021/jp507259g

Huang, K., Rhys, A., and Mott, N. F. (1950). Theory of light absorption and non-radiative transitions in F-centres. *Proc. Royal Soc. London Series A Math. Phys. Sci.* 204, 406–423. doi: 10.1098/rspa.1950.0184

Hughes, J. L., Conlon, B., Wydrzynski, T., and Krausz, E. (2010). The assignment of $Q_Y(1,0)$ vibrational structure and Q_x for chlorophyll a. *Phys. Procedia* 3, 1591–1599. doi: 10.1016/j.phpro.2010.01.226

Hughes, J. L., Prince, B. J., Krausz, E., Smith, P. J., Pace, R. J., and Riesen, H. (2004). Highly efficient spectral hole-burning in oxygen-evolving photosystem II preparations. *J. Phys. Chem. B* 108, 10428–10439. doi: 10.1021/jp0492523

Huo, P., and Coker, D. F. (2010). Iterative linearized density matrix propagation for modelling coherent excitation energy transfer in photosynthetic light harvesting. *J. Chem. Phys.* 133:184108. doi: 10.1063/1.3498901

Hush, N. S. (1958). Adiabatic rate processes at electrodes. *J. Chem. Phys.* 28:962. doi: 10.1063/1.1744305

Hush, N. S., and Reimers, J. R. (2000). Solvent effects on transition metal complex spectra. *Chem. Rev.* 100:775. doi: 10.1021/cr980409v

Jaaniso, R., and Avarmaa, R. (1986). Measurement of the inhomogeneous distribution function and homogeneous spectra of an impurity molecule in a glassy matrix. *Sov. J. Appl. Spectroscopy* 44, 365–370. doi: 10.1007/BF00661051

Jankowiak, R., Reppert, M., Zazubovich, V., Pieper, J., and Reinot, T. (2011). Site selective and single complex laser-based spectroscopies: a window on excited state electronic structure, excitation energy transfer, and electron-phonon coupling of selected photosynthetic complexes. *Chem. Rev.* 111, 4546–4598. doi: 10.1021/cr100234j

Kjær, C., Gruber, E., Nielsen, S. B., and Andersen, L. H. (2020). Color tuning of chlorophyll a and b pigments revealed from gas-phase spectroscopy. *Phys. Chem. Chem. Phys.* 22, 20331–20336. doi: 10.1039/D0CP03210G

Kobayashi, R., and Amos, R. D. (2006). The application of CAM-B3LYP to the charge-transfer band problem of the zincbacteriochlorin–bacteriochlorin complex. *Chem. Phys. Lett.* 420, 106–109. doi: 10.1016/j.cplett.2005.12.040

Kreisbeck, C., Kramer, T., and Aspuru-Guzik, A. (2014). Scalable high-performance algorithm for the simulation of exciton-dynamics. Application to the light harvesting complex II in the presence of resonant vibrational modes. *J. Chem. Theory Comput.* 10:4045. doi: 10.1021/ct500629s

Laisk, A., Nedbal, L., and Govindjee (eds.). (2009). *Photosynthesis In Silico: Understanding Complexity From Molecules to Ecosystems*. Dordrecht: Springer. doi: 10.1007/978-1-4020-9237-4

Leiger, K., Linnanto, J. M., and Freiberg, A. (2017). Vibronic origin of the Q_Y absorption tail of bacteriochlorophyll *a* verified by fluorescence excitation spectroscopy and quantum chemical simulations. *J. Phys. Chem. Lett.* 8, 4231–4235. doi: 10.1021/acs.jpclett.7b01704

Magyar, R. J., and Tretiak, S. (2007). Dependence of spurious charge-transfer excited states on orbital exchange in TDDFT: large molecules and clusters. *J. Chem. Theory Comput.* 3, 976–987. doi: 10.1021/ct600282k

Malý, P., Somsen, O. J. G., Novoderezhkin, V. I., Mančal, T., and van Grondelle, R. (2016). The role of resonant vibrations in electronic energy transfer. *Chemphyschem* 17, 1356–1368. doi: 10.1002/cphc.201500965

May, V., and Kühn, O. (2008). *Charge and Energy Transfer Dynamics in Molecular Systems*. Weinheim: Wiley.

Mennucci, B. (2012). Polarizable continuum model. *Wiley Interdiscip. Rev. Comput. Mol. Sci.* 2, 386–404. doi: 10.1002/wcms.1086

Müh, F., Lindorfer, D., Schmidt am Busch, M., and Renger, T. (2014). Towards a structure-based exciton Hamiltonian for the CP29 antenna of photosystem II. *Phys. Chem. Chem. Phys.* 16, 11848–11863. doi: 10.1039/C3CP55166K

Pajusalu, M., Rätsep, M., and Freiberg, A. (2014). Temperature dependent electron–phonon coupling in chlorin-doped impurity glass and in photosynthetic FMO protein containing bacteriochlorophyll a. *J. Lumin.* 152, 79–83. doi: 10.1016/j.jlumin.2013.12.011

Palm, D. M., Agostini, A., Pohland, A.-C., Werwie, M., Jaenicke, E., and Paulsen, H. (2019). Stability of water-soluble chlorophyll protein (WSCP) depends on phytyl conformation. *ACS Omega* 4, 7971–7979. doi: 10.1021/acsomega.9b00054

Peach, M. J. G., Benfield, P., Helgaker, T., and Tozer, D. J. (2008). Excitation energies in density functional theory: an evaluation and a diagnostic test. *J. Chem. Phys.* 128:044118. doi: 10.1063/1.2831900

Pieper, J., Artene, P., Rätsep, M., Pajusalu, M., and Freiberg, A. (2018). Evaluation of electron–phonon coupling and spectral densities of pigment–protein complexes by line-narrowed optical spectroscopy. *J. Phys. Chem. B* 122, 9289–9301. doi: 10.1021/acs.jpcb.8b05220

Pieper, J., and Freiberg, A. (2014). "Electron-phonon and exciton-phonon coupling in light-harvesting, insights from line-narrowing spectroscopies," in *The Biophysics of Photosynthesis*, eds J. Golbeck, and A. van der Est (New York, NY: Springer), 45–77. doi: 10.1007/978-1-4939-1148-6_2

Purchase, R., and Völker, S. (2009). Spectral hole burning: examples from photosynthesis. *Photosyn. Res.* 101, 245–266. doi: 10.1007/s11120-009-9484-5

Rätsep, M., Cai, Z.-L., Reimers, J. R., and Freiberg, A. (2011). Demonstration and interpretation of significant asymmetry in the low-resolution and high-resolution Q_Y fluorescence and absorption spectra of bacteriochlorophyll *a*. *J. Chem. Phys.* 134:024506. doi: 10.1063/1.3518685

Rätsep, M., and Freiberg, A. (2003). Resonant emission from the B870 exciton state and electron-phonon coupling in the LH2 antenna chromoprotein. *Chem. Phys. Lett.* 377, 371–376. doi: 10.1016/S0009-2614(03)01193-X

Rätsep, M., and Freiberg, A. (2007). Electron-phonon and vibronic couplings in the FMO bacteriochlorophyll *a* antenna complex studied by difference fluorescence line narrowing. *J. Lumin.* 127, 251–259. doi: 10.1016/j.jlumin.2007.02.053

Rätsep, M., Linnanto, J., and Freiberg, A. (2009a). Mirror symmetry and vibrational structure in optical spectra of chlorophyll *a*. *J. Chem. Phys.* 130:194501. doi: 10.1063/1.3125183

Rätsep, M., Linnanto, J. M., and Freiberg, A. (2019a). Higher order vibronic sidebands of chlorophyll *a* and bacteriochlorophyll *a* for enhanced excitation energy transfer and light harvesting. *J. Phys. Chem. B* 123, 7149–7156. doi: 10.1021/acs.jpcb.9b06843

Rätsep, M., Linnanto, J. M., Muru, R., Biczysko, M., Reimers, J. R., and Freiberg, A. (2019b). Absorption-emission symmetry breaking and the different origins of vibrational structures of the ^1Q_Y and ^1Q_x electronic transitions of pheophytin *a*. *J. Chem. Phys.* 151:165102. doi: 10.1063/1.5116265

Rätsep, M., Pajusalu, M., and Freiberg, A. (2009b). Wavelength-dependent electron-phonon coupling in impurity glasses. *Chem. Phys. Lett.* 479, 140–143. doi: 10.1016/j.cplett.2009.07.094

Rätsep, M., Wu, H. M., Hayes, J. M., and Small, G. J. (1998). Stark hole-burning spectroscopy of a photosynthetic complex: LH2 of purple bacteria. *Spectrochim. Acta A* 54, 1279–1289. doi: 10.1016/S1386-1425(98)00076-6

Rebane, K. K. (1970). *Impurity Spectra of Solids*. New York, NY: Plenum Press.

Rebane, K. K., and Avarmaa, R. A. (1982). Sharp line vibronic spectra of chlorophyll and its derivatives in solid solutions. *Chem. Phys.* 68, 191–200. doi: 10.1016/0301-0104(82)85094-5

Reimers, J. R. (2001). A practical method for the use of curvilinear coordinates in calculations of normal-mode projected displacements and Duschinsky rotation matrices for large molecules. *J. Chem. Phys.* 115, 9103–9109. doi: 10.1063/1.1412875

Reimers, J. R., Cai, Z.-L., Kobayashi, R., Rätsep, M., Freiberg, A., and Krausz, E. (2013). Assignment of the Q-bands of the chlorophylls: coherence loss via Q_x - Q_y mixing. *Sci. Rep.* 3:2761. doi: 10.1038/srep02761

Reimers, J. R., Cai, Z.-L., Kobayashi, R., Rätsep, M., Freiberg, A., and Krausz, E. (2014). Formation of water-chlorophyll clusters in dilute samples of chlorophyll-a in ether at low temperature. *Phys. Chem. Chem. Phys.* 16, 2323–2330. doi: 10.1039/C3CP53729C

Reimers, J. R., and Krausz, E. (2014). An analytical data inversion method for magnetic circular dichroism spectra dominated by the "B-term". *Phys. Chem. Chem. Phys.* 16, 2315–2322. doi: 10.1039/C3CP53730G

Ren, J., Shuai, Z., and Kin-Lic Chan, G. (2018). Time-dependent density matrix renormalization group algorithms for nearly exact absorption and fluorescence spectra of molecular aggregates at both zero and finite temperature. *J. Chem. Theory Comput.* 14, 5027–5039. doi: 10.1021/acs.jctc.8b00628

Renge, I., Mauring, K., and Avarmaa, R. (1987). Site-selection optical spectra of bacteriochlorophyll and bacteriopheophytin in frozen solutions. *J. Lumin.* 37, 207–214. doi: 10.1016/0022-2313(87)90161-X

Renge, I., Rätsep, M., and Freiberg, A. (2011). Intermolecular repulsive–dispersive potentials explain properties of impurity spectra in soft solids. *J. Lumin.* 131, 262–265. doi: 10.1016/j.jlumin.2010.10.008

Renger, T., Voigt, J., May, V., and Kühn, O. (1996). Dissipative exciton motion in a chlorophyll a/b dimer of the light harvesting complex of photosystem II: simulation of pump - probe spectra. *J. Phys. Chem.* 100, 15654–15662. doi: 10.1021/jp960486z

Rivera, E., Montemayor, D., Masia, M., and Coker, D. F. (2013). Influence of site-dependent pigment-protein interactions on excitation energy transfer in photosynthetic light harvesting. *J. Phys. Chem. B* 117, 5510–5521. doi: 10.1021/jp4011586

Romero, E., Augulis, R., Novoderezhkin, V. I., Ferretti, M., Thieme, J., Zigmantas, D., et al. (2014). Quantum coherence in photosynthesis for efficient solar-energy conversion. *Nat. Phys* 10, 676–682. doi: 10.1038/nphys3017

Shafizadeh, N., Ha-Thi, M. H., Soep, B., Gaveau, M. A., Piuzzi, F., and Pothier, C. (2011). Spectral characterization in a supersonic beam of neutral chlorophyll a evaporated from spinach leaves. *J. Chem. Phys.* 135:114303. doi: 10.1063/1.3637048

Sild, O., and Haller, K. (eds.). (1988). *Zero-Phonon Lines And Spectral Hole Burning in Spectroscopy and Photochemistry.* Berlin: Springer. doi: 10.1007/978-3-642-73638-4

Sirohiwal, A., Berraud-Pache, R., Neese, F., Izsák, R., and Pantazis, D. A. (2020). Accurate computation of the absorption spectrum of chlorophyll a with pair natural orbital coupled cluster methods. *J. Phys. Chem. B* 124, 8761–8771. doi: 10.1021/acs.jpcb.0c05761

Skyner, R. E., McDonagh, J. L., Groom, C. R., van Mourik, T., and Mitchell, J. B. O. (2015). A review of methods for the calculation of solution free energies and the modelling of systems in solution. *Phys. Chem. Chem. Phys.* 17, 6174–6191. doi: 10.1039/C5CP00288E

Tomasi, J. (2011). Selected features of the polarizable continuum model for the representation of solvation. *Wiley Interdiscip. Rev. Comput. Mol. Sci.* 1, 855–867. doi: 10.1002/wcms.54

Tomasi, J., Mennucci, B., and Cammi, R. (2005). Quantum mechanical continuum solvation models. *Chem. Rev.* 105, 2999–3093. doi: 10.1021/cr9904009

Tomasi, S., and Kassal, I. (2020). Classification of coherent enhancements of light-harvesting processes. *J. Phys. Chem. Lett.* 11, 2348–2355. doi: 10.1021/acs.jpclett.9b03490

Umetsu, M., Wang, Z.-Y., Kobayashi, M., and Nozawa, T. (1999). Interaction of photosynthetic pigments with various organic solvents: magnetic circular dichroism approach and application to chlorosomes. *Biochim. Biophys. Acta – Bioenerg.* 1410, 19–31. doi: 10.1016/S0005-2728(98)00170-4

van Grondelle, R., Dekker, J. P., Gillbro, T., and Sundström, V. (1994). Energy transfer and trapping in photosynthesis. *Biochim. Biophys. Acta* 1187, 1–65. doi: 10.1016/0005-2728(94)90166-X

Wilson, E. B., Decius, J. C., and Cross, P. C. (1955). *Molecular Vibrations: The Theory of Infrared and Raman Vibrational Spectra.* New York, NY: McGraw-Hill Book Company. doi: 10.1149/1.2430134

Yanai, T., Tew, D. P., and Handy, N. C. (2004). A new hybrid exchange-correlation functional using the Coulomb-attenuating method (CAM-B3LYP). *Chem. Phys. Lett.* 393, 51–57. doi: 10.1016/j.cplett.2004.06.011

Yu, H. S., He, X., Li, S. L., and Truhlar, D. G. (2016). MN15: a Kohn–Sham global-hybrid exchange–correlation density functional with broad accuracy for multi-reference and single-reference systems and noncovalent interactions. *Chem. Sci.* 7, 5032–5051. doi: 10.1039/C6SC00705H

Zazubovich, V., Tibe, I., and Small, G. J. (2001). Bacteriochlorophyll a Frank-Condon factors for the S_0-S_1(Q_y) transition. *J. Phys. Chem. B* 105, 12410–12417. doi: 10.1021/jp012804m

Zuehlsdorff, T. J., and Isborn, C. M. (2018). Combining the ensemble and Franck-Condon approaches for calculating spectral shapes of molecules in solution. *J. Chem. Phys.* 148:024110. doi: 10.1063/1.5006043

The Role of Norrish Type-I Chemistry in Photoactive Drugs: An *ab initio* Study of a Cyclopropenone-Enediyne Drug Precursor

Spencer J. Léger[1,2], Barbara Marchetti[1], Michael N. R. Ashfold[3] and Tolga N. V. Karsili[1]*

[1] *Department of Chemistry, University of Louisiana at Lafayette, Lafayette, LA, United States,* [2] *Department of Chemical Engineering, University of Louisiana at Lafayette, Lafayette, LA, United States,* [3] *School of Chemistry, University of Bristol, Bristol, United Kingdom*

We present a contemporary mechanistic description of the light-driven conversion of cyclopropenone containing enediyne (CPE) precursors to ring-opened species amenable to further Bergman cyclization and formation of stable biradical species that have been proposed for use in light-induced cancer treatment. The transformation is rationalized in terms of (purely singlet state) Norrish type-I chemistry, wherein photoinduced opening of one C–C bond in the cyclopropenone ring facilitates non-adiabatic coupling to high levels of the ground state, subsequent loss of CO and Bergman cyclization of the enediyne intermediate to the cytotoxic target biradical species. Limited investigations of substituent effects on the ensuing photochemistry serve to vindicate the experimental choices of Popik and coworkers (*J. Org. Chem.*, 2005, **70**, 1297–1305). Specifically, replacing the phenyl moiety in the chosen model CPE by a 1,4-benzoquinone unit leads to a stronger, red-shifted parent absorption, and increases the exergicity of the parent → biradical conversion.

Keywords: photodissociation, photostability, photophysics, physical organic chemistry, photochemistry, photoactive drugs

INTRODUCTION

Drug discovery is one of the fastest growing and most potent fields in modern day science (Elion, 1993; Takenaka, 2001; Paul et al., 2010; Rask-Andersen et al., 2011; Swinney and Anthony, 2011; Warren, 2011; Lee et al., 2012). The use and development of state-of-the-art experimental methods, coupled with molecular modeling and artificial intelligence, are revolutionizing contemporary drug discovery (Chan et al., 2019; Henstock, 2019; Mak and Pichika, 2019). These methods have also been vital for developing thorough understandings of the physiological activities of a diverse range of drugs.

Photoinitiated drug activation, wherein UV/visible light is used to drive the action of a drug, already finds use in the context of psoralens and the treatment of a range of skin conditions (Stern et al., 1980; Menter et al., 2009). The more widespread use of light-sensitive drugs, however, is still in its infancy (Farrer et al., 2010; Vernooij et al., 2018; Shi et al., 2019, 2020; Imberti et al., 2020). Such photoinitiation therapies are based on the premise that light-irradiation of a chromophore leads to formation of an excited state, with a total energy well above that of the ground state. In most cases, the total energy of the excited state species exceeds many of the activation barriers associated with ground state reactions. Electronic excitation thus provides a means of activating a reaction

that is otherwise unfavorable in the ground state configuration. The excited states formed by electronic excitation can decay in many ways, both radiative (e.g., fluorescence) and non-radiative (examples of which include internal conversion, reaction (e.g., isomerization) and dissociation). Such non-radiative decay processes are usually controlled (either in part or exclusively) by conical intersections (CIs) between potential energy surfaces, which arise when two or more electronic states—e.g., an excited state and the ground state—become degenerate along a given reaction path (Domcke et al., 2004, 2011; Credo Chung et al., 2007; Xie et al., 2018). The region of degeneracy is then viewed as a CI when orthogonal nuclear motions are considered. Within the chemical physics community, CIs are now widely recognized as mediators of ultrafast internal conversion between electronic states. However, the concept, involvement and importance of CIs has yet to be fully appreciated within the wider scientific community when discussing and utilizing molecular photochemistry. This manuscript is intended, in part, to help bridge the gap between synthetic photochemistry and mechanistic photophysics—by highlighting the crucial roles of CIs in a system wherein, hitherto, such processes have been generally unrecognized and thus ignored.

Photodissociations are a class of non-radiative excited state decay processes available to molecules with labile leaving groups. The initial photoexcitation in such cases may directly populate a so-called $^1n\sigma^*$ or $^1\pi\sigma^*$ state, i.e., a state formed by promoting an electron from a non-bonding (n) or bonding π valence orbital to an antibonding σ^* orbital (Cronin et al., 2004; Ashfold et al., 2006, 2010; Devine et al., 2006; Nix et al., 2007; Roberts and Stavros, 2014; Marchetti et al., 2016). In many other cases, the primary photoexcitation may involve a strongly absorbing $\pi^* \leftarrow \pi$ transition; light-driven bond fission in such cases only occurs after non-adiabatic coupling between the $\pi\pi^*$ state and an $(n/\pi)\sigma^*$ continuum. In either scenario, the σ^* character lowers the overall bond order of the bond around which the orbital is localized and encourages dissociation (or predissociation) along the relevant bond-stretch coordinate.

For completeness, we note that light irradiation already finds many other roles in medicine—most notably in photodynamic therapy (PDT). PDT relies on the sensitized formation of the highly reactive excited singlet ($^1\Delta_g$) state of molecular oxygen (henceforth $^1O_2$), which can then oxidize biomolecules in the environment of cancerous cells and thereby restrict their biochemistry and eventual cell division. The sensitized formation of $^1O_2$ requires the introduction and photoexcitation of a strongly absorbing chromophore with a high propensity for intersystem crossing (ISC). Resonant energy transfer between the photo-produced triplet state chromophore molecules and O_2 elevates the latter to its reactive singlet state. Though effective, PDT has recognized shortcomings: e.g., (i) the eventual formation of $^1O_2$ is indirect (relying on the excitation of, and energy transfer from, the chromophore species) and (ii) cancerous cells are usually hypoxic and successful PDT thus relies on the presence of dissolved O_2 in the chromophore solution at the point that it is administered—thus limiting the control possible when performing PDT.

Light-activated chemotherapy drugs offer a direct means of targeted cancer therapy. Cyclopropenone-containing enediyne precursors are one such class of photoinitiated drugs that have been identified as potential candidates for photoinduced cancer therapy (Poloukhtine and Popik, 2005a,b; Poloukhtine et al., 2008; Pandithavidana et al., 2009). Upon photoexcitation, these molecules photodissociate, eliminating CO and forming an enediyne which then undergoes a Bergman cyclization to form a cycloalkene biradical product (Jones and Bergman, 1972; Luxon et al., 2018) that is capable of oxidizing DNA. The overall mechanism for one such precursor−2, 3-benzobicyclo[8.1.0]undec-1(10)-en-4-yn-11-one—henceforth variously abbreviated as CPE and as **A**—is illustrated in **Scheme 1**.

The present manuscript reports the use of contemporary multi-reference electronic structure methods to explore mechanistic details of the reaction paths that lead to the observed (Poloukhtine and Popik, 2005a) photoinduced CO elimination from CPE and the ensuing Bergman rearrangement of **B** to **C** and how these processes might be affected by selected changes to the phenyl ring.

COMPUTATIONAL METHODOLOGY

All calculations were conducted for the isolated (i.e., gas phase) molecule. The ground state minimum energy geometry of CPE (**A**) was optimized using the Coulomb-Attenuated Model Becke-3rd parameter-Lee-Yang-Parr (CAM-B3LYP) functional (Yanai et al., 2004) of Density Functional Theory (DFT), coupled to the 6-31G(d) Pople basis set (Hehre et al., 1970). Since the reaction of interest (**Scheme 1**) starts with photoinduced elimination
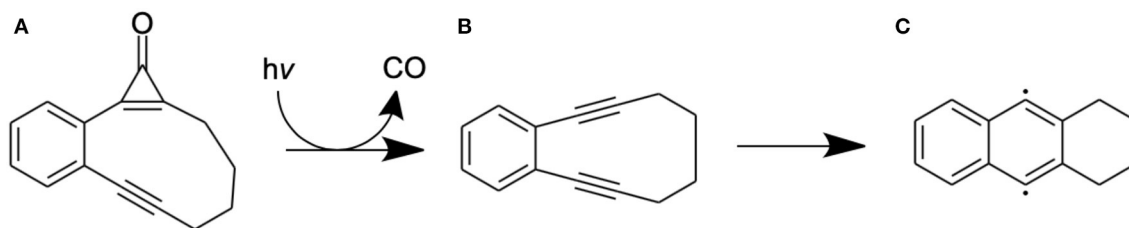
SCHEME 1 | Molecular structures associated with the photoinduced dissociation of the model cyclopropenone-containing enediyne **(A)** and the subsequent Bergman rearrangement of **(B)** to the biradical **(C)**.

of CO, two-dimensional potential energy (PE) profiles of the ground and first excited electronic states of this CPE along the two C–CO stretch coordinates of the cyclopropenone moiety were first investigated using Time-Dependent Density Functional Theory (TD-DFT) (Van Caillie and Amos, 2000; Furche and Ahlrichs, 2002; Scalmani et al., 2006), with the above functional and basis set. As shown in **Supplementary Figure 1** in the Electronic Supplementary Information (ESI), these test calculations returned a maximum on the excited state PE surface when both C–CO bond distances were extended in tandem, but minima when either C–CO bond was extended while the other was held fixed. This hinted that the photoinduced CO elimination involves an initial ring-opening prior to release of the CO moiety.

Guided by these computations, the lowest triplet spin configuration of the ring-opened species formed by breaking the C–C bond nearer the phenyl ring was optimized at the CAM-B3LYP/6-31G(d) level of theory and used as a proxy for the singlet ring-opened structure and energy (since calculations for the ground singlet state inevitably resulted in reformation of the ring-closed CPE molecule).

PE profiles connecting the ground state CPE structure to the optimized ring-opened biradical structure and then onwards to the bicyclic structure **B** were then computed using the complete active space second-order perturbation theory (CASPT2) method, (Roos et al., 1982; Andersson et al., 1990, 1992; Park and Shiozaki, 2017) based on a state-averaged complete active space self-consistent field (SA-CASSCF) reference wavefunction (comprising five singlet and four triplet states) and coupled to the cc-pVDZ basis set (Dunning, 1989). The PE path was constructed using successive linear interpolations in internal coordinates (LIICs) and each LIIC was checked to ensure that the intermediate geometries represented a sensible interpolation between the optimized ground state CPE, the ring-opened species and then **B**. All of these CASSCF and CASPT2 computations employed an active space involving 10 electrons distributed in 10 orbitals—the five highest occupied (**1**–**5**) and the five lowest virtual (**6**–**10**) orbitals shown in **Supplementary Figure 2** of the ESI, where **5** and **6** are, respectively, the highest occupied molecular orbital (HOMO) and lowest unoccupied molecular orbital (LUMO) in the ground state. A further more limited set of PE profiles mapping the Bergman rearrangement of **B** to the biradical **C** were then computed using CASPT2/cc-pVDZ methods, based on a SA-CASSCF reference wavefunction comprising just two singlet and two triplet states (since our primary interest was in determining the magnitude of any energy barrier to **B** → **C** conversion on the ground state PE surface) and an active space comprising 10 electrons in 10 orbitals (shown in **Supplementary Figure 3** of the ESI where, again, orbitals **5** and **6** are, respectively the HOMO and LUMO of the ground state molecule). In all cases, an imaginary level shift of 0.3 E_h was used to aid convergence and mitigate against the involvement of intruder states.

Vertical excitation energies (VEEs) and transition dipole moments were extracted from the associated CASSCF/CASPT2 calculations at the ground state equilibrium geometries of **A** (and **B**) to derive oscillator strengths (f) for transitions to the first few excited states (just the respective S$_1$ states in the case of **B**) using

Equation (1).

$$f = \frac{2}{3} \left(E_i - E_0\right) \cdot \sum_{\alpha = x,y,z} |\mu_{0i}|^2_\alpha \quad , \qquad (1)$$

where E_i and E_0 are, respectively, the energies of the excited state of interest and the ground state and the μ_{0i} are the associated transition dipole moments along α ($\alpha = x$, y, and z). The different x and y coordinates used in describing the transitions in **A** and **B** are shown by the red and green arrows in **Supplementary Figures 2, 3**; the z coordinate in both cases is out of the page.
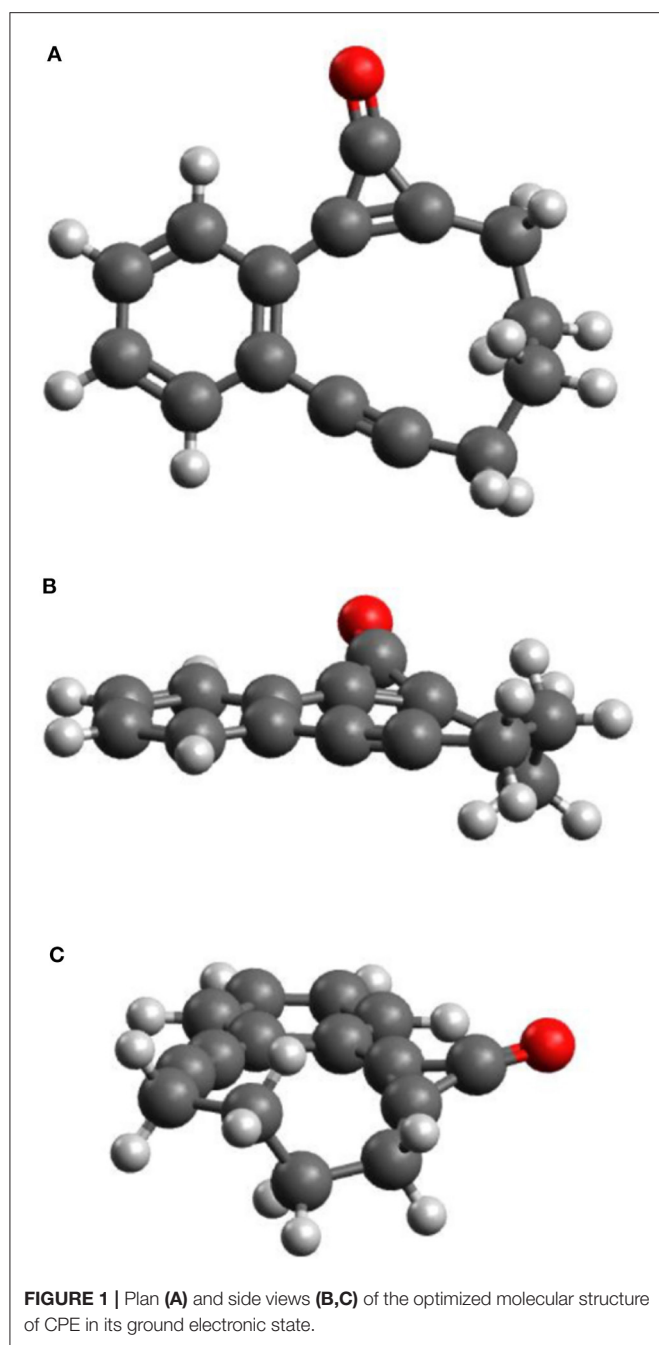
Additional CASPT2 computations using the same basis set and imaginary level shift together with a (10,8) active space were undertaken for three analogs of CPE wherein the phenyl ring had been substituted symmetrically with methoxy (OMe) or cyano (CN) groups in the 1- and 4-positions, or replaced with a 1,4-benzoquinone ring, in order to explore substituent effects on the VEEs and transition strengths. **Supplementary Figure 4** in the ESI shows the highest occupied and lowest virtual orbitals in the ground state of each system. These variants will henceforth be referred to as 1,4-MeO-CPE, 1,4-CN-CPE and 1,4-O=CPE. The latter was selected as (2,3-dimethyl substituted) 1,4-O=CPE has been synthesized (from the dimethylated analog of 1,4-MeO-CPE), shown to form the corresponding enediyne by photoinduced CO elimination and touted as a potential cytotoxin (Poloukhtine and Popik, 2005b). The other two substituted CPEs were selected to compare and contrast the effect of strongly π-accepting (i.e., CN) and π-donating (i.e., MeO) substitutents. The ground state energies of the **A**, **B,** and **C** analogs of 1,4-MeO-CPE, 1,4-CN-CPE and 1,4-O=CPE, relative to bare CPE, were optimized using the high-level CBS-QB3 method (Saracino et al., 2003; Cysewski, 2007; Rayne and Forest, 2010). All DFT and CBS-QB3 calculations were performed using Gaussian 16 (Frisch et al., 2016), while all CASSCF/CASPT2 computations were undertaken in Molpro 2018 (Werner et al., 2018).

RESULTS AND DISCUSSION

Ground State Structure and Vertical Excitation Energies

Figures 1A–C display plan and side-on views of the ground state optimized geometry of CPE. The phenyl, cyclopropenone and alkyne moieties lie in a common plane, while the C$_4$H$_8$ alkyl link adopts a non-planar configuration. Given the cyclic nature of CPE, the geometry around the cyclopropenone unit can be viewed as a strained form of bare cyclopropenone—with an intra-large-ring C–C=C bond angle of ~175° (*cf.* an H–C=C bond angle of ~125° in cyclopropenone)–and the alkyne moiety adopts a strained form of butyne.

Table 1 lists the vertical excitation energies (VEEs) to the first few excited singlet and triplet states of CPE and the dominant orbital promotions involved in the first two singlet excitations. The calculated VEE of the more intense S$_2$-S$_0$ transition agrees well with that reported for CPE in Poloukhtine and Popik (2005a) and Poloukhtine and Popik (2006a), but the calculated S$_1$-S$_0$ transition energy is below that associated with the observed weaker, longer wavelength absorption maximum.

FIGURE 1 | Plan **(A)** and side views **(B,C)** of the optimized molecular structure of CPE in its ground electronic state.

TABLE 1 | Vertical excitation energies (VEEs) and oscillator strengths (*f*) of transitions to the first few singlet and triplet excited states of CPE, calculated at the CASPT2/AVDZ level of theory.

Transition	Dominant orbital promotions	VEE/eV	*f*
S_1-S_0	6←5 (0.86); 7←5 (0.16); 8←5 (0.03)	3.00	0.0053
S_2-S_0	6←3 (0.55); 7←4 (0.33); 6←4 (0.30)	4.43	0.0127
T_1-S_0	6←4 (0.70); 6←5 (0.36); 7←4 (0.30)	2.87	0
T_2-S_0	6←5 (0.79); 6←4 (0.32); 7←5 (0.19)	3.09	0
T_3-S_0	6←3 (0.67); 7←4 (0.51); 6←2 (0.22)	4.03	0

*The second column details the orbital (see **Supplementary Figure 2**) promotions that make the larger contributions (expressed as coefficients in parentheses) to the respective excitations.*

cyclopropenone unit. The participating n/π and π^* orbitals show significant spatial overlap, reflected in a calculated S_2-S_0 oscillator strength some 2.5× larger than that of the S_1-S_0 transition (**Table 1**). This suggests a significant contribution from the phenyl-ring centered π-bonding region and, for brevity, we will henceforth refer to S_2 as a $\pi\pi^*$ excited state also.

For completeness, **Table 1** also lists the calculated VEEs to the first three triplet states. Excitations to these states from the singlet ground state are spin-forbidden and thus calculated to have zero oscillator strength. We also note the near degeneracy of the T_1 and T_2 states in the vertical region, and that the T_2 and S_1 states share a common dominant electronic configuration at this geometry.

Reaction Path Following Photoexcitation

Figure 2 displays the PE profiles along the reaction path depicted in **Scheme 1**. Panel (a) shows the profiles returned from a LIIC along the dimensionless coordinate Q_a connecting the minimum energy geometries of ground state CPE and the (triplet) intermediate formed via ring-opening of the cyclopropenone unit. As noted previously (Poloukhtine and Popik, 2006b), the alternative ring-opened intermediate that would be formed by cleaving the other C–C bond in the cyclopropenone unit (i.e., the bond further from the phenyl ring) lies at significantly higher energy (∼0.35 eV in the present calculations) and is not considered further. As such, Q_a is predominantly the C–C bond stretch indicated by the black arrow in **Figure 2A**. Along this path, the PE of the S_0 state shows a steady increase—as would be expected for the rupture of a C–C σ-bond. The PE of the S_1 state, in contrast, shows a small barrier and then decreases along this ring-opening coordinate. At this point, it is important to recall that LIIC pathways must, by construction, return upper estimates of any barriers that would be derived by locating and optimizing the true transition states, and we henceforth assume minimal barrier to distortion along Q_a on the S_1 PE surface. The topography of the S_1 potential can be understood by recognizing that the electronic configuration of the S_1 state (predominantly $\pi\pi^*$ in the vertical region) gains increasing $n\sigma^*$ character upon C–C bond extension. The decline in the S_1 state PE, together with the progressive increase in the S_0 state PE, leads to an inevitable crossing at $Q_a = 0.9$. This region of conical intersection is likely to encourage non-adiabatic coupling between the S_1 and S_0 states,

Reference to **Table 1** and the orbitals displayed in **Supplementary Figure 2** shows that the first excited singlet (S_1) state of CPE has $\pi\pi^*$ character and is formed by electron promotion between orbitals that include π-electron density distributed over the phenyl ring, cyclopropenone and alkyne moieties. The S_2 state has both $n\pi^*$ and $\pi\pi^*$ character and is formed by promotion from a 'mixed' bonding orbital that involves a non-bonding $p\sigma$ component (localized on the O atom) and a π-bonding component that is mainly localized on the phenyl ring but also conjugates across the C=C bond of the

i.e., to facilitate internal conversion to high vibrational levels of the S_0 state of CPE. These topological details serve to reinforce the earlier conclusion that the light-induced decarbonylation in cyclopropenones is a stepwise process initiated on the S_1 PE surface (Poloukhtine and Popik, 2006b).

This photoinduced ring opening can be viewed as another example of a singlet-mediated Norrish type I α-C–C bond cleavage in a ketone. Norrish type I reactions have traditionally been assumed to start with efficient $S_1 \rightarrow T_1$ ISC (Norrish and Bamford, 1936, 1937; Diau et al., 2001, 2002), and indeed, reference to **Figure 2A** suggests that $S_1 \rightarrow T_1$ ISC in CPE could constitute another route to the ring-opened species. However, the recent literature includes a growing number of predictions and/or demonstrations of purely singlet-state enabled fission of the C–C bond in the α-position (relative to the carbonyl group) (Maeda et al., 2010; Nádasdi et al., 2010; Marchetti et al., 2019), notably in strained cyclic ketones like cyclobutanone (Xia et al., 2015; Shemesh et al., 2016; Kao et al., 2020). In all such cases investigated to date, the C–C=O moiety remaining after photochemical cleavage of the other α-C–C bond is predicted to be near linear at the CI (Marchetti et al., 2019)—as is found in the present case also (see **Figure 2**). The photoinduced C–C bond fission in CPE is another such example, not least because—as we now show—**Scheme 1** requires further chemistry that can only occur on the S_0 PE surface. As **Supplementary Figure 5** in the ESI shows, the Mulliken charge distributions for the optimized ring-opened structure of the isolated molecule in its T_1 state and for the S_0 state molecule at that same geometry are similar, and far from limiting biradical or zwitterionic in character. Clearly, however, the degree of charge separation is likely to be different in solution and to be solvent-dependent.

The highly vibrationally-excited S_0 molecules formed by non-adiabatic coupling from the S_1 state may relax to reform the starting CPE molecule or follow a rival path on the S_0 PE surface. Given the experimental observations (Poloukhtine and Popik, 2005a, 2006b), one possible rival path must involve CO loss from the ring-opened biradical to form intermediate **B** in **Scheme 1**. To model this process, PE profiles were first computed simply by stepping the C–CO bond stretch coordinate (R_{C-CO}), but this revealed an obvious discontinuity in the S_0 and T_1 PE profiles at $R_{C-CO} \sim 1.8$ Å. This was traced to a localized linear to bent change in the geometry of the C–C=O unit, that we assume to be a signature of the onset of a π-stacking interaction between the emerging CO product and the alkyne group. Thus, the overall C–CO bond fission following opening of the cyclopropenone ring was modeled using two successive LIICs—Q_b, to cover the region from the minimum energy geometry of the triplet ring-opened structure to the relaxed bent geometry at $R_{C-CO} \sim 1.8$ Å, then Q_c, from the bent geometry at $R_{C-CO} \sim 1.8$ Å to long range.

The S_0 and excited state PE profiles associated with Q_b in **Figure 2B** show several features of note. The PE profile of the T_1 state (which is the most stable configuration of the ring-opened species) increases steadily. Unsurprisingly, given that the S_1 and T_1 states at these geometries are well-approximated as spin-flip variations of the same electronic configuration, the S_1 PE profile shows a similar increase. The PE of the S_0 state, in contrast, declines steadily along Q_b. This finding can be understood by inspecting the HOMO of the ring-opened species, which shows antibonding π* character around the C–CO bond. Occupancy of this orbital reduces the C–CO bond strength and, as with the initial ring-opening step, this HOMO gains progressive σ* character upon C–CO bond extension—leading to eventual bond
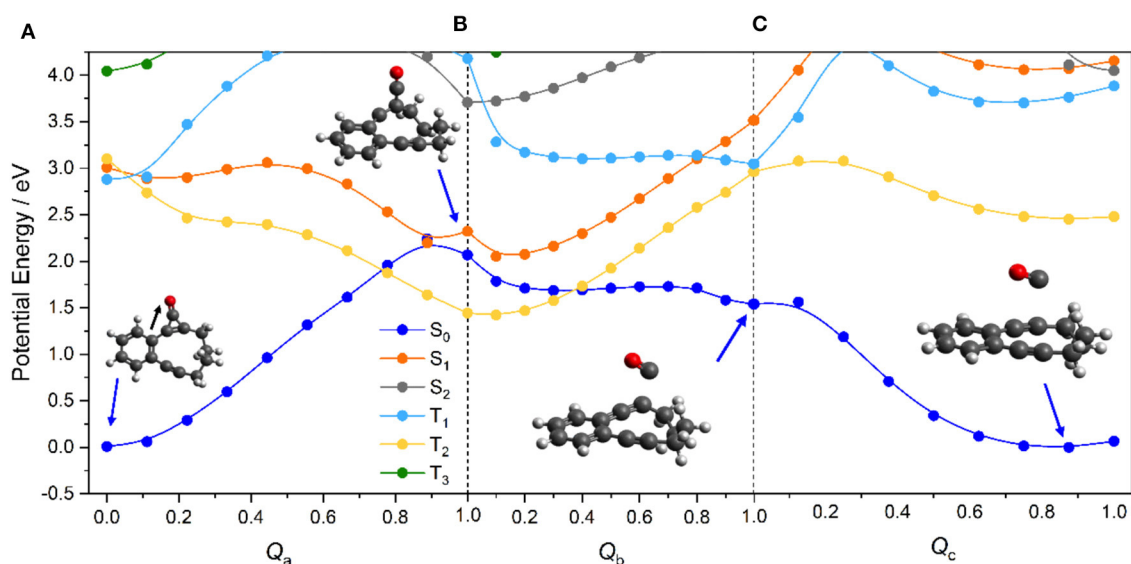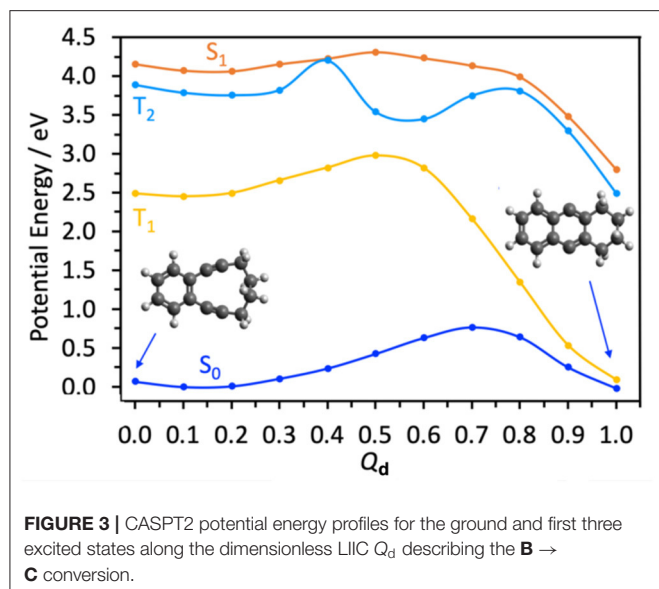

FIGURE 2 | CASPT2 potential energy profiles for the ground and first few excited states of CPE along the sequence of dimensionless LIICs (panels (a) through (c) as discussed in the text) involved in the photoinduced conversion of **A** → **B** (+ CO) products, with the molecular geometries at various critical points depicted. The color coding of the states shown in the inset in panel **(A)** defines the state ordering at $Q_a = 0$. Note, the energetic ordering of the states labeled T_1 and T_2 switches once Q_a > 0, and thereafter the adiabatic PE profiles of the T_1 and T_2 states are described by, respectively, the yellow and pale blue curves—here and in later figures.

FIGURE 3 | CASPT2 potential energy profiles for the ground and first three excited states along the dimensionless LIIC Q_d describing the **B → C** conversion.

TABLE 2 | Vertical excitation energies (VEEs) and oscillator strengths (f) of transitions to the lowest singlet and triplet excited states of **B**, calculated at the CASPT2/AVDZ level of theory.

Transition	Dominant orbital promotions	VEE/eV	f
S_1-S_0	6←4 (0.61); 7←5 (0.52); 6←5 (0.18)	4.09	0.0050
T_1-S_0	6←5 (0.89); 7←4 (0.18); 6←5+[7←4]² (0.13)	2.42	0
T_2-S_0	6←4 (0.61); 7←5 (0.52); 6←5 (0.12)	3.82	0

*The second column details the three orbital (see **Supplementary Figure 3**) promotions that make the largest contribution (expressed as coefficients in parentheses) to the respective excitations. []² implies a double excitation.*

fission. **Figure 2C** shows the corresponding PE profiles along Q_c. Of particular relevance to the current narrative, the PE profile of the S_0 state shows a continued steady decrease *en route* to forming the alkyne intermediate (structure **B** in **Scheme 1**).

Scheme 1 shows this alkyne intermediate undergoing a Bergman cyclization to form a ring-closed bicyclic biradical (structure **C**). **Figure 3** shows the calculated (by CASPT2) energy profile for this final step on the S_0 PE surface, along a LIIC (Q_d) linking structures **B** and **C**. This shows the di-alkyne intermediate **B** and the tricyclic biradical species **C** having essentially the same minimum energies, and separated by an intervening energy barrier with $\Delta E \sim 0.8$ eV. Reference to **Figure 2** shows that the minimum energy of **A** is also very similar to that of the **B** (+CO) limit. Noting the earlier comment that any energy barrier returned by a LIIC calculation will necessarily be an upper estimate of the true transition state energy and that the calculated barrier energy in **Figure 3** is well below that of the CI between the S_1 and S_0 PE surfaces of CPE (**Figure 2A**) suggests that both **B** and **C** could be thermodynamically viable products following photoexcitation of CPE, within which population may partition—consistent with the experimental observation of **B** formation [and the ensuing Bergman cyclisation to **C** at quite modest temperatures (84°C)] (Poloukhtine and Popik, 2005a).

Traditional organic photosyntheses such as that used to drive the transformation **A → C** employ prolonged illumination, so it is also prudent to consider possible photoinduced chemistry of the product **B** (Poloukhtine and Popik, 2005a,b, 2006a,b; Poloukhtine et al., 2008). **Table 2** lists the calculated VEEs to the S_1, T_1, and T_2 states of **B** (all of which are best viewed as having $\pi\pi^*$ character) and the S_1-S_0 oscillator strength and dominant contributing promotions based on the orbitals displayed in **Supplementary Figure 3**. **Figure 3** shows the calculated PE profiles of these three excited states along Q_d. As **Table 2** shows, the S_1-S_0 transition of **B** is predicted to have a similar oscillator strength to that of CPE but to have an appreciably larger VEE— which matches reasonably with the absorption maximum of

the product formed by 300 nm irradiation of CPE reported in Poloukhtine and Popik (2005a).
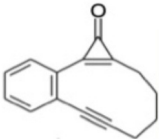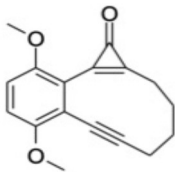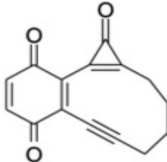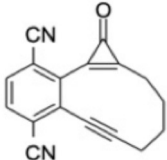
The PE profiles shown in **Figure 3** hint that secondary photoexcitation of **B** could feasibly aid **C** formation. Specifically, we note the near degeneracy of the S_1 and T_2 states at small Q_d and the possibility of strong non-adiabatic coupling around $Q_d \sim 0.4$, where the S_1 potential samples a region of configuration space that supports a conical intersection between the T_2 and (not shown) T_3 potentials. Any S_1 population undergoing (spin-orbit induced) transfer to the T_2 potential in this region could thereafter follow an energetically "down-hill" path via the T_2/T_1 conical intersection at $Q_d \sim 0.55$ and relax into the potential well of the low-lying triplet form of **C**. Higher level theory could inform on the possible importance of spin-orbit enabled transfer to the T_1 potential, but electron paramagnetic resonance (EPR) studies as a function of illumination time might be the best way of exploring the relative importances of one vs. sequential two photon production of **C** by near UV irradiation under synthetically relevant solution phase conditions.

Substituent Effects on the Electronic Absorption and Potential Reactivity of CPEs

Table 3 compares the VEEs, the x, y, and z components of the respective transition dipole moments and the overall oscillator strengths for forming the S_1 and S_2 states of bare CPE and the 1,4-MeO-CPE, 1,4-O=CPE and 1,4-CN-CPE analogs returned by the CASPT2 calculations. The orbital promotions that make the greatest contributions to the S_1-S_0 and S_2-S_0 transitions in each of the substituted molecules are included in **Supplementary Figure 4** in the ESI.

Even a cursory inspection of **Table 3** suffices to show that such symmetric changes at the 1- and 4-positions on the phenyl ring have a substantial effect on the electronic absorption of CPE. All are predicted to enhance the S_1-S_0 oscillator strength (*cf.* bare CPE), most strikingly in the cases of 1,4-MeO-CPE and the 1,4-benzoquinone derivative. Each involves net loss of electron density from the cyclopropenone carbonyl group (reflected in the negative TDM$_y$ values in **Table 3**); the S_1 molecules have some zwitterionic character—in accord with conclusions reached in earlier theoretical studies of alkyl- or aryl-substituted cyclopropenones (Poloukhtine and Popik, 2006b). Substituting the phenyl ring with π-accepting (i.e.,

TABLE 3 | Vertical excitation energies (VEEs), *x, y,* and *z* components of the respective transition dipole moments [TDMs (in atomic units)] and oscillator strengths (*f*) for the S_1-S_0 and S_2-S_0 transitions of (a) bare CPE, (b) 1,4-methoxy substituted CPE, (c) the 1,4-benzoquinone derivative, and (d) 1,4-cyano substituted CPE, calculated at the CASPT2/AVDZ level of theory.

Molecule	Transition	VEE/eV	TDM_x	TDM_y	TDM_z	*f*
(a)	S_1-S_0	3.00	−0.070	0.220	0.136	0.0053
	S_2-S_0	4.43	0.319	0.120	0.024	0.0127
(b)	S_1-S_0	3.25	0.872	−0.047	0.067	0.0706
	S_2-S_0	3.75	0.260	−0.581	0.433	0.0325
(c)	S_1-S_0	2.54	0.308	−0.781	0.086	0.0443
	S_2-S_0	3.81	−0.708	1.610	0.039	0.2887
(d)	S_1-S_0	3.25	0.256	−0.253	0.124	0.0115
	S_2-S_0	3.68	−0.371	−0.252	−0.021	0.0182

CN) or π-donating (i.e., MeO) groups increases the VEE of the S_1-S_0 transition (*cf.* bare CPE), but the enhanced conjugation introduced by replacing the phenyl ring by a 1,4-benzoquinone ring causes an obvious red-shift in the S_1-S_0 absorption.

The effects on the S_2-S_0 transitions are more substituent specific, with the calculated TDMs suggesting accumulation of electron density on the substituted phenyl ring in the case of 1,4-MeO-CPE and on the cyclopropenone sub-unit in the case of 1,4-O=CPE. In all cases, substitution is predicted to reduce the VEE of the S_2-S_0 transition (*cf.* bare CPE)—in accord with the available experimental data for 1,4-O=CPE and CPE (Poloukhtine and Popik, 2005a,b)

Table 4 shows the effect of substituents on the relative stabilities of the bicyclic enediyne and the Bergman cyclized product (henceforth labeled **B′** and **C′**) relative to the corresponding **B** and **C** products from photoexcitation of bare CPE. CO elimination (i.e., **A′**→ **B′**) is favored, energetically, by either CN substitution or by replacing the phenyl ring with a 1,4-benzoquinone unit, whereas 1,4-MeO substitution leads to a **B′** product that is marginally less stable than for bare CPE. The former stabilizations can be plausibly understood by considering the extended π-systems in the enediyne product. Thermodynamically, 1,4-O=CPE is in a class of its own with
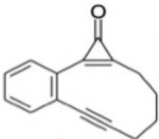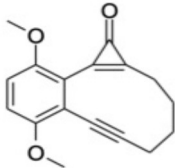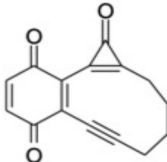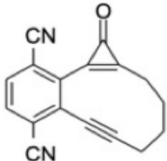
regard to the final **B′**→ **C′** electrocyclization reaction, consistent with its adoption as a precursor of choice by (Poloukhtine and Popik, 2006a).

CONCLUSIONS

This study offers a contemporary mechanistic description of the light-driven conversion of cyclopropenone containing enediyne precursors like CPE to ring-opened species amenable to further Bergman cyclization, resulting in stable biradical species that have been proposed for future use in light-induced cancer treatment (Poloukhtine and Popik, 2005a,b, Poloukhtine and Popik, 2006a; Poloukhtine et al., 2008). The initial photoinduced cleavage of the C–C bond in the cyclopropenone ring closer to the phenyl group is shown to follow Norrish type-I chemistry. In the present case, this can be accommodated by purely singlet-state chemistry, i.e., efficient non-adiabatic coupling from the photo-prepared S_1 state to high levels of the ground (S_0) PE surface, upon which subsequent nuclear rearrangements lead to CO loss and formation of **B**, followed by the electrocyclization of **B** to yield the cytotoxic target biradical species **C**.

Viewed from the perspective of the photoexcited **A*** precursor in **Scheme 1**, the reactions through to ground state **B** (and **C**)

TABLE 4 | CBS-QB3 calculated enthalpy changes associated with the respective $A' \to B'$ and $B' \to C'$ conversions in (b) 1,4-methoxy substituted CPE, (c) the 1,4-benzoquinone derivative, and (d) 1,4-cyano substituted CPE, each referenced to the corresponding $A \to B$ and $B \to C$ conversions in bare CPE (a).

Molecule	ΔH / eV	
	$\Delta H_{(A' \to B')} - \Delta H_{(A \to B)}$	$\Delta H_{(B' \to C')} - \Delta H_{(B \to C)}$
(a)	0	0
(b)	0.025	−0.014
(c)	−0.080	−0.407
(d)	−0.142	−0.001

products are exoergic processes, the efficiencies of which are likely to be sensitive to the relative rates of reaction and internal energy loss to the solvent. Deliberate (or otherwise)

secondary photoexcitation of the enediyne intermediate **B** is suggested as a way of boosting the yield of the target diradical species **C**. The present limited investigation of the effects of chemically modifying the phenyl moiety in **A** serves to vindicate the experimental choices made by Popik and coworkers (Poloukhtine and Popik, 2006a). Specifically, replacing the phenyl moiety in CPE by a 1,4-benzoquinone unit is shown to both red-shift and boost the absorption of the **A'** precursor and to increase the exoergicity of the required $A' \to C'$ conversion—complementing current efforts to use visible-light-responsive photocatalysts to trigger alkyne generation from (non-visible light absorbing) cyclopropenones (Mishiro et al., 2019).

DATA AVAILABILITY STATEMENT

The raw data supporting the conclusions of this article will be made available by the authors, without undue reservation.

AUTHOR CONTRIBUTIONS

TK and MA designed the project. SL, BM and TK undertook the underlying data. All authors contributed to drafting the manuscript.

ACKNOWLEDGMENTS

SUPPLEMENTARY MATERIAL

The Supplementary Material for this article can be found online at: https://www.frontiersin.org/articles/10.3389/fchem.2020.596590/full#supplementary-material

REFERENCES

Andersson, K., Malmqvist, P., and Roos, B. O. (1992). Second-order perturbation theory with a complete active space self-consistent field reference function. *J. Chem. Phys.* 96, 1218–1226. doi: 10.1063/1.462209

Andersson, K., Malmqvist, P. A., Roos, B. O., and Sadlej, A. (1990). Second-order perturbation theory with a CASSCF reference function. *J. Phys. Chem.* 94, 5483–5488. doi: 10.1021/j100377a012

Ashfold, M. N. R., Cronin, B., Devine, A. L., and Dixon, R. (2006). The role of πσ* excited states in the photodissociation of heteroaromatic molecules. *Science* 312, 1637–1640. doi: 10.1126/science.1125436

Ashfold, M. N. R., King, G. A., Murdock, D., and Nix, M. G. (2010). πσ* excited states in molecular photochemistry. *Phys. Chem. Chem. Phys.* 12, 1218–1238. doi: 10.1039/B921706A

Chan, H. C. S., Shan, H., Dahoun, T., Vogel, H., and Yuan, S. (2019). Advancing drug discovery via artificial intelligence. *Trends Pharmacol. Sci.* 40, 592–604. doi: 10.1016/j.tips.2019.06.004

Credo Chung, W., Lan, Z., Ohtsuki, Y., Shimakura, N., Domcke, W., and Fujimura, Y. (2007). Conical intersections involving the dissociative $^1\pi\sigma^*$ state

in 9H-adenine: a quantum chemical ab initio study. *Phys. Chem. Chem. Phys.* 9, 2075–2084. doi: 10.1039/B618745E

Cronin, B., Nix, M. G. D., Qadiri, R. H., and Ashfold, M. N. (2004). High resolution photofragment translational spectroscopy studies of the near ultraviolet photolysis of pyrrole. *Phys. Chem. Chem. Phys.* 6, 5031–5041. doi: 10.1039/b411589a

Cysewski, P. (2007). Accurate gas phase acidities of carboxylic acids estimated by scaling the vibrational contribution of ab initio gibbs free energies. *J. Mol. Model.* 13, 801–808. doi: 10.1007/s00894-007-0200-0

Devine, A. L., Cronin, B., and Nix, M. G. D. (2006). High resolution photofragment translational spectroscopy studies of the near ultraviolet photolysis of imidazole. *J. Chem. Phys.* 125:184302. doi: 10.1063/1.2364504

Diau, E. W. G., Kötting, C., Sølling, T. I., and Zewail, A. H. (2002). Femtochemistry of norrish type-I reactions: III. highly excited ketones—theoretical. *ChemPhysChem* 3, 57–78. doi: 10.1002/1439-7641(20020118)3:1<57::AID-CPHC57>3.0.CO;2-F

Diau, E. W. G., Kötting, C., and Zewail, A. H. (2001). Femtochemistry of norrish type-I reactions: experimental, I. and theoretical studies of acetone and related

ketones on the S1 surface. *ChemPhysChem* 2, 273–293. doi: 10.1002/1439-7641(20010518)2:5<273::AID-CPHC273>3.0.CO;2-H

Domcke, W., Yarkony, D. R., and Koeppel, H. (2004). *Conical Intersections: Electronic Structure, Dynamics & Spectroscopy*. doi: 10.1142/5406

Domcke, W., Yarkony, D. R., and Koeppel, H. (2011). *Conical Intersections: Theory, Computation and Experiment*. Singapore: World Scientific. doi: 10.1142/7803

Dunning, T. H. (1989). Gaussian basis sets for use in correlated molecular calculations. I. The atoms boron through neon and hydrogen. *J. Chem. Phys.* 90, 1007–1023. doi: 10.1063/1.456153

Elion, G. B. (1993). The quest for a cure. *Annu. Rev. Pharmacol. Toxicol.* 33, 1–25. doi: 10.1146/annurev.pa.33.040193.000245

Farrer, N. J., Woods, J. A., Salassa, L., and Zhao, Y. (2010). A potent trans-diimine platinum anticancer complex photoactivated by visible light. *Angew. Chemie Int. Ed.* 49, 8905–8908. doi: 10.1002/anie.201003399

Frisch, M. J., Trucks, G. W., and Schlegel, H. B. (2016). *Gaussian 16, Revision A.03*. Wallingford, CT: Gaussian Inc.

Furche, F., and Ahlrichs, R. (2002). Adiabatic time-dependent density functional methods for excited state properties. *J. Chem. Phys.* 117, 7433–7447. doi: 10.1063/1.1508368

Hehre, W. J., Ditchfield, R., Stewart, R. F., and Pople, J. (1970). Self-consistent molecular orbital methods. IV. use of gaussian expansions of slater-type orbitals. Extension to second-row molecules. *J. Chem. Phys.* 52, 2769–2773. doi: 10.1063/1.1673374

Henstock, P. V. (2019). Artificial intelligence for pharma: time for internal investment. *Trends Pharmacol. Sci.* 40, 543–546. doi: 10.1016/j.tips.2019.05.003

Imberti, C., Zhang, P., Huang, H., and Sadler, P. J. (2020). New designs for phototherapeutic transition metal complexes. *Angew. Chemie Int. Ed.* 59, 61–73. doi: 10.1002/anie.201905171

Jones, R. R., and Bergman, R. G. (1972). p-Benzyne. Generation as an intermediate in a thermal isomerization reaction and trapping evidence for the 1,4-benzenediyl structure. *J. Am. Chem. Soc.* 94, 660–661. doi: 10.1021/ja00757a071

Kao, M.-H., Venkatraman, R. K., and Ashfold, M. N. R. (2020). Effects of ring-strain on the ultrafast photochemistry of cyclic ketones. *Chem. Sci.* 11, 1991–2000. doi: 10.1039/C9SC05208A

Lee, J. A., Uhlik, M. T., and Moxham, C. M. (2012). Modern phenotypic drug discovery is a viable, neoclassic pharma strategy. *J. Med. Chem.* 55, 4527–4538. doi: 10.1021/jm201649s

Luxon, A. R., Orms, N., Kanters, R., and Krylov, A. I. (2018). An ab initio exploration of the bergman cyclization. *J. Phys. Chem. A* 122, 420–430. doi: 10.1021/acs.jpca.7b10576s

Maeda, S., Ohno, K., and Morokuma, K. (2010). A theoretical study on the photodissociation of acetone: insight into the slow intersystem crossing and exploration of nonadiabatic pathways to the ground state. *J. Phys. Chem. Lett.* 1, 1841–1845. doi: 10.1021/jz100551y

Mak, K.-K., and Pichika, M. R. (2019). Artificial intelligence in drug development: present status and future prospects. *Drug Discov. Today* 24, 773–780. doi: 10.1016/j.drudis.2018.11.014

Marchetti, B., Karsili, T. N. V., and Ashfold, M. N. R. (2016). A 'bottom up', ab initio computational approach to understanding fundamental photophysical processes in nitrogen containing heterocycles, DNA bases and base pairs. *Phys. Chem. Chem. Phys.* 18, 20007–20027. doi: 10.1039/C6CP00165C

Marchetti, B. V., Karsili, T. N., and Ashfold, M. N. R. (2019). Exploring norrish type I and type II reactions: an ab initio mechanistic study highlighting singlet-state mediated chemistry. *Phys. Chem. Chem. Phys.* 21, 14418–14428. doi: 10.1039/C8CP07292B

Menter, A., Korman, N. J., Elmets, C. A., and Feldman, S. (2009). Guidelines of care for the management of psoriasis and psoriatic arthritis: section 3. Guidelines of care for the management and treatment of psoriasis with topical therapies. *J. Am. Acad. Dermatol.* 60, 643–659. doi: 10.1016/j.jaad.2008.12.032

Mishiro, K., Kimura, T., Furuyama, T., and Kunishima, M. (2019). Phototriggered active alkyne generation from cyclopropenones with visible light-responsive photocatalysts. *Org. Lett.* 21, 4101–4105. doi: 10.1021/acs.orglett.9b01280

Nádasdi, R., Zügner, G. L., Farkas, M., Dóbé, S., and Maeda, S. (2010). Photochemistry of methyl ethyl ketone: quantum yields and S1/S0-diradical mechanism of photodissociation. *ChemPhysChem* 11, 3883–3895. doi: 10.1002/cphc.201000522

Nix, M. G. D., Devine, A. L., Cronin, B., and Ashfold, M. N. (2007). Ultraviolet photolysis of adenine: dissociation via the $^1\pi\sigma^*$ state. *J. Chem. Phys.* 126:124312. doi: 10.1063/1.2712843

Norrish, R. G. W., and Bamford, C. H. (1936). Photodecomposition of aldehydes and ketones. *Nature* 138:1016a0. doi: 10.1038/1381016a0

Norrish, R. G. W., and Bamford, C. H. (1937). Photo-decomposition of aldehydes and ketones. *Nature* 140, 195–196. doi: 10.1038/140195b0

Pandithavidana, D. R., Poloukhtine, A., and Popik, V. V. (2009). Photochemical generation and reversible cycloaromatization of a nine-membered ring cyclic enediyne. *J. Am. Chem. Soc.* 131, 351–356. doi: 10.1021/ja8077076

Park, J. W., and Shiozaki, T. (2017). Analytical derivative coupling for multistate CASPT2 theory. *J. Chem. Theory Comput.* 13, 2561–2570. doi: 10.1021/acs.jctc.7b00018

Paul, S. M., Mytelka, D. S., and Dunwiddie, C. T. (2010). How to improve R&D productivity: the pharmaceutical industry's grand challenge. *Nat. Rev. Drug Discov.* 9, 203–214. doi: 10.1038/nrd3078

Poloukhtine, A., Karpov, G., and Popik, V. V. (2008). Towards photoswitchable enediyne antibiotics. *Curr. Top. Med. Chem.* 8, 460–469. doi: 10.2174/156802608783955700

Poloukhtine, A., and Popik, V. V. (2005a). Application of photochemical decarbonylation of cyclopropenones for the *in situ* generation of reactive enediynes. Construction of a cyclopropenone-containing enediyne precursor by using a cyclopropenone acetal building block. *J. Org. Chem.* 70, 1297–1305. doi: 10.1021/jo048065y

Poloukhtine, A., and Popik, V. V. (2006a). Mechanism of the cyclopropenone decarbonylation reaction. A density functional theory and transient spectroscopy study. *J. Phys. Chem. A* 110, 1749–1757. doi: 10.1021/jp0563641

Poloukhtine, A., and Popik, V. V. (2006b). Two-photon photochemical generation of reactive enediyne. *J. Org. Chem.* 71, 7417–7421. doi: 10.1021/jo061285m

Poloukhtine, A., and Popik, V. V. (2005b). Photoswitchable enediynes: use of cyclopropenone as photocleavable masking group for the enediyne triple bond. *Chem. Commun.* 617–619. doi: 10.1039/b414951c

Rask-Andersen, M., Almén, M. S., and Schiöth, H. B. (2011). Trends in the exploitation of novel drug targets. *Nat. Rev. Drug Discov.* 10, 579–590. doi: 10.1038/nrd3478

Rayne, S., and Forest, K. (2010). Theoretical studies on the pKa values of perfluoroalkyl carboxylic acids. *J. Mol. Struct. Theochem.* 949, 60–69. doi: 10.1016/j.theochem.2010.03.003

Roberts, G. M., and Stavros, V. G. (2014). The role of $\pi\sigma^*$ states in the photochemistry of heteroaromatic biomolecules and their subunits: insights from gas-phase femtosecond spectroscopy. *Chem. Sci.* 5, 1698–1722. doi: 10.1039/c3sc53175a

Roos, B. O., Linse, P., and Siegbahn, P. E. M. (1982). A simple method for the evaluation of the second-order-perturbation energy from external double-excitations with a CASSCF reference wavefunction. *Chem. Phys.* 66, 197–207. doi: 10.1016/0301-0104(82)88019-1

Saracino, G. A. A., Improta, R., and Barone, V. (2003). Absolute pKa determination for carboxylic acids using density functional theory and the polarizable continuum model. *Chem. Phys. Lett.* 373, 411–415. doi: 10.1016/S0009-2614(03)00607-9

Scalmani, G., Frisch, M. J., Mennucci, B., Tomasi, J., and Cammi, R. (2006). Geometries and properties of excited states in the gas phase and in solution: theory and application of a time-dependent density functional theory polarizable continuum model. *J. Chem. Phys.* 124:94107. doi: 10.1063/1.2173258

Shemesh, D., Nizkorodov, S. A., and Gerber, R. B. (2016). Photochemical reactions of cyclohexanone: mechanisms and dynamics. *J. Phys. Chem. A* 120, 7112–7120. doi: 10.1021/acs.jpca.6b06184

Shi, H., Imberti, C., Huang, H., Hands-Portman, I., and Sadler, P. J. (2020). Biotinylated photoactive Pt(IV) anticancer complexes. *Chem. Commun.* 56, 2320–2323. doi: 10.1039/C9CC07845B

Shi, H., Imberti, C., and Sadler, P. J. (2019). Diazido platinum(IV) complexes for photoactivated anticancer chemotherapy. *Inorg. Chem. Front.* 6, 1623–1638. doi: 10.1039/C9QI00288J

Stern, R. S., Kleinerman, R. A., and Parrish, J. A. (1980). Phototoxic reactions to photoactive drugs in patients treated with PUVA. *Arch. Dermatol.* 116, 1269–1271. doi: 10.1001/archderm.116.11.1269

Swinney, D. C., and Anthony, J. (2011). How were new medicines discovered? *Nat. Rev. Drug Discov.* 10, 507–519. doi: 10.1038/nrd3480

Takenaka, T. (2001). Classical vs reverse pharmacology in drug discovery. *BJU Int.* 88, 7–10. doi: 10.1111/j.1464-410X.2001.00112.x

Van Caillie, C., and Amos, R. D. (2000). Geometric derivatives of density functional theory excitation energies using gradient-corrected functionals. *Chem. Phys. Lett.* 317, 159–164. doi: 10.1016/S0009-2614(99)01346-9

Vernooij, R. R., Joshi, T., Horbury, M. D., and Graham, B. (2018). Spectroscopic studies on photoinduced reactions of the anticancer prodrug, trans,trans,trans-[Pt(N$_3$)$_2$(OH)$_2$(py)$_2$]. *Chem. A Eur. J.* 24, 5790–5803. doi: 10.1002/chem.201705349

Warren, J. (2011). Drug discovery: lessons from evolution. *Br. J. Clin. Pharmacol.* 71, 497–503. doi: 10.1111/j.1365-2125.2010.03854.x

Werner, H.-J., Knowles, P. J., Knizia, G., Manby, F., R., Schütz, M., Celani, P., et al. (2018). *MOLPRO, Version 1, a Package of ab initio Programs.* Available online at: https://www.molpro.net

Xia, S.-H., Liu, X.-Y., Fang, Q., and Cui, G. (2015). Excited-state ring-opening mechanism of cyclic ketones: a MS-CASPT2//CASSCF study. *J. Phys. Chem. A* 119, 3569–3576. doi: 10.1021/acs.jpca.5b00302

Xie, C., Malbon, C. L., Yarkony, D. R., and Xie, D. (2018). Signatures of a conical intersection in adiabatic dissociation on the ground electronic state. *J. Am. Chem. Soc.* 140, 1986–1989. doi: 10.1021/jacs.7b11489

Yanai, T., Tew, D. P., and Handy, N. C. (2004). A new hybrid exchange–correlation functional using the coulomb-attenuating method (CAM-B3LYP). *Chem. Phys. Lett.* 393, 51–57. doi: 10.1016/j.cplett.2004.06.011

Conflict of Interest: The authors declare that the research was conducted in the absence of any commercial or financial relationships that could be construed as a potential conflict of interest.

The handling editor declared a past collaboration with the authors TK and MA.

Simulating Quantum Vibronic Dynamics at Finite Temperatures With Many Body Wave Functions at 0 K

Angus J. Dunnett* and Alex W. Chin

Sorbonne Université, CNRS, Institut des NanoSciences de Paris, Paris, France

For complex molecules, nuclear degrees of freedom can act as an environment for the electronic "system" variables, allowing the theory and concepts of open quantum systems to be applied. However, when molecular system-environment interactions are non-perturbative and non-Markovian, numerical simulations of the complete system-environment wave function become necessary. These many body dynamics can be very expensive to simulate, and extracting finite-temperature results—which require running and averaging over many such simulations—becomes especially challenging. Here, we present numerical simulations that exploit a recent theoretical result that allows dissipative environmental effects at finite temperature to be extracted efficiently from a single, zero-temperature wave function simulation. Using numerically exact time-dependent variational matrix product states, we verify that this approach can be applied to vibronic tunneling systems and provide insight into the practical problems lurking behind the elegance of the theory, such as the rapidly growing numerical demands that can appear for high temperatures over the length of computations.

Keywords: open quantum systems, tunneling, thermal relaxation, decoherence and noise, vibronic, matrix product state (MPS)

1. INTRODUCTION

The dissipative quantum dynamics of electronic processes play a crucial role in the physics and chemistry of materials and biological life, particularly in the ultra-fast and non-equilibrium conditions typical of photophysics, nanoscale charge transfer and glassy, low-temperature phenomena (Miller et al., 1983). Indeed, the through-space tunneling of electrons, protons and their coupled dynamics critically determine how either ambient energy is transduced, or stored energy is utilized in supramolecular "devices," and real-time dynamics are especially important when the desired processes occur against thermodynamical driving forces, or at the single-to-few particle level (Devault, 1980; May and Kühn, 2008).

In many physio-chemical systems, a reaction, energy transfer, or similar event proceeds in the direction of a free energy gradient, necessitating the dissipation of energy and the generation of entropy (Dubi and Dia Ventra, 2011; Benenti et al., 2017). A powerful way of modeling the microscopic physics at work during these irreversible dynamics is the concept of an "open" quantum system (Breuer and Petruccione, 2002; Weiss, 2012). Here a few essential and quantized degrees of freedom constituting the "system" are identified and explicitly coupled to a much larger number of "environmental" degrees of freedom. Equations of motion for the coupled system and

environment variables are then derived and solved, with the goal of obtaining the behavior of the "system" degrees of freedom once the unmeasureable environmental variables are averaged over their uncertain initial and final states. It is in this "tracing out" of the environment that the originally conservative, reversible dynamics of the global system gives way to apparently irreversible dynamics in the behavior of the system's observable variables. The effective behavior of the system "opened" to the environment is entirely contained within its so-called reduced density matrix, which we shall later define. Important examples of the emergent phenomenology of reduced density matrices include the ubiquitous processes of thermalization, dephasing, and decoherence.

In the solid state, a typical electronic excitation will interact weakly with the lattice vibrations of the material, particularly the long-wavelength, low frequency modes. Under such conditions it is often possible to treat the environment with low-order perturbation theory and—given that the lattice "environment" relaxes back to equilibrium very rapidly—it is possible to derive a Markovian master equation for the reduced density matrix, such as the commonly used Bloch-Redfield theory (Breuer and Petruccione, 2002; May and Kühn, 2008; Weiss, 2012). However, in sufficiently complex molecular systems, such as organic bio-molecules, the primary environmental degrees of freedom acting on electronic states are typically the stochastic vibrational motions of the atomic nuclear coordinates. Unlike the solid state, these vibrations can: (1) couple non-perturbatively to electronic states, (2) relax back to equilibrium on timescales that are longer than the dynamics they induce in the system, and (3) have frequencies ω such that $\hbar\omega \gg K_B T$, where T is the environmental temperature, and so must be treated quantum mechanically (zero-point energy and nuclear quantum effects). In this regime, the theory and numerical simulation of open quantum systems becomes especially challenging, as the detailed dynamics of the interacting system and environmental quantum states need to be obtained, essentially requiring the solution of a correlated (entangled) many body problem.

One well-known and powerful approach to this problem in theoretical chemistry is the Multi-layer Multiconfigurational Time-dependent Hartree (ML-MCTDH) technique, which enables vibronic wave functions to be efficiently represented and propagated without the *a priori* limitations due to the "curse of dimensionality" associated with many body quantum systems (Lubich, 2015; Wang and Shao, 2019). However, computationally demanding methods based on the propagation of a large wave function from a definite initial state will typically struggle when dealing with finite-temperature environments (*vide infra*), as the probability distribution of initial states requires extensive sampling. For this reason, the majority of ML-MCTDH studies have been effectively on zero-temperature systems.

In this article we will explore a recent and intriguing development in an alternative approach to real-time dynamics and chemical rate prediction. This approach is based on the highly efficient representation and manipulation of large, weakly entangled wave functions with DMRG, Matrix-Product, and Tensor-Network-State methods (Orus, 2014). These methods, widely used in condensed matter, quantum information and cold atom physics, have recently been applied to a range of open system models, including chemical systems, but—as wave function methods—are typically used at zero-temperature (Prior et al., 2010, 2013; Chin et al., 2013; Alvertis et al., 2019; Schröder et al., 2019; Xie et al., 2019). However, a remarkable new result due to Tamascelli et al. shows that it is indeed possible to obtain the *finite-temperature* reduced dynamics of a system based on a simulation of a "pure," i.e., zero-temperature wave function (Tamascelli et al., 2019).

In principle, this opens the way for many existing wave function methods to be extended into finite temperature regimes, although the present formulation of Tamascelli et al.'s T-TEDOPA mapping is most easily implemented with matrix product states (MPS). In this article, we shall investigate this extension to finite temperature in the regime of relevance for molecular quantum dynamics, that is, non-perturbative vibrational environments, and present numerical data that verifies the elegance and utility of the method, as well as some of the potential issues arising in implementation.

The structure of the article is as follows. In section 2, we will summarize Tamascelli et al.'s T-TEDOPA mapping. In section 3, we verify the theory by comparing numerical simulations against an exactly solvable open system model, and also employ further numerical investigations to provide some insight into the manner in which finite temperatures are handled within this method. By looking at the observables of the environment, we find that the number of excitations in the simulations grows continuously over time, which may place high demands on computational resources in some problems. In section 4, we will present results for a model system inspired by electron transfer in a multi-dimensional vibrational environment, and show how the temperature-driven transition from quantum tunneling to classical barrier transfer are successfully captured by this new approach. This opens a potentially fruitful new phase for the application of tensor network and related many body approaches for the simulation of non-equilibrium dynamics in a wide variety of vibronic materials and molecular reactions.

2. T-TEDOPA

In this section we shall summarize the essential features of the T-TEDOPA approach, closely following the original notation and presentation of Tamascelli et al. (2019). Our starting point is the generic Hamiltonian for a system coupled to a bosonic environment consisting of a continuum of harmonic oscillators

$$H_{SE} = H_S + H_E + H_I, \qquad (1)$$

where

$$H_I = A_S \otimes \int_0^\infty d\omega \hat{O}_\omega, H_E = \int_0^\infty d\omega \omega a_\omega^\dagger a_\omega. \qquad (2)$$

The Hamiltonian H_S is the free system Hamiltonian, which for chemical systems, molecular photophysics and related problems will often be a description of a few of the most relevant diabatic states at some reference geometry of the environment(s) (May

FIGURE 1 | (A) A generic open quantum system contains a few-level "system" (S) that interacts with a much larger thermal heat bath of bosonic oscillators (the environment, E). The continuum of oscillator modes are initially uncorrelated with the system and each is thermally occupied with characteristic temperature $T = \beta^{-1}$. Coupling and stochastic fluctuations of the environment lead to the effective thermalization of the system, once the environmental states have been traced over. **(B)** In the T-TEDOPA approach, the harmonic environment is extended to include modes of negative frequency, and all modes (positive and negative frequency) are initially in their ground states. It can be formally demonstrated that the thermalization of S in **(A)** can always be obtained from the pure zero-temperature state in **(B)**, provided the spectral density of the original environment is known.

and Kühn, 2008). A_S is the system operator which couples to the bath. For the bath operators we take the displacements

$$O_\omega = \sqrt{J(\omega)}(a_\omega + a_\omega^\dagger), \tag{3}$$

thus defining the spectral density $J(\omega)$. This has been written here as a continuous function, but coupling to a discrete set of vibrational modes in, say, a molecular chromophore, can be included within this description by adding suitable structure to the spectral density, i.e., sets of Lorentzian peaks or Dirac functions (Wilhelm et al., 2004; Schulze and Kuhn, 2015; Mendive-Tapia et al., 2018). The state of the system+environment at time t is described by a mixed state described by a density matrix $\rho_{SE}(t)$. The initial condition is assumed to be a product of system and environment states $\rho_{SE}(0) = \rho_S(0) \otimes \rho_E(0)$ where $\rho_S(0)$ is an arbitrary density matrix for the system and $\rho_E(0) = \exp(-H_E\beta)/\mathcal{Z}$, with the environment partition function given by $\mathcal{Z} = \text{Tr}\{\exp(-H_E\beta)\}$. Such a product state is commonly realized in photophysics, where the reference geometry for the environment is the electronic ground state and the electronic system is excited according to the Franck-Condon principle into some manifold of electronic excited states without nuclear motion (Mukamel, 1995; May and Kühn, 2008). Indeed, this can also occur following any sufficiently rapid non-adiabatic event, just as ultra-fast charge separation at a donor-acceptor interface (Gélinas et al., 2019; Smith and Chin, 2015). The environment thus begins in a thermal equilibrium state with inverse temperature β, and the energy levels of each harmonic mode are statistically populated, as shown in **Figure 1A**. For a very large (continuum) of modes, the number of possible thermal configurations of the initial probability distribution grows extremely rapidly with temperature, essentially making a

naive sampling of these configurations impossible for full wave function simulations. We note, however, that some significantly better sampling methods involving sparse grids and/or stochastic mean-field approaches have been proposed and demonstrated (Alvermann and Fehske, 2009; Binder and Burghardt, 2019).

The initial thermal condition of the environmental oscillators is also a Gaussian state, for which is it further known that the influence functional (Weiss, 2012)—which is a full description of the influence of the bath on the system—will depend only on the two-time correlation function of the bath operators

$$S(t) = \int_0^\infty d\omega \langle O_\omega(t) O_\omega(0) \rangle. \tag{4}$$

Any two environments with the same $S(t)$ will have the same influence functional and thus give rise to the same reduced system dynamics, i.e., the same $\rho_S(t) = \text{Tr}\{\rho_{SE}(t)\}$. That the reduced systems dynamics are completed specified by the spectral density and temperature of a Gaussian environment has been known for a long time (Weiss, 2012), but the key idea of the equivalence—and thus the possibility of the interchange—of environments with the same correlation functions has only recently been demonstrated by Tamascelli et al. (2018).

The time dependence in Equation (4) refers to the interaction picture so that the bath operators evolve under the free bath Hamiltonian: $O_\omega(t) = e^{iH_E t} O_\omega(0) e^{-iH_E t}$. Using Equation (3) and $\langle a_\omega^\dagger a_\omega \rangle = n_\beta(\omega)$ we have

$$S(t) = \int_0^\infty J(\omega)[e^{-i\omega t}(1 + n_\beta(\omega)) + e^{i\omega t} n_\beta(\omega)]. \tag{5}$$

Making use of the relation

$$\frac{1}{2}(1 + \coth(\omega\beta/2)) \equiv \begin{cases} n_\omega(\beta), \omega \geq 0 \\ -(n_{|\omega|}(\beta) + 1), \omega < 0 \end{cases} \quad (6)$$

we can write Equation (5) as an integral over all positive and negative ω

$$S(t) = \int_{-\infty}^{\infty} d\omega \text{sign}(\omega) \frac{J(|\omega|)}{2}(1 + \coth(\frac{\omega\beta}{2}))e^{-i\omega t}. \quad (7)$$

But Equation (7) is exactly the two-time correlation function one would get if the system was coupled to a bath, now containing positive and negative frequencies, at zero temperature, with a temperature weighted spectral density given by

$$J_\beta(\omega) = \text{sign}(\omega) \frac{J(|\omega|)}{2}(1 + \coth(\frac{\omega\beta}{2})). \quad (8)$$

Thus, we find that our open system problem is completely equivalent to the one governed by the Hamiltonian

$$H = H_S + H_E^{\text{ext}} + H_I^{\text{ext}}, \quad (9)$$

in which the system couples to an extended environment, where

$$H_I^{\text{ext}} = A_S \otimes \int_{-\infty}^{\infty} d\omega \sqrt{J_\beta(\omega)}(a_\omega + a_\omega^\dagger),$$
$$H_E^{\text{ext}} = \int_{-\infty}^{\infty} d\omega \omega a_\omega^\dagger a_\omega, \quad (10)$$

and which has the initial condition $\rho_{SE}(0) = \rho_S(0) \otimes |0\rangle_E \langle 0|$. The system now couples to a bath consisting of harmonic oscillators of positive and negative frequencies which are initially in their ground states, as shown in **Figure 1B**. This transformed initial condition is now far more amenable to simulation as the environment is now described by a *pure*, single-configuration wave function, rather than a statistical mixed state, and so *no* statistical sampling is required to capture the effects of temperature on the reduced dynamics!

Analyzing the effective spectral density of Equation (8), it can be seen that the new extended environment has thermal detailed balance between absorption and emission processes encoded in the ratio of the coupling strengths to the positive and negative modes in the extended *Hamiltonian*, as opposed to the operator statistics of a thermally occupied *state* of the original, physical mode, i.e.,

$$\frac{J_\beta(\omega)}{J_\beta(-\omega)} = \frac{\langle a_\omega a_\omega^\dagger \rangle_\beta}{\langle a_\omega^\dagger a_\omega \rangle_\beta} = e^{\beta\omega} \quad (11)$$

Indeed, from the system's point of view, there is no difference between the absorption from an occupied, positive energy, bath mode and the emission into an unoccupied, negative energy, bath mode.

In fact, the equivalence between these two environments goes beyond the reduced system dynamics as there exists a unitary transformation which links the extended environment
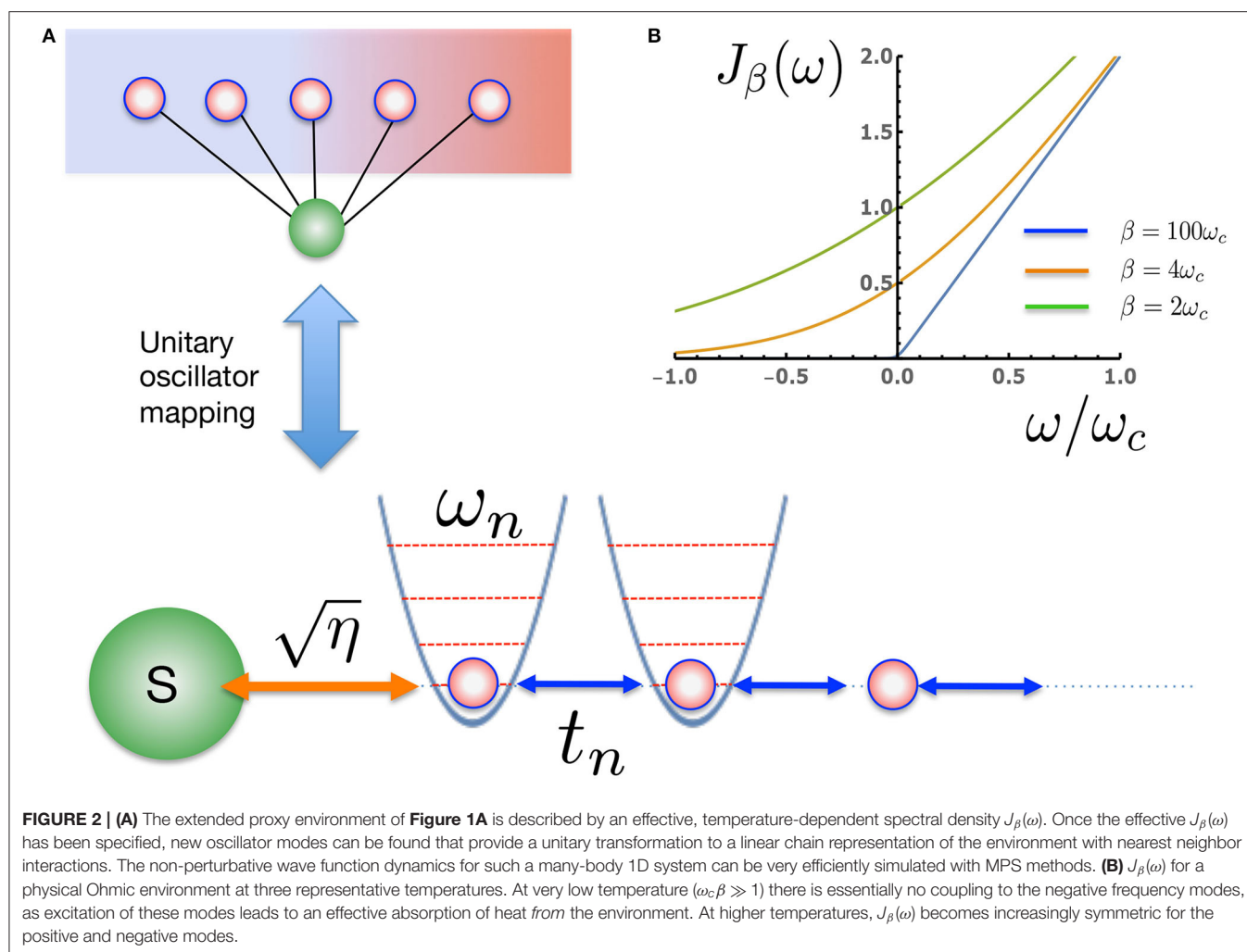
to the original thermal environment. This means that one is able to reverse the transformation and calculate thermal expectations for the actual bosonic bath such as $\langle a_\omega^\dagger(t) a_\omega(t) \rangle_\beta$. This is particularly useful for molecular systems in which environmental (vibrational) dynamics are also important observables that report on the mechanisms and pathways of physio-chemical transformations (Musser et al., 2015; Schnedermann et al., 2016, 2019). This is a major advantage of many body wave function approaches, as the full information about the environment is available, c.f. effective master equation descriptions which are obtained *after* averaging over the environmental state. We note that the idea of introducing a second environment of negative frequency oscillators to provide finite temperature effects in pure wave functions was previously proposed in the thermofield approach of de Vega and Bañuls (2015). This approach explicitly uses the properties of two-mode squeezed states to generate thermal reduced dynamics, but the original thermofield approach, unlike the T-TEDOPA mapping, considered the positive and negative frequency environments as two separate baths.

Following this transformation a further step is required to facilitate efficient simulation of the many-body system+environment wave function. This is to apply a unitary transformation to the bath modes which converts the *star*-like geometry of H_I^{ext} into a *chain*-like geometry, thus allowing the use of MPS methods (Chin et al., 2010, 2013; Prior et al., 2013). We thus define new modes $c_n^{(\dagger)} = \int_{-\infty}^{\infty} U_n(\omega) a_\omega^{(\dagger)}$, known as chain modes, via the unitary transformation $U_n(\omega) = \sqrt{J_\beta(\omega)} p_n(\omega)$ where $p_n(\omega)$ are orthonormal polynomials with respect to the measure $d\omega J_\beta(\omega)$. Thanks to the three term recurrence relations associated with all orthonormal polynomials $p_n(\omega)$, only one of these new modes, $n = 1$, will be coupled to the system, while all other chain modes will be coupled only to their nearest neighbors (Chin et al., 2010). Our interaction and bath Hamiltonians thus become

$$H_I^{\text{chain}} = \kappa A_S(c_1 + c_1^\dagger),$$
$$H_E^{\text{chain}} = \sum_{n=1}^{\infty} \omega_n c_n^\dagger c_n + \sum_{n=1}^{\infty} (t_n c_n^\dagger c_{n+1} + h.c). \quad (12)$$

The chain coefficients appearing in Equation (12) are related to the three-term recurrence parameters of the orthonormal polynomials and can be computed using standard numerical techniques (Chin et al., 2010). The full derivation of the above Hamiltonian is given in the **Appendix**. Since the initial state of the bath was the vacuum state, it is unaffected by the chain transformation.

We have thus arrived at a formulation of the problem of finite-temperature open systems in which the many-body environmental state is initialized as a pure product of trivial ground states, whilst the effects of thermal fluctuations and populations are encoded in the Hamiltonian chain parameters and system-chain coupling. These parameters must be determined once for each temperature but—in principle—the actual simulation of the many body dynamics is now no more complex than a zero-temperature simulations. This thus opens

FIGURE 2 | (A) The extended proxy environment of **Figure 1A** is described by an effective, temperature-dependent spectral density $J_\beta(\omega)$. Once the effective $J_\beta(\omega)$ has been specified, new oscillator modes can be found that provide a unitary transformation to a linear chain representation of the environment with nearest neighbor interactions. The non-perturbative wave function dynamics for such a many-body 1D system can be very efficiently simulated with MPS methods. **(B)** $J_\beta(\omega)$ for a physical Ohmic environment at three representative temperatures. At very low temperature ($\omega_c\beta \gg 1$) there is essentially no coupling to the negative frequency modes, as excitation of these modes leads to an effective absorption of heat *from* the environment. At higher temperatures, $J_\beta(\omega)$ becomes increasingly symmetric for the positive and negative modes.

up the use of powerful $T = 0K$ wave function methods for open systems, such as those based on MPS, numerical renormalization group and ML-MCTDH (Lubich, 2015; Wang and Shao, 2019). However, while this seems remarkable—and we believe this mapping to be a major advance—there must be a price to be paid elsewhere. We shall now demonstrate with numerical examples where some of the computational costs for including finite-T effects may appear and discuss how they might effect the feasibility and precision of simulations. We also propose a number of ways to mitigate these potential problems within the framework of tensor network approaches.

3. NUMERICAL TESTS AND COMPUTATIONAL EFFICIENCY

All numerical results in the following sections are obtained by representing the many body system-environment wave function as a MPS and evolving it using time-dependent variational methods. All results have been converged w.r.t. the parameters of MPS wave functions (bond dimensions, local Hilbert space dimensions, integrator time steps), meaning that the results

and discussion should—unless explicitly stated—pertain to the essential properties of the T-TEDOPA mapping itself. Extensive computational details and background theory can be founds in Orus (2014), Schollwock (2011), Lubich et al. (2015), Paeckel et al. (2019), and Haegeman et al. (2016).

3.1. Chain Dynamics and Chain-Length Truncation

Before looking at the influence of thermal bath effects on a quantum system, we first investigate the effects of the changing chain parameters that appear due to the inclusion of temperature in the effective spectral density $J_\beta(\omega)$. As a consequence of the nearest-neighbor nature of Equation (12) (see **Figure 2**), the chain mapping establishes a kind of causality among the bath modes which is extremely convenient for simulation. Starting from $t = 0$ the system will interact first with the chain mode $n = 1$ which, as well as acting back on the system, will in turn excite the next mode along the chain and so on. The dynamics thus have a well-defined light-cone structure in which a perturbation travels outwards from the system along the chain to infinity. This means that we may truncate the chain at any distant mode $n = N$
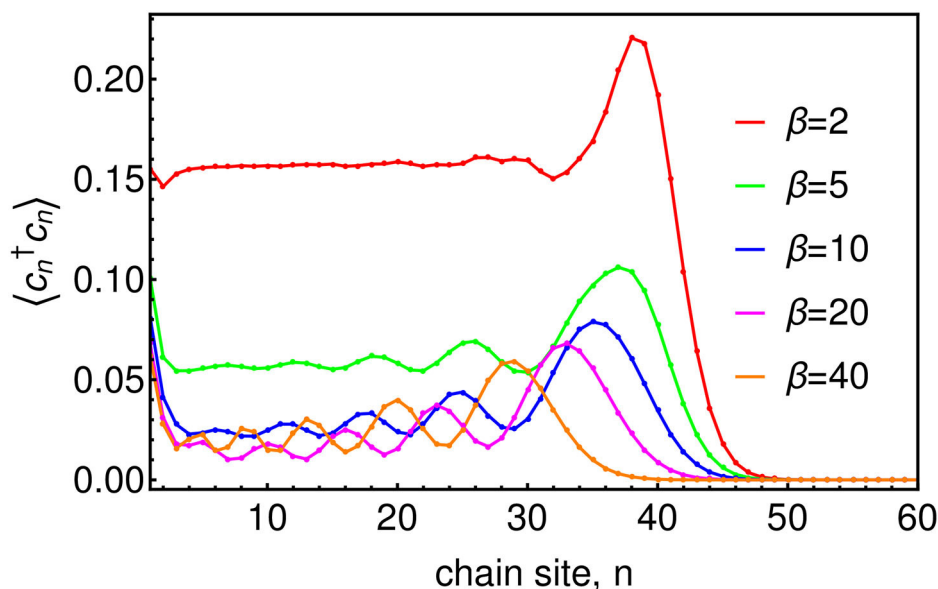
FIGURE 3 | Chain mode occupations $\langle c_n^\dagger c_n \rangle$ at time $\omega_c t = 45$ for baths of several temperatures. The system, which in this case is the Ohmic SBM, with $\omega_0 = 0.2\omega_c$ and $\alpha = 0.1$, is attached at site $n = 1$ of the chain.

without causing an error in the system or bath observables up to a certain time $T_{LC}(N)$ which is the time it takes for the edge of the light-cone to reach the Nth chain mode. Beyond $T_{LC}(N)$ there will be reflections off the end of the chain leading to error in the bath observables, however these reflections will not cause error in the system observables until the time $t \approx 2T_{LC}(N)$. **Figure 3** shows a snapshot of the chain mode occupations for the Ohmic spin-boson model considered in the next section. One can see that the velocity of the wave-front that travels outward from the system depends on temperature, with hotter baths leading to faster propagation and thus requiring somewhat longer chains.

To enable simulation we are also required to truncate the infinite Fock space dimension of each chain mode to a finite dimension d, introducing an error for which there exist rigorously derived bounds (Woods et al., 2015). The initial state $|\Psi(0)\rangle_{SE} = |\psi(0)\rangle_S \otimes |0\rangle_E$ (here we specialize to the case where the system is initially in a pure state) can then be encoded in an MPS and evolved under one of the many time-evolution methods for MPS. We choose to use the one-site Time-Dependent-Variational-Principle (1TDVP) as it has been shown to be a efficient method for tracking long-time thermalization dynamics and has previously been shown to give numerically exact results for the zero-temperature spin-boson model in the highly challenging regime of quantum criticality (Schröder and Chin, 2016). In our implementation of 1TDVP the edge of the light-cone is automatically estimated throughout the simulation by calculating the overlap of the wave-function $|\Psi(t)\rangle_{SE}$ with its initial value $|\Psi(0)\rangle_{SE}$ at each chain site. This allows us expand the MPS dynamically to track to expanding light-cone, providing roughly a 2-fold speed-up compared to using a fixed length MPS.

3.2. Two-Level System Dynamics: Dephasing and Divergence of Chain Occupations Due to Energy Exchange

To confirm the accuracy of this approach in terms of reduced system dynamics we now explore the effects of a dissipative environment on a quantum two-level system. First, we compare the numerical results against the analytically solvable Independent-Boson-Model (IBM) (Mahan, 2000; Breuer and Petruccione, 2002). This is a model of pure dephasing, defined by $H_S = \frac{\omega_0}{2}\sigma_z$ and $A_S = \sigma_z$, where $\{\sigma_x, \sigma_y, \sigma_z\}$ are the standard Pauli matrices. We take an Ohmic spectral density with a hard cut-off $J(\omega) = 2\alpha\omega\Theta(\omega - \omega_c)$ and choose a coupling strength of $\alpha = 0.1$ and a gap of $\omega_0 = 0.2\omega_c$ for the two level system (TLS). The initial state of the system is a positive superposition of the spin-up and spin-down states, and we monitor the decay of the TLS coherence, which is quantified by $\langle \sigma_x(t) \rangle$. All results were converged using a Fock space dimension of $d = 6$ for the chain modes and maximum MPS bond-dimension $D_{\max} = 4$. We find that the results obtained using the T-TEDOPA method agree very well with the exact solution (see **Figure 4**) and correctly reproduce the transition from under-damped to over-damped decay as the temperature is increased (Mahan, 2000; Breuer and Petruccione, 2002).

As a second numerical example we take the Spin-Boson-Model (SBM), identical to the IBM considered above except that now the TLS couples to the bath via $A_S = \sigma_x$. Unlike the previous case, the bath can now drive transitions within the TLS, so that energy is now dynamically exchanged between the TLS and its environment. Indeed, as A_S no longer commutes with H_S, no exact solution for this model is known (Weiss, 2012). It has thus become an important testing ground for numerical approaches to non-perturbative simulations of open systems and
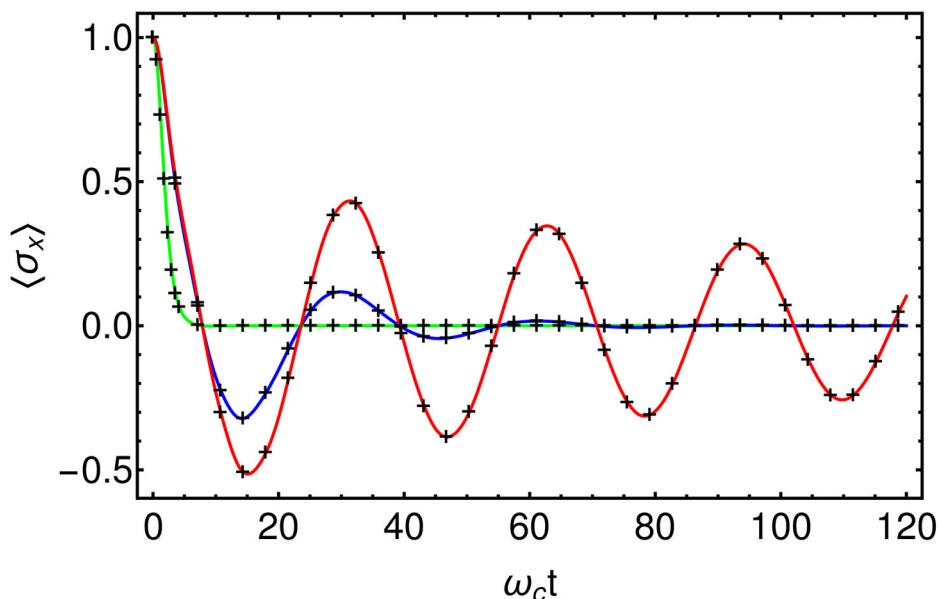
FIGURE 4 | Comparison of T-TEDOPA (Black crosses) with the exact solution for the Independent-Boson-Model at $\beta = 100$ (Red), $\beta = 10$ (Blue), and $\beta = 1$ (Green). $H_S = \frac{\omega_0}{2}\sigma_z$, $A_S = \sigma_z$, $J(\omega) = 2\alpha\omega_c(\frac{\omega}{\omega_c})^s\Theta(\omega - \omega_c))$, $\alpha = 0.1$, $s = 1$, $\omega_0 = 0.2\omega_c$.

has been widely applied to the physics of decoherence, energy relaxation and thermalization in diverse physical, chemical and biological systems—see Weiss, 2012; De Vega and Alonso, 2017 for extensive references. In our example, we prepare the spin in the upper spin state ($\langle\sigma_z\rangle = +1$) and allow the bath to thermalize by environmental energy exchange (see **Figure 1A**). Here, instead of presenting the spin dynamics for this model we will here interest ourselves in the observables of the bath as these will provided insight into the manner in which a finite temperature bath is being mimicked by an initially empty tight-binding chain. In **Figure 5**, we plot the bath mode occupations $\langle a_\omega^\dagger a_\omega\rangle$ for several temperatures. Each observation was taken after the spin had decayed into its thermal steady state and thus provides a kind of absorption spectrum for the system. We note that these data refer to the modes of the extended environment of Equation (9) rather than the original bosonic bath and thus the mode energies run from $-\omega_c$ to ω_c.

We find that for zero temperature ($\beta = \infty$) the bath absorption spectrum contains a single peak at a frequency around $\omega_p = 0.17\omega_c$, suggesting that the spin emits into the bath at a re-normalized frequency that is lower than the bare gap of the TLS ($\omega_0 = 0.2\omega_c$). This agrees well with the renormalized gap $\omega_0^r = \omega_0(\omega_0/\omega_c)^{\frac{\alpha}{1-\alpha}}$ predicted by the non-perturbative variational polaron theory of Silbey and Harris (1984), which for the parameters used here gives $\omega_0^r = 0.167\omega_c$.

Moving to non-zero temperature we see that a peak begins to form at a corresponding negative frequency, which we interpret as being due the spin absorbing thermal energy from the bath by the *emission* (creation) of negative energy quanta. In accordance with detailed balance, the ratio between the positive and negative frequency peaks approaches unity as temperature is increased and by $\beta\omega_c = 2$ the two peaks have merged to form a

single, almost symmetric, distribution, reflecting the dominance of thermal absorption and emission over spontaneous emission at high temperature. Indeed, as shown in the right inset of **Figure 5** the ratio of the peak heights we extract obeys $\frac{\langle n_\omega\rangle+1}{\langle n_{-\omega}\rangle} = e^{\epsilon\beta}$ with $\epsilon = 0.118$. Thus we see that the chain is composed of two independent vacuum reservoirs of positive and negative energy which the system emits into at rates which effectively reproduce the emission and absorption dynamics that would be induced by a thermal bath.

However, the introduction of positive and negative modes has an interesting and important consequence for the computational resources required for simulation. Shown in the left inset of **Figure 5** is the total mode occupation as a function of time for some of the different temperatures simulated. One sees that for $\beta = \infty$ (zero temperature) the total occupation of the bath modes increases initially and then plateaus at a certain steady state value corresponding to the total number of excitations created in the bath by the TLS during its decay. In contrast, for finite temperature, the total mode occupation increases indefinitely at a rate which grows with temperature. This is despite the fact that for the finite temperature baths the total excitation number will also reach a steady state once the TLS has decayed. The reason for this is clear. The thermal occupation of the physical bath mode with frequency ω is obtained by subtracting its negative, from its positive energy counterpart in the extended mode basis, i.e., $\langle n_\omega\rangle_\beta = \langle n_\omega\rangle_{|0\rangle_E} - \langle n_{-\omega}\rangle_{|0\rangle_E}$. While $\langle n_\omega\rangle_\beta$ will reach a steady state, the components $\langle n_\omega\rangle_{|0\rangle_E}$ and $\langle n_{-\omega}\rangle_{|0\rangle_E}$ will be forever increasing, reflecting the fact that the TLS reaches a *dynamic* equilibrium with the bath in which energy is continuously being absorbed from and emitted into the bath at equal rates, thus filling up the positive and negative reservoirs. Since, it is the modes of the *extended* environment that
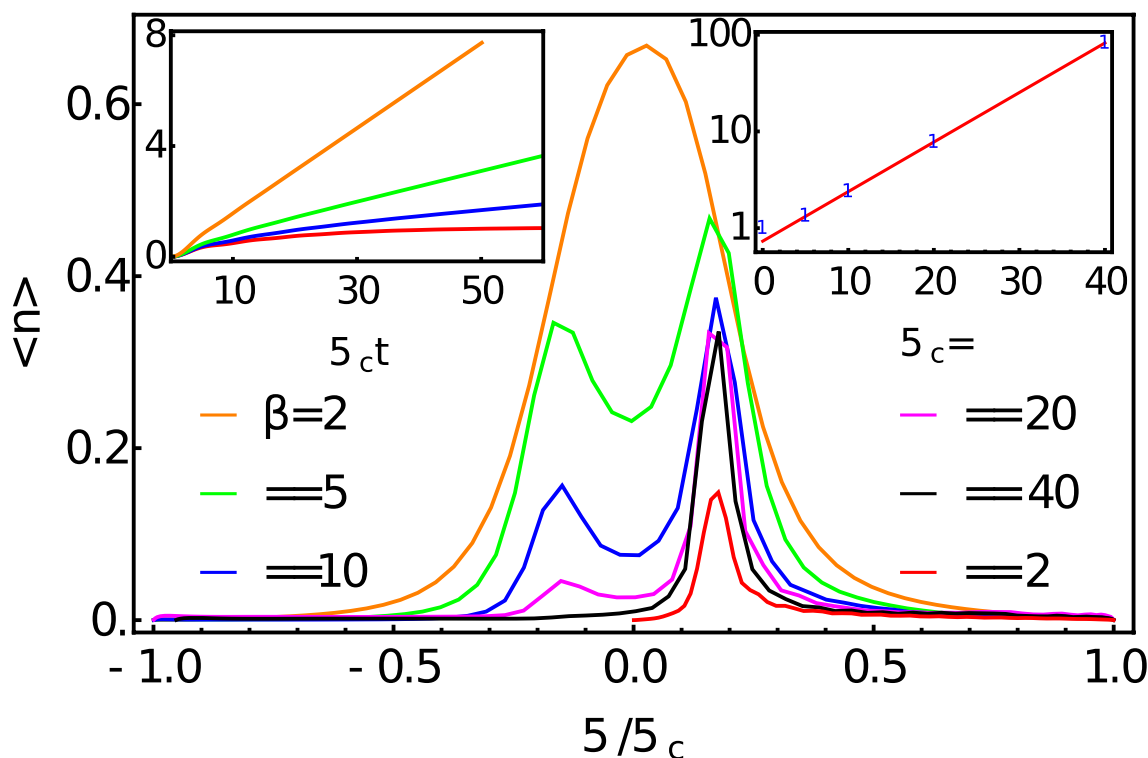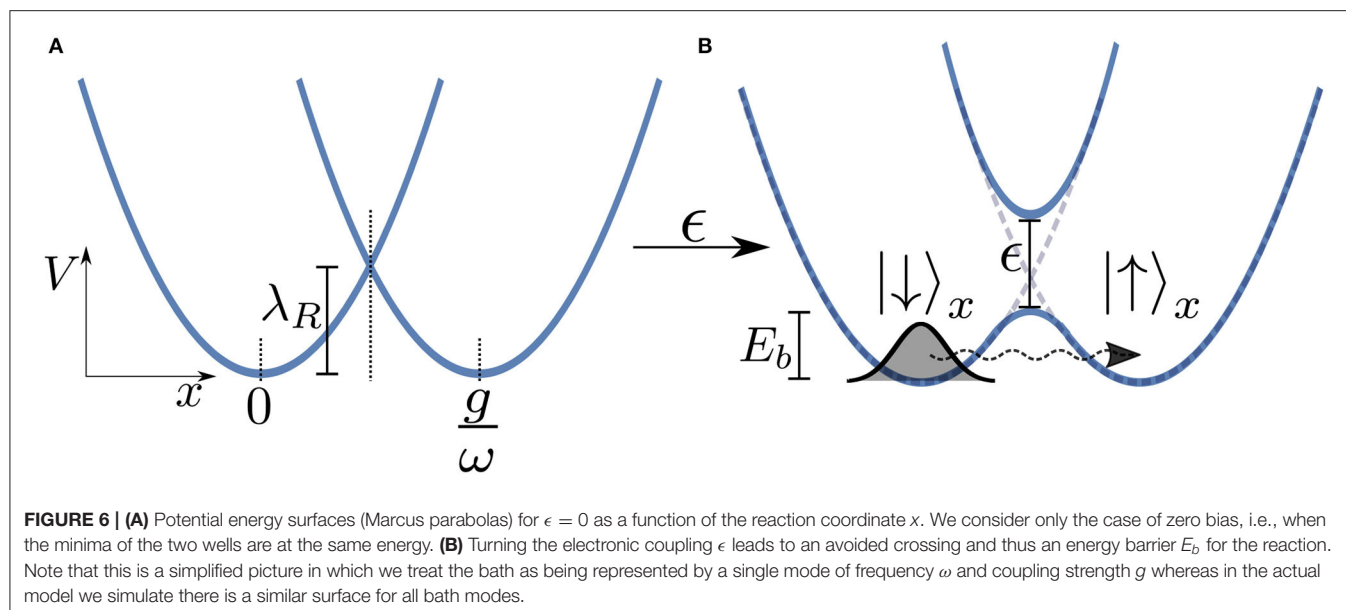
FIGURE 5 | Bath mode occupations $\langle n_\omega \rangle = \langle a_\omega^\dagger a_\omega \rangle$ for the extended environment after the TLS has decayed. The TLS is governed by a Hamiltonian $H_S = \frac{\omega_0}{2} \sigma_z$ where $\omega_0 = 0.2\omega_c$ and is coupled to an Ohmic bath with a hard cut-off via $A_S = \sigma_x$. The coupling strength is $\alpha = 0.1$. Left inset: total mode occupation as a function of time $\langle n \rangle_{\text{tot}} = \int_{-\infty}^{\infty} d\omega \langle n_\omega \rangle$. Right inset shows $\frac{\langle n_{\omega_p} \rangle + 1}{\langle n_{\omega_n} \rangle}$ plotted on a log scale against the inverse temperature, demonstrating the detailed balance of the absorption and emission rates.

appear in the numerical simulation, one will always encounter potentially large errors once the filling of the modes exceeds their capacity set by the truncation to d Fock states per oscillator. The rate at which this filling occurs increases with temperature and is linear in time. However, as the relaxation time of the system is also broadly proportional to temperature for $\beta\omega_c \ll 1$, this may not be a problem, if one is only interested in the short-time transient dynamics. Where this may pose problems is for the extraction of converged properties of relaxed, i.e., locally thermalized excited states, such as their (resonance) fluorescence spectra, or multidimensional optical spectra (Mukamel, 1995). While these ever-growing computational resources must—as argued above—be present in any simulation approach, we note that one possible way to combat the growth of local dimensions could be to use the dynamical version of Guo's Optimized Boson Basis (OBB) which was introduced into 1TDVP for open systems by Schroeder et al. (Guo et al., 2012; Schröder and Chin, 2016).

4. ELECTRON TRANSFER

Having established that the T-TEDOPA mapping allows efficient computational access to finite temperature open dynamics, we now study the chemically relevant problem of tunneling electron transfer. Electron transfer is a fundamental problem in chemical dynamics and plays an essential role in a vast variety of crucial

processes including the ultra-fast primary electron transfer step in photosynthetic reaction centers and the electron transport that powers biological respiration (Devault, 1980; Marcus, 1993; May and Kühn, 2008). The problem of modeling electron transfer between molecules comes down to accurately treating the coupling between the electronic states and environmental vibrational modes, and often involves the use of first principle techniques to parameterize the total spectral functions of the vibrational and outer solvent, or protein environment (Mendive-Tapia et al., 2018; Schröder et al., 2019; Zuehlsdorff et al., 2019). In many molecular systems—and particularly biological systems where the transfer between electronic states is affected by coupling to chromophore and protein modes—the system-bath physics is highly non-perturbative and $J(\omega)$ has very sharp frequency-dependence (May and Kühn, 2008; Womick et al., 2011; Kolli et al., 2012; Chin et al., 2013). Until recently, and even at zero temperature, a fully quantum mechanical description of the coupling to a continuum of environmental vibrations was challenging due to the exponential scaling of the vibronic wave functions. However, with advances in numerical approaches driven by developments in Tensor-Networks and ML-MCTDH, the exact quantum simulation of continuum environment models can now be explored very precisely at zero temperature. Given this, we now explore how the T-TEDOPA mapping can extend this capability to finite temperature quantum tunneling.

FIGURE 6 | (A) Potential energy surfaces (Marcus parabolas) for $\epsilon = 0$ as a function of the reaction coordinate x. We consider only the case of zero bias, i.e., when the minima of the two wells are at the same energy. **(B)** Turning the electronic coupling ϵ leads to an avoided crossing and thus an energy barrier E_b for the reaction. Note that this is a simplified picture in which we treat the bath as being represented by a single mode of frequency ω and coupling strength g whereas in the actual model we simulate there is a similar surface for all bath modes.

Here, we will again adapt the spin-boson model to analyse a typical donor-acceptor electron transfer system, as shown in **Figure 6**. In this model the electron transfer process is modeled using two states representing the reactant and product states which we take to be the eigenstates of σ_x with $|\downarrow\rangle$ representing the reactant and $|\uparrow\rangle$ the product. We take our system Hamiltonian to be $H_S = \frac{\epsilon}{2}\sigma_z + \lambda_R \frac{1+\sigma_x}{2}$, and the coupling operator as $A_S = \frac{1+\sigma_x}{2}$, where λ_R is the reorganization energy which for an Ohmic bath is $\lambda_R = 2\alpha\omega_c$. The electron tunnels from the *environmentally relaxed* reactant state to the product state by moving through a multi-dimensional potential energy landscape along a collective reaction coordinate which is composed of the displacements of the ensemble of bath modes (this is effectively the coordinate associated with the mode that is directly coupled to the system in the chain representation of the environment). **Figure 6A** shows two potential energy surfaces—Marcus parabolas—of the electronic system for $\epsilon = 0$. Although in the actual model we simulate the reaction coordinate is composed of the displacements of an infinite number of modes, in **Figure 6** we present a simplified picture in which the electron moves along a single reaction coordinate, x. The potential minimum of the reactant state corresponds to the bath in its undisplaced, vacuum state, whereas at the potential minimum of the product state each bath mode is displaced by an amount depending on its frequency and the strength of its coupling to the TLS $\sqrt{J(\omega)}/\omega$. The presence of the reorganization energy in H_S ensures that these two minima are degenerate in energy and thus detailed balance will ensure an equal forward and backward rate.

Turning on the coupling ϵ between the two levels leads to an avoided crossing in the two energy surfaces in an adiabatic representation of the vibronic tunneling system, leading to two potential wells. In such a semi-classical (Born-Oppeheimer) picture, we see that the electron must overcome a kind of effective energy barrier E_b that scales with the total reorganization energy of the entire environment λ_R in order for the reaction

to progress. We thus might well expect to see thermally activated (exponential) behavior whereby the tunneling rate $\propto \exp(-\beta E_b)$. However, at low temperatures this behavior should be dramatically quenched and dissipative quantum tunneling should become dominant and strongly dependent on the spectral function of the environment (Weiss, 2012).

4.1. Numerical Results

For our numerical investigation we take an Ohmic spectral density with $\alpha = 0.8$ for which the dynamics are expected to be incoherent at all temperatures, i.e., the energy surfaces of **Figure 6B** are well-separated and friction is such that there will be no oscillatory tunneling dynamics between reactant and product. In **Figure 7**, we present results for this model at several temperatures using the T-TEDOPA mapping and 1TDVP. The expectation of σ_x can be taken to be a measure of the progress of the reaction, starting at the value of -1 when the system is entirely in the reactant state, and approaching 0 as the electron tunnels through the barrier and the populations thermalize. We find that as the temperature is increased the dynamics tend to an exponential decay to the steady state, whereas non-exponential behavior is observed for lower temperatures. In **Figure 7B**, we show the expectation of σ_y, which is the conjugate coordinate to the σ_x and which may thus be interpreted as a kind of momentum associated with the tunneling. We find that there is a sharp initial spike in $\langle\sigma_y\rangle$ which decays with oscillations which are increasingly damped at higher temperatures. As we might have predicted, these transient dynamics occur on a timescale of $\tau \approx \omega_c^{-1}$, which the fastest response time of an environment with an upper cut-off frequency of ω_c. This is approximately the timescale over which the environment will adjust to the sudden presence of the electron, and essentially sets the timescale for the formation of the adiabatic landscape (or, alternatively, for the formation of the dressed polaron states), after which the tunneling dynamics proceed. This period is related to the
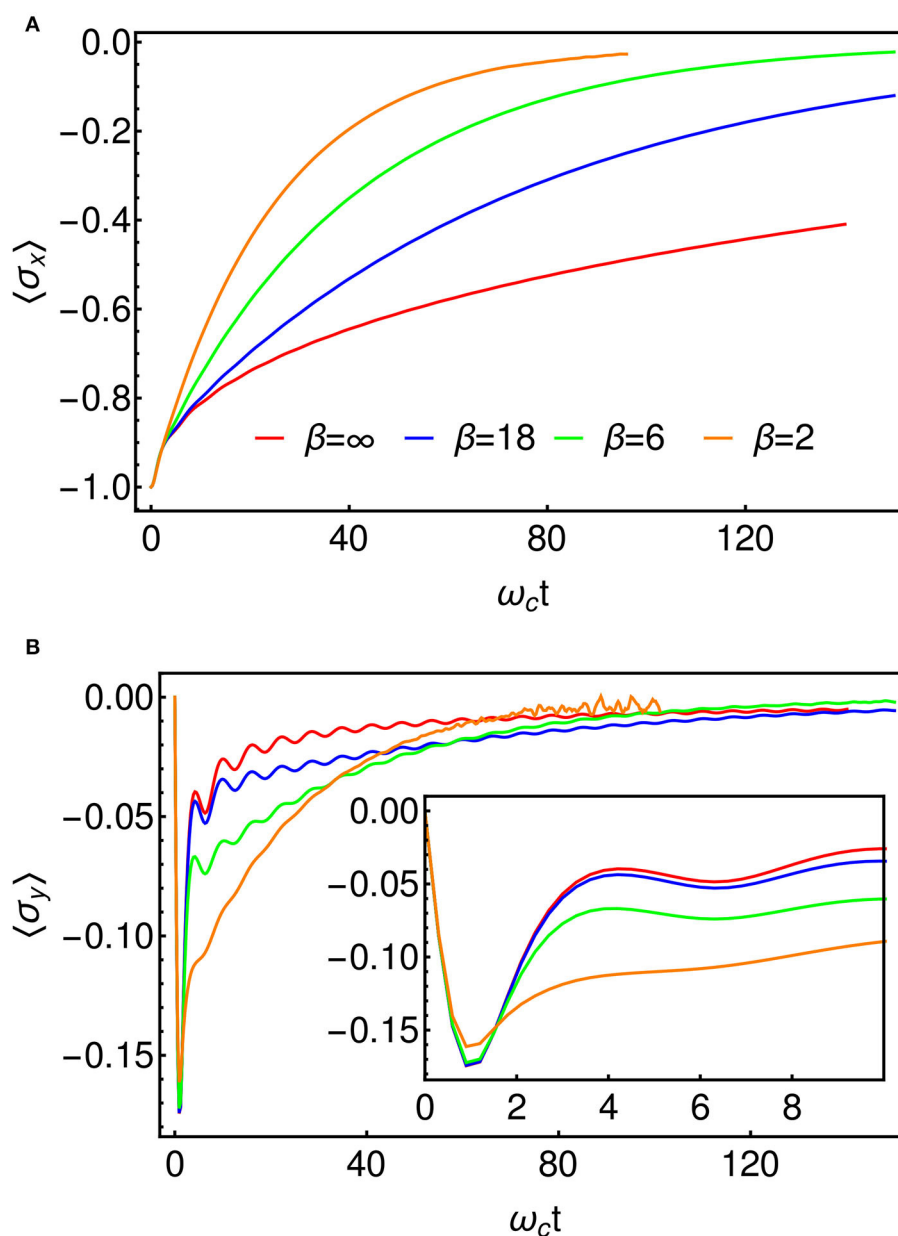
FIGURE 7 | (A) $\langle\sigma_x(t)\rangle$ for several temperatures, which represents the progress of the reaction. The decay to the steady state is exponential at high temperature. **(B)** $\langle\sigma_y(t)\rangle$, representing the momentum along the reaction coordinate. We encounter some noise beyond about $\omega_c t = 50$ in the $\beta = 2$ data. This is as a result of the truncation of the local Hilbert spaces of the bath modes (cf. section 3). The inset shows an enlarged view of the initial fast dynamics which appear to be broadly independent of temperature.

slippage of initial conditions that is sometimes used to fix issues of density matrix positivity in perturbative Redfield Theory (Gaspard and Nagaoka, 1999), although here the establishment of these conditions is described exactly and in real-time. We also see that the crossover to the tunneling regime happens faster as the temperature increases, meaning that the effective initial conditions—particularly $\langle\sigma_y(t)\rangle$—are temperature dependent.

We extract approximate reaction rates from the TLS dynamics by fitting each $\langle\sigma_x(t)\rangle$ to an exponential decay $-e^{-\Gamma t}$ on

timescales $t > \tau$. We thus obtain the rates $\Gamma(\epsilon, \beta)$ for the various values of β and ϵ simulated. The values of ϵ were chosen to be small compared to the characteristic vibrational frequency of the bath, $\epsilon \ll \omega_c$ and to the reorganization energy, $\epsilon \ll \lambda_R$ and thus lie in the non-adiabatic regime which is the relevant regime for electron transfer. One may then perform a perturbative expansion in ϵ, otherwise known as the "Golden Rule" approach which, for an Ohmic bath, yields the following formulas for the high and low temperature limits corresponding respectively to
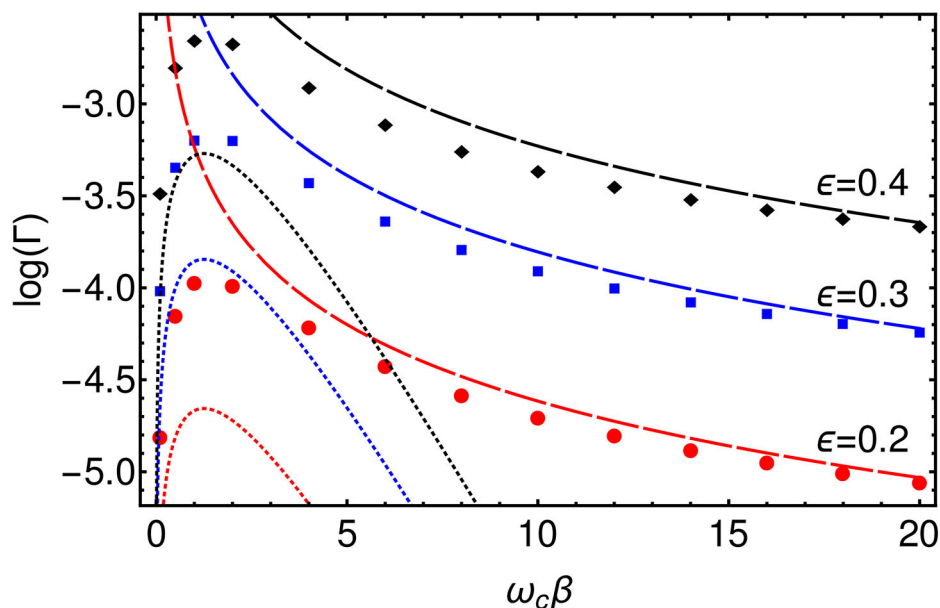
FIGURE 8 | Log plot of the rates, Γ, extracted from $\langle \sigma_x(t) \rangle$ for $\epsilon = 0.2$ (Red), $\epsilon = 0.3$ (Blue), and $\epsilon = 0.4$ (Red) as a function of β. (Dashed lines) High temperature ($T \gg \omega_c$), classical, limit of Golden Rule formula. (Dotted lines) Low temperature ($T \ll \omega_c$), quantum, limit of Golden Rule formula.

the classical and quantum regimes (Weiss, 2012).

$$\Gamma(\beta) = \begin{cases} \frac{\sqrt{\pi}}{4\sqrt{\alpha}} \epsilon^2 \left(\frac{\pi}{\beta\omega_c}\right)^{2\alpha-1}, \beta\omega_c \gg 1 \\ \frac{\epsilon^2}{4} \sqrt{\frac{\pi\beta\omega_c}{2\alpha}} \exp\left(-\frac{\alpha\beta\omega_c}{2}\right), \beta\omega_c \ll 1 \end{cases} . \quad (13)$$

The golden rule result is based on second-order perturbation in the tunneling coupling ϵ, but it is exact to all orders in the system-environment coupling α. Additionally, the Ohmic form of the spectral function generates a non-trivial power-law dependence of the tunneling rate on the temperature for $\beta\omega_c \gg 1$ in which the rate may either decrease or increase as the temperature is lowered, depending on the value of α. We plot these formulas along with the numerically evaluated rates in **Figure 8**. There is a good agreement in the high and low temperature limits between the Golden Rule expressions and the T-TEDOPA results, and one clearly sees that the temperature dependence of the rate is non-monotonic with a transition from power law growth (quantum, $2\alpha - 1 > 0$) to power-law decay (classical, $\propto \sqrt{\beta}$) as the temperature increases from $T = 0$. We note that for the parameters we present here, the intermediate regime where thermally activated behavior is predicted $\beta\omega_c \sim 1$ is not observed for the Ohmic environment, and one essentially switches from tunneling limited by the effect of friction on the attempt frequency to the low-temperature polaronic tunneling of Equation (13).

5. CONCLUSION

In this article we have shown how the combination of the Tamasceli's remarkable T-TEDOPA mapping and

non-perturbative variational Tensor-Network dynamics can be applied to chemical and photophysical systems under laboratory conditions. Through numerical experiments we have carefully investigated how the T-TEDOPA mapping allows the effects of finite temperatures to be obtained efficiently without any need for costly sampling of the thermal environment state, or the explicit use of density matrices. However, analysis of these environmental dynamics reveals how incorporating finite temperatures can lead to more expensive simulations, due to the filling-up of the chain modes and the longer chains that are needed to prevent recurrence dynamics. Yet, we believe that this method, and others like it, based on the exact quantum many-body treatment of vibrational modes (Somoza et al., 2019), could present an attractive complementary approach to the Multi-Layer Multi-Configurational Time-Dependent Hartree Method (MLMCTDH) commonly used in chemical dynamics. One possible direction for this would be to consider a problem in which a (discretized) potential surface for a reaction is contained within the system Hamiltonian, while the environment bath provides the nuclear thermal and quantum fluctuations that ultimately determine both real-time kinetics and thermodynamical yields for the process, as is currently captured in methods such as Ring Polymer Molecular Dynamics (Craig and Manolopoulos, 2004). Furthermore, the Tensor-Network structures are not limited to the simple chain geometries we consider here but can in fact adopt a tree structure, thus enabling the treatment of complex coupling to multiple independent baths (Schröder et al., 2019). Such trees tensor networks have recently been interfaced with *ab initio* methods to explore ultra-fast photophysics of real molecules and their pump-probe spectra (Schnedermann et al., 2019),

but such efforts have so far been limited to zero temperature. Finally, the cooperative, antagonistic or sequential actions of different types of environments, i.e., light and vibrations (Wertnik et al., 2018), or even the creation of new excitations, such as polaritons (Memmi et al., 2017; Del Pino et al., 2018; Herrera and Owrutsky, 2020), could play a key role in sophisticated new materials for energy transduction, catalysis or regulation (feedback) of reactions, and T-TDEPODA-based tensor networks are currently being used to explore these developing areas.

DATA AVAILABILITY STATEMENT

The datasets presented in this study can be found in online repositories. The names of the repository/repositories and accession number(s) can be found below: https://github.com/angusdunnett/MPSDynamics.

AUTHOR CONTRIBUTIONS

AD implemented the T-TEDOPA mapping in a bespoke 1TDVP code and performed the numerical simulations. AD and AC wrote the manuscript. AC oversaw the project. All authors contributed to the article and approved the submitted version.

REFERENCES

Alvermann, A., and Fehske, H. (2009). Sparse polynomial space approach to dissipative quantum systems: Application to the sub-ohmic spin-boson model. *Phys. Rev. Lett.* 102:150601. doi: 10.1103/PhysRevLett.102.150601

Alvertis, A. M., Schröder, F. A. Y. N., and Chin, A. W. (2019). Non-equilibrium relaxation of hot states in organic semiconductors: Impact of mode-selective excitation on charge transfer. *J. Chem. Phys.* 151:084104. doi: 10.1063/1.5115239

Benenti, G., Casati, G., Saito, K., and Whitney, R. (2017). Fundamental aspects of steady-state conversion of heat to work at the nanoscale. *Phys. Rep.* 694, 1–124. doi: 10.1016/j.physrep.2017.05.008

Binder, R., and Burghardt, I. (2019). First-principles quantum simulations of exciton diffusion on a minimal oligothiophene chain at finite temperature. *Faraday Discuss.* 221, 406–427. doi: 10.1039/C9FD00066F

Breuer, H.-P., and Petruccione, F. (2002). *The Theory of Open Quantum Systems*. Oxford University Press.

Chin, A., Prior, J., Rosenbach, R., Caycedo-Soler, F., Huelga, S. F., and Plenio, M. B. (2013). The role of non-equilibrium vibrational structures in electronic coherence and recoherence in pigment-protein complexes. *Nat. Phys.* 9, 113–118. doi: 10.1038/nphys2515

Chin, A. W., Rivas, Á., Huelga, S. F., and Plenio, M. B. (2010). Exact mapping between system-reservoir quantum models and semi-infinite discrete chains using orthogonal polynomials. *J. Math. Phys.* 51:092109. doi: 10.1063/1.3490188

Craig, I. R., and Manolopoulos, D. E. (2004). Quantum statistics and classical mechanics: real time correlation functions from ring polymer molecular dynamics. *J. Chem. Phys.* 121, 3368–3373. doi: 10.1063/1.1777575

De Vega, I., and Alonso, D. (2017). Dynamics of non-Markovian open quantum systems. *Rev. Modern Phys.* 89:015001. doi: 10.1103/RevModPhys.89.015001

de Vega, I., and Bañuls, M.-C. (2015). Thermofield-based chain-mapping approach for open quantum systems. *Phys. Rev. A* 92:052116. doi: 10.1103/PhysRevA.92.052116

Del Pino, J., Schröder, F. A., Chin, A. W., Feist, J., and Garcia-Vidal, F. J. (2018). Tensor network simulation of polaron-polaritons in organic microcavities. *Phys. Rev. B* 98:165416. doi: 10.1103/PhysRevB.98.165416

Devault, D. (1980). Quantum mechanical tunnelling in biological systems. *Q. Rev. Biophys.* 13, 387–564. doi: 10.1017/S003358350000175X

Dubi, Y., and Dia Ventra, M. (2011). *Colloquium*: heat flow and thermoelectricity in atomic and molecular junctions. *Rev. Modern Phys.* 83, 131–155. doi: 10.1103/RevModPhys.83.131

Gaspard, P., and Nagaoka, M. (1999). Slippage of initial conditions for the redfield master equation. *J. Chem. Phys.* 111, 5668–5675. doi: 10.1063/1.479867

Gélinas, S., Rao, A., Kumar, A., Smith, S. L., Chin, A. W., Clark, J., et al. (2014). Ultrafast long-range charge separation in organic semiconductor photovoltaic diodes. *Science* 343, 512–516. doi: 10.1126/science.1246249

Guo, C., Weichselbaum, A., von Delft, J., and Vojta, M. (2012). Critical and strong-coupling phases in one-and two-bath spin-boson models. *Phys. Rev. Lett.* 108:160401. doi: 10.1103/PhysRevLett.108.160401

Haegeman, J., Lubich, C., Oseledets, I., Vandereycken, B., and Verstraete, F. (2016). Unifying time evolution and optimization with matrix product states. *Phys. Rev. B* 94:165116. doi: 10.1103/PhysRevB.94.165116

Herrera, F., and Owrutsky, J. (2020). Molecular polaritons for controlling chemistry with quantum optics. *J. Chem. Phys.* 152:100902. doi: 10.1063/1.5136320

Kolli, A., O'Reilly, E. J., Scholes, G. D., and Olaya-Castro, A. (2012). The fundamental role of quantized vibrations in coherent light harvesting by cryptophyte algae. *J. Chem. Phys.* 137:174109. doi: 10.1063/1.4764100

Lubich, C. (2015). Time integration in the multiconfiguration time-dependent Hartree method of molecular quantum dynamics. *Appl. Math. Res. Express* 2015, 311–328. doi: 10.1093/amrx/abv006

Lubich, C., Oseledets, I., and Vandereycken, B. (2015). Time integration of tensor trains. *SIAM J. Num. Anal.* 53, 917–941. doi: 10.1137/140976546

Mahan, G. D. (2000). *Many-Particle Physics*. Boston, MA: Springer US. doi: 10.1007/978-1-4757-5714-9

Marcus, R. A. (1993). Electron transfer reactions in chemistry. Theory and experiment. *Rev. Modern Phys.* 65:599. doi: 10.1103/RevModPhys.65.599

May, V., and Kühn, O. (2008). *Charge and Energy Transfer Dynamics in Molecular Systems*. Weinheim: John Wiley & Sons.

Memmi, H., Benson, O., Sadofev, S., and Kalusniak, S. (2017). Strong coupling between surface plasmon polaritons and molecular vibrations. *Phys. Rev. Lett.* 118:126802. doi: 10.1103/PhysRevLett.118.126802

Mendive-Tapia, D., Mangaud, E., Firmino, T., de la Lande, A., Desouter-Lecomte, M., Meyer, H.-D., et al. (2018). Multidimensional quantum mechanical modeling of electron transfer and electronic coherence in plant cryptochromes: the role of initial bath conditions. *J. Phys. Chem. B* 122, 126–136. doi: 10.1021/acs.jpcb.7b10412

Miller, W. H., Schwartz, S. D., and Tromp, J. W. (1983). Quantum mechanical rate constants for bimolecular reactions. *J. Chem. Phys.* 79, 4889–4898. doi: 10.1063/1.445581

Mukamel, S. (1995). *Principles of Nonlinear Optical Spectroscopy*, Vol. 6. New York, NY: Oxford University Press.

Musser, A. J., Liebel, M., Schnedermann, C., Wende, T., Kehoe, T. B., Rao, A., et al. (2015). Evidence for conical intersection dynamics mediating ultrafast singlet exciton fission. *Nat. Phys.* 11, 352–357. doi: 10.1038/nphys3241

Orus, R. (2014). A practical introduction to tensor networks: matrix product states and projected entangled pair states. *Ann. Phys.* 349, 117–158. doi: 10.1016/j.aop.2014.06.013

Paeckel, S., Kohler, T., Swoboda, A., Manmana, S. R., Schollwock, U., and Hubig, C. (2019). Time-evolution methods for matrix-product states. *Ann. Phys.* 411:167998. doi: 10.1016/j.aop.2019.167998

Prior, J., Chin, A. W., Huelga, S. F., and Plenio, M. B. (2010). Efficient simulation of strong system-environment interactions. *Phys. Rev. Lett.* 105:050404. doi: 10.1103/PhysRevLett.105.050404

Prior, J., de Vega, I., Chin, A. W., Huelga, S. F., and Plenio, M. B. (2013). Quantum dynamics in photonic crystals. *Phys. Rev. A* 87:013428. doi: 10.1103/PhysRevA.87.013428

Schnedermann, C., Alvertis, A. M., Wende, T., Lukman, S., Feng, J., Schröder, F. A., et al. (2019). A molecular movie of ultrafast singlet fission. *Nat. Commun.* 10, 1–11. doi: 10.1038/s41467-019-12220-7

Schnedermann, C., Lim, J. M., Wende, T., Duarte, A. S., Ni, L., Gu, Q., et al. (2016). Sub-10 fs time-resolved vibronic optical microscopy. *J. Phys. Chem. Lett.* 7, 4854–4859. doi: 10.1021/acs.jpclett.6b02387

Schollwock, U. (2011). The density-matrix renormalization group in the age of matrix product states. *Ann. Phys.* 326, 96–192. doi: 10.1016/j.aop.2010.09.012

Schröder, F. A., and Chin, A. W. (2016). Simulating open quantum dynamics with time-dependent variational matrix product states: towards microscopic correlation of environment dynamics and reduced system evolution. *Phys. Rev. B* 93:075105. doi: 10.1103/PhysRevB.93.075105

Schröder, F. A. Y. N., Turban, D. H. P., Musser, A. J., Hine, N. D. M., and Chin, A. W. (2019). Tensor network simulation of multi-environmental open quantum dynamics via machine learning and entanglement renormalisation. *Nat. Commun.* 10:1062. doi: 10.1038/s41467-019-09039-7

Schulze, J., and Kuhn, O. (2015). Explicit correlated exciton-vibrational dynamics of the FMO complex. *J. Phys. Chem. B* 119, 6211–6216. doi: 10.1021/acs.jpcb.5b03928

Silbey, R., and Harris, R. A. (1984). Variational calculation of the dynamics of a two level system interacting with a bath. *J. Chem. Phys.* 80, 2615–2617. doi: 10.1063/1.447055

Smith, S. L., and Chin, A. W. (2015). Phonon-assisted ultrafast charge separation in the PCBM band structure. *Phys. Rev. B* 91:201302. doi: 10.1103/PhysRevB.91.201302

Somoza, A. D., Marty, O., Lim, J., Huelga, S. F., and Plenio, M. B. (2019). Dissipation-assisted matrix product factorization. *Phys. Rev. Lett.* 123:100502. doi: 10.1103/PhysRevLett.123.100502

Tamascelli, D., Smirne, A., Huelga, S. F., and Plenio, M. B. (2018). Nonperturbative treatment of non-markovian dynamics of open quantum systems. *Phys. Rev. Lett.* 120:030402. doi: 10.1103/PhysRevLett.120.030402

Tamascelli, D., Smirne, A., Lim, J., Huelga, S. F., and Plenio, M. B. (2019). Efficient simulation of finite-temperature open quantum systems. *Phys. Rev. Lett.* 123:090402. doi: 10.1103/PhysRevLett.123.090402

Wang, H., and Shao, J. (2019). Quantum phase transition in the spin-boson model: a multilayer multiconfiguration time-dependent Hartree study. *J. Phys. Chem. A* 123, 1882–1893. doi: 10.1021/acs.jpca.8b11136

Weiss, U. (2012). *Quantum Dissipative Systems, 4th Edn.* Singapore: World Scientific. doi: 10.1142/8334

Wertnik, M., Chin, A., Nori, F., and Lambert, N. (2018). Optimizing co-operative multi-environment dynamics in a dark-state-enhanced photosynthetic heat engine. *J. Chem. Phys.* 149:084112. doi: 10.1063/1.5040898

Wilhelm, F., Kleff, S., and Von Delft, J. (2004). The spin-boson model with a structured environment: a comparison of approaches. *Chem. Phys.* 296, 345–353. doi: 10.1016/j.chemphys.2003.10.010

Womick, J. M., Liu, H., and Moran, A. M. (2011). Exciton delocalization and energy transport mechanisms in r-phycoerythrin. *J. Phys. Chem. A* 115, 2471–2482. doi: 10.1021/jp111720a

Woods, M., Cramer, M., and Plenio, M. (2015). Simulating bosonic baths with error bars. *Phys. Rev. Lett.* 115:130401. doi: 10.1103/PhysRevLett.115.130401

Xie, X., Liu, Y., Yao, Y., Schollwock, U., Liu, C., and Ma, H. (2019). Time-dependent density matrix renormalization group quantum dynamics for realistic chemical systems. *J. Chem. Phys.* 151:224101. doi: 10.1063/1.5125945

Zuehlsdorff, T. J., Montoya-Castillo, A., Napoli, J. A., Markland, T. E., and Isborn, C. M. (2019). Optical spectra in the condensed phase: capturing anharmonic and vibronic features using dynamic and static approaches. *J. Chem. Phys.* 151:074111. doi: 10.1063/1.5114818

APPENDIX

The chain mapping used in section 2 is based on the theory of orthogonal polynomials. A polynomial of degree n is defined by

$$p_n(x) = \sum_{m=0}^{n} a_m x^m. \tag{A1}$$

The space of polynomials of degree n is denoted $\mathbb{P}_n$ and is a subset of the space of all polynomials $\mathbb{P}_n \subset \mathbb{P}$. Given a measure $d\mu(x)$ which has finite moments of all orders on some interval $[a, b]$, we may define the inner product of two polynomials

$$\langle p, q \rangle_\mu = \int_a^b d\mu(x) p(x) q(x). \tag{A2}$$

This inner product gives rise to a unique set of orthonormal polynomials $\{\tilde{p}_n \in \mathbb{P}_n, n = 0, 1, 2, \dots\}$ which all satisfy

$$\langle \tilde{p}_n, \tilde{p}_m \rangle = \delta_{n,m}. \tag{A3}$$

This set forms a complete basis for $\mathbb{P}$, and more specifically the set $\{\tilde{p}_n \in \mathbb{P}_n, n = 0, 1, 2, \dots m\}$ is a complete basis for $\bigcup_{r=1}^{m} \mathbb{P}_r$.

It is often useful to express the orthonormal polynomials in terms of the orthogonal *monic* polynomials $\pi_n(x)$ which are the unnormalized scalar multiples of $\tilde{p}_n(x)$ whose leading coefficient is 1 $(a_n = 1)$

$$\tilde{p}_n(x) = \frac{\pi_n(x)}{||\pi_n||}. \tag{A4}$$

The key property of orthogonal polynomials for the construction of the chain mapping is that they satisfy a three term recurrence relation

$$\pi_{k+1}(x) = (x - \alpha_k)\pi_k(x) - \beta_k \pi_{k-1}(x), \tag{A5}$$

where it can be easily shown that

$$\alpha_k = \frac{\langle x\pi_k, \pi_k \rangle}{\langle \pi_k, \pi_k \rangle}, \quad \beta_k = \frac{\langle \pi_k, \pi_k \rangle}{\langle \pi_{k-1}, \pi_{k-1} \rangle}. \tag{A6}$$

Now that we have defined the orthogonal polynomials we may use them to construct the unitary transformation that will convert the star Hamiltonian of Equation (9) with

$$H_I^{\text{ext}} = A_S \otimes \int_{-\infty}^{\infty} d\omega \sqrt{J_\beta(\omega)}(a_\omega + a_\omega^\dagger), \quad H_E^{\text{ext}} = \int_{-\infty}^{\infty} d\omega \omega a_\omega^\dagger a_\omega, \tag{A7}$$

into the chain Hamiltonian of Equation (12). The transformation is given by

$$c_n^{(\dagger)} = \int_{-\infty}^{\infty} U_n(\omega) a_\omega^{(\dagger)}, \tag{A8}$$

where

$$U_n(\omega) = \sqrt{J_\beta(\omega)}\tilde{p}_n(\omega) = \sqrt{J_\beta(\omega)}\frac{\pi_n(\omega)}{||\pi_n||}, \tag{A9}$$

and the polynomials $\tilde{p}_n(\omega)$ are orthonormal with respect to the measure $d\omega J_\beta(\omega)$. The unitarity of $U_n(\omega)$ follows immediately from the orthonormality of the polynomials.

Applying the above transformation to the interaction Hamiltonian we have

$$H_I^{\text{ext}} = A_S \otimes \sum_{n=0}^{\infty} \int_{-\infty}^{\infty} d\omega J_\beta(\omega) \frac{\pi_n(\omega)}{||\pi_n||}(c_n^\dagger + c_n) \tag{A10}$$

For the zeroth order monic polynomial we have $\pi_0 = 1$ and so we may insert this into the above expression

$$H_I^{\text{ext}} = A_S \otimes \sum_{n=0}^{\infty} \int_{-\infty}^{\infty} d\omega J_\beta(\omega) \frac{\pi_n(\omega)\pi_0}{||\pi_n||}(c_n^\dagger + c_n). \tag{A11}$$

Recognizing the inner product in the above expression and making use of the orthogonality of the polynomials we have

$$H_I^{\text{ext}} = A_S \otimes \sum_{n=0}^{\infty} ||\pi_n|| \delta_{n,0}(c_n^\dagger + c_n) = A_S \otimes ||\pi_0||(c_0^\dagger + c_0), \tag{A12}$$

and thus, in the new basis, only one mode now couples to the system.

Now for the environment part of the Hamiltonian we have

$$H_E^{\text{ext}} = \sum_{n,m=0}^{\infty} \int_{-\infty}^{\infty} d\omega J_\beta(\omega) \omega \frac{\pi_n(\omega)\pi_m(\omega)}{||\pi_n||\,||\pi_m||} c_n^\dagger c_m. \tag{A13}$$

Substituting for $\omega \pi_n(\omega)$ from the three term recurrence relation of Equation (A5) yields

$$H_E^{\text{ext}} = \sum_{n,m=0}^{\infty} \int_{-\infty}^{\infty} d\omega \frac{J_\beta(\omega)}{||\pi_n||\,||\pi_m||}\Big[\pi_{n+1}(\omega) + \alpha_n \pi_n(\omega)$$
$$+ \beta_n \pi_{n-1}(\omega)\Big]\pi_m(\omega) c_n^\dagger c_m. \tag{A14}$$

Again, evaluating the inner products we have

$$H_E^{\text{ext}} = \sum_{n,m=0}^{\infty} \frac{1}{||\pi_n||}\Big[||\pi_m||\delta_{n+1,m} + \alpha_n ||\pi_m||\delta_{n,m}$$
$$+ \beta_n ||\pi_m||\delta_{n-1,m}\Big]c_n^\dagger c_m \tag{A15}$$
$$= \sum_{n=0}^{\infty} \sqrt{\beta_{n+1}}c_n^\dagger c_{n+1} + \alpha_n c_n^\dagger c_n + \sqrt{\beta_{n+1}}c_n^\dagger c_{n-1},$$

where in the second line we have used the fact that

$$\frac{||\pi_{n+1}||}{||\pi_n||} = \sqrt{\beta_{n+1}}. \tag{A16}$$

We thus arrive at the nearest-neighbor coupling Hamiltonian of Equation (12) and are able to identify the chain coefficients as

$$\kappa = ||\pi_0||,$$
$$\omega_{n+1} = \alpha_n, \tag{A17}$$
$$t_n = \sqrt{\beta_n}.$$

Note that in Equation (12) the chain sites are labeled starting from $n = 1$ and not $n = 0$ as in Equation (A15). All that remains now to calculate the chain coefficients for a particular spectral density $J_\beta(\omega)$ is to compute the recurrence coefficients, α_n and β_n, and this may done iteratively using Equations (A5) and (A6) and numerically evaluating the inner product integrals using a quadrature rule.

Spectroscopic and Photophysical Investigation of Model Dipyrroles Common to Bilins: Exploring Natural Design for Steering Torsion to Divergent Functions

Clayton F. Staheli[1], Jaxon Barney[1,2], Taime R. Clark[1], Maxwell Bowles[1,3], Bridger Jeppesen[1], Daniel G. Oblinsky[4], Mackay B. Steffensen[1] and Jacob C. Dean[1]*

[1]Department of Physical Science, Southern Utah University, Cedar City, UT, United States, [2]Department of Chemistry, The Pennsylvania State University, State College, PA, United States, [3]Department of Chemistry, North Carolina State University, Raleigh, NC, United States, [4]Department of Chemistry, Princeton University, Princeton, NJ, United States
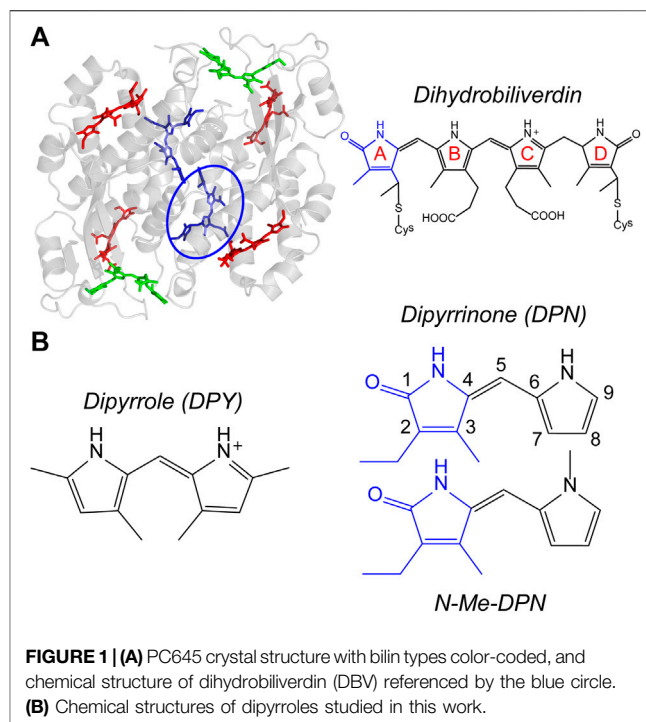
Biliproteins are a unique class of photosynthetic proteins in their diverse, and at times, divergent biophysical function. The two contexts of photosynthetic light harvesting and photoreception demonstrate characteristically opposite criteria for success, with light harvesting demanding structurally-rigid chromophores which minimize excitation quenching, and photoreception requiring structural flexibility to enable conformational isomerization. The functional plasticity borne out in these two biological contexts is a consequence of the structural plasticity of the pigments utilized by biliproteins—linear tetrapyrroles, or bilins. In this work, the intrinsic flexibility of the bilin framework is investigated in a bottom-up fashion by reducing the active nuclear degrees of freedom through model dipyrrole subunits of the bilin core and terminus free of external protein interactions. Steady-state spectroscopy was carried out on the dipyrrole (DPY) and dipyrrinone (DPN) subunits free in solution to characterize their intrinsic spectroscopic properties including absorption strengths and nonradiative activity. Transient absorption (TA) spectroscopy was utilized to determine the mechanism and kinetics of nonradiative decay of the dipyrrole subunits, revealing dynamics dominated by rapid internal conversion with some $Z{\rightarrow}E$ isomerization observable in DPY. Computational analysis of the ground state conformational landscapes indicates enhanced complexity in the asymmetric terminal subunit, and the prediction was confirmed by heterogeneity of species and kinetics observed in TA. Taken together, the large oscillator strengths ($f \sim 0.6$) of the dipyrrolic derivatives and chemically-efficient spectral tunability seen through the ~100 nm difference in absorption spectra, validate Nature's "selection" of multi-pyrrole pigments for light capture applications. However, the rapid deactivation of the excited state via their natural torsional activity when free in solution would limit their effective biological function. Comparison with phytochrome and phycocyanin 645 crystal structures reveals binding motifs within the *in vivo* bilin environment that help to facilitate or inhibit specific inter-pyrrole twisting vital for protein operation.

Keywords: torsional deactivation, Z-E isomerization, light harvesting, photoreception, Bilins, Dipyrroles, Phycobiliproteins

INTRODUCTION

The light harvesting process in photosynthesis constitutes the initial step that triggers the subsequent chain of electron transfer events and chemical reactions. It involves first the absorption of light by a chromophore, or pigment, followed by the transport of that energy to a reaction center site where it is finally converted into a charge separation. This process typically occurs at efficiencies approaching unity, despite the tens to hundreds of pigment-pigment energy transfer events required to span the spatial extent of the light-harvesting apparatus (Glazer, 1989; MacColl, 1998; Wientjes et al., 2013; Mirkovic et al., 2017). Such remarkable efficiencies are accomplished by utilization of antenna proteins that augment reaction centers for dramatically enhanced light capture, while simultaneously providing a pigment-coupling network to facilitate rapid and directional excitation transport prior to quenching processes. These features are realized by elegant molecular design at the single antenna-protein level where a specific arrangement of pigments, in orientations and positions enforced by local interactions with the surrounding protein scaffold, lead to a collectively optimized spectral and energetic landscape of the pigment network as a whole.

Phycobiliproteins are light harvesting antennas utilized by cyanobacteria and red algae in the form of phycobilisome supermolecular complexes, and also by cryptophyte algae where they are individually suspended in the thylakoid lumen (Glazer and Wedemayer, 1995; Scholes et al., 2012). These proteins are unique in their characteristically different, yet variable light capture properties compared to chlorophyll-based light harvesting proteins such as LHCII, chlorosomes, and the photosystems. Typically, their absorptions occur in the region between the prominent Soret and Q_y bands of chlorophyll and red of the primary carotenoid absorptions, enabling the capture of light filtered through Chl-based photosynthetic organisms. They achieve this targeted light capture by employing linear tetrapyrrole pigments called bilins, enabling significant freedom to structural and therefore spectral properties of their light harvesting machinery. That tunability in light capture is granted specifically by variable pigment conjugation, local contortions of the bilin geometry imposed by particular interactions with the protein scaffold, and finally the spatial configuration of neighboring pigments. These features taken together also imparts rapid and efficient energy transfer/funneling throughout and between light harvesting complexes. The light-harvesting strategy of cryptophyte algae involves suspending single phycobiliproteins in the lumen, each with a set of different bilin types to allow for extensive energy funneling within a single protein. A model example is the phycocyanin 645 (PC645) protein shown in **Figure 1A**, where specific bilin types are color-coded. These proteins all have a $(\alpha\beta)_2$-type structure with pseudo-twofold symmetry between each αβ monomer. The β subunit binds three bilins, while the extended polypeptide α subunit binds a single bilin which typically lies near the center of the protein (Harrop et al., 2014). The types of bilins differ in their extent of conjugation as well as the number of covalent linkages to the apoprotein, with either one linkage at the A ring or two at

FIGURE 1 | (A) PC645 crystal structure with bilin types color-coded, and chemical structure of dihydrobiliverdin (DBV) referenced by the blue circle. **(B)** Chemical structures of dipyrroles studied in this work.

rings A and D (**Figure 1A**, right) (Glazer, 1985; Glazer, 1989; MacColl, 1998; Harrop et al., 2014). Among the various cryptophyte phycobiliproteins sequenced and whose crystal structures have been solved, significant homology is demonstrated both in sequence and αβ conformation (Harrop et al., 2014), showing that light capture differences occurs predominantly by exchanging bilin types.

While the comparatively flexible, linear bilin structure is advantageous for bestowing spectral tunability to the organism, this same feature also introduces the possibility for deactivation pathways which are parasitic to light harvesting via "twisting" motions about the respective methine bonds separating pyrrolic rings. Generally, the torsional freedom about bonds separating two parts of a conjugated system, as in the case of bilins, will lead to nonradiative deactivation of the excited molecule through direct internal conversion or by isomerization through a conical intersection. The latter of which is a common pathway utilized in nature to initiate signaling through photoreception. One example of this is the initial step in vision where the retinal molecule isomerizes in less than 100 fs following photon absorption (Wang et al., 1994; Polli et al., 2010), leading to a conformational change in the rhodopsin protein followed by a transduction cascade (Palczewski, 2012; Molday and Moritz, 2015). Perhaps more relevant to bilin light harvesting however, are photosensory phytochromes and cyanobacteriochromes found in plants, bacteria, cyanobacteria, and fungi which incorporate a single bilin photoswitch capable of undergoing isomerization following light absorption. This behavior ultimately results in downstream photomorphogenesis among other dynamical processes vital for growth and survival (Rockwell et al., 2006; Ulijasz and

Vierstra, 2011). In canonical phytochromes, the isomerization event takes the red-absorbing species (P_r) to the Lumi-R intermediate state, before completing the process to the far-red absorbing meta-stable P_{fr} form. The process primarily involves rotation of the D pyrrole ring from a nominally Z conformation (about the nearest methine double bond) to E, coincidentally with local protein adjustments in the binding pocket to promote the transformation and stabilization of each state. The reaction occurs typically with a quantum yield of ~0.15 (Lamparter et al., 1997; Dasgupta et al., 2009), and it is both thermally and photochemically reversible. The remaining ~85% of the phytochrome population reverts back to the ground state in 3 ps via internal conversion, apparently outcompeting the isomerization pathway (Dasgupta et al., 2009).

A fascinatingly stark contrast is noted between the two biological contexts/functions utilizing bilins. Torsional dynamics between pyrrole rings must be eliminated in photosynthetic light harvesting to retain the electronic excitation long enough for many energy transfer events. While that torsional freedom is supported and controlled in the photoreception mechanism of phytochromes and cyanobacteriochromes. In both contexts however, the local pigment-protein and water interactions appear crucial to confer bilin function in a controllable fashion. Here, we seek to characterize the innate torsional freedom and conformational landscape of bilins absent explicit protein interactions. In this way, the importance and extent of individual protein/water contacts in facilitating the functionality of bilins can be assessed from an appropriate reference point—the free molecule in solution.

In order to do this in a bottom-up fashion however, the tetrapyrrole structure (incorporating three methine bridges with six separate torsional coordinates) must be broken down into dipyrrolic subunits which incorporate only a single methine group with two torsional degrees of freedom, thereby simplifying the nuclear degrees of freedom responsible for relevant excited state dynamics. In doing so, one finds two unique subunits representative of either the terminal pyrrolinone-pyrrole pair (dipyrrinone, DPN), or the central dipyrrole pair (DPY) devoid of the carbonyl group.

While little has been reported on the spectroscopic properties of the dipyrrole "core" subunit specifically, it is a spectroscopic analogue to a common marine cyanobacterial light-harvesting bilin called phycourobilin (PUB). In the case of the PUB pigment, the electronic conjugation extends only over the central B and C rings which are subsequently bound to the terminal pyrrolinone rings via methylene groups (i.e. single bonds). Incorporating a bilin with such a restricted conjugation length enables the organism to efficiently capture light further into the blue-green region, which is an ecological requirement for these organisms to do photosynthesis in subsurface oceanic waters where the penetration depth of blue light is best. Given this property, it has been suggested that PUB is the most abundant phycobilin in the ocean (Blot et al., 2009). Since the dipyrrole core of PUB is responsible for the relevant visible absorption, at least a cursory comparison of its spectroscopic properties can be made to the model DPY subunit studied in this work.

There has been interest in dipyrrinone since the discovery of phototherapy of neonatal jaundice through photochemistry of bilirubin. The bilirubin structure is effectively two dipyrrinone halves separated by a methylene bridge, and the operative mechanism responsible for its photochemistry is in fact Z→E isomerization at the D pyrrole ring with a quantum yield of ~0.1 (Mazzoni et al., 2003), with the remainder of the excited population decaying back to the ground state (~15 ps) similar to the photochemistry of phytochrome (Zietz and Blomgren, 2006; Zietz and Gillbro, 2007). Studies on single dipyrrinone derivatives have yielded similar results, with rapid deactivation attributed to twisting motion of the two rings leading mainly to the recovery of the ground state Z isomer (Lamola et al., 1983; Zietz and Gillbro, 2007; Sakata et al., 2016). These results suggest the intrinsic nature of the dipyrrinone bilin subunit to undergo ring twisting in the excited state when free in solution, and a seminal work by Lightner et. al. elegantly demonstrated the suppression of this behavior by chemically linking the two rings. In that work, the fluorescence quantum yield went from $\Phi_F < 10^{-4}$ to 0.81 when the rings were constrained by a methylene bridge across the pyrrolic nitrogens (Hwang and Lightner, 1994). Recently, the same effect was demonstrated in a bilirubin fluorescent protein where Φ_F was found to be 0.51 due to the anchoring of the pyrrolinone ring by at least three direct hydrogen bonds from nearby amino-acids (Cao et al., 2019).

In this work, we seek to elucidate the local conformational landscape/flexibility, excited-state deactivation mechanism(s), as well as the spectroscopic properties of the two types of bilin dipyrrolic subunits absent of any bonds or interactions to an external scaffolding. Structures of the model dipyrrole core (DPY) and terminal dipyrrinone (DPN) subunits studied here are shown in **Figure 1B**. Steady-state spectroscopy and photophysical characterization was performed on each subunit, in conjunction with density functional theory (DFT) analysis of the conformational landscapes of each. In addition, femtosecond transient absorption spectroscopy was carried out to directly evaluate the excited state decay mechanism and the associated kinetics therein. Taken together, this bottom-up approach allows for a comprehensive analysis of the light capture ability and inherent excited-state torsional freedom of each part of the bilin framework, and those results precipitate the importance of specific interactions within the *in vivo* bilin environment in steering biological function.

MATERIALS AND METHODS

Experimental

DPY (3, 5, 3′, 5′-Tetramethyl-1H, 2′H-2, 2′-methanylylidene-bis-pyrrole hydrochloride) was purchased from Sigma-Aldrich and used without further purification. DPN and N-methyl-DPN syntheses were adapted from Chepelev, et al. and Huggins et al. (Chepelev et al., 2006; Huggins et al., 2007). The reduced alkylation at the pyrrole site of the DPN derivatives studied here has been shown to significantly reduce facile dimer formation in nonpolar solvents; however, the dimer association constant, K_a, for DPN in nonpolar solvents such as chloroform still reaches

~3,850 M^{-1} due to extensive H-bonding at the pyrrolic amine and pyrrolinone carbonyl sites (Huggins et al., 2007). In order to disentangle monomer and dimer dynamics in solution, we compared the results of DPN with *N*-methyl-DPN (**Figure 1B**) which significantly inhibits H-bond formation that leads to dimer formation.

Steady-state UV-vis absorption spectroscopy was carried out on an Agilent 8453 UV-vis spectrometer, and molar extinction coefficients for each sample-solvent combination was determined by linear fitting of 4–5 different concentrations in the 10^{-6}–10^{-5} M concentration range (A < 0.9) in a 1 cm quartz cuvette. The oscillator strength, *f*, for the S_0–S_1 transitions and the radiative rate constant, k_r^0, for each was estimated by calculation directly from the extinction spectra according to classical light theory (Turro et al., 2010). Corrected fluorescence spectra were collected using a PTI (Photon Technology International) fluorometer, and samples were contained in a 1 cm quartz cuvette with a maximum sample optical density (OD) of <0.3 to avoid inner filter effects. Fluorescence quantum yields, Φ_F, were determined against references rhodamine 6G in ethanol solvent ($\Phi_F = 0.94$) for DPY (Fischer and Georges, 1996), and 9,10-diphenylanthracene in ethanol ($\Phi_F = 0.88$) (Mardelli and Olmsted, 1977) for DPN derivatives. Spectroscopic/photophysical properties for each sample were determined in both polar-protic methanol solvent and dichloromethane solvent for comparison. For DPY in methanol, 0.1 M HCl was added at 0.5% by volume to ensure complete protonation at both pyrrole sites in accordance with its native protonation state *in vivo* (Kneip et al., 1999; Rohmer et al., 2006; Corbella et al., 2018; Toa et al., 2019).

Transient absorption (TA) spectroscopy was undertaken at the Center for Ultrafast Optics and Lasers (CUOL) at Ft. Lewis College, and employed a 1 kHz Spectra-Physics Solstice Ace regenerative amplifier pumping a TOPAS Prime OPA for the pump pulse, while also seeding the white light generation stage of the Newport Transient Absorption Spectrometer. The white light continuum probe pulse was generated using a rotating CaF$_2$ substrate. All TA measurements reported here were taken with the pump wavelength set to the peak of the S_0–S_1 transition for each sample, and the power was kept below 1 mW. The pump-probe polarization angle was set to magic angle, and each data set shown is an average of 10–20 scans each taken at 200 ms integration time. For TA experiments, samples were placed in a 1 mm cuvette with an OD < 0.5 at the peak absorption. Global analysis of the chirp-corrected data was performed using the Glotaran program (Snellenburg et al., 2012).

Computational

All calculations were carried out in the Gaussian 16 suite (Frisch et al., 2016). Ground state geometry optimizations, harmonic frequency calculations, thermochemical calculations, and ground state potential energy scans were done using density functional theory at the M05-2X(Zhao and Truhlar, 2007)/6–311++G(d,p) level of theory with implicit solvation by methanol approximated using the polarizable continuum model (PCM). Time-dependent density function theory (TDDFT) at the same level of theory was used for vertical excitation calculations. Recent computational

work on DPN using the hybrid semiempirical DFT/MRCI approach found that the first electronic transition of DPN resulted in negligible double-excitation character, justifying the TDDFT approach used here (Lyskov et al., 2020).

RESULTS

Conformational Landscapes

The torsional freedom of linear tetrapyrroles provides both spectral tunability when external contacts are made to contort the local geometry across a dipyrrole pair (such as the case in photosynthetic light harvesting), or the ability to isomerize across the methine bridge of a dipyrrole pair (photoswitching). The latter has been found to generally occur at the bilin terminus, however, this is largely due to covalent and electrostatic confinement of the core dipyrrole pair in the *in vivo* setting. In an effort to assess the local flexibility of each dipyrrole subunit isolated from these interactions, the ground state conformational minima of DPY, DPN, and *N*-Me-DPN were calculated along with the relative Gibbs free energies of each. **Figure 2A** shows the dominant nuclear degrees of freedom that separate the various conformational families found for DPY and DPN derivatives.

For DPY, two-fold symmetry exists about the methine carbon given the protonated form studied here, leading to only three distinct conformers shown in **Figure 2B**. The DPY conformers differ in their torsional state across both methine bonds (C_4–C_5 and C_5–C_6). Given the resonance/symmetry in this case, the two torsional coordinates are identical and labeled as *Z* or *E* for each. The global Gibbs energy minimum structure is the *Z,Z* isomer with both NH groups facing one another, ultimately leading to a small N-C_4--C_6-N ring twist angle of ~18°, while simultaneously minimizing the steric contributions of the methyl substituents. The same effect would be exacerbated in the fully alkylated case as is found *in vivo* to stabilize the *Z,Z* form. The other conformational minima are separated by significant Gibbs energy of 8.22 and 24 kJ/mol for the *Z,E* and *E,E* isomers. For the *Z,E* isomer, the first pyrrolic NH lies in the ring plane with the adjacent methyl group staggered about it to stabilize a fully planar structure. The *E,E* isomer structure reveals a highly twisted configuration (53°) motivated by the close proximity of flanking methyl substituents. This interaction pushes the conformational free energy significantly higher than the other *Z* forms. The relative Gibbs free energies are shown in **Figure 3** for comparison. The additional steric interactions of the *Z,E* and *E,E* forms give way to Gibbs energies well above *kT*; therefore we expect only a negligible population at room temperature, likely not observable in experiment.

The ground state potential energy surface of DPN is significantly more complex than DPY due to the asymmetric nature of the pyrrolinone-pyrrole pair, along with the ethyl torsional freedom which adds to the heterogeneity of the ground state. **Figure 2A** gives the primary degrees of freedom for DPN along with the labels used to classify each. These include the twist coordinate about the methine double bond (C_4–C_5) separating *Z,E* families, the twist coordinate about the methine single bond (C_5–C_6) separating *syn*/*anti* configurations, and
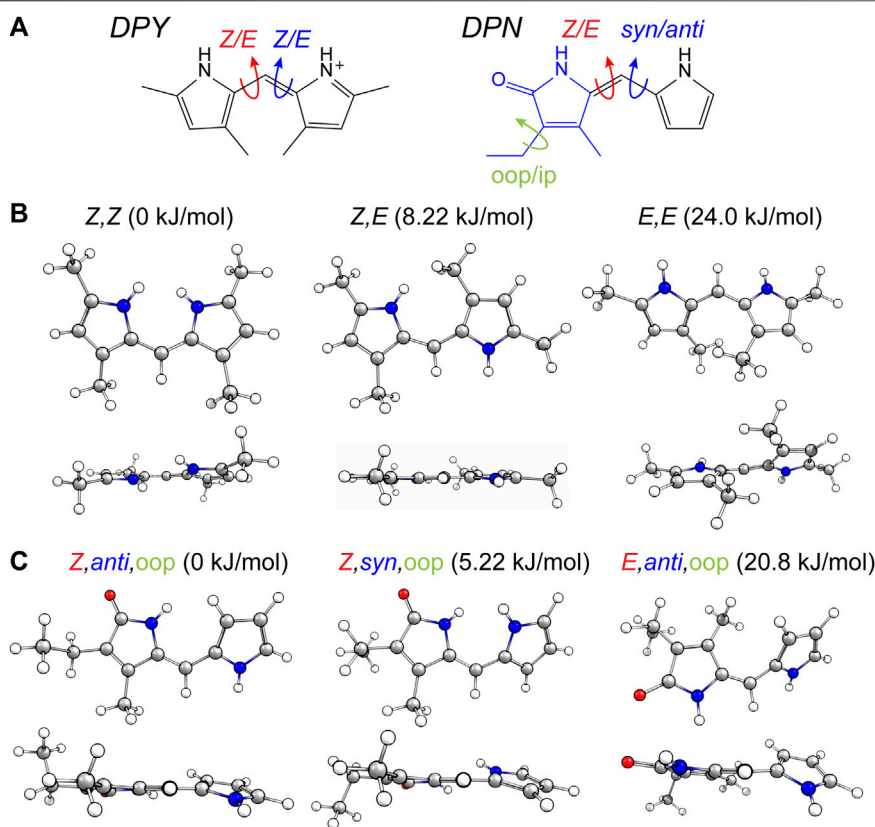
FIGURE 2 | (A) Conformational degrees of freedom for DPY and DPN. **(B,C)** Calculated conformers of **(B)** DPY and **(C)** DPN with associated relative Gibbs free energies.
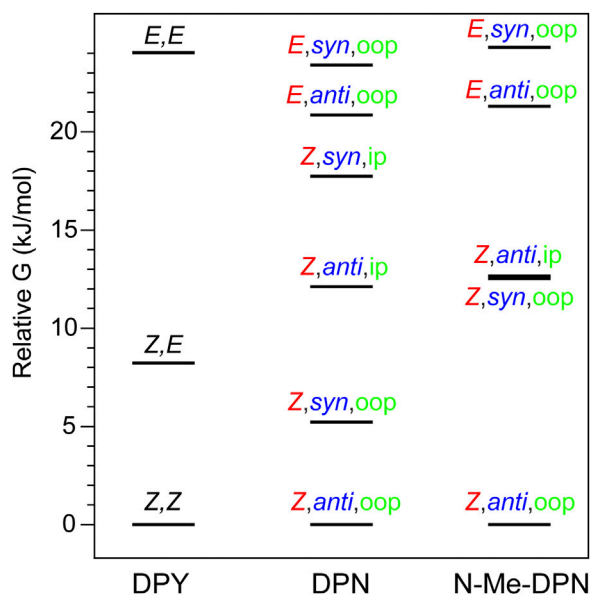

FIGURE 3 | Gibbs free energy diagram for DPY, DPN, and *N*-Me-DPN conformational families.

finally the pyrrolinone ethyl torsional configurations as either out-of-plane (oop) or in-plane (ip) relative to the pyrrolinone ring plane. The three lowest energy families are shown in **Figure 2C**, and already it is found by inspection that all conformers are nonplanar across the di-ring framework, generating degenerate pairs of minima associated with a positive or negative di-ring twist angle across the $N-C_4--C_6-N$ dihedral. The ethyl group freedom further produces auxiliary minima associated with the oop configurations above or below the pyrrolinone plane. Therefore, there exists four near-degenerate minima for each "oop" family and two for "ip" families. For example, the *Z,anti*,oop conformational family contains four independent minima associated with combinations of +/− di-ring twist angles along with the two ethyl orientations. Nevertheless, the *Z,anti* torsional family is found to be the global minimum for both ethyl oop/ip, and is separated by ~5 kJ/mol from the higher *Z,syn* family which positions the pyrrole NH groups adjacent one another. Interestingly, with a methyl substitution at the C_7 position as in the DPY case, the ordering would likely be opposite. However, the nominal configuration of the torsionally-active pair in the phytochrome case is indeed the *Z,anti* conformation, so DPN is a representative model for that case. Comparing these families in
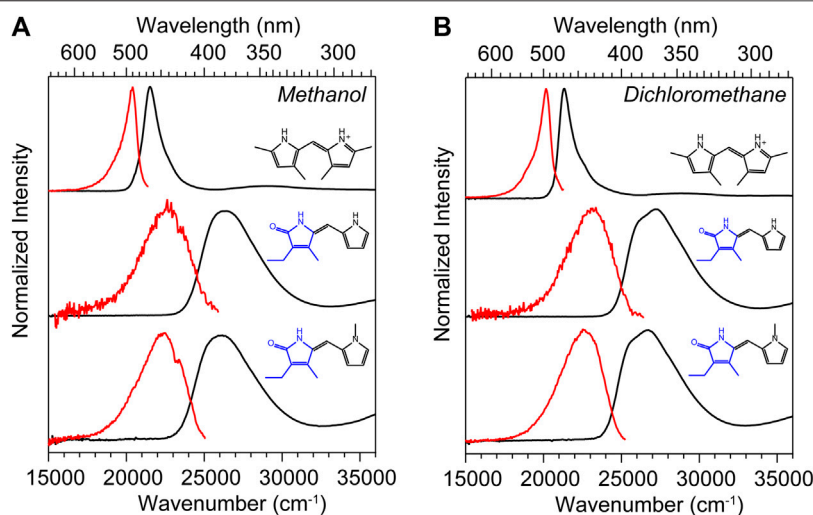
FIGURE 4 | UV-vis absorption (black) and corrected fluorescence (red) spectra for DPY, DPN, and *N*-Me-DPN in **(A)** methanol and **(B)** dichloromethane.

TABLE 1 | Spectroscopic properties of DPY, DPN, and *N*-Me-DPN in methanol and dichloromethane solvents determined from steady-state measurements. Band maxima are all given in wavenumbers (cm^{-1}).

	v_{max}^{abs} (λ_{max}, nm)	v_{max}^{fl} (λ_{max}, nm)	Stokes Shift (cm^{-1})	ε_{max} ($M^{-1}cm^{-1}$)	f
DPY (MeOH)	21,505 (465)	20,408 (490)	1,097	102140	0.692
DPY (DCM)	21,322 (469)	20,161 (496)	1,161	147390	0.965
DPN (MeOH)	26,316 (380)	22,573 (443)	3,743	32,610	0.641
DPN (DCM)	27,174 (368)	23,148 (432)	4,026	26,480	0.51
N-Me-DPN (MeOH)	26,178 (382)	22,371 (447)	3,807	32,340	0.657
N-Me-DPN (DCM)	26,738 (374)	22,676 (441)	4,062	25,880	0.528

the *N*-methyl substituted DPN (**Figure 3**), it is found that the *Z,syn* conformation is highly destabilized from the additional steric clash of the *N*-Me and adjacent amide NH.

Spectroscopy and Photophysics

The UV-vis absorption spectra (black) and corrected fluorescence spectra (red) are shown for all three compounds in methanol and dichloromethane solvents in **Figures 4A,B** respectively, and the wavenumber and wavelength positions for the absorption and emission maxima for each spectrum are given in **Table 1** along with other observed and derived spectral properties. Immediately striking from a cursory comparison is the vastly different breadths of the absorption and fluorescence bands associated with the S_0–S_1 transition. DPY shows significantly more narrow bandshapes, and are red-shifted by nearly 5,000 cm^{-1} (85 nm) compared to DPN compounds leading to absorption well into the visible range (λ_{max} = 465 nm). We can attribute the broadening in

DPN spectra at least in part to the conformational heterogeneity predicted by calculations, with the additional possibility of dimerization. However, calculation of the binding free energy for DPN and *N*-Me-DPN H-bonded dimers yields $\Delta G_{dimerization}$ = −2.77 and +12.1 kJ/mol respectively (structures given in **Supplementary Figure S2** of the Supplementary Material). This suggests that dimerization of the *N*-methyl derivative should be minimal as anticipated. Despite this prediction, the breadth of spectra for both DPN compounds are very similar perhaps indicating a lack of substantial dimer formation at least in methanol. The small inflection at ~23,000 cm^{-1} in the DPN and *N*-Me-DPN fluorescence spectra in methanol is due to incomplete subtraction of a methanol Raman band following subtraction of the methanol background.

Reflecting on the global minimum conformers of DPY and DPN, the red-shift associated with DPY is at least partially associated with a smaller inter-ring twist angle (18° vs. 30°)—a property of bilins which has been shown to drastically tune the absorption wavelength (Tang et al., 2015; Wiebeler et al., 2019; Xu et al., 2020). However we cannot rule out the possibility of the influence of the DPN carbonyl on the electronic structure itself. According to vertical excitation energy calculations however, the S_0–S_1 transitions are described exclusively by a HOMO→LUMO ($\pi \to \pi^*$) excitation for both derivatives showing nominally the same electron delocalization length. Another remarkable feature of all spectra in **Figure 4** is the dramatic Stokes shift between band maxima of ~1,000 cm^{-1} (~25 nm) for DPY and ~4,000 cm^{-1} (~63 nm) for DPN. Given the similarity in lineshapes, the massive wavenumber difference must be due in part to a dramatic geometry change between S_0 and S_1, and in the case of DPN possibly an emissive conformer population among many separately absorbing populations.

Table 1 summarizes the absorption strength of each molecule via their molar extinction coefficients (at λ_{max}) along with the calculated oscillator strengths for the electronic transition. All compounds demonstrate large oscillator strengths for their S_0–S_1

	k_r (s^{-1})	τ_r (s)	Φ_F	k_{nr} (s^{-1})	τ_{nr} (s)
DPY(MeOH)	2.23E+08	4.48E-09	1.15E-04	1.94E+12	5.15E-13
DPY (DCM)	3.06E+08	3.27E-09	6.02E-04	5.08E+11	1.97E-12
DPN (MeOH)	3.13E+08	3.19E-09	3.43E-04	9.13E+11	1.10E-12
DPN (DCM)	2.63E+08	3.80E-09	1.01E-03	2.60E+11	3.84E-12
N-Me-DPN (MeOH)	3.14E+08	3.18E-09	2.17E-04	1.45E+12	6.91E-13
N-Me-DPN (DCM)	2.63E+08	3.80E-09	6.16E-04	4.27E+11	2.34E-12

transition, on average $f \sim 0.6$. This is a remarkable result given their relatively small and atomically "cheap" structures, and highlights the effectiveness of this naturally-designed molecular framework for light capture. We note that despite the smaller ε_{max} measured for DPN compounds, the integrated intensity of the broad absorption yields an oscillator strength comparable to its DPY counterpart. As predicted, the absorption wavelength and band shape of DPY is found to be very similar to the phycourobilin chromophore found in cyanobacterial phycobiliproteins, and as a result the peak molar extinction coefficient is also very comparable ($\varepsilon_{max \; PUB} = 104000 \, M^{-1} \, cm^{-1}$) (Glazer and Hixon, 1977). Notably, various forms of chlorophyll yield a ε_{max} of 35,000–90,000 $M^{-1} \, cm^{-1}$ for the red-most Q_y transition with comparable widths to DPY, suggesting the chemically simpler pigments studied here may be even better light absorbers in their respective spectral regions (Scheer, 1991).

Table 2 gives photophysical characteristics of each of the sample/solvent combinations. k_r is the radiative rate constant calculated from the integrated intensity of the main absorption band, and τ_r is therefore the natural lifetime and falls in the typical nanosecond time scale. The fluorescence quantum yields of all compounds are exceedingly low ($\sim 10^{-4}$), in agreement with previous studies on dipyrrinones (Hwang and Lightner, 1994). We speculate then, that the torsional motion activated following electronic absorption is as extensive as other free dipyrrinones in solution. Taking these data together, the total nonradiative rate constant, k_{nr}, for each and its associated time constant are also given in **Table 2**. One can see that deactivation of the S_1 excited molecule takes place on average in a few picoseconds or less. DPY in methanol yields the smallest Φ_F and therefore fastest nonradiative decay at ~ 500 fs.

Transient Absorption Spectroscopy

To elucidate the exact mechanism for rapid excited state decay of DPY and DPN, transient absorption spectroscopy was undertaken for each. **Figures 5A,B** show the evolution of transient absorption spectra of DPY in methanol, with the absorption and fluorescence spectra given above as reference. At very early times, the symmetrical feature incorporating both negative-going S_0–S_1 ground state bleach (GSB) and S_1–S_0 stimulated emission (SE) signals can be immediately identified, and is centered at 21,500 cm^{-1}. In addition, a large excited state absorption (ESA) signal is present at 29,250 cm^{-1} at time zero. Before a dynamic Stokes shift can be observed however, the SE

signal disappears within ~ 500 fs as a new photo-induced absorption (PIA) signal around 20,400 cm^{-1} appears within 1 ps. Within the same timeframe, the ESA signal to the blue decays and significant GSB is lost. Within 15 ps, nearly all of the ESA signal has vanished while most of the ground state has been re-populated—signaling facile internal conversion. During this time, the induced absorption signal peaks around 2.5 ps and continuously narrows and blue-shifts before itself decaying away to reveal a broader PIA signal after 10 ps. This early time behavior is indicative of formation of a hot ground state population, S_0^*, immediately after the internal conversion curve-crossing event at the S_1 potential energy minimum. As the population cools, the PIA signal blue-shifts and narrows before disappearing upon reaching equilibrium in the ground state. While similar ESA and SE behavior could be expected with a substantial geometry change as the molecule leaves the Franck-Condon region of the S_1 surface, the concomitant loss of GSB can only be explained by cooling within the ground state. Interestingly though, a fraction of the GSB signal remains even at 3 ns along with the broader positive signal at 20,800 cm^{-1}.

The dynamics in dichloromethane solvent (**Figures 5C,D**) are nearly identical except for occurring at a lower rate. The slower evolution in these data clearly bear out the cooling behavior of the hot ground state population and finally the remaining product population at lower yield. The slower deactivation of the S_1 state in dichloromethane is somewhat unexpected given the viscosity and polarity are both reduced compared to methanol (thereby enabling less hindered twisting about the methine bridge). Therefore, we surmise that H-bonding interactions between DPY and the polar protic methanol solvent must manipulate the excited potential energy surface to allow the excited molecule to sample the conical intersection more efficiently. Alternatively, the H-bonding at the pyrrole amines may alter the electronic structure directly leading to a reduced bond order of the C-C bonds making up the methine bridge.

The transient absorption spectra and time evolution for DPN in methanol and dichloromethane are given in **Figure 6**. Immediately after excitation, the GSB peaks just blue of the absorption band due to a positive PIA peaking at 23,580 cm^{-1} present already within the time resolution of the experiment. The signal spans out as far as 16,000 cm^{-1}, with a negative SE signal appearing at $\sim 21,000$ cm^{-1} separating the two sections of the broad positive feature. Similar to the results of DPY, the ground state rapidly refills (loss of GSB) coincidentally with the blue-shift and narrowing of the PIA. This behavior again signifies cooling on the ground state surface following an internal conversion event. Internal conversion in this case must occur within the pulse overlap time (<120 fs) given the immediate appearance of the hot ground state signature. Curiously though, the residual SE signal decays in this case within ~ 5 ps—much longer than the proposed internal conversion timescale. To this point, it is found that between 5 and 20 ps, as the hot ground state population has thermalized, a second population is revealed and evolves with slower kinetics. This is observed in the remaining GSB signal at ~ 20 ps which is red-shifted by 1,000 cm^{-1} from the early time GSB. A marked feature of these distinct species is the seemingly red-shifting inflection between the primary GSB and PIA signals
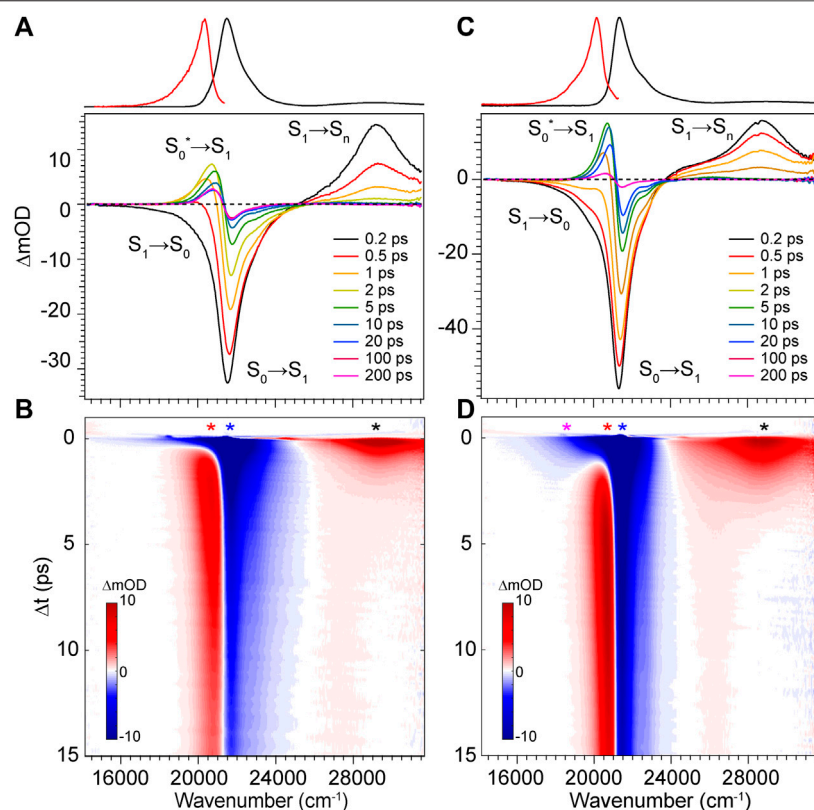
FIGURE 5 | Transient absorption spectra for DPY in **(A,B)** methanol and **(C,D)** dichloromethane. Asterisks in b and d denote wavenumber positions for transients shown in **Figure 7**. Absorption (black) and fluorescence (red) spectra are shown at the top for reference.

in **Figure 6B**. Finally, this signal decays over the next 50 ps to lastly show a very small and broad GSB around 27,000 cm^{-1} with residual PIA ~23,000 cm^{-1}. Similar spectral dynamics are observed in this progression (shifting GSB/PIA inflection) except toward the blue direction; these longer time data can be found in **Supplementary Figure S3** of the Supplementary Material. The sum of these observations points to at least three independent ground state populations. These species could be various DPN conformers given the increased complexity of the DPN potential energy surface (**Figure 3**), and/or some dimer contribution in addition.

To address this question, we performed TA spectroscopy on the *N*-methyl DPN derivative which locks out dimer formation by eliminating two H-bond sites. These results are given in **Supplementary Figure S4** of the Supplementary Material, and show nearly identical spectral features with remarkably similar dynamics, except for the final remaining GSB/PIA signals which are absent in those data. In fact, unlike DPN, all of the population has returned entirely to the ground state by the end of the 200 ps experiment. The longer-lived blue-most absorbing population in DPN can therefore be tentatively assigned to a small fraction of dimer in solution, with the intermediate red-absorbing population assigned to the *Z,syn*,oop family of conformers. Boltzmann analysis yields ~12% of the total population belonging to this family at

thermal equilibrium, and is consistent with the relative GSB intensities shown in **Figure 6**.

The TA data for DPN in dichloromethane (**Figures 6C,D**) shows two primary signals peaking ~27,350 cm^{-1} and 22,150 cm^{-1}. Unlike in methanol, these features decay directly with approximately the same kinetics and little to no spectral changes therein. In this case, the positive signal at 22,150 cm^{-1} is then assigned to an ESA given the static band profile. Keeping in mind the large dimer association constant of DPN in chloroform, this single species is assumed to be $(DPN)_2$, and its excited-state dynamics are dominated by internal conversion with a time constant of ~3 ps.

DISCUSSION

Excited State Decay Mechanism of Model Dipyrrole Subunits

With the combination of photophysical data derived from steady-state spectroscopy measurements and time-resolved transient absorption, we are now in a position to address the excited state behavior of these model bilin subunits free in solution. First, in order to determine the exact time/rate constants associated with the excited state decay pathways of DPY and DPN, global analysis of the chirp-corrected data was performed.
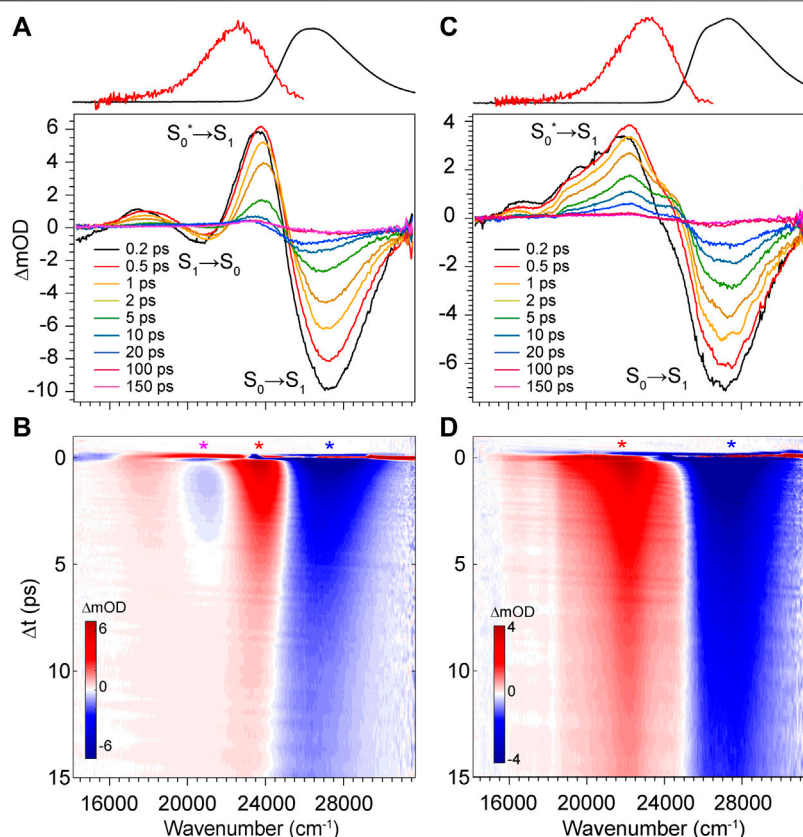
FIGURE 6 | Transient absorption spectra of DPN in **(A,B)** methanol and **(C,D)** dichloromethane. Asterisks in b and d denote wavenumber positions for transients shown in **Figure 9**. Absorption (black) and fluorescence (red) spectra are shown at the top for reference.

For DPY, a sequential model was applied to the data given the homogeneity of the ground state population. The evolutionary-associated spectra (EAS) along with the fit to selected transients (positions marked with asterisks in **Figure 5**) are given in **Figures 7A,B** respectively for DPY in methanol.

A total of four components was required to capture the somewhat complex evolution of all features. The component represented by EAS1 decays with τ_1 = 0.46 ps and clearly captures the SE, initial GSB, and ESA band near 29,000 cm^{-1}. We therefore assign this component to direct internal conversion and highlight that the timescale is on the order of torsional nuclear motion. EAS2 shows a significantly reduced GSB signal along with the PIA peaking near 20,300 cm^{-1} and trailing to the red. The decay of these features at τ_2 = 0.92 ps to EAS3 with the PIA now blue-shifted by 600 cm^{-1} indicates the first mode of vibrational cooling of the hot ground state population, S_0^*. Finally EAS3 decays on a 5.2 ps timescale associated predominantly with a second mode of vibrational relaxation given the still large reduction in GSB and PIA from EAS3→EAS4, and is likely from a bottleneck near the ground state minimum where the state density drastically decreases (Owrutsky et al., 1994). The final EAS4 is associated with the remaining signals at the end of the experiment and apparently static as found in **Figure 7B** at longer times. This remaining population is assigned to the

fraction of molecules that underwent $Z{\to}E$ isomerization to generate a new ground state photoproduct, and we surmise that EAS3 also incorporates this small fraction of isomerizing population occurring on a similar timescale since no other components were needed to fit the data.

The global analysis results for dichloromethane experiments are shown in **Figures 7C,D** and are qualitatively similar to the results in methanol. The features are sharper due to the reduced inhomogeneous broadening of the nonpolar solvent, and as anticipated the time constants for each mode of decay are larger. This is somewhat surprising in the initial internal conversion step as indicated previously, but the subsequent vibrational cooling steps are expectedly longer due to significantly weaker ion-dipole and H-bonding interactions with the protonated DPY (Owrutsky et al., 1994). A summary of all time constants from global analysis can be found in **Table 3**.

The product absorption of the photoisomer shown in EAS4 in both cases is red-shifted from the Z,Z isomer. Evaluating the TDDFT vertical excitation energies of all conformers (**Supplementary Material**), only the E,E isomer has an absorption red of the Z,Z global minimum. The photoproduct can then be tentatively assigned to the high energy E,E conformer, suggestive of a mechanism involving concerted twisting about both C_4-C_5 and C_5-C_6 bonds. Such a scenario was predicted for
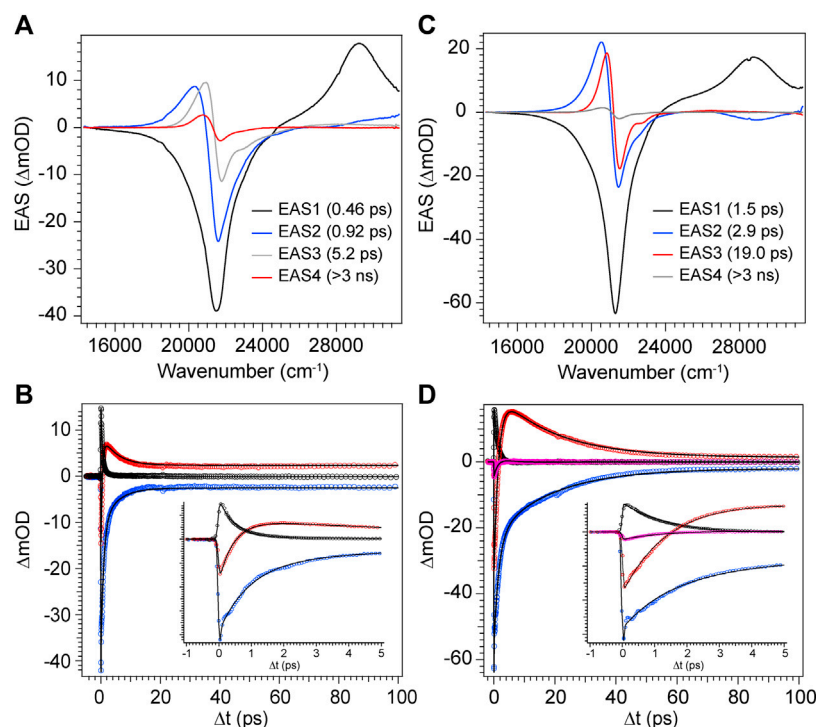
FIGURE 7 | Global analysis results from DPY TA data. **(A,C)** Evolutionary-associated spectra (EAS) with associated time constants for DPY in **(A)** methanol and **(C)** dichloromethane. **(B,D)** Selected experimental transients (open circles) with fits from the employed global sequential model for DPY in **(B)** methanol and **(D)** dichloromethane.
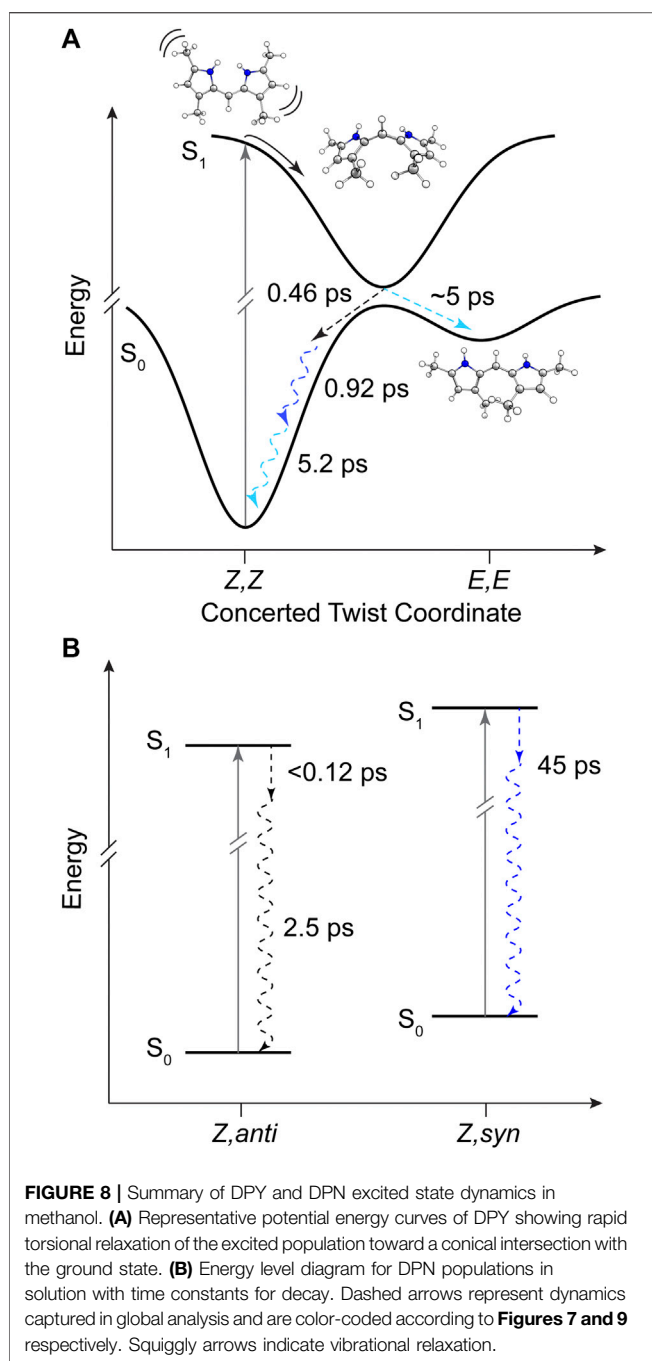
TABLE 3 | Time constants extracted from global analysis of transient absorption data for DPY, DPN, and *N*-Me-DPN.

	DPY (MeOH)	DPY (DCM)	DPN (MeOH)	DPN (DCM)	N-Me DPN (MeOH)
τ_1 (ps)	0.463	1.47	2.51	2.89	2.17
τ_2 (ps)	0.915	2.93	44.7	19.0	23.1
τ_3 (ps)	5.19	19.4	>3000	>3000	-
τ_4 (ps)	>3000	>3000	-	-	-

an unalkylated DPN derivative previously (Zietz and Blomgren, 2006), and can be rationalized in this case by the symmetric nature of the DPY molecule. The S_0-S_1 electronic transition is effectively a HOMO→LUMO transition according to TDDFT results, and inspection of those molecular orbitals (**Supplementary Figure S5**) reflect their symmetric nature (resonance) and consequently symmetric bond order change. Thus, the electronic transition serves to simultaneously elongate both methine bridge bonds in response to their increased antibonding character in S_1. In support of this conclusion, when comparing the DPY conformers the inter-ring twist angle of the *E,E* configuration is found to be the most twisted

by far (53°). Given the expected ~90° twisted excited state minimum common to dipyrroles, the *E,E* ground state minimum would therefore be nearest to the conical intersection ultimately presenting the first "trap" to the isomerizing population. A representative potential energy diagram summarizing the excited state dynamics of DPY in methanol is given in **Figure 8A**.

The decay of excited DPN in methanol was modeled with independently decaying components, and the decay-associated spectra (DAS) are shown in **Figure 9A**. As mentioned previously, the appearance of the hot ground state population (via the band-shape and spectral evolution of the PIA signal red of the GSB) immediately after the coherent artifact suggests that the internal conversion event for the dominant DPN population (*Z,anti*,oop monomer) occurs within 120 fs. This assignment can be substantiated by the comparable spectral dynamics of the PIA near 24,000 cm^{-1} to that of DPY. The first resolvable component, DAS1, then is associated with the primary mode of vibrational cooling of that internally converted population within the ground state. DAS2 decays with a 44.7 ps time constant and captures the red-shifted GSB near 26,000 cm^{-1}. This component can be assigned to the minor *Z,syn* conformer population, and the DAS partially incorporates a SE signal peaking very close to the steady-state fluorescence spectrum. We can therefore assume that this longer-lived population is the primary emitting species, and the red-shifted absorption compared to *Z,anti* then partially explains the extensive

FIGURE 8 | Summary of DPY and DPN excited state dynamics in methanol. **(A)** Representative potential energy curves of DPY showing rapid torsional relaxation of the excited population toward a conical intersection with the ground state. **(B)** Energy level diagram for DPN populations in solution with time constants for decay. Dashed arrows represent dynamics captured in global analysis and are color-coded according to **Figures 7 and 9** respectively. Squiggly arrows indicate vibrational relaxation.

Stokes shift in **Figure 4A**. DAS3 represents the signals remaining at the end of the 200 ps experiment and is assigned either to a residual dimer population based on its absence in the *N*-Me-DPN data, or to a very small population of isomerized product which is also absent in *N*-Me-DPN. The latter can be justified considering the added steric contribution of the bulky amino methyl group to inhibit the isomerization reaction. The agreement between experiment and model was quite good, as demonstrated by the fit to selected transients in **Figure 9B**. A representative energy level diagram summarizing these dynamics is given in **Figure 8B**.

DPN in dichloromethane solvent is presumed to be dominated by H-bonded dimers, and the two primary TA signals decayed with very little change in band structure. As such, the data was successfully fit to a sequential model and the results are given in **Figures 9C,D**. Comparison of EAS1 and EAS2 show that about half of the excited population has returned to the ground state within 2.89 ps. EAS2 is very similar to EAS1 and is either a separate dimer population or vibrational relaxation within the ground state, or a combination of both. At the end of the experiment, EAS3 shows some remaining population which has not yet returned to the ground state, with an intensity similar to DAS3 in **Figure 9A**. We note that in both solvents, the GSB intensity immediately after time zero is drastically lower in magnitude compared to DPY despite similar initial steady-state absorbances. Such a result implies that much of the GSB is lost within the pulse overlap time for DPN in both solutions, including for dimers present in solution, consistent with dynamics dominated by ultrafast internal conversion.

The steady-state photophysics (**Table 2**) and TA analysis are in excellent agreement regarding the rate of deactivation of excited DPY when taking τ_1 as τ_{IC}. This yields a non-radiative rate constant, k_{nr}, of 2.17 ps^{-1} ($\tau = 0.461$ ps) and 0.67 ps^{-1} ($\tau = 1.49$ ps) for methanol and dichloromethane solvents compared to 1.94 ps^{-1} ($\tau = 0.515$ ps) and 0.51 ps^{-1} ($\tau = 1.96$ ps) found from steady-state results. The heterogeneity of the DPN ground state precludes this comparison for DPN.

In all samples, the decay pathway dominating the rate was direct internal conversion to the original ground state in <3 ps. Furthermore, the ultrafast decay (<120 fs) of the dominant *Z,anti* DPN species highlights the enhanced flexibility of the terminal bilin subunit when in an analogous starting conformation to biological phytochromes, in agreement with photosensory biliproteins and conformational results. With this in mind, $Z \rightarrow E$ isomerization was only definitively observed for DPY, at least in part due to the lower internal conversion rate. Interestingly, the *E,E* conformer was formed in the process as the ground state configuration lies closer to the excited state relaxed geometry. These results implicate a symmetric, concerted twisting mechanism for DPY photo-induced isomerization.

Nature's Selection of Multi-Pyrrolic Pigments and Design Motifs for Bilin Function

The remarkably large oscillator strengths found for these chemically simple dipyrroles immediately illustrates Nature's "selection" of the pyrrole class of compounds as the base unit for light capturing pigments in nearly all biological contexts. In addition, comparing the absorption regions for the seemingly similar DPY and DPN frameworks reveals an extraordinarily large difference of nearly 100 nm with the former absorbing blue light and the latter near-UV. This "design" characteristic/sensitivity provides a synthetically efficient method to tune the region of light capture for photosynthetic organisms depending on available light quality, and further corroborates the functional
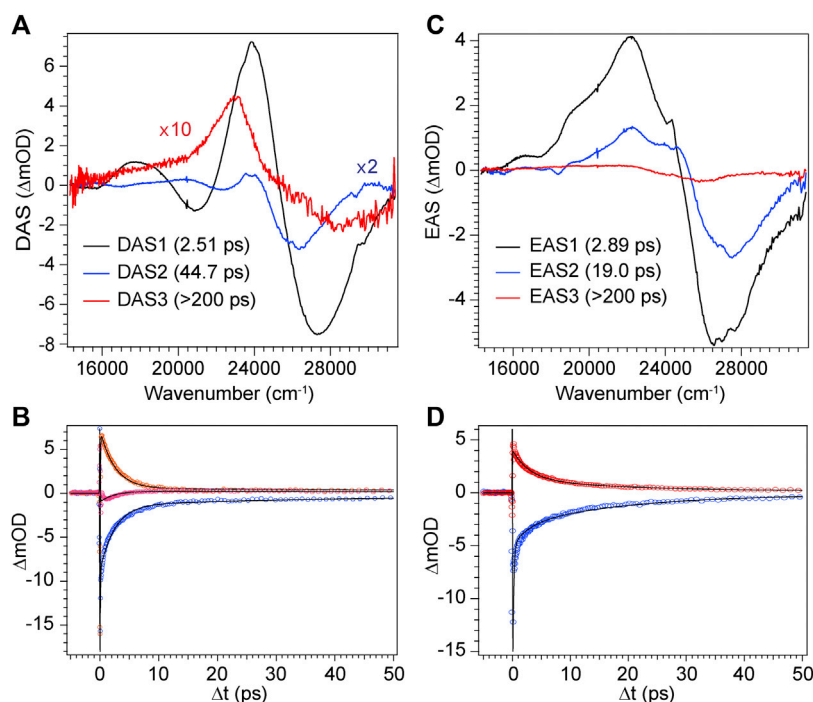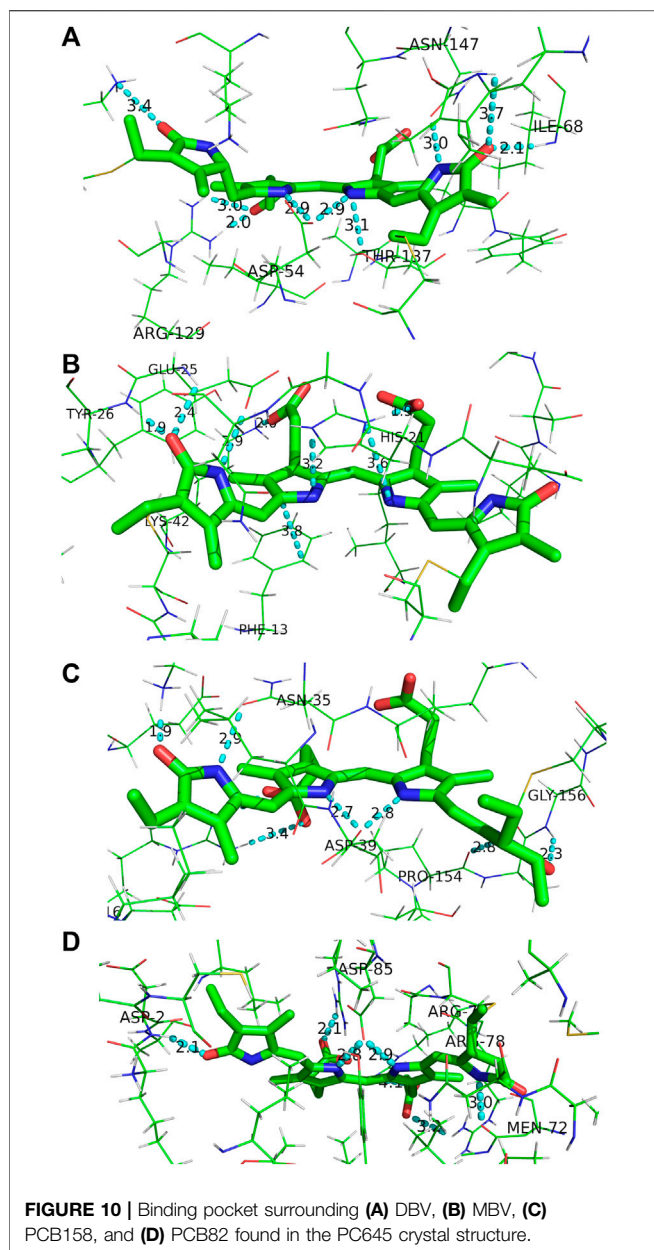
FIGURE 9 | Global analysis results from DPN TA data. **(A)** Decay-associated spectra (DAS) with associated time constants for DPN in methanol and **(C)** EAS with associated time constants for DPN in dichloromethane. **(B,D)** Selected experimental transients (open circles) with fits from the employed global model for DPN in **(B)** methanol and **(D)** dichloromethane.

connection between bilin derivatization *in vivo* and spectral tuning.

Outside of these ideal static spectral properties, the dynamics following photon absorption are of utmost importance to the final function of the natural biliproteins which bind the bilin. The dynamics observed in these simpler, free subunits reiterates the inherent tendency for large amplitude torsional motion within any multi-pyrrolic system following an electronic transition. While the terminal subunit indeed has a greater propensity for this behavior, as predicted from natural bilin photosensors, both regions of the bilin framework are prone to large-scale inter-ring twisting. Free of a protein scaffolding to bind or facilitate a controlled twist, this free motion deactivates the excited molecule rapidly back to its ground state before any sizable *E*-isomer population is generated. To avoid this loss in the phytochrome case (*Dr*BphP), the A–C pyrrole rings all contain at least one anchor to the protein scaffold with ring A being covalently attached by a Cys linkage, and rings B and C anchored by propionate groups at the C_3/C_7 positions which electrostatically attach to nearby Arg, His, and Ser amino acids (Rockwell et al., 2006). Additionally, the positive charge of the protonated core delocalized over rings B and C is closely associated with the negative charge and C=O of local His and Asp residues. These structural features ultimately restricts any twisting of the core and locks the bilin center of mass to the protein scaffold. The isomerizing ring D however, is contorted out of the bilin plane via electrostatic interaction with a nearby

histidine (His290), but is generally less confined than rings A–C. Other than the single H-bond to His290, the binding pocket surrounding ring D is hydrophobic with phenyl rings from neighboring Phe residues "boxing" off the sides of the pocket (~4 Å distance) with Met groups capping the top. In the multistep isomerization process, this binding pocket plays a vital role in stabilizing the Lumi-R intermediate and P_{fr} product, and the individual steps of the mechanism are highly coupled events between bilin and protein (Rockwell et al., 2006; Ulijasz and Vierstra, 2011). Similarly, in the prominent red/green family of cyanobacteriochromes, the indole group of a nearby Trp residue closes the binding pocket around ring D via a π-stacking interaction (3.5 Å) in the native/dark state, which is then displaced following photon absorption by some 14 Å allowing an influx of water into the binding pocket (Xu et al., 2020). Both scenarios reveal a local malleability at least near the ring D region of the chromophore to confer the concerted structural changes needed to stabilize the photoproduct.

To compare the phytochrome scenario to the functionally-opposing case of photosynthetic light-harvesting, it is instructive to assess the local pigment-protein binding motifs of the various types of bilins associated with a model phycobiliprotein antenna complex. To that end, we have chosen the highly studied PC645 protein from *Chroomonas sp.* which incorporates two nearly identical sets of phycocyanobilins (PCBs), mesobiliverdins (MBVs), and dihydrobiliverdins (DBVs) for the two near-symmetric αβ halves. We note that amino acid sequences of

FIGURE 10 | Binding pocket surrounding **(A)** DBV, **(B)** MBV, **(C)** PCB158, and **(D)** PCB82 found in the PC645 crystal structure.

this class of phycobiliproteins are highly conserved (Harrop et al., 2014), and comparison herein is considered general for cryptophyte phycobiliproteins.

Firstly, all of the bilins in PC645 are covalently attached to the protein at the ring A position by a Cys linkage, and the DBVs in the center of the protein have an additional linkage at ring D to immediately anchor that part of the otherwise torsionally-active part of the chromophore. This is especially crucial in the DBV case to inhibit twisting, as it is the only bilin to incorporate a methylene bridge (C-C-C) instead of a methine bridge between rings C and D naturally increasing the flexibility at its terminus. The methylene bridge however blocks electronic conjugation out to ring D enabling DBVs to capture light further blue compared to the other incorporated bilins. The additional Cys linkage at

ring D is therefore a targeted design motif to restrict excitation losses due to twisting about the methylene, while still expanding the spectral cross section of the protein to the blue region.

The local binding pocket of the DBV, MBV, PCB158, and PCB82 bilins are shown in **Figure 10**. Beginning with DBV (β-subunit D, **Figure 10A**), ring A (right) is found to participate in three H-bonds with Ile68 and Asn147 in addition to the Cys covalent bond, and also stacking within 3.8 Å of the neighboring DBV. The core dipyrrole is secured on both sides, with the propionic tail of ring C within 2.0 Å of the guanidine group on Arg129, and the Asp54 carboxylate straddling the central rings within 3 Å. The latter feature has also been shown to stabilize the protonated form of DBV and PCBs under physiological conditions (Corbella et al., 2018). Lastly, the ring D carbonyl is in line with the Lys67 NH_3^+ group to further lock the ring in place at a position adjacent to its Cys linkage. We note that all of the bilins nominally have propionic groups pointing outward to the protein-solvent interface, and MBVs and PCBs are relatively close to the interface compared to the imbedded DBVs. Seemingly in all biliproteins, the propionic tails of the B and C rings help lock in the planarity of the bilin core to restrict excessive twisting of the center of the chromophore. Comparing with the torsional freedom of DPY which lacks these auxiliary groups to the electronic system, this feature is an obvious design requirement *in vivo* to ensure no twisting will occur at the center of the chromophore. In addition, the ubiquitous planarity of the core dipyrrole ensures a conjugation length that spans at least two pyrrole units resulting in an absorption always in the visible region, as demonstrated by the absorption spectrum of DPY.

For MBV (**Figure 10B**) covalently attached to the α subunit, ring A (right) is primarily anchored by the single Cys linkage, and rings B and C are again locked in place via interactions between propionic carboxylates with proximate (~2 Å) His21 imidazole N and Lys42 ammonium groups. In addition, ring C is sandwiched by His21 and the phenyl ring from Phe13. Finally, ring D is held *anti* to ring C at a NC--CN twist angle of 113° by three H-bonds with the carbonyl acceptor engaged in a strong H-bond with the Tyr26 amide NH in addition to a 2.4 Å H-bond with the neighboring Glu25 residue. Finally, the Glu25 carboxylate is within 3.0 Å of the ring D NH group locking in the large twist angle. Presumably this latter feature is what blue-shifts the MBV absorption relative to PCB despite its more extensively conjugated chemical structure spanning all four rings (Tang et al., 2015; Wiebeler et al., 2019). This intermediate absorption gives way to enhanced capture between DBVs and PCBs and fills out the center of the otherwise bimodal absorption spectrum. This central MBV band can indeed be observed at 77 K (Dean et al., 2016).

Next, the PCB158 (β-subunit D, **Figure 10C**) is situated at the solvent interface of the β subunit with the propionic groups likely solvated. Ring A accepts a H-bond from the Gly156 amide, and donates one to a neighboring Pro amide carbonyl. Similar to the β-subunit bound DBV, rings B and C are straddled by a Asp carboxylate locking the two in a planar configuration. Ring D is engaged in a strong ion-dipole interaction between the pyrrolinone C=O and Lys28 ammonium end group less than 2 Å away. A secondary interaction to lock in the slightly contorted inter-ring conformation (133°) is from a H-bond of the pyrrolic NH to a Asn carbonyl.

Finally, the terminal energy acceptor, PCB82 (β-subunit D, **Figure 10D**), similarly situated at the periphery of the protein, takes on a more planarized local conformation with the NC--CN dihedral angle between rings D and C at 168°. This binding pocket-steered conformation ensures that PCB82's absorption is the most red-shifted among the bilin network to place it at the bottom of the energy funnel. This then traps the excitation at the outermost edge of the protein for subsequent transfer to nearby antennas or the thylakoid membrane-bound proteins. Interestingly though, ring D only has one close H-bond to a nearby Asp amide NH, with the pyrrolic NH nominally pointing toward the solvent interface. The other pyrrole rings are engaged in similar interactions to the other β-subunit bound bilins discussed above, with the propionic groups and central Asp providing significant anchor points to planarize the core.

In all cases, strong electrostatic interactions between each pyrrole ring with neighboring amino acids act to lock the full bilin structure in place in a rigid fashion. The ring D region of all bilins incorporated in the cryptophyte light-harvesting protein are firmly secured by a series of electrostatic interactions, and at times even covalent linkages (DBVs). This contrasts the relatively loose binding pocket typically observed in photosensory phytochromes and cyanobacteriochromes, where weaker and more mobile contacts (such as π−π stacking interactions with nearby aromatic residues) help facilitate structural changes between rings C and D following light absorption. This comparison, along with the disparate excited-state dynamics of the free subunits in solution, demonstrates the design principles utilized by photosynthetic organisms to foster specific molecular function. These insights gleaned from billions of years of evolutionary chemical design are crucial to the design and development of artificial, organic light-harvesting devices and photoswitching materials, which provide a cost-effective option for solar light harvesting applications.

DATA AVAILABILITY STATEMENT

The raw data supporting the conclusions of this article will be made available by the authors, without undue reservation.

AUTHOR CONTRIBUTIONS

CS-Acquired steady-state spectroscopic data, carried out photophysical analysis, and performed computational analysis.
JB-Acquired steady-state spectroscopic data and carried out photophysical analysis. TC-Acquired steady-state spectroscopic data, carried out photophysical analysis. MB-Carried out synthesis of DPN samples. BJ-Assisted in acquisition of steady-state spectroscopic data. DO-Assisted and advised in quantum chemistry calculations. MS-Advised and carried out synthesis of DPN and N-Me-DPN samples. JD-Advised spectroscopy and photophysical analysis, performed transient absorption spectroscopy and analysis, and coordinated manuscript construction.

FUNDING

ACKNOWLEDGMENTS

SUPPLEMENTARY MATERIAL

The Supplementary Material for this article can be found online at: https://www.frontiersin.org/articles/10.3389/fchem.2021.628852/full#supplementary-material.

REFERENCES

Blot, N., Wu, X.-J., Thomas, J.-C., Zhang, J., Garczarek, L., Böhm, S., et al. (2009). Phycourobilin in trichromatic phycocyanin from oceanic cyanobacteria is formed post-translationally by a phycoerythrobilin lyase-isomerase. *J. Biol. Chem.* 284 (14), 9290–9298. doi:10.1074/jbc.M809784200

Cao, X., Zhang, C., Gao, Z., Liu, Y., Zhao, Y., Yang, Y., et al. (2019). Ultrafast internal conversion dynamics of bilirubin bound to UnaG and its N57A mutant. *Phys. Chem. Chem. Phys.* 21 (5), 2365–2371. doi:10.1039/c8cp07553k

Chepelev, L. L., Beshara, C. S., MacLean, P. D., Hatfield, G. L., Rand, A. A., Thompson, A., et al. (2006). Polypyrroles as Antioxidants: kinetic studies on reactions of bilirubin and biliverdin dimethyl esters and synthetic model compounds with peroxyl radicals in solution. Chemical calculations on selected typical structures. *J. Org. Chem.* 71 (1), 22–30. doi:10.1021/jo051359e

Corbella, M., Toa, Z. S. D., Scholes, G. D., Luque, F. J., and Curutchet, C. (2018). Determination of the protonation preferences of bilin pigments in cryptophyte antenna complexes. *Phys. Chem. Chem. Phys.* 20 (33), 21404–21416. doi:10.1039/c8cp02541j

Dasgupta, J., Frontiera, R. R., Taylor, K. C., Lagarias, J. C., and Mathies, R. A. (2009). Ultrafast excited-state isomerization in phytochrome revealed by

femtosecond stimulated Raman spectroscopy. *Proc. Natl. Acad. Sci. USA* 106 (6), 1784. doi:10.1073/pnas.0812056106

Dean, J. C., Mirkovic, T., Toa, Z. S. D., Oblinsky, D. G., and Scholes, G. D. (2016). Vibronic enhancement of algae light harvesting. *Chem.* 1(6), 858–872. 10.1016/j.chempr.2016.11.002

Fischer, M., and Georges, J. (1996). Fluorescence quantum yield of rhodamine 6G in ethanol as a function of concentration using thermal lens spectrometry. *Chem. Phys. Lett.* 260 (1), 115–118. 10.1016/0009-2614(96)00838-X

Frisch, M. J., Trucks, G. W., Schlegel, H. B., Scuseria, G. E., Robb, M. A., Scalmani, G., et al. (2016). *Gaussian 16*. Wallingford CT: Gaussian, Inc..

Glazer, A. N., and Hixon, C. S. (1977). Subunit structure and chromophore composition of rhodophytan phycoerythrins. Porphyridium cruentum B-phycoerythrin and b-phycoerythrin. *J. Biol. Chem.* 252 (1), 32–42.

Glazer, A. N. (1989). Light guides. Directional energy transfer in a photosynthetic antenna. *J. Biol. Chem.* 264 (1), 1–4.

Glazer, A. N. (1985). Light harvesting by phycobilisomes. *Annu. Rev. Biophys. Biophys. Chem.* 14 (1), 47–77. doi:10.1146/annurev.bb.14.060185.000403

Glazer, A. N., and Wedemayer, G. J. (1995). Cryptomonad biliproteins — an evolutionary perspective. *Photosynth. Res.* 46 (1), 93–105. doi:10.1007/bf00020420

Harrop, S. J., Wilk, K. E., Dinshaw, R., Collini, E., Mirkovic, T., Teng, C. Y., et al. (2014). Single-residue insertion switches the quaternary structure and exciton states of cryptophyte light-harvesting proteins. *Proc. Natl. Acad. Sci. USA* 111 (26), E2666. doi:10.1073/pnas.1402538111

Huggins, M. T., Musto, C., Munro, L., and Catalano, V. J. (2007). Molecular recognition studies with a simple dipyrrinone. *Tetrahedron* 63 (52), 12994–12999. 10.1016/j.tet.2007.10.033

Hwang, K.-O., and Lightner, D. A. (1994). Synthesis and spectroscopic properties of N,N-bridged dipyrrinones. *Tetrahedron* 50 (7), 1955–1966. 10.1016/S0040-4020(01)85059-6

Kneip, C., Hildebrandt, P., Schlamann, W., Braslavsky, S. E., Mark, F., and Schaffner, K. (1999). Protonation state and structural changes of the tetrapyrrole chromophore during the Pr → Pfr phototransformation of Phytochrome: A resonance Raman spectroscopic study. *Biochemistry-Us* 38 (46), 15185–15192. doi:10.1021/bi990688w

Lamola, A. A., Braslavsky, S. E., Schaffner, K., and Lightner, D. A. (1983). Spectral study of the photochemistry of dipyrrole models for bilirubin bound to human serum albumin. *Photochem. Photobiol.* 37 (3), 263–270. doi:10.1111/j.1751-1097.1983.tb04471.x

Lamparter, T., Mittmann, F., Gärtner, W., Börner, T., Hartmann, E., and Hughes, J. (1997). Characterization of recombinant phytochrome from the cyanobacterium Synechocystis. *Proc. Natl. Acad. Sci. USA* 94 (22), 11792. doi:10.1073/pnas.94.22.11792

Lyskov, I., Anda, A., Wong, Y. X., Tilley, A. J., Hall, C. R., Thia, J., et al. (2020). Bilirubin analogues as model compounds for exciton coupling. *Phys. Chem. Chem. Phys.* 22 (27), 15567–15572. doi:10.1039/d0cp01421d

MacColl, R. (1998). Cyanobacterial phycobilisomes. *J. Struct. Biol.* 124 (2–3), 311–334. doi:10.1006/jsbi.1998.4062

Mardelli, M., and Olmsted, J. (1977). Calorimetric determination of the 9,10-diphenyl-anthracene fluorescence quantum yield. *J. Photochem.* 7(4), 277–285. 10.1016/0047-2670(77)85005-3

Mazzoni, M., Agati, G., Troup, G. J., and Pratesi, R. (2003). Analysis of wavelength-dependent photoisomerization quantum yields in bilirubins by fitting two exciton absorption bands. *J. Opt. A-Pure Appl. Op.* 5 (5), S374–S380. doi:10.1088/1464-4258/5/5/395

Mirkovic, T., Ostroumov, E. E., Anna, J. M., van Grondelle, R., Govindjeeand Scholes, G. D. (2017). Light absorption and energy transfer in the antenna complexes of photosynthetic organisms. *Chem. Rev.* 117 (2), 249–293. doi:10.1021/acs.chemrev.6b00002

Molday, R. S., and Moritz, O. L. (2015). Photoreceptors at a glance. *J. Cell Sci.* 128 (22), 4039. doi:10.1242/jcs.175687

Owrutsky, J. C., Raftery, D., and Hochstrasser, R. M. (1994). Vibrational-relaxation dynamics in solutions. *Annu. Rev. Phys. Chem.* 45, 519–555. doi:10.1146/annurev.physchem.45.1.519

Palczewski, K. (2012). Chemistry and biology of vision. *J. Biol. Chem.* 287 (3), 1612–1619. doi:10.1074/jbc.R111.301150

Polli, D., Altoè, P., Weingart, O., Spillane, K. M., Manzoni, C., Brida, D., et al. (2010). Conical intersection dynamics of the primary photoisomerization event in vision. *Nature* 467 (7314), 440–443. doi:10.1038/nature09346

Rockwell, N. C., Su, Y.-S., and Lagarias, J. C. (2006). Phytochrome structure and signaling mechanisms. *Annu. Rev. Plant Biol.* 57 (1), 837–858. doi:10.1146/annurev.arplant.56.032604.144208

Rohmer, T., Strauss, H., Hughes, J., de Groot, H., Gärtner, W., Schmieder, P., et al. (2006). 15N MAS NMR studies of Cph1 Phytochrome: chromophore dynamics and intramolecular signal transduction. *J. Phys. Chem. B.* 110 (41), 20580–20585. doi:10.1021/jp062454

Sakata, Y., Fukushima, S., Akine, S., and Setsune, J.-i. (2016). Solvent-dependent dual-mode photochromism between T- and P-types in a dipyrrinone derivative. *Chem. Commun.* 52(6), 1278–1281. doi:10.1039/c5cc07625k

Scheer, H. (1991). *Chlorophylls*. Boca Raton, Fla: CRC Press.

Scholes, G. D., Mirkovic, T., Turner, D. B., Fassioli, F., and Buchleitner, A. (2012). Solar light harvesting by energy transfer: from ecology to coherence. *Energ. Environ. Sci.* 5 (11), 9374–9393. doi:10.1039/C2ee23013e

Snellenburg, J. J., Laptenok, S. P., Seger, R., Mullen, K. M., and van Stokkum, I. H. M. (2012). Glotaran: a java-based graphical user interface for the R package TIMP. *J. Stat. Softw.* 49 (3), 1–22. doi:10.18637/jss.v049.i03

Tang, K., Ding, W.-L., Höppner, A., Zhao, C., Zhang, L., Hontani, Y., et al. (2015). The terminal phycobilisome emitter, L_{CM}: a light-harvesting pigment with a phytochrome chromophore. *Proc. Natl. Acad. Sci. USA* 112 (52), 15880–15885. doi:10.1073/pnas.1519177113

Toa, Z. S. D., Dean, J. C., and Scholes, G. D. (2019). Revealing structural involvement of chromophores in algal light harvesting complexes using symmetry-adapted perturbation theory. *J. Photochem. Photobiol. B* 190, 110–117. 10.1016/j.jphotobiol.2018.11.007

Turro, N. J., Ramamurthy, V., and Scaiano, J. C. (2010). *Modern molecular photochemistry of organic molecules*. Sausalito, CA: University Science Books.

Ulijasz, A. T., and Vierstra, R. D. (2011). Phytochrome structure and photochemistry: recent advances toward a complete molecular picture. *Curr. Opin. Plant Biol.* 14(5), 498–506. doi:10.1016/j.pbi.2011.06.002

Wang, Q., Schoenlein, R. W., Peteanu, L. A., Mathies, R. A., and Shank, C. V. (1994). Vibrationally coherent photochemistry in the femtosecond primary event of vision. *Science* 266 (5184), 422. doi:10.1126/science.7939680

Wiebeler, C., Rao, A. G., Gärtner, W., and Schapiro, I. (2019). The effective conjugation length is responsible for the red/green spectral tuning in the cyanobacteriochrome Slr1393g3. *Angew. Chem. Int. Edit.* 58 (7), 1934–1938. 10.1002/anie.201810266

Wientjes, E., van Amerongen, H., and Croce, R. (2013). Quantum yield of charge separation in photosystem II: functional effect of changes in the antenna size upon light acclimation. *J. Phys. Chem. B.* 117 (38), 11200–11208. doi:10.1021/jp401663w

Xu, X., Höppner, A., Wiebeler, C., Zhao, K.-H., Schapiro, I., and Gärtner, W. (2020). Structural elements regulating the photochromicity in a cyanobacteriochrome. *Proc. Natl. Acad. Sci. USA* 117 (5), 2432–2440. doi:10.1073/pnas.1910208117

Zhao, Y., and Truhlar, D. G. (2007). Density functionals for noncovalent interaction energies of biological importance. *J. Chem. Theory Comput.* 3 (1), 289–300. doi:10.1021/Ct6002719

Zietz, B., and Blomgren, F. (2006). Conical intersection in a bilirubin model – a possible pathway for phototherapy of neonatal jaundice. *Chem. Phys. Lett.* 420 (4), 556–561. 10.1016/j.cplett.2006.01.028

Zietz, B., and Gillbro, T. (2007). Initial photochemistry of bilirubin probed by femtosecond spectroscopy. *J. Phys. Chem. B.* 111 (41), 11997–12003. doi:10.1021/jp073421c

Advantages of publishing in Frontiers

OPEN ACCESS
Articles are free to read
for greatest visibility
and readership

FAST PUBLICATION
Around 90 days
from submission
to decision

HIGH QUALITY PEER-REVIEW
Rigorous, collaborative,
and constructive
peer-review

TRANSPARENT PEER-REVIEW
Editors and reviewers
acknowledged by name
on published articles

Frontiers
Avenue du Tribunal-Fédéral 34
1005 Lausanne | Switzerland

Visit us: www.frontiersin.org
Contact us: frontiersin.org/about/contact

**REPRODUCIBILITY OF
RESEARCH**
Support open data
and methods to enhance
research reproducibility

DIGITAL PUBLISHING
Articles designed
for optimal readership
across devices

FOLLOW US
@frontiersin

IMPACT METRICS
Advanced article metrics
track visibility across
digital media

EXTENSIVE PROMOTION
Marketing
and promotion
of impactful research

LOOP RESEARCH NETWORK
Our network
increases your
article's readership